DISSERTATION

Engineering high bandwidth semiconductor mid-infrared frequency combs

ausgeführt zum Zwecke der Erlangung des akademischen Grades eines Doktors der technischen Wissenschaften

unter der Leitung von

Associate Prof. Dr. Benedikt Schwarz
Institut für Festkörperelektronik

eingereicht an der

Technischen Universität Wien
Fakultät für Elektrotechnik und Informationstechnik

von

Maximilian Ludwig Beiser, MSc

Mat.Nr. 01215025

Götzis, 6.6.2023

Supervisor:	Assoc. Prof. Dipl.-Ing. Dr. Benedikt Schwarz
Co-Supervisor:	Assoc. Prof. Aaron Maxwell Andrews, PhD
1. Appraiser:	Associate Prof. Dr. Thomas Fromherz
2. Appraiser:	ao. Univ.-Prof. Dr. Patricia Lustoza de Souza
Tag der mündlichen Prüfung:	23.06.2023

"What could we do with layered structures with just the right layers? What would the properties of materials be if we could really arrange the atoms the way we want them?"

Richard P. Feynman, 1959

Kurzfassung

Lichtquellen im mittleren Infrarot sind sehr interessant für spektroskopische Anwendungen. Quantenkaskadenlaser (QCL) und Interbandkaskadenlaser (ICL) sind monolithische Bauelemente die Emissionswellenlängen im mittleren Infrarot anbieten mit einem hohen Grad an Flexibilität eben diese zu adaptieren. Seit den ersten erfolgreichen Experimenten haben sie sich sehr rasch entwickelt und moderne Geräte können sogar die gleichen Wellenlängen detektieren die sie emittieren. Der Betrieb der Laser auf dem Chip hängt stark von ihrem Stromverbrauch ab, dabei sind ICLs im Vergleich zu QCLs besser. ICLs haben einen optimalen Betriebspunkt zwischen 3-4 µm und werden mit Epitaxie meist auf GaSb gewachsen. Abgesehen von den meist auf GaSb basierenden ICLS, gibt es seit einigen Jahren auf Entwicklungen auf InAs mit vielversprechenden Ergebnissen jenseits des optimierten 4 µm Betriebspunkts. In dieser Arbeit wird eine neue Methode zur Kompensation der durch die InGaSb Schicht induzierten Verspannung vorgestellt. Eine zusätzliche Schicht aus InAlAs erlaubt das Wachstum von sehr hohen kumulierten Schichtdicken. Neue numerische Erkenntnisse wurden zusammengefasst zu einer Anleitung wie die Bandbreite von Quantenkaskadenlaserfrequenzkämmen verändert werden kann. Frequenzkämme sind Laser die eine Vielzahl äquidistanter Moden emittieren. Der Abstand zwischen den Moden ist die Umlaufzeit des Resonators. Aufbauend auf der Opacak-Schwarz Mastergleichung wurde die Wechselwirkung der intrinsischen Kerr Nichtlinearität und der Gruppendispersion untersucht. Die numerische Studie zeigte, dass der Laser durch Kompensation der Nichtlinearität mit Dispersionskompensation in einen FM Kamm Zustand gebracht werden kann. Es wurde zusätzlich gezeigt, dass im Widerspruch zu weitverbreiteten Methoden es nicht von Vorteil ist, nur die Facetenreflektivitäten zu verändern, um den Laser in einen gesperrten Laserzustand zu bringen. Der Bereich in dem der Laser eine hohe Anzahl von Moden emittiert ist überraschend schmal. Der Laser kann in diesen Parameterbereich mit niedrigen Reflektivitäten und hohen Kerr Nichtlinearitäten gebracht werden. Die beste vorgestellte Methode um hohe Bandbreiten in QCLs zu erzielen, war die Modulation des Resonators mit einer Radiofrequenz nahe zur Umlaufzeit. Die experimentelle Implementierung ist einfach und erlaubt die vollständige Rückgewinnung der ungesperrten Laserbandbreite. Der Transfer dieser experimentellen Methode von QCLs zu ICLs zeigte Pulsemission, die mit Verschobener Welleninterferenz Fouriertransformierter Spektroskopie charakterisiert wurde. Die Messungen zeigten Pulsbreiten unterhalb von Pikosekunden und einem frequenzmodulierten Kamm Zustand mit Injektionsverriegelung. Ein technologischer Meilenstein wurde mit dem erfolgreichen Wachstum und Betrieb eines Mehrstapel THz QCLs geschafft. Die emittierte Bandbreite von 1.37 optischen Oktaven mit einer Breite von 1.9 zu 4.5 THz, setzte einen neuen Meilenstein und stellt einen weiteren Schritt zum Schliessen der Terahertzlücke dar. Das Ziel dieser Arbeit ist es einerseits eine neue Verspannungskompen-

sationmethode zu diskutieren und andererseits die Möglichkeiten von Interbandkaskadenlasern als Plattform für zukünftige hochintegrierte Sensoren aufzuzeigen. Das zweite Ziel ist die Untersuchung wie man allgemein breitbandige Laser Frequenzkämme im mittleren Infrarot herstellt, ausgehend vom Kristallwachstum Oktaven überspannender THz QCLs, über die Herstellung von QCL Ringkämmen die die Verbindung von Chaostheorie mit Frequenzkammphysik erlaubten, bis hin zu Experimenten mit ICL Frequenzkämmen und ultrakurzer Pulsemission.

Abstract

Light sources in the mid-infrared are of great interest for spectroscopic sensing. Quantum Cascade Lasers (QCL) and Interband Cascade Lasers (ICL) are monolithic devices that offer emission wavelengths in the mid-infrared and a high level of flexibility to design devices for applications. Since their first experimental demonstrations they developed rapidly and state of the art devices can detect the same wavelength as they emit. On-chip operation of devices strongly depends on the power consumption of the device, there ICLs intrinsically do better than QCLs. ICLs own a sweet spot between 3-4 µm and are grown epitaxially mostly on GaSb substrates. Aside from the commonly used GaSb-based ICLs, recent developments on InAs showed promising results for emission beyond the 4 µm sweet spot. In this work a novel scheme to compensate for the InGaSb induced strain in the heterostructure is established. Inserting an additional layer of InAlAs allowed the growth of high cumulative InAs heterostructures. New numerical insights were summarized in a guideline how to engineer the bandwidth of quantum cascade laser frequency combs. Frequency combs are lasers that emit a number of equidistant modes. The spacing between this modes equals the cavity roundtrip time, which allows to use this lasers as rulers in the frequency domain. An important aspect of this technology is the bandwidth of the comb. Based on the Opacak-Schwarz master equation the interplay of the intrinsic Kerr nonlinearity with the group velocity dispersion was examined. The numerical study revealed that the laser can be brought to a FM comb state with dispersion compensation of the Kerr nonlinearity. It was explored that contradictory to commonly used methods, it is not useful to solely change the reflectivities of one facet to tune the laser into a locked laser state. The regime where a locked laser state emits a high number of modes was found to be surprisingly narrow. The laser can be tuned into this parameter space with low reflectivities and high Kerr nonlinearities. The best method to achieve high bandwidth emission in QCLs was demonstrated to inject a RF signal close to the cavity roundtrip time. The experimental implementation is straight forward and allows to recover the unlocked laser state bandwidth. The transfer of this experimental technique from QCLs to ICLs showed pulse emission, that was characterized by Shifted Wave Interference Fourier Transform Spectroscopy. The measurements showed pulse widths below picoseconds and a FM comb state with injection locking. A breakthrough was achieved with the successful growth and operation of a multistack THz QCL structure. The emitted bandwidth was 1.37 optical octaves spanning from 1.9 to 4.5 THz. In addition the engineering of broadband laser frequency combs in the mid-infrared is discussed, ranging from high performance fabrication of quantum cascade laser frequency combs to MBE growth of ultrabroadband THz QCLs. The results of this work connected on the one hand chaos theory with frequency comb physics and on the other hand, set a new milestone for the bandwidth of THz QCL.

CONTENTS

CHAPTER

ONE

INTRODUCTION

The contemporary world heavily relies on advanced technology and precise engineering to address daily challenges and provide solutions to society. The trend towards digitization and interconnectivity drives the demand for integrated systems on handheld devices. Industry 4.0 and the Internet of Things (IoT) will significantly impact daily life, encompassing automation and decentralized healthcare. The next frontier of this interconnected, individualized healthcare system involves the detection and analysis of bodily parameters through digital handheld devices. While capacitive sensors are the current standard in industry, mid-infrared spectroscopy presents a refined method to enhance precision and measurement accuracy for laser-based sensing devices. The electromagnetic infrared spectrum, ranging from 850 nm to 300 µm, contains characteristic vibrational and rotational absorption lines of a multitude of molecules and biomolecular markers. Figure 1.1 illustrates the spectral region from 3.5 µm to 12.5 µm, displaying selected absorption lines.

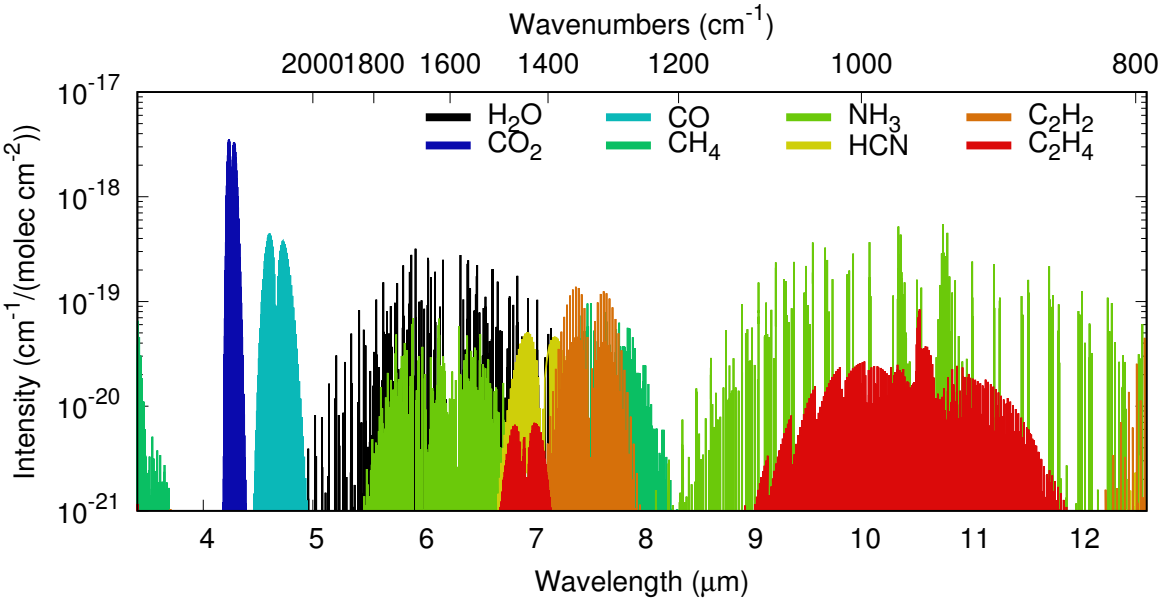

Figure 1.1: Absorption lines of different molecules in the mid-infrared spectral region. Note, carbondioxide has a strong absorption line around 4.2 µm, ethene a broad absorption profile from 9 to 12 µm. Figure reproduced with data from HITRAN [1].

The infrared (IR) region is a part of the electromagnetic spectrum with a frequency range of approximately 10^{14} to 10^{16} Hz, or wavelengths ranging from about 750 nm to 1 mm. Infrared radiation is emitted by all objects with temperatures above absolute zero, making it a valuable tool for sensing and imaging in many fields, including physics, chemistry, biology, and engineering. The infrared region can be divided into several branches based on its wavelength range:

- Near-infrared (NIR): Wavelengths ranging from 750 nm to 2500 nm. This branch of IR is commonly used in applications such as remote sensing, medical imaging, and spectroscopy.
- Mid-infrared (MIR): Wavelengths ranging from 2500 nm to 50 µm. MIR spectroscopy is used to identify and quantify specific chemical compounds based on their absorption lines in the electromagnetic spectrum.
- Far-infrared (FIR): Wavelengths ranging from 50 µm to 1 mm. FIR radiation is used in a variety of applications, including thermal imaging, spectroscopy, and astronomical observations.

Each branch of the infrared region has unique properties and applications, making it an important tool for a wide range of scientific and technological fields. The Terahertz gap refers to the frequency range between microwaves and infrared light in the electromagnetic spectrum, which is approximately 0.1 to 10 THz. This region is referred to as a "gap" because of the difficulty in generating, detecting, and measuring signals in this frequency range. The main challenges in the terahertz gap include the lack of efficient sources and

detectors, as well as the low interaction of terahertz radiation with matter. Additionally, the materials used in conventional microwave and infrared devices do not operate effectively in this frequency range, leading to difficulties in device design and fabrication. Despite these challenges, the terahertz gap has garnered significant interest due to its potential applications in various fields, such as medical imaging, non-destructive testing, and spectroscopy. Advances in technology, such as the development of new sources and detectors, are helping to overcome the limitations posed by the terahertz gap and unlock its potential for a range of applications. Controlled light emission and detection in the mid-infrared, commonly referred to as the "molecular fingerprint region," is especially relevant for medical applications, breath gas analysis, free-space communications, and extraplanetary missions [2, 3, 4]. To make these applications possible, multiple technological milestones have been achieved. One such milestone was the invention of the first ruby laser in 1960 by Maiman, which opened up the possibility of using lasers as tools and for fundamental research. This invention was referred to as a "solution looking for a problem" [5]. This event marked a significant milestone in the history of laser technology and paved the way for further developments in this field. Over the next few decades, laser technology advanced rapidly and expanded into new areas of application. In the late 1960s and early 1970s, the first gas and semiconductor lasers were developed, which led to the creation of compact, low-cost laser systems. The widespread use of lasers in areas such as communication, manufacturing, and medical applications led to the development of more efficient and versatile laser systems. In the 1980s and 1990s, the development of fiber-optic communication systems made it possible to transmit laser signals over long distances using optical fibers. This paved the way for the widespread use of lasers in telecommunications and paved the way for the Internet as we know it today. In recent years, laser technology has continued to evolve and expand into new areas of application. The development of high-powered, ultrafast lasers has made it possible to perform precise cutting and welding operations in manufacturing, while advances in laser medicine have made it possible to perform minimally invasive surgical procedures with high precision. The future of laser technology appears promising, with advancements in areas such as quantum computing and photonics poised to disrupt numerous industries. Among the laser types attracting significant interest for these applications is the Quantum Cascade Laser.

Quantum Cascade Laser A tailorable source of light that is capable of exciting atomic states and furthermore function as a versatile high precision tool was an overarching goal in science for decades. The first semiconductor lasers quickly evolved to a a technological platform for electrical pumped compact devices with large optical gain. Along with the subsequent developments around semiconductor heterostructures and the increasing knowledge about laser dynamics, another technology appeared that multiplied the degrees

of freedom for scientists. The development of molecular beam epitaxy (MBE) of A. Y. Cho and J. R. Arthur [6] allowed crystal growth with atomic precision. The exceptional control of layer thickness and layer composition of semiconductor heterostructures was a quantum leap for the research community. Epitaxy provided the possibilities to design fundamentally new concepts for semiconductors. The ability to engineer and design heterostructures with nanometer thick layers, which can be varyed with different material compositions, induced world records in high mobility electronics and allowed novel transistor technologies for computers [7].

The proposal of Kazarinov and Suris for light amplification in semiconductor heterostructures [8] showed the feasability of population inversion in a biased superlattice. The experimental observation of serial tunneling in superlattices [9] hinted a first idea of a staircase-like energy structure [10]. Still the scientific community had to wait for nearly a decade to see the first working cascaded laser heterostructure in 1994 by Faist et al.[11], which was titled the quantum cascade laser (QCL). The first functional device was operated at 10 K with an efficiency of 0.15%. Later on also single mode emission was achieved by using a DFB grating [3]. Subsequent developments lowered threshold current densities and increased the power output. State-of-the-art devices exceeded Watt level power outputs and reached wall plug efficiencies of up to 25 % [12]. A principle design and working scheme is shown in figure 1.2. Another cascade laser is the formerly labelled type-II quantum cascade laser, the interband cascade laser (ICL) proposed by Yang in 1995 [13].

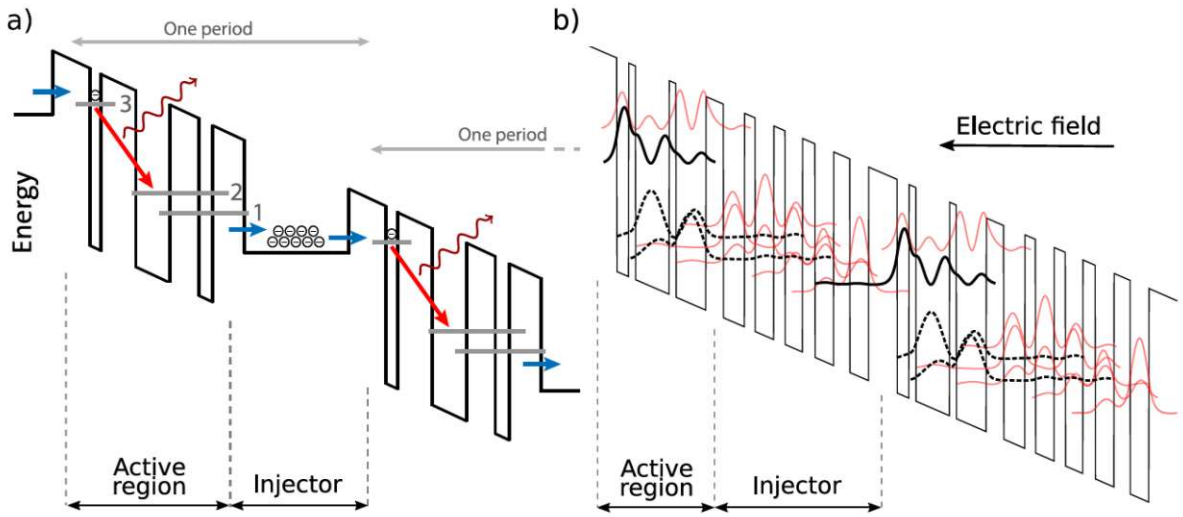

Figure 1.2: QCL active region in a heterostructure. a) Operation principle in the conduction band. The injector forward the electrons towards their transition down the biased cascade. The active transition from energy level 1 to energy level 2 emits a photon. The injector extracts the transitioned electron. b) Band structure of a three well active region design of a QCL. Figure reproduced with permission from [14].

Interband Cascade Lasers In the shadow of the rapid progress of QCLs towards room-temperature operation in continuous wave mode [15], the epitaxially more complex interband lasers lacked research and effort, as epitaxial growth of antimonide based devices on a competitive level to arsenide based devices is extraordinarily challenging. The material system on GaSb or InAs as substrate has mixed group V interfaces, which induce a manifold of problems for controlled growth parameters. Furthermore the ICL combines a type-II broken bandgap with an interband transition (InAs/GaSb) and the cascading principle of QCLs in the same device. A semimetallic-interface (InAs/GaSb) generates holes and carriers, which are forwarded by related injectors towards the lasing interband transition, which consists of a W-style based quantum well with InAs/InGaSb/InAs layers. A more detailled explaination of device principles will be given later on in chapter 2. The first experimental demonstration of an ICL was achieved in 1997 [16] (see figure 1.3), although limited to cryogenic temperatures. Multiple design improvements of the band structure for gain region, the hole injector and novel carrier rebalancing[17] was introduced. The modern state-of-the-art ICL can operate at room temperature and in continuous wave mode, reaching a maximum power output of several hundred milliwatts. In combination with their low power threshold power density, applications on the NASA mars rover missions highlight future possibilities in remote gas sensing [4]. Aside from the application point of view, in a technological context ICLs have been grown dominantly on GaSb as substrate, only in the last decade, first experiments with InAs-based ICL were performed by Rui Yang et al. [18]. Changing the substrate from GaSb to InAs allows to optimize the device for long wavelength emission beyond the 3 - 4 µm sweet spot. In combination with their low-power consumption, this would allow for exciting integrated solutions for handheld sensing devices.

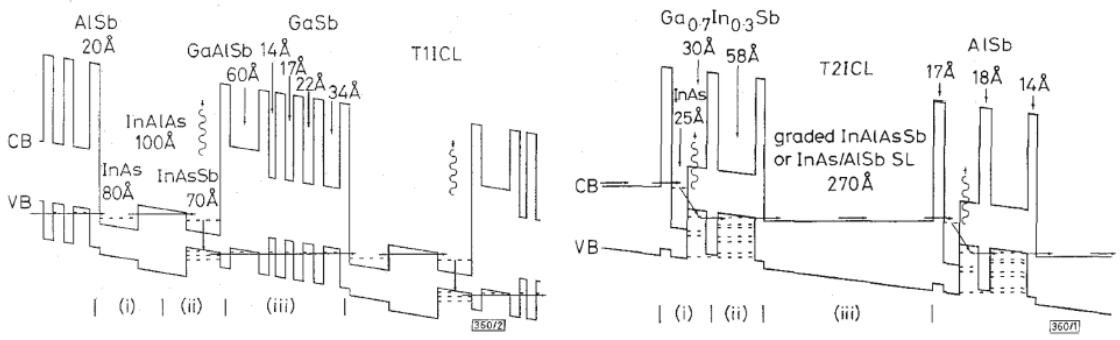

Figure 1.3: First schematic suggestion of a type-II broken bandgap cascade laser. Figure reproduced with permission from [13].

A recent proposal suggests the possibility of ICLs in the SiGeSn system, offering fascinating potential for scalability of production and integration [19]. An experimental demonstration is still missing, it can be assumed that transferring type-II broken bandgaps

from III-V to silicon based fabrication is a non trivial task. From an application based point of view, one of the most appealing recent developments are ICL frequency combs, where ICLs are injection locked to function as a ruler in the frequency domain [20, 21]. Such techniques could be emphasized to use this laser type for integrated dual-comb spectroscopy.

Frequency Combs Optical frequency combs consist of equidistantly spaced laser lines with a governing phase relation of the neighboring laser frequency comb modes. The intrinsic link of optical frequencies to radio frequencies lead to high precision measurements with a novel metrology tool [22]. Semiconductor laser frequency combs are the scaled down, compact, cheap and electrically pumped realization of the former table top sized experimental setup. Despite the high usability of laser systems like ICLs or QCLs for spectroscopy, the requirement to measure gases or liquids on-chip in the molecular fingerprint region requires highly precise measurements of their absorption lines. The invention of frequency combs in the early 2000s paved the way towards unmatched precision in physics [23, 24]. The discovery of QCL frequency combs in 2012 brought frequency combs another step closer towards integrated on-chip spectroscopy [25]. The applications range from single shot sub-microsecond mid-IR spectroscopy on proteins with QCL combs [26] to the search for exoplanets with microresonator based frequency combs [27]. The first ICL frequency comb was passively mode-locked [20] and did not show conclusive proof of comb operation. The rigorous experimental investigation of ICL combs with a novel method to characterize its coherence, revealed a pulse width in the picosecond range [28]. An outstanding and appealing application of frequency combs is dual-comb spectroscopy in the mid-infrared. The combination of of broad optical spectra and high brightness with the intrinsic equidistance in the frequency domain allows the detection of fundamental rovibrational lines. The working scheme is the combination of two combs with different repetition frequencies by a beam splitter and the detection on a photodetector (figure 1.5). The two combs differ in path and slightly in their repetition frequency. One comb shines through an interaction region with the analyte and the other comb works as a local oscillator reference. The reference combs beam is also detected on the reference photodetector. The sample interaction shows in the intensity difference of the combined comb spectrum (figure 1.5 a) [30], [31], [32].

1.1 Motivation and outline

An integrated on-chip laser light source with emission in the mid-infrared that is capable of being operated as frequency comb, holds a promising potential for integrated frequency comb spectroscopy. The power efficiency of ICLs in combination with the powerful concept of dual-comb spectroscopy offers an exciting perspective for handheld battery driven

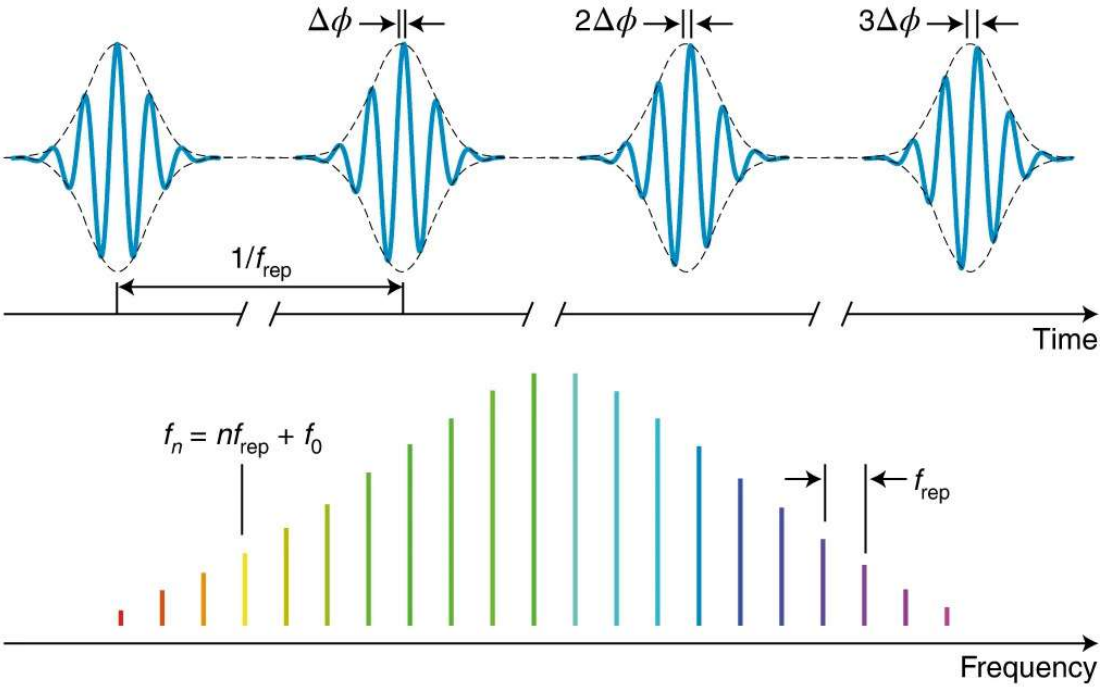

Figure 1.4: Top: Time-domain output of a mode-locked laser. The train of pulses is separated by the inverse repetition frequency. The electric field of the pulse differs by the carrier-envelope offset phase $\Delta\phi_{CEO}$. In the frequency domain this gives the characteristic 'ruler' with the equidistant separation of the adjacent teeth of the comb $f_n = nf_{rep} + f_0$. Figure reproduced from [29] with permission of the Springer Nature group (2012).

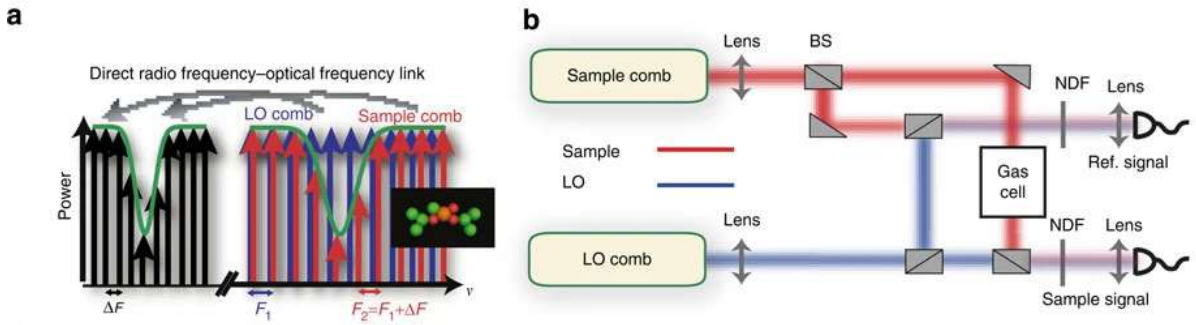

Figure 1.5: Working principle of dual comb spectroscopy. (a) Two frequency combs with detuned comb spacings induce a heterodyne beating on a fast detector. The absorption curve of the sample utters in the intensity difference of the difference signal. (b) The sample comb beam and the local oscillator (LO) omb beam are combined by a beamsplitter (BS) and shine on a photodetector. Figure reproduced from [33] with permission from Springer Nature group (2014).

devices. The mature technology of semiconductor manufacturing and the principle of measuring frequencies with a laser as a 'ruler' promises the availability of a highly integrated spectroscopy systems on a single chip. This could potentially allow to analyse biomarkers in breath-gas on a mobile phone or portable device. In the age of digitalization and industry 4.0 this could be a potential mass market application and open up a multibillion dollar industry.

This work intends to cover the fabrication technology of high performance lasers that can be operated as frequency combs and give insight into the growth of III-V materials especially for interband cascade devices. Current technology is lacking high bandwidth frequency combs in the mid-infrared to extend the capabilities of on-chip spectroscopy to a higher number of detectable molecules. The thesis is structured as follows. Starting with a look at the theoretical basics of semiconductor heterostructures 2, cascade devices will be investigated regarding physics and concepts relevant to this work. In chapter 3 the fundamentals of crystal growth with molecular beam epitaxy are discussed and non-destructive characterization methods discussed in chapter 4. Chapter 5 gives an overview into the crystal growth and its challenges of InAs-based heterostructures for interband devices. A novel method for strain compensation in ICLs is proposed and successfully tested on a model-system. Chapter 6 gives an overview of the authors work about integrated frequency combs. It highlights the possibilities for extraordinarily difficult characterization methods supported by excellent fabrication and growth. Chapter summarizes the efforts on the fabrication and characterization of high performance interband cascade laser frequency combs. The closing comment in chapter 8 concludes this work and embraces the outlook for implications of the achievements into further research and ongoing projects. Standard fabrication recipes and growth sheets of the most relevant heterostructures can be found in the appendix.

CHAPTER

TWO

PRINCIPLES OF CASCADE LASERS AND FREQUENCY COMBS

This chapter discusses the working principles and theoretical basics of quantum cascade devices. Starting with an overview over the electronic properties of semiconductor heterostructures we will lay the groundwork for understanding the working principles of Quantum Cascade Lasers (QCL) and Interband Cascade Lasers (ICLs) as well as the fundamentals of frequency combs. Understanding the underlying physics of QCLs and ICLs allows for engineering of band structures and tailoring of their optoelectronic properties to required specifications for potential applications.

2.1 Bulk semiconductor crystals

Our examination of semiconductor physics starts with the consideration of a bulk crystal. The definition of a crystal is the periodic spatial arrangement of atoms in a lattice, where the length scale of the periodic lattice is much larger than the interatomic separation distance. Material properties do not solely depend on the type of elements in the crystal lattice, but are also strongly influenced by their spatial arrangement. The majority of physical effects in crystals can be traced back to their periodicity. One can describe the crystal atoms as points shifted by a translation vector

$$\mathbf{T} = n_1\mathbf{a}_1 + n_2\mathbf{a}_2 + n_3\mathbf{a}_3, \tag{2.1}$$

where $\mathbf{a}_i$ are the primitive vectors of the Bravais lattice and n_i are integer numbers. This unit cell is repeating the lattice without overlap or void into the next neighbor cell. A Bravais lattice is therefore an infinite array of atoms with their corresponding translation points [34]. The primitive vectors can differ, leading to different Bravais lattices. Its primitive vectors allow for 14 different symmetry groups and therefore 14 different dif-

ferent Bravais lattices. The symmetry can be primitive, body centered, base centered or face centered. The unit cell can be cubic, tetragonal, orthorhombic, rhombohedral, monoclinic, triclinic or hexagonal. Most III-V semiconductors crystallize in the zincblende crystal structure (figure 2.1). The zincblende structure is a face centered cubic unit

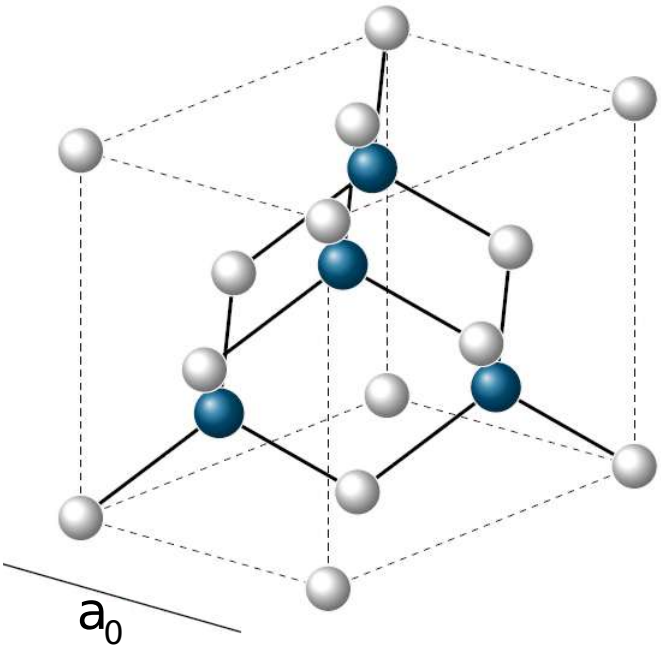

Figure 2.1: Unit cell of the zincblende crystal structure. The lattice constant a_0 gives the constant between neighboring same-element atoms. Figures produced by the author himself.

cell with sublattices. The sublattice in this case is occupied with different atoms from group III and group V. Semiconductors can be distinguished to elemental and compound semiconductors. Elemental semiconductors are for instance Si, Ge and Sn. Compound semiconductors can be built from II-VI or III-V elements. Figure 2.2 shows an overview of the periodic table for III-V semiconductors.

2.1.1 Reciprocal lattice

Equation 2.1 describes the crystal lattice in real space, but one can also express it in terms of energy. Asides from the description of a crystal lattice in real space as in equation 2.1,

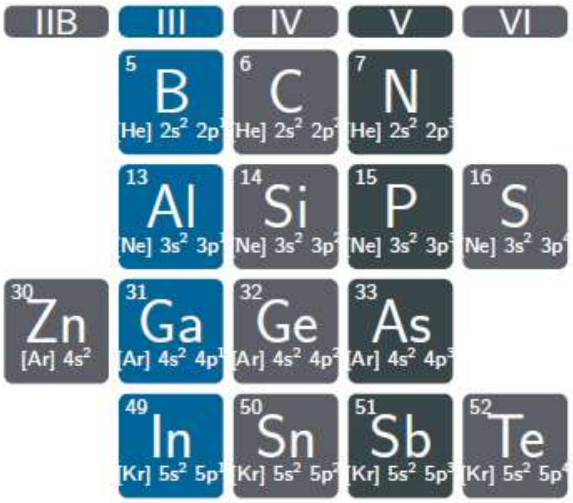

Figure 2.2: Excerpt of the periodic system, where the third (blue) and fifth (black) main group elements can be used for compound III-V semiconductors.

a periodic arrangement can be also described as

$$e^{i\mathbf{K}\cdot(\mathbf{r}+\mathbf{T})} = e^{i\mathbf{K}\cdot(\mathbf{r})}, \tag{2.2}$$

with the plane wave $e^{i\mathbf{K}\cdot(\mathbf{r})}$ [35, 36].

This representation is the reciprocal lattice, the Fourier transform of the real space definition in equation 2.1. Its construction can be done too with primitive vectors by the relation

$$\mathbf{b}_i = 2\pi \frac{(\mathbf{a}_j \times \mathbf{a}_k)}{(\mathbf{a}_1 \times \mathbf{a}_2)\cdot \mathbf{a}_3}. \tag{2.3}$$

Reciprocal lattice vector correspond to parallel lattice planes of the Bravais lattice with a separation distance of $2\pi/|\mathbf{k}|$.

2.1.2 Directions and planes in crystals

The planes in a crystal lattice need to be defined in a relation to their primitive vectors or the reciprocal lattice [37]. One method to give information about the reference plane of the crystal structure can be given with indices. The so called Miller indices are a set

of three integer numbers

$$(hkl) = \left(\frac{a_1}{x_1} + \frac{a_2}{x_2} + \frac{a_3}{x_3}\right), \tag{2.4}$$

reduced to their lowest value of the primitive vector $a_i = |\mathbf{a_i}|$. A different interpretation is to see the indices as coefficients for a linear combination of reciprocal lattice vectors

$$\mathbf{G} = h\mathbf{b}_1 + k\mathbf{b}_2 + l\mathbf{b}_3. \tag{2.5}$$

Figure 2.3 shows three important planes for a simple cubic unit cell. If a plane is parallel to a primitive vector, therefore parallel to a crystal orientation, the Miller index is 0. The index can also be negative, this is noted as bar on top of the number $(\bar{1}10)$. Crystal planes can also be symmetric and then equivalent as a set, e.g. the simple cubic unit cell owns (100), (010), (001), $(\bar{1}00)$, $(\ 0\bar{1}0)$, and $(00\bar{1})$ which are denoted as {100} planes. The planes of a crystal are important for instance for ordering substrate material for crystal growth, the plane orientation can determine the epitaxial growth mode. In figure 2.4 three commonly used wafer orientations are displayed.

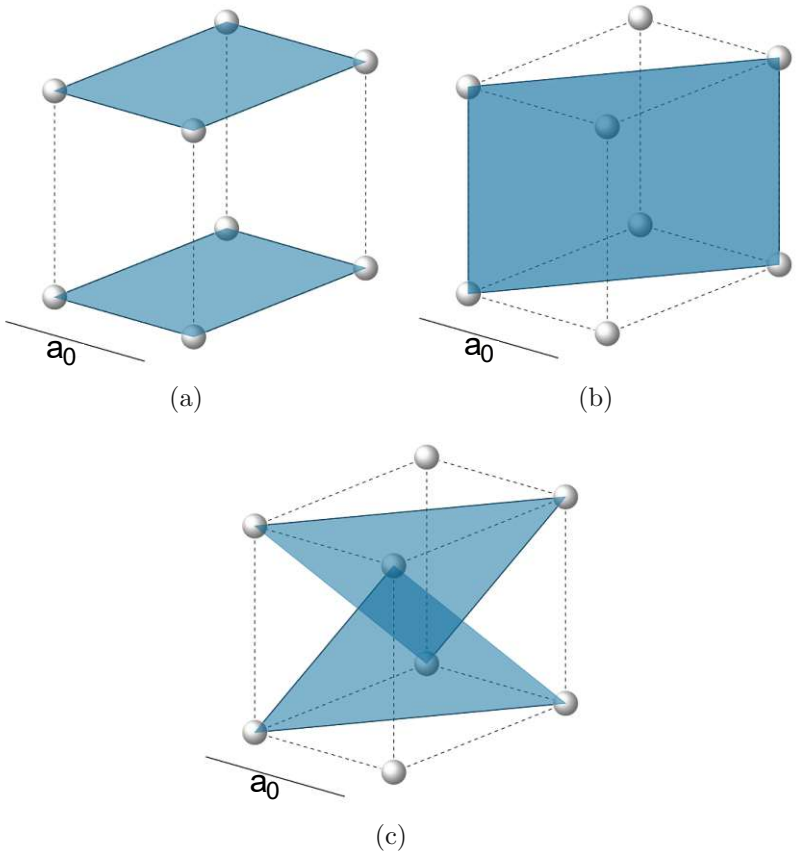

(a) (b) (c)

Figure 2.3: (a) (100) (b) (110) (c) (111) crystal planes in a basic cubic cell with the lattice constant a_0.

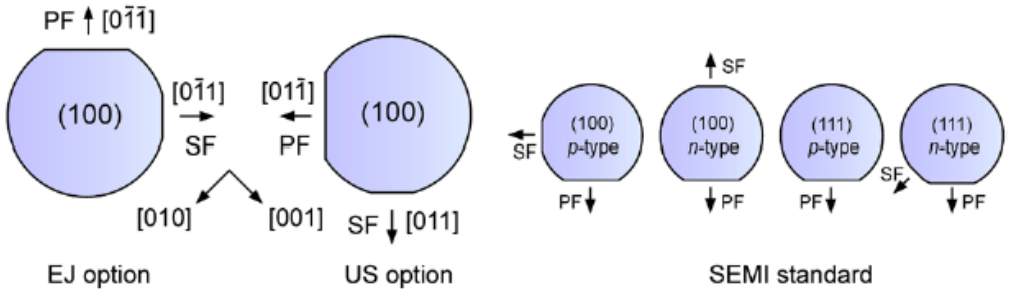

Figure 2.4: Crystal plane orientation of wafers for semiconductor manufacturing. Options depend on the country of origin and the desired doping (p- or n-type). Figure reproduced from [38] with permission from Springer Nature Group (2020).

2.2 Electronic bandstructure of semiconductor heterostructures

The following section discusses the electronic bandstructure and useful approximations for heterostructures restricted to one dimension. In the case of layer thicknesses in the range of the thermal de-Broglie wavelength, quantization effects have to be considered. Hereby quantum mechanics gives valuable insights for engineering and tailoring of electronic properties of heterostructures. If the thickness of layers approaches the thermal de-Broglie wavelength, it leads to quantization effects. Its theoretical treatment can give insights for engineering purposes and tailor the electronic properties of the heterostructure.

2.2.1 Band alignment of heterostructures

Combining different materials introduces heterogenities and thereby band discontinuities. The relative thickness and composition of different material systems to each other is important as exactly this allows to engineer the energy band structure to the cascaded staircase of QCLs and ICLs. The alignment of the conduction and valence band of is governed by two types (see figure 2.5). In type-I band alignments the band gaps fully overlap e.g. as in a GaAs/AlGaAs or InGaAs/InAlAs material system. In type-II band alignments (also referred to as staggered) the band gaps overlap partially, the conduction band edge of the well is energetically lower than the valence band in the barrier. This band alignment can be found in InAs/AlSb, GaSb/AlSb and InGaAs/GaAsSb heterostructures. A special type-II alignment is the broken type-II band alignment, e.g. as in InAs/GaSb, where the conduction band edge of InAs is lower than the valence band of GaSb. Their band alignment is used for a semimetallic-interface, a central feature of the ICL. This will be discussed in more detail later on in section 2.4.

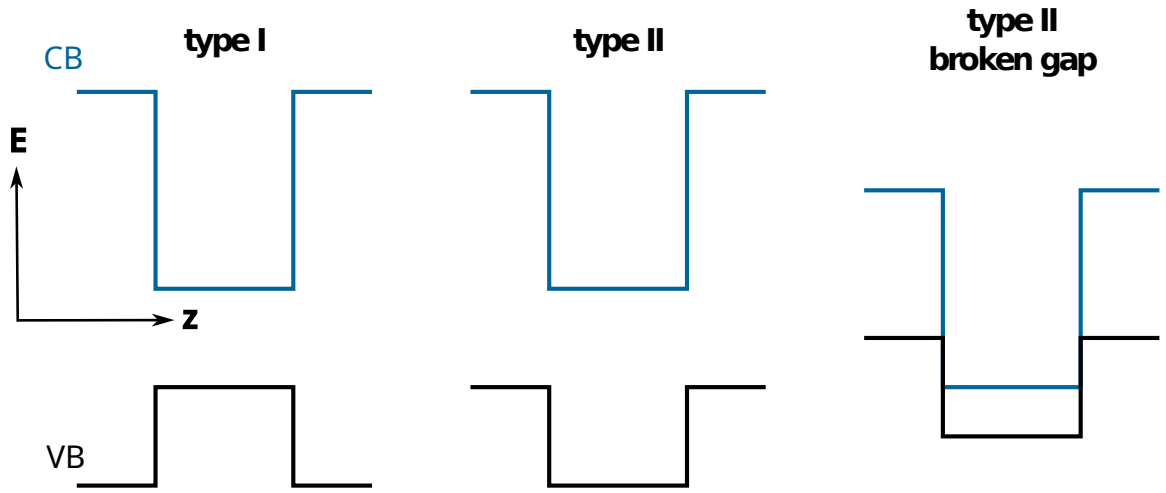

Figure 2.5: Band alignments of semiconductor heterostructures. A type I band alignment is limited to the band gap of the well material. Type I is also referred to as straddling gap. Type II is not limited to the band gap of the well material, with the type II broken band gap alignment allowing the design of semimetallic interfaces, a central building block of ICLs. CB denotes the conduction band, VB the valence band.

2.2.2 Finite Quantum Well

Combining different semiconductor materials allows for designing a fascinating physical system, the quantum well, an essential building block of semiconductor heterostructures. A straight forward example to obtain an analytic solution is a finite one dimensional quantum well, as illustrated in figure 2.6. The stationary, time-independent Schrödinger equation of a particle in the potential reads as

$$\left(-\frac{\hbar^2}{2m}\frac{d}{dz^2}+V(z)\right)\psi_n(z)=E_n\psi_n(z) \qquad \text{with} \quad V(z)\begin{cases}0 & \text{for} \quad |z|<\frac{a}{2},\\ V_0 & \text{for} \quad |z|\geq\frac{a}{2}.\end{cases} \tag{2.6}$$

The Ansatz consists of counter propagating waves $\exp(\pm ikz)$ inside the well and an exponential decaying function $\exp(\pm\kappa z)$ in the barrier, with the wavenumbers $k=\sqrt{2mE/\hbar^2}$ and $\kappa=\sqrt{2m(V_0-E_n)/\hbar^2}$. The continuity conditions at $z=\pm a/2$ read as

$$k\cdot\tan\left(\frac{ka}{2}\right)=\kappa \quad \text{for symmetric } \psi_n \tag{2.7}$$

$$k\cdot\tan\left(\frac{ka}{2}-\frac{\pi}{2}\right)=\kappa \quad \text{for antisymmetric } \psi_n. \tag{2.8}$$

The quantum well in figure 2.6 shows the ground state and the first excited state. Their energy difference

$$\Delta E_{12}=\frac{3\pi^2\hbar^2}{2ma^2}, \tag{2.9}$$

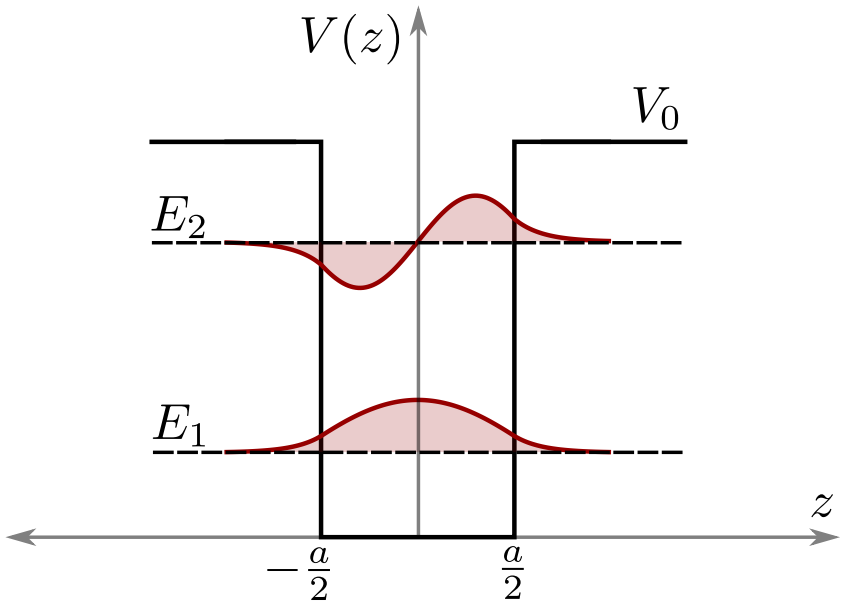

Figure 2.6: Schematic of a finite quantum well with potential depth V_0 and width a. The wavefunctions are drawn in red with their corresponding energy levels $E_{1,2}$. Figure adapted from [39].

is depending on the well width a and the potential well depth V_0, which depicts the engineering knob for optoelectronics. With adjusting the well width a, one can change the energy difference between the energy levels and thereby the transition energy and its wavelength. A more detailed discussion regarding potential wells and transition rules can be found in [36, 40].

2.2.3 Envelope function approximation

The rigorous analytic determination of the energy levels of heterostructures and tuning parameters like doping, thickness and composition of individual layers based on their wavefunctions is a complex task. This task can be tackled, by making use of appropriate approximations in order to simplify the problem. The envelope function approximation as proposed by Bastard [41, 42] connects the electronic wavefunction with a corresponding envelope function. The Bloch theorem states that the probability density of electrons is identical in every point of the crystal lattice and is invariant to translation

$$|\psi(\mathbf{k},\mathbf{r})|^2 = |\psi(\mathbf{k},\mathbf{r}+\mathbf{T})|^2. \tag{2.10}$$

Building up on the previous term the electrons wavefunction ψ gets decomposed into a sum of Bloch functions $f_n(\mathbf{k},\mathbf{r})$ (highlighted in figure 2.7)

$$\psi(\mathbf{r},\mathbf{k}) = \sum_n f_n(\mathbf{k},\mathbf{r}) u_{n,0}(\mathbf{r}). \tag{2.11}$$

The envelope function is then represented by

$$f_n(r_\parallel, z) = \frac{1}{\sqrt{S}} \exp(ik_\parallel r_\parallel)\chi_n(z), \tag{2.12}$$

with the crystal growth direction z, the in-plane surface area S and the in-plane coordinate $r_\parallel$. Figure 2.7 scetches the idea of the connection between the electron wavefunction of the crystal atoms with an envelope function.

2.2.4 Simple Band effective mass model

The envelope function needs to fulfil the continuity conditions at the interfaces with

$$\phi(r_+) = \phi(r_-). \tag{2.13}$$

For the effective mass Hamiltonian the second interface condition reads as

$$\frac{1}{m_+}\frac{\partial\phi(r_+}{\partial r} = \frac{1}{m_-}\frac{\partial\phi(r_-}{\partial r}. \tag{2.14}$$

The Hamiltonian and the Schrödinger equation can then be rewritten in the z-direction as

$$H_{env}\phi(z) = E\phi(z), \tag{2.15}$$

$$-\frac{\hbar^2}{2m_0}\frac{d}{dz}\left[\frac{1}{m^*(z)}\frac{d}{dz}\right] + V_{eff}(z) = E\phi(z), \tag{2.16}$$

which gives us the single band effective mass that is only valid for the 1-band Hamiltonian. For multiband $k \cdot p$ it looks different, more about this in the following. In summary the envelope function allows to calculate multilayer semiconductor heterostructures with sufficient and appropriate accuracy to extract information for engineering purposes. It is neither useful nor required to solve the equations for every atomic level, as conduction band electrons are not localized at a specific atom and only weakly bound.

2.2.5 $k \cdot p$ approximation

A highly relevant approximation for numerics and simulations of semiconductor band structures is the $k \cdot p$ method. The idea here is to expand a solution of the Schroedinger equation at high-symmetry points with perturbation theory, neglecting spin-orbit coupling. Based on the derivation in [44, 45] we start to expand the band structure in a point

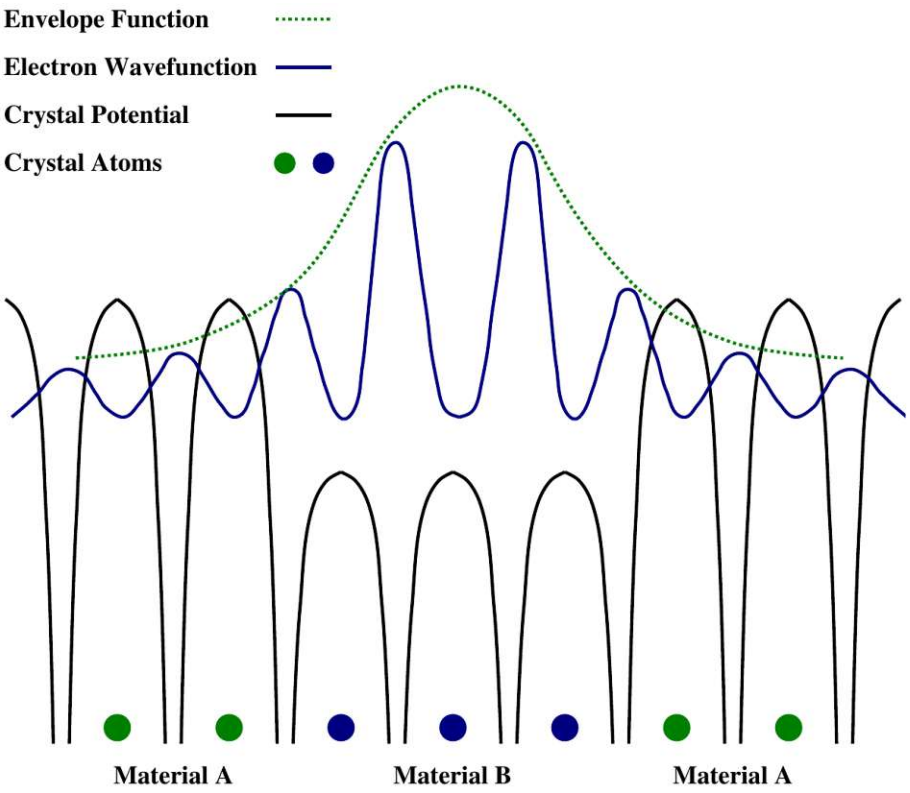

Figure 2.7: Envelope function approximation scheme. The wavefunctions of the crystal atoms are approximated with the envelope function. The envelope function changes with the material properties. Figure adapted and reproduced with permission from [43].

of symmetry (Γ-point), where $\mathbf{k}_0 = 0$

$$\left(\frac{\mathbf{p}^2}{2m} + V(\mathbf{r}) + \frac{\hbar}{4m_0^2c^2}(\sigma \times \nabla V(\mathbf{r})\mathbf{p}\right)\psi(\mathbf{r}) = E\psi(\mathbf{r}), \tag{2.17}$$

with the wavefunction ψ expressed in terms of Bloch waves

$$\psi_n(\mathbf{k}, \mathbf{r}) = \exp(i\mathbf{k}, \mathbf{r})u_n(\mathbf{k}, \mathbf{r}). \tag{2.18}$$

The interaction of the electron spin with the magnetic field induced by its motion through the crystal lattice gives us the spin-orbit coupling term $\sigma \times \nabla V(\mathbf{r})\mathbf{p}$, which is neglected in the following. The quantum mechanical momentum operator $\mathbf{p} = -i\hbar\nabla$ acts on the Bloch wavefunction

$$-i\hbar\nabla(\exp(i\mathbf{kr})u_{n,\mathbf{k}}(\mathbf{r})) = \exp(\mathbf{p} + \hbar\mathbf{k})u_{n,\mathbf{k}}(\mathbf{r}), \tag{2.19}$$

simplifying the Schrödinger equation to

$$\left(\frac{\mathbf{p}^2}{2m_0} + V(\mathbf{r} + \frac{\hbar^2k^2}{2m_0}) + \frac{\hbar}{m_0}\mathbf{k}\cdot\mathbf{p}\right)u_n(\mathbf{k}, \mathbf{r}) = Eu_n(\mathbf{k}, \mathbf{r}). \tag{2.20}$$

The solutions of the Schrödinger equation in the Γ-point fulfil the condition

$$H_0 u_{n,0}(\mathbf{r}) = E_{n0} u_{n,0}(\mathbf{r}). \tag{2.21}$$

Expanding the approximate solution with a perturbation theory approach allows to rewrite the conduction band

$$E_c(\mathbf{k}) = E_{c,0} + \frac{\hbar^2 k^2}{2m_0} + \frac{\hbar^2}{m_0} \sum_{m \neq c} \frac{\langle u_{c,0} | \mathbf{k} \cdot \mathbf{p} | u_{m,0} \rangle^2}{E_{c,0} - E_{m,0}}. \tag{2.22}$$

The dispersion relation for considering only one valence band is

$$E_c(\mathbf{k}) = E_{c,0} + \frac{\hbar^2 k^2}{2m_0} \frac{p_{cv}^2}{E_g}, \tag{2.23}$$

with the matrix element $p_{cv} = \langle u_{c,0} | \mathbf{p} | u_{m,0} \rangle$. The effective mass m^* depends on the materials band gap and the Kane energy. It reads as

$$m^* = m_0 \frac{E_g}{E_g + E_P}, \tag{2.24}$$

where we introduced the Kane energy

$$E_P = \frac{2}{m_0} p_{cv}^2. \tag{2.25}$$

The effective mass is proportional to the band gap $E_g = E_c(0) - E_v(0)$, as the Kane energy can be considered constant for common III-V semiconductor materials. This connects the model above (single band effective mass) with the 2-band $k \cdot p$ modelling. Apparently the solution is a superposition of functions, which fulfil Bloch's theorem. The key feature of the method is that it is not required to find a complete set of basic functions in general. Although the more basic functions we find and have, the higher the precision of the approximation becomes. Close to the Γ-Point the method is sufficient, but starts to become imprecise for large values of $\vec{k}$.

2.2.6 Interband vs. intersubband transitions

Quantum cascade devices can make use of either interband or intersubband transitions. Transitions from conduction (CB) to valence band (VB) are interband, within the same band intersubband transitions (Fig. 2.2.6). In optoelectronics the intersubband transitions take place in the conduction band. Within light-matter interaction, the momentum gets modified to $\mathbf{p} = \mathbf{p} + e\mathbf{A}$. The vector potential $\mathbf{A}(\mathbf{r}, t)$ is defined as

$$\mathbf{A}(\mathbf{r}, t) = \mathbf{e}\mathbf{Re}\left[A(\mathbf{r}) \exp(i\omega t)\right]. \tag{2.26}$$

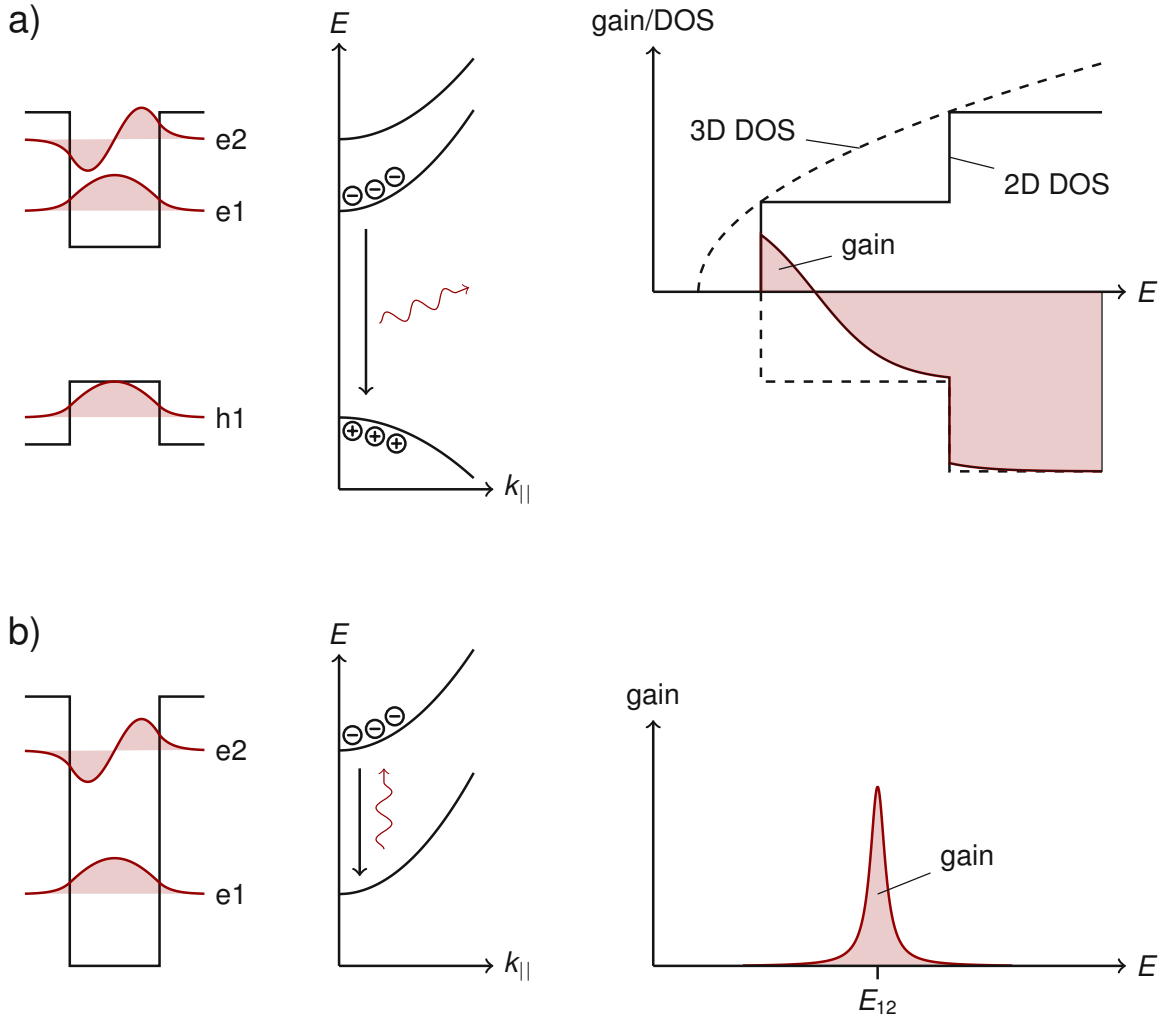

Figure 2.8: (a) Interband transition of electron states e2 and e1 to the hole state h1 vs. (b) intersubband transitions of e2 to e1 in quantum wells. The gain profile for (a) interband transitions yields in a broad profile vs. (b) intersubband transitions following a narrow distribution around the energy E_{12}. Figure reproduced with permission from [46].

This approach leads to the time-dependent and perturbed Hamiltonian H'

$$H' = \frac{e}{2m_0}\left[\mathbf{pA} + \mathbf{Ap}\right]. \tag{2.27}$$

Assuming that the interaction of the electromagnetic field with the quantum well does not modify its states [45, 47]. The Schrödinger equation reads

$$\left[\frac{\mathbf{p}^2}{2m_0} + V(\mathbf{r})\right]\psi = E\psi, \tag{2.28}$$

The perturbation leads to transitions from the initial to the final state, described by Fermis golden rule [48]

$$W_{i\to f} = \frac{2\pi}{\hbar}|\langle f|H'|i\rangle|^2\delta\left(E_f - E_i - \hbar\omega\right). \tag{2.29}$$

The expansion of the matrix element $|\langle f|H'|i\rangle|^2$ gives the perturbed Hamiltonian as

$$H'(\mathbf{r},t) = \left[H'(\mathbf{r})\mathrm{e}^{i\omega t} + H'^{*}(\mathbf{r})\mathrm{e}^{-i\omega t}\right], \tag{2.30}$$

$$\text{with } H'(\mathbf{r}) = \frac{e}{2m_0}A(\mathbf{r})\hat{\mathbf{e}}\cdot\mathbf{p}. \tag{2.31}$$

We assume the wavelength of the electromagnetic radiation to be much larger than the lattice constant (dipole approximation) and neglect the vector potential $\mathbf{A}$. The matrix element then reads with the envelope function F_i and F_f and the Bloch functions u_g, u_f for the energy bands g and h

$$\langle f|\hat{\mathbf{e}}\cdot\mathbf{p}|i\rangle = \langle F_i u_g|\hat{\mathbf{e}}\cdot\mathbf{p}|F_f u_h\rangle \tag{2.32}$$

$$= \langle F_i|\hat{\mathbf{e}}\cdot\mathbf{p}|F_f\rangle\langle u_g|u_h\rangle + \langle F_i|F_f\rangle\langle u_g|\hat{\mathbf{e}}\cdot\mathbf{p}|u_h\rangle \tag{2.33}$$

$$= \underbrace{\langle F_i|\hat{\mathbf{e}}\cdot\mathbf{p}|F_f\rangle\,\delta_{gh}}_{\text{intersubband}} + \underbrace{\langle F_i|F_f\rangle\langle u_g|\hat{\mathbf{e}}\cdot\mathbf{p}|u_h\rangle}_{\text{interband}}. \tag{2.34}$$

The first term is only non-zero for intersubband transitions and the second term only non-zero for interband transitions.

2.2.7 Doping in semiconductors

Aside from changing the quantum well thickness to alter the energy levels, the addition of other, foreign atoms can be used as engineering knob to adjust the Fermi levels and the conductivity of semiconductor materials. The insertion of atoms differing to the layer materials compound is called doping. Depending on the number of their chemical main-group, atoms will either introduce a free electron or a free hole, which is termed as n-type or p-type doping. A common dopand for III-V compound semiconductors is silicon for

n-type doping.

Doping of III-V materials is commonly done with silicon, rubidium or gallium tellurium. Note that tellurium can work as n-type dopand in ICLs. It is not used as pure element, but as compound with GaTe due to the lower vapor pressure. Elements of the fourth main-group as Si and Sn can be used as n-type dopands, but work as p-type dopands in GaSb. Note, that with Si in GaAs, doping concentrations up to $7 \times 10^{18}\mathrm{cm}^{-3}$ can be reached [49], an important number for the MBE growth of THz QCLs. Commonly doping that happens purely with one carrier type is a rare method. This mechanism leads to different regimes depending on the temperature, displayed in figure 2.9. The

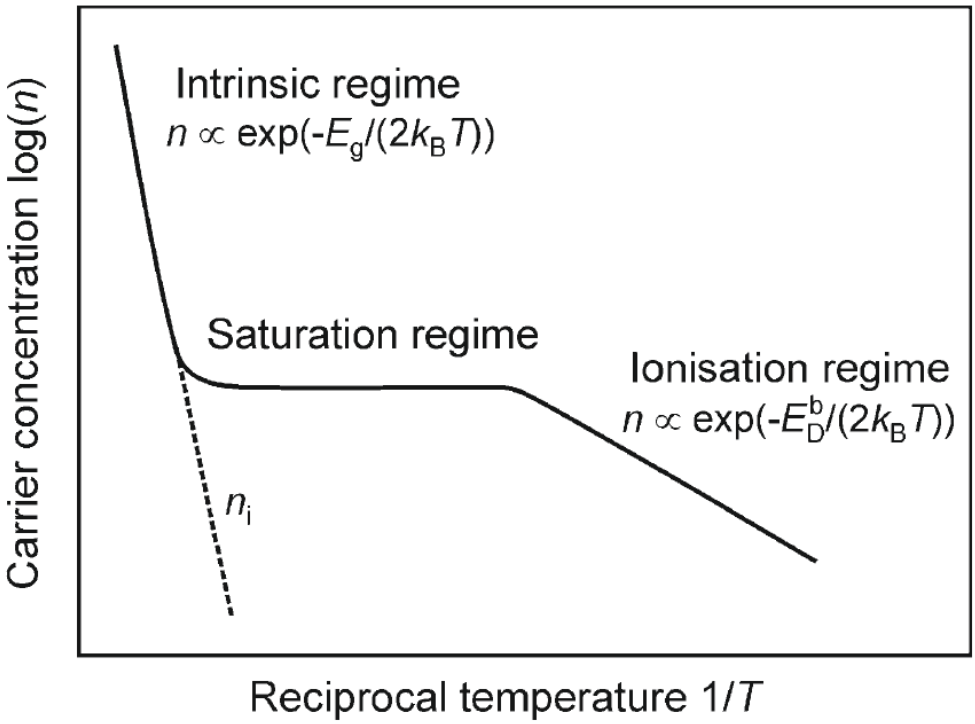

Figure 2.9: Arrhenius plot for the different regimes of a moderately doped bulk semiconductor with the carrier concentration n vs. the reciprocal temperature $1/T$. The intrinsic regime of the intrinsic carrier concentration n_i follows an exponential depending on the energy gap E_g, until the donors are saturated and approach a constant behaviour. The ionisation regime requires further lowering of temperature, the carrier concentration follows the donor energy E_D. Figure reproduced from [38] with permission of Springer Nature Group (2020).

Arrhenius plot gives the carrier concentration versus the reciprocal temperature. The carrier concentration is plotted logarithmically and splits up into three regimes. The intrinsic regime of high temperatures follows an exponential curve. The saturation regime is the range where donors are all ionized and the carrier density starts to saturate towards a constant rate. The ionisation regime for low temperatures governs a range where donors

still own their electrons and could be ionized with further lowering of the temperature, with the ionization energy as the slope.

2.2.8 Scattering mechanisms

The operation of semiconductor lasers and cascade laser devices with electrical pumping comes along with losses and scattering mechanisms. In the following the most important mechanisms are highlighted. Figure 2.10 gives a schematic overview for the mechanisms explained below.

Absorption The photons that are produced by recombination can be absorbed in the semiconductor heterostructure. Free carrier absorption, intervalence band absorption and inter-valley absorption in the conduction band are the most dominant absorption processes, depending on wavelength, doping and material parameters. Recently it was shown for ICLs, that avoiding valence band absorption acts as a key performance metric. [50]. All of the mentioned scattering mechanisms lead to different upper-state lifetimes

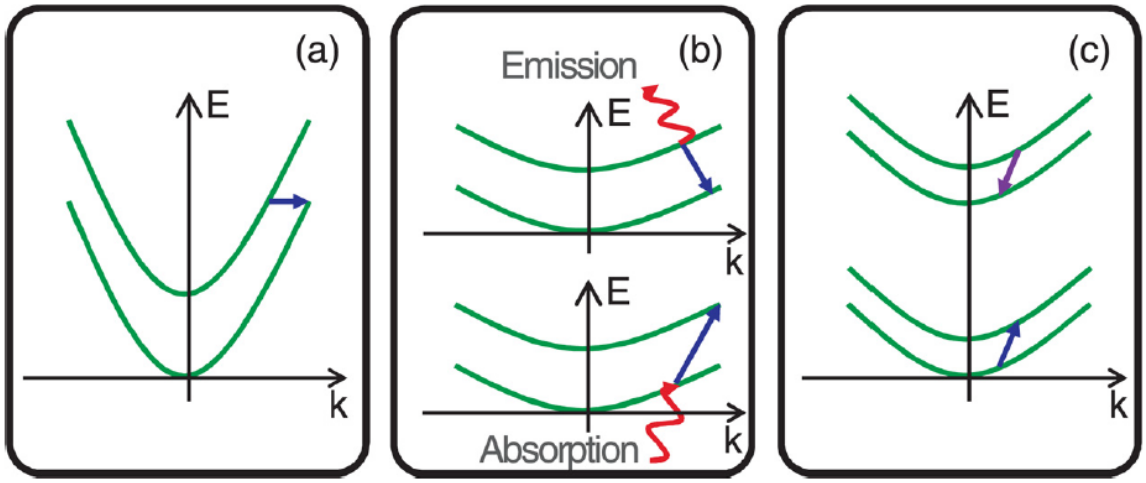

Figure 2.10: Different classes of scattering processes. (a) elastic scattering (b) inelastic scattering (c) carrier-carrier scattering. Figure reproduced from [51] with permission of AIP publishing (2014).

in QCLs and ICLs. QCLs typically exhibit an ultrafast lifetime of picoseconds [52], ICLs are in the nanosecond range. This difference recommends ICLs as excellent candidates for pulse generation and mode-locking [53, 28].

Phonon Scattering In quantum cascade heterostructures, the most dominant scattering mechanism is the interaction between electrons and phonons. Phonons are quantized lattice vibrations in the semiconductor crystals, and their interaction with electrons results in inter-level transitions and energy transfer between the electron system and the crystal

lattice. Vibrational modes vary based on the crystal structure, with acoustic phonons having linear dispersion and optical phonons having a quasi constant frequency. Longitudinal modes propagate in the direction of the displacement, while transverse modes propagate perpendicular to it. In polar crystals like III-V semiconductors, the most efficient process is LO phonon scattering, which empties the lower laser level but also depopulates the upper laser level at high temperatures. The emission of an LO phonon requires initial energy higher than the LO phonon energy, which can be achieved through high subband separation or kinetic energy.

Interface roughness scattering Semiconductor heterostructures may be grown close to atomic-level precision, but imperfections at the interfaces still cause elastic scattering of electrons. These imperfections may result from different regimes for the surface mobilities of the semiconductor materials that is used, leading to island formation during growth, or an unfinished layer of material A when material B is being grown. Interface roughness is a major contributor to the broadening of intersubband transitions in QCLs. A statistical model based on Gaussian fluctuations of step height Δ and correlation length Λ can be used to examine the role of interface roughness scattering. The average roughness Δ is typically in the range of the lattice parameter and the correlation length Λ is a few nanometers, depending on the materials used and growth direction. Both theoretical and experimental studies have shown that interface roughness scattering has a significant impact on carrier transport and optical gain in THz QCLs [54].

Alloy Scattering In contrast to binary semiconductors like GaAs, which have periodically arranged atoms, ternary (e.g. $Al_xGa_{1-x}As$) and quaternary (e.g. $In_xAl_yGa_{1-x-y}As$) compound semiconductor alloys have atoms of the same group randomly distributed in the lattice. These fluctuations, similar to interface roughness, disrupt the translational invariance of the potential that the electron experiences in the heterostructure layer plane. As a result, alloy scattering reduces the electron mobility in ternary and quaternary semiconductors. However, this type of scattering plays a minor role in THz QCLs because the wave functions are mostly confined to binary materials like GaAs [55].

Auger-Meitner Recombination In an Auger-Meitner process, a photon is not emitted when an electron in the conduction band and a hole in the valence band recombine. Instead, the energy is transferred to a third carrier (either an electron or a hole) which must comply with the laws of energy and momentum conservation. The third carrier then typically relaxes to a lower energy with the help of phonons, thereby contributing to the heating of the device and specially in ICLs to limiting the temperature performance [17].

Shockley-Read-Hall model The Shockley-Read-Hall (SRH) model explains non-radiative recombination caused by trap-assisted processes in non-ideal semiconductors. This happens when defects or impurities in the crystal lattice create energy levels within the bandgap that enable the recombination of an electron and a hole. This process was first described by Shockley, Read and Hall in the 1950s and can occur through four transitions involving the capture or release of electrons or holes [56]. The recombination rate is proportional to the density of traps, which is related to the material quality, so high-quality crystal growth is crucial for making effective semiconductor lasers. The SRH recombination rate is defined by

$$R_{SRH} = \frac{np - n_i^2}{t_P(n + n_0) + t_n(p + p_0)}, \tag{2.35}$$

where the injected electrons, holes and intrinsic carriers are noted by n, p and n_i. The capture time for an electron (hole) by a trap is tn (t_p) if all traps are empty (occupied). The parameters n_0 and p_0 denote the carrier concentration when the Fermi level matches the trap level E_t, given by

$$n_0 = n_i \left(\frac{E_t - E_i}{k_B T} \right), \quad p_0 = n_i \left(\frac{E_i - E_T}{k_B T} \right). \tag{2.36}$$

2.3 Quantum Cascade Laser

After laying the theoretical groundwork we can now introduce cascade devices, being the key technology this work is based on. Conventional band gap lasers are limited to their transition energy, which prevents them from emission wavelengths in the mid-infrared and terahertz range. In such band gap devices, the width of the band gap itself imposes an upper limit on the achievable wavelengths or respectively a lower limit on the frequency and thus energy of the emitted radiation. Depending on the energy of the incoming photon, it gets absorbed if its energy exceeds the band gap energy. A laser that circumvents the band gap limitations is the quantum cascade laser, the QCL is an intersubband transition using device to generate mid-infrared light. It uses stacked quantum wells which are connected in series and therefore called cascaded. The QCL gain region consists of a three-level system, the upper laser level $|3\rangle$, the lower laser level $|2\rangle$ and the ground state $|1\rangle$ (see figure 2.11). The main feature of the QCL is the recycling of electrons over the complete laser structure with its injector section. The injected electrons can transition multiple times within the active region, enabling quantum efficiencies above 100% [57]. The change of the photon flux ϕ generated by the transition in relation to the

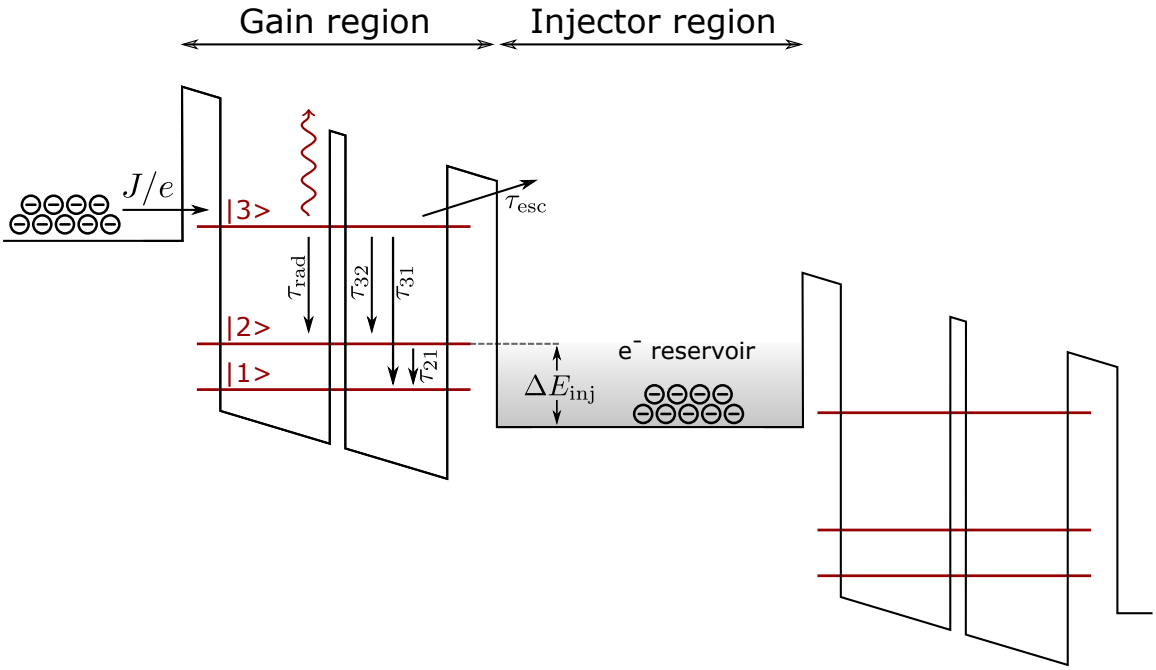

Figure 2.11: Bandstructure of a QCL consisting of the three level laser system and the injector regions. The injected electrons with the current J transition from the laser level $|3\rangle$ to level $|2\rangle$ and get exctracted to the injection level to the next cascade $|1\rangle$. The transition lifetime of the lasing state is denoted with τ_{32}, the transition for the escaped carriers τ_{esc}, the transition lifetime for the extraction to state $|1\rangle$ with τ_{21} and build the reservoir of electrons. Figure reproduced with permission from [46].

total photon flux gives us the gain in the material

$$G = \frac{1}{\Phi}\frac{d\Phi}{dy}, \tag{2.37}$$

with the gain coefficient G, the injection current density J and the photon flux Φ

$$\Phi = \frac{\epsilon_0 n c E_0^2}{2\hbar\omega} wL. \tag{2.38}$$

The geometrical dimensions w and L give the area of the active medium. The photon flux change

$$\frac{d\Phi}{dy} = W_{32}^{max} w(n_3 - n_2), \tag{2.39}$$

relates the maximum transition rate W_{32}^{max} (see section 2.2.6) with the occupation numbers of the electrons in the upper and lower laser level n_3 and n_2. The gain G can then be rewritten in terms of the dipole matrix element z_{if}, the refractive index n and the layer thickness L_p.

$$G = \frac{we^2 |\langle z_{if} \rangle|^2}{\epsilon_0 n c L_p}(n_3 - n_2). \tag{2.40}$$

The number of electrons in the upper laser level is given by

$$n_3 = \eta_i \frac{J}{e}\tau_3, \tag{2.41}$$

with the injection efficiency η_i and the upper state lifetime τ_3. The number of electrons in the lower laser level is given by

$$n_2 = n_3 \frac{\tau_2}{\tau_{32}}, \tag{2.42}$$

with the lower state lifetime τ_2 and the scattering time from the upper laser level to the lower laser level τ_{32}. This allows to formulate a material specific gain coefficient

$$g_c = \frac{we |\langle z_{if} \rangle|^2}{\epsilon n c L_p} \eta_i \tau_3 \left(1 - \frac{\tau_2}{\tau_{32}}\right). \tag{2.43}$$

The lasing threshold current density is reached, when the material gain exceeds the losses

$$J_{th} = \frac{\alpha_w + \alpha_m}{g_c \Gamma}, \tag{2.44}$$

with the facet and waveguide losses α_m, α_w and the mode confinement factor of the optical mode Γ. The temperature dependent threshold current is given by the exponential fit

$$J_{th} = J_0 \exp(T/T_0), \tag{2.45}$$

with the characteristic temperature T_0. A more explicit discussion including derivations can be found in [52]. Figure 2.12 shows a typical light-current-voltage characteristic of a QCL. Sweeping the injected current gives a characteristic curve of this laser type, the LIV. It gives information about the output power, quality of the electrical contacting, mode hopping, etc. The curve consists of three significant areas: Alignment, threshold and rollover. The band alignment induces a steep increase in voltage as it needs to be aligned to allow the propagation of carriers. The slope of this process is the differential resistance of the laser. The threshold is the intersection of the interpolated slope line with the abscissa. The threshold current density is a better figure of merit as it takes the device area into account. The rollover of the device marks the point in which the output power of the laser is not increased by increase of the pumping power anymore, but decreases surpassing the rollover point. Exceeding this point can lead to a damaged or broken device. The external quantum efficiency η_e represents the number of photons emitted per electron. It is given by the experimental slope of the P(I) curve

$$\frac{dP}{dI} = \eta_e \frac{h\nu}{e}. \tag{2.46}$$

2.3.1 State of the art

Based on developments of semiconductor heterostructures and molecular beam epitaxy in the 1980s [8, 9, 10], QCLs underwent fast progress since their first demonstration in 1994 [11]. Shortly afterwards the first mid-IR continuous wave operated QCL was functional at low temperatures [59]. The first cw operation of a QCL at room temperature was reported in 2002 [60] and in the same year the first THz QCL based on GaAs/AlGaAs was published [61]. For QCLs, a broad range of emission wavelengths in the range from 2.75 µm to 24 µm [62, 63] have been demonstrated. However the closing of the Terahertz gap, the missing availability of devices between 0.1 to 10 THz, is a still unsolved problem, which will be covered in more detail in chapter 6. In this following paragraphs, the most important III-V material systems for QCLs are introduced and discussed shortly, based on [45]. Important parameters are conduction band offsets (CBO) and effective masses. Reviews of the QCL history and more relevant recent topics in the field are given in [12, 64].

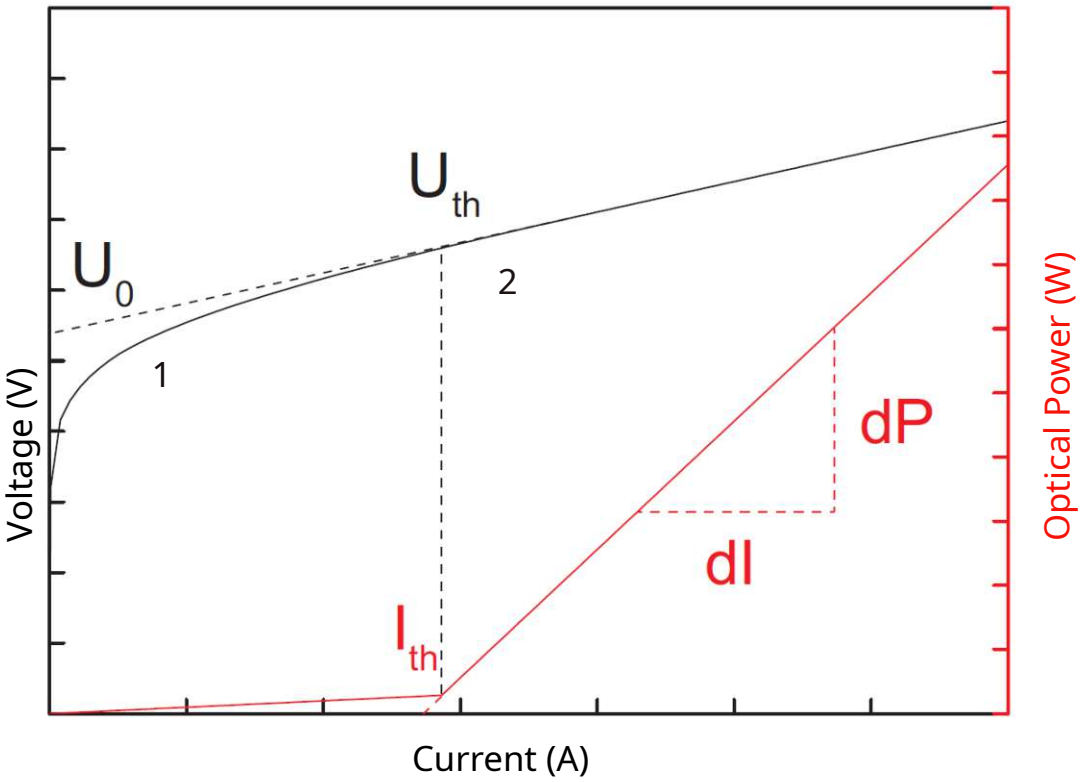

Figure 2.12: Typical Light-Current-Voltage characteristic of a QCL. Important points are the band alignment (1) and threshold (2), defined by the threshold voltage U_{th} and the threshold current I_{th}. The quantum efficiency is given by the ratio of dP/dI. Figure adapted and reproduced with permission from [58].

GaAs/AlGaAs on GaAs substrate One of the most mature material systems to grow with MBE is the GaAs/AlGaAs system. The vicinity of the AlGaAs and GaAs lattice constants enables variable aluminium percentages in the laser barriers [65], which further allows to adjust their conduction band offset (CBO). The CBO can range from 0 to 390 meV for 45% aluminum content, which is the origin for the widespread use of this material system for THz QCLs. The effective electron mass is $m_c^* \approx 0.0067 m_0$.

InGaAs/InAlAs on InP substrate Since the first demonstration of an operational QCL [66] the InGaAs/InAlAs material system evolved to a reliable platform for mid-infrared QCLs. The ternaries need to be lattice matched to InP for a CBO of 520 meV. Typical emission wavelengths are above 6 µm. MBE systems that are equipped with a phosphorous source can be utilized for InP regrowth for the QCL waveguide and the fabrication of buried heterostructures. The effective mass of $m_c^* \approx 0.0044 m_0$ leads to higher gain than other material systems and in combination with the strain engineering of high indium contents in the wells and low indium contents in the barriers it allows a range for the CBO from 500 to 900 meV.

InGaAs/GaAsSb on InP substrate Replacing the InAlAs barrier from above with GaAsSb allows for the growth and design of long-wavlength QCLs due to the CBO of 360 meV [67, 68]. The mixed group V compound is challenging to grow. The lattice matching composition of GaAsSb on InP induces ordering mechanisms that allow for growth in a optimum set of growth parameters.

InAs/AlSb on InAs substrate Compared to already mentioned material systems, the CBO of InAs/AlSb of 2.1 eV is very high. It is a well suited candidate for short wavelength applications, although the interband transitions can limit this. The effective electron mass is low with $m_c^* \approx 0.0023 m_0$. The feasability was demonstrated with a THz QCL in a magnetic field [69]. An overview to the development of the maximum operation temperature and wavelength is given in figure 2.13 below.

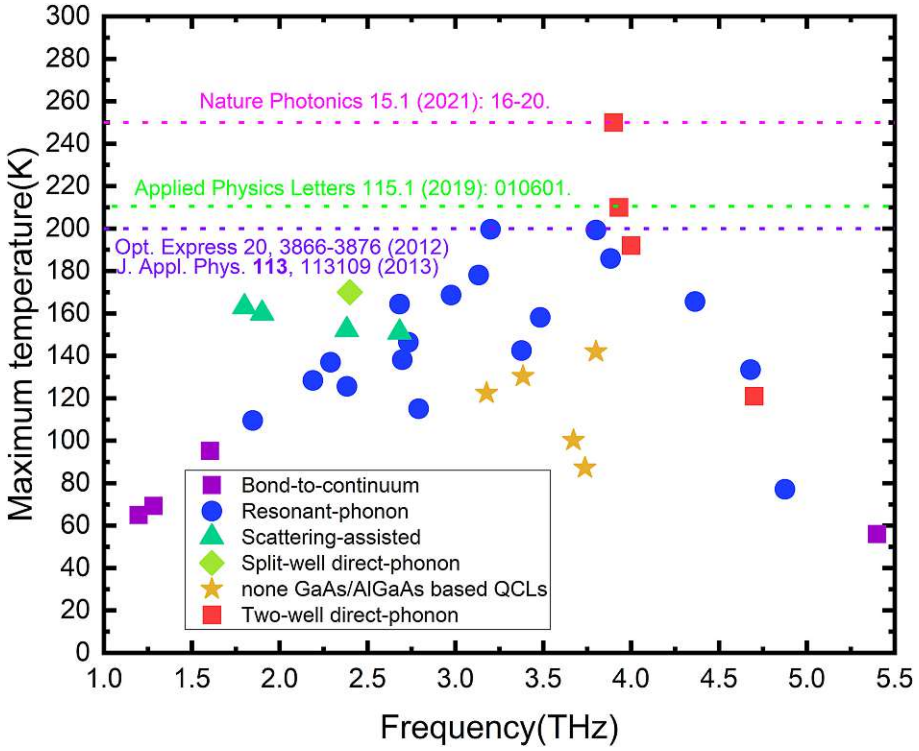

Figure 2.13: QCL temperature performance of different state-of-the-art THz QCL designs with the maximum lasing temperature vs. lasing frequency. The highest lasing temperature is reached with pulsed operation. The orange star markers highlight the THz QCLs based on GaAs/AlGaAs. A material system used for the first thermoelectrically cooled THz QCL [70]. Figure reproduced from [71] with permission of Elsevier Group (2021). CC BY-NC-ND 4.0.

2.4 Interband Cascade Laser

In parallel to the QCL as coherent light source in the mid-infrared, III-V band gap lasers developed as useful and important tool, although no band gap laser achieved room temperature CW operation during the 1990s. A laser type that combines the advantages of the cascading principle of QCLs, with a band gap transition are ICLs [13]. The namegiving transition has typical lifetimes in the nanosecond range, leading therefore to significantly lower threshold current densities than QCLs with their picosecond lifetime due to the intersubband transition. Starting from the initial proposal in 1995 by Yang [13], it took roughly a decade to demonstrate the first pulsed operation of GaSb-based ICLs at room temperature in 2002. The first ICL concept did rely on type-II interband transitions of a electron-hole recombination from an InAs well to a GaSb well. In 2002 the first ICL was demonstrated at room temperature [72]. Following this first demonstration, in 2008 the first room temperature continuous wave operation of a 3.75 µm ICL was achieved. [73]. Continuous wave operation of ICL devices was facilitated by avoiding mode leakage into the substrate by using a thick bottom cladding layer. The thickness was increased from 2.1 to 2.7 µm for a 3.3 µm 12-stage ICL [74]. In an additional next step the current threshold density was reduced by lowering the number of active regions from 12 to 5. Although not published, shortening the thickness of electron injectors from 25 to 20 nm contributed further, resulting in a threshold current density of 1.15 kA/cm^2.

In a subsequent iteration the so called "W" design, consisting of two InAs quantum wells sandwiching the InGaSb hole well, was introduced and then successfully demonstrated. It increases the optical matrix element and the optical gain, because the electron-hole wave functions can be designed to inherit more overlap of the probability density. After this adaption the "W"-ICL started to outperform the initial designs, leading to the first pulsed ICLs demonstrated in 1997 at 3.8 µm [75]. The cascading of the interband transition in the W quantum well requires a mechanism to recycle the number of electrons, as a solely conduction band based transport is not possible. This problem is solved by the semimetallic interface (SMIF). The heterojunction of InAs and GaSb owns a type-II broken band gap alignment with the GaSb conduction band edge above the one from InAs. At zero bias of the band structure, the GaSb hole wave function is designed as such to be below the InAs electron wave function. At non-zero bias the energies can be shifted to reduce the energy level distance and let the CB and VB couple to generate electrons and holes that are propagated by their injectors to the active W quantum well. This improvements lead to the W quantum well as established ICL core feature [76].

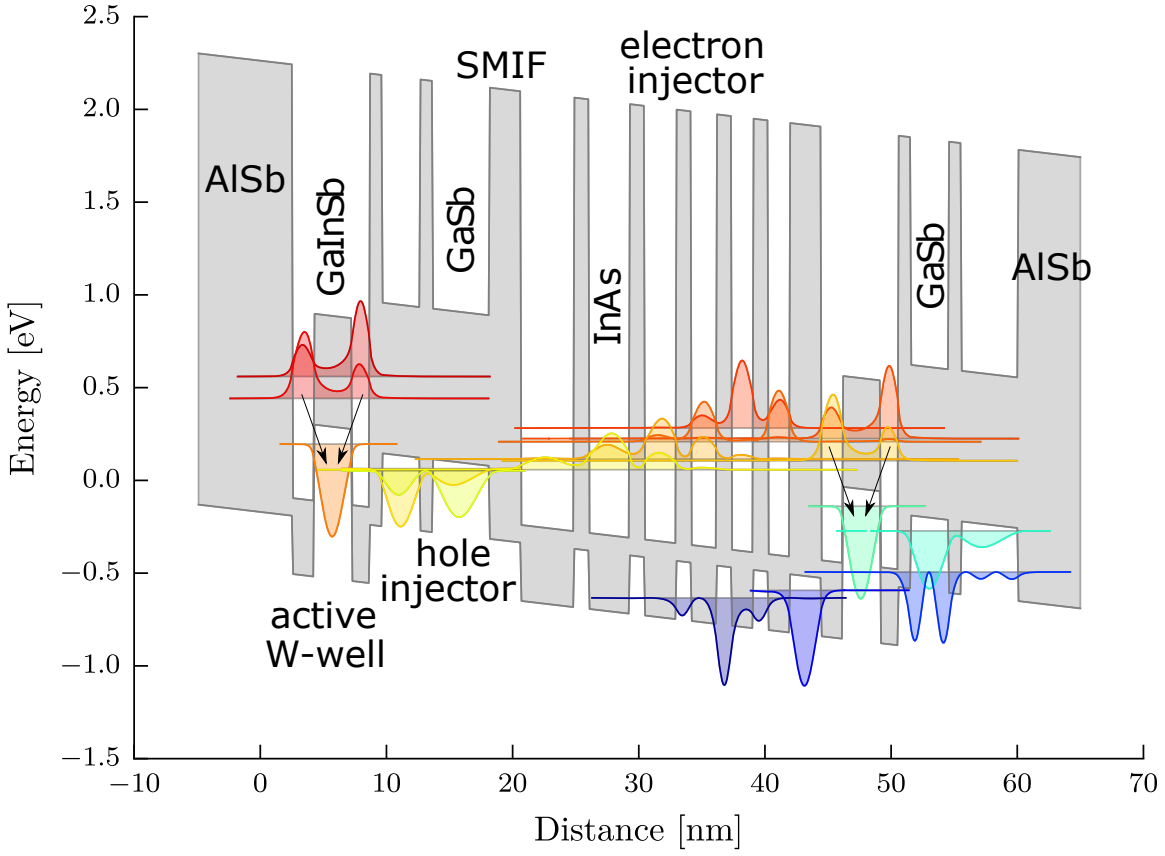

Figure 2.14: Schematic of the ICL working principle. Electrons and holes are generated with the semimetallic interface (SMIF). The carriers are injected into the active W quantum well and emit a photon with the recombination. Reproduced with permission from [17], Journal of Physics:D (2015). Licensed by CC BY-ND 4.0 .

2.4.1 State of the art

The wide spread standard design for ICLs nowadays is a 5-12 period active region. The active region allows the adaption of the emission wavelength and device performance. State of the art devices evolved over multiple iterations and advancements, key problems were mode leakage into the substrate and unbalanced carrier populations, that harmed the lasing transition. An important design improvement was ICL carrier rebalancing of Vurgaftman et al. in 2015 [17]. The work demonstrated performance improvement by increasing the doping of the electron injectors InAs layers. Massive n-type doping with densities as high as $2 \times 10^{18}\mathrm{cm}^{-3}$ in the electron injector was implemented in order to balance the lack of holes generated by the SMIF. Hereby the threshold current density was lowered by a factor of three. The concept lead to performance improvements at the wavelength region of 4.7 to 5.2 µm [77]. Recently ICLs grown on InAs were reported as viable alternative to the established GaSb based ICLs. Up to 20 active cascades were required to shift the emission wavelength to 10.7 µm [18]. The current upper wavelength limit for devices at room temperature in cw mode is 5.2 µm [78]. The design of ICLs with longer emission wavelength implicates the growth of increasing InAs/AlSb superlattice

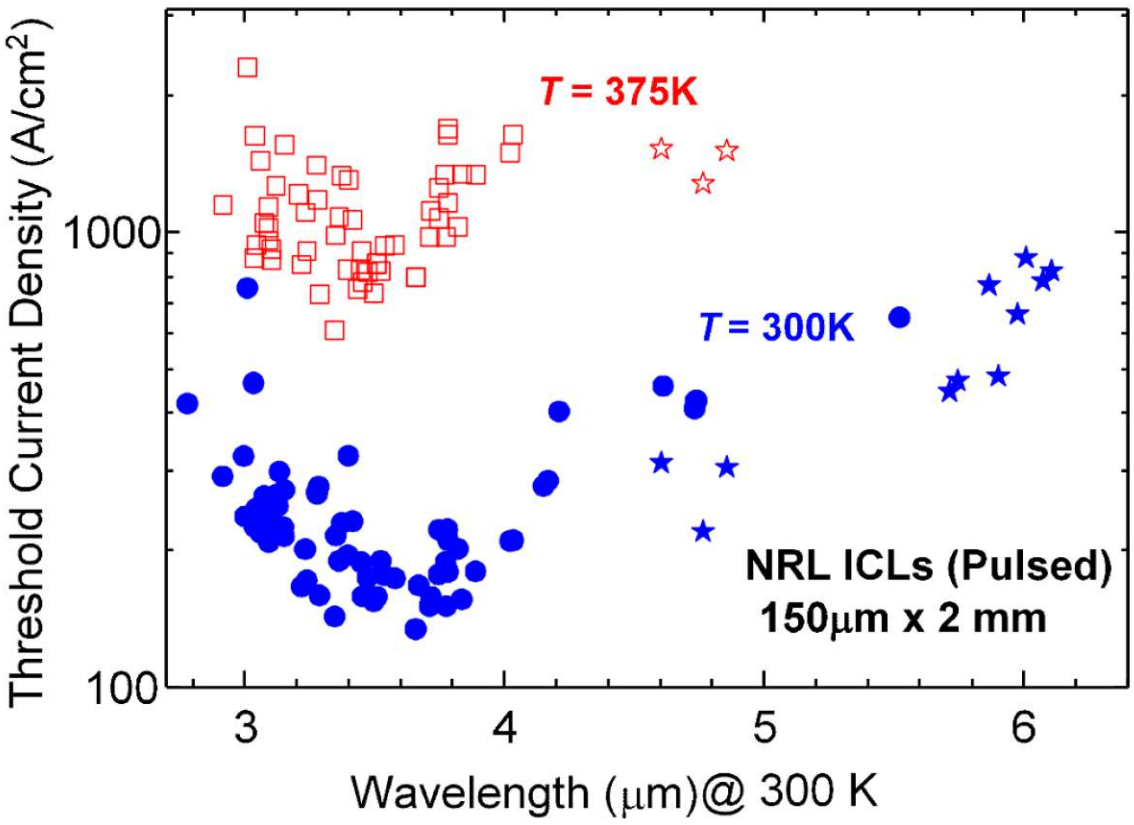

Figure 2.15: Threshold current density versus emission wavelength of ICLs. Low threshold devices can be found in the sweet spot island between 3 and 4 µm. Reproduced with permission from [76], MDPI photonics (2020). Licensed by CC BY-ND 4.0 .

claddings for mode confinement on GaSb substrates. The usage of InAs as substrate offers the possibility to grow highly doped InAs layers as plasmonic waveguides. The longest reported wavelength of InAs-based ICLs cw operation is 11 µm at 97 K for InAs-based ICLs [79] and 13.2 µm at 120 K in pulsed operation [80]. In the near past research efforts also looked into transferring ICL active regions to silicon as substrate [81]. This would allow better integration with semiconductor production lines and allow for highly integrated sensor systems. Despite the effort, no successful growth of ICLs on a silicon as substrate has been reported yet. Another rather exotic approach was the theoretical proposal to grow ICL bandstructures on SiGeSn [19]. A functional ICL on silicon or InP would unlock a manifold of fascinating possibilities and is a topic of ongoing research. A more in depth discussion of applications and technological approaches regarding ICLs can be found in [18, 76]. Nowadays ICLs offer a valuable monolithic platform due to low threshold current densities and their low power consumption, making them excellent candidates for on-chip integrated battery-driven devices [21]. Wall-plug efficiencies up to 18% in cw operation match the current record of 22 % [82] in QCLs.

2.4.2 W quantum well

The key feature of the ICL is the so called type-II broken band gap W quantum well (W-QW). As displayed in figure 2.16, the maximum shows the band structure and probability densities of the ground states. In figure 2.16 the maximum of the hole probability density is located inside the InGaSb quantum well. The maximum of the electron probability density is in the InAs wells. As the maxima for W-QW are located in different layers, the recombination mechanism for these W-wells is an indirect transition (type-II) in contrast to the direct transition (type-I) as the maxima are in different layers. Optimizing the overlap between hole and electron wavefunction increases the recombination rate and subsequently the transition energy and oscillator strength. A fundamental advantage of ICLs is the possibility to tune the transition energy of the lasing transition with variation of the InAs/InGaSb layer thickness. The emission wavelength is not solely restricted to the band gap thereby. Note, that the feasible design of W quantum wells is limited by the achievable MBE growth. The thickness and the composition of the InGaSb layer should not exceed the lattice constant mismatch of two percent, which would lead to excessive compressive strain. Disregard of this can induce to relaxation effects and defects, subsequently increasing losses and decreasing device performance.

2.4.3 Semimetallic Interface

The ICL is based on the recombination of electrons and holes in the active laser transition. The generation of its carriers takes place at the semimetallic interface. It connects the active regions with a recycling mechanism to establish the cascading scheme. Its

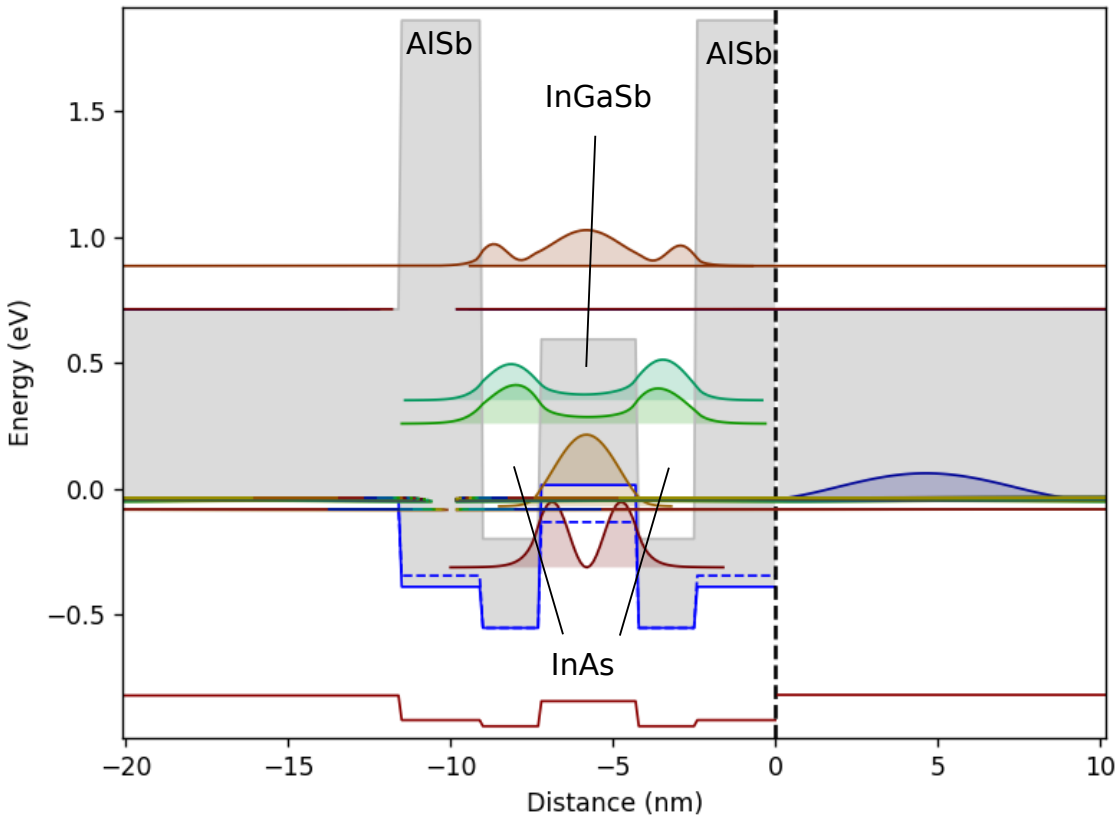

Figure 2.16: Type-II broken band gap potential well, commonly referred to as W quantum well. The electron probabilty density is green, the hole density is red.

functionality strongly depends on the energy difference between the GaSb valence band edge and the InAs conduction band edge. Furthermore the transitions lifetime needs to be significantly lower than the W-quantum well recombination to achieve population inversion. The SMIF is a central feature of this laser type and builds up on a type-II broken band gap of GaSb/InAs quantum wells. In figure 2.17 a GaSb/InAs quantum well structure between two AlSb barriers is displayed. The GaSb band edge at zero bias is below the InAs band edge. Applying bias to the heterostructure starts to tilt the energy band and shifts the carriers due to the Stark effect from the InAs conduction band edge above the GaSb valence band edge. The dispersion relation underlines this mechanism

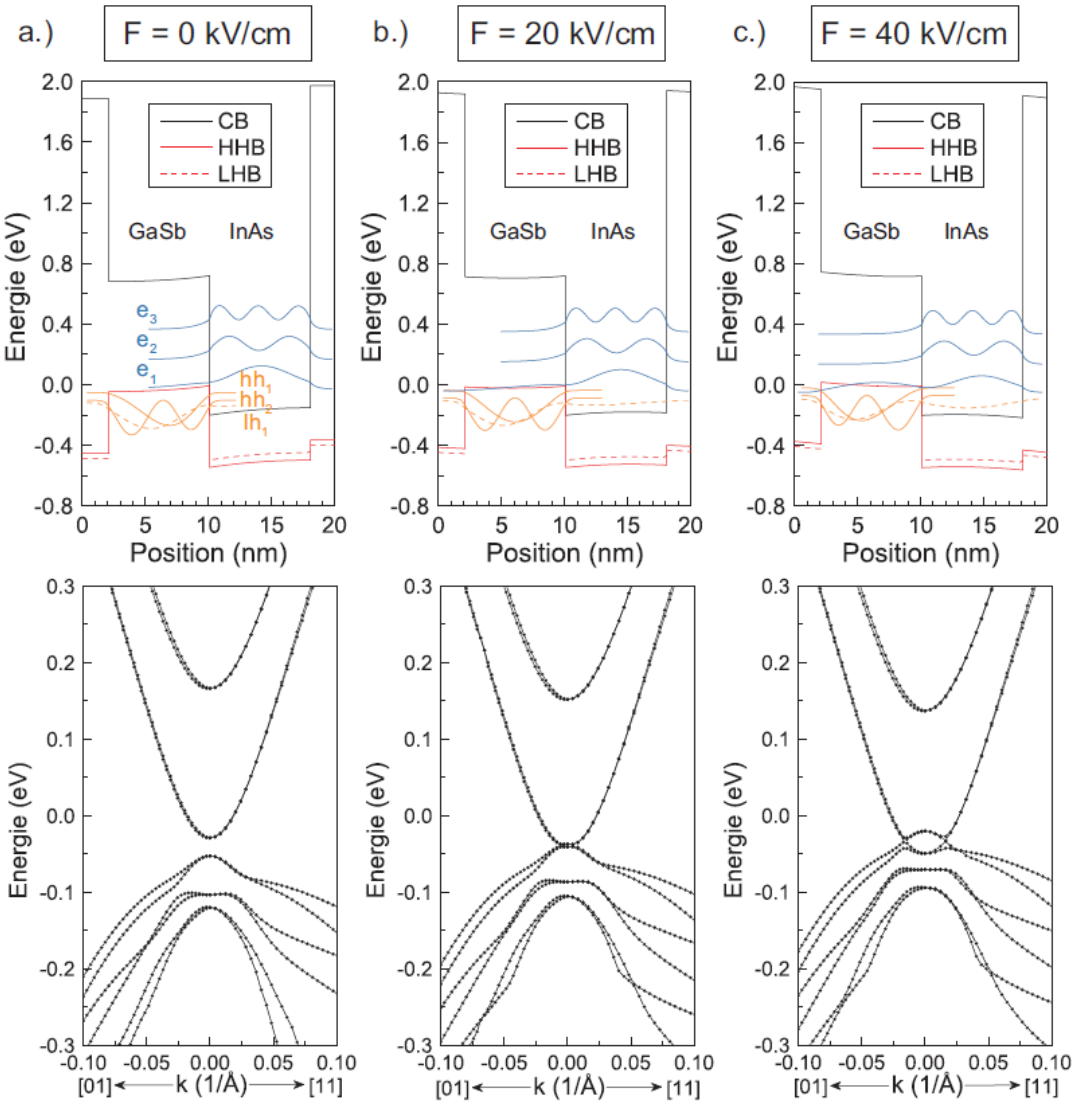

Figure 2.17: Semimetallic interface of GaSb/InAs with the band structure for different bias points (a) 0 kV/cm (b) 20 kV/cm and (c) 40 kV/cm. In the lower part the dispersion relations in k-space are shown in addition. At 40 kV/cm the CB and VB overlap and allow the extraction of carriers. Reproduced with permission from [58].

further. Increasing the applied bias moves the valence band and conduction band edges

closer to each other until they overlap. The overlap allows then the extraction of electrons and holes with injector regions at the bias point. The energy difference E_{SMIF} between electron and hole wavefunctions

$$E_{SMIF} = q_A(d_e - d_h) - E_i, \tag{2.47}$$

depends linearly on the electric field $_A$. The quantization induces an effective band gap E_i, the distances of the center of masses are labelled for the electron d_e and the hole d_h wave functions to the interface of the SMIF. Typical values for the energetic distance are approximately 100 meV at zero bias [83].

2.4.4 Injector regions

The main components of the ICL, the SMIF and the W-QW have to be connected with a heterostructure that forwards both electrons and holes towards the lasing transition in the W-QW. The connection between the building blocks is established by two individual injector regions, the hole injector and the electron injector.

Electron injector The energy level of the electrons from the SMIF InAs quantum well and the upper laser level state of the InAs W-QW need to be aligned properly to allow the smooth transitioning of electrons and to prevent a recombination channel of holes with holes over the electron injector. The AlSb barrier thickness is an important influence for device and laser properties. A thin barrier increases the absorption between the valence bands and a thick barrier lowers the tunneling rate between the InAs layers. Finding a sweet spot for optimized performance is key when designing an ICL. State of the art injectors spread the wave functions over multiple InAs quantum wells in contrast to high localization in subsequent layers.

Hole injector The hole injector propagates holes from the SMIF to the W-QW lasing transition. It serves a double function, firstly inhibiting the recombination of electrons from the upper laser level state and secondly injecting holes into the lower laser level. The hole injector design consists mostly of two GaSb wells with AlSb barriers. Devices with three GaSb hole wells did not show better behaviour [76]. Less hole wells implicate also thinner growth of the heterostructure and in general better performance. The energy separation of the lower lasing level and the hybridized hole wave function is the crucial parameter to adjust the hole tunneling rate into the lower lasing transition. This might be connected to intervalence band absorption [50]. Literature recommends an energy spacing of 100 meV [84].

2.4.5 Waveguiding

Aside from the design of the active region with the SMIF, W-QW and related injectors, the emitted light of the laser active region needs to be confined by a waveguide structure. This requires to design the epitaxially grown materials accordingly. A proper waveguide design needs to confine the optical mode by using the refractive index contrast of different material systems. This can be done by utilizing either quaternary materals like $Al_xGa_{1-x}As_ySb_{1-y}$ or AlSb/InAs superlattices [85]. Originally from diode lasers, in 2008 GaSb layers were added to sandwich the active region, referred to as seperate confinement layers (SCL) [73]. Employing superlattices offers a high degree of freedom and flexibility to design their effective band gap and tune a transition into the first active W quantum well. Furthermore the superlattice approach allows for engineering of the interfaces for strain compensation, therefore representing the dominant approach in the community over the past decades. Aside from the refractive index also the electrical conductivity of the used materials is a crucial parameter. The waveguide design is not supposed to interfere with the electrical properties of the device. A figure of merit is the confinement factor defined as

$$\Gamma = \frac{\int_{AR} |E(z)|^2 dz}{\int_{-\infty}^{\infty} |E(z)|^2 dz}, \qquad 0 \leq \Gamma \leq 1 \tag{2.48}$$

with the integral $\int_{AR} |E(z)|$ over the electric field of the optical mode in the active region. The waveguide needs to maximize the overlap of the lasing mode(s) within the active region and simultaneously minimize internal losses. Another possibility to facilitate vertical confinement in growth direction are plasmonic enhanced waveguides. The viability of such plasmonic waveguides strongly depends on the target wavelength of the laser. Plasmonic waveguides are dielectric waveguides with a significant decrease of the materials refractive index due to highly doped layers. For e.g. InAs for this purpose has to be doped to the reachable limit of many MBE systems of $3 \times 10^{19}\text{cm}^{-3}$. This method allows for low waveguide losses while keeping the grown heterostructure thickness in a reasonable range. The main problem are the doping concentrations for the plasmonic waveguide layers. On the one hand, sufficient doping is required to ensure electrical transport from top to bottom contact. On the other hand too high concentrations increase the optical losses. However, the optical mode can be confined perpendicular to the growth direction by fabricating a ridge waveguide. Ridge waveguides widths can range from anywhere between a couple of µm up to several tens of µm. The waveguide structure can be fabricated using wet or dry etching processes, see chapter 6. Following the definition of the laser structure by etching, the sidewalls of the ridges are commonly passivated with silicon nitride to avoid leakage currents, ICLs waveguide design is possible with the design of the epitaxial structure. State of the art devices employ a combination of superlattice claddings and an plasmonic

layer (e.g. InAs n+ in the case of InAs-based ICLs) [18]. In ICLs also low doped substrate material confinement layers are used as spacing between the transitional superlattice and the active region. However, the refractive index of a doped semiconductor is given by the Drude approximation

$$n(\omega, N_d) = \sqrt{\epsilon(\omega, N_d)} = \sqrt{\epsilon_\infty \left(1 - \frac{\omega_p^2}{\omega^2(\frac{j}{\omega T})}\right)} \tag{2.49}$$

with the plasma frequency $\omega_P = \sqrt{\frac{N_d}{\epsilon_0 \epsilon_\infty m^*}}$ and the relaxation time $\tau = \frac{\mu m^*}{e}$, the mobility μ and the doping dependent effective mass m^* [38]. In figure 2.18 an exemplary simulation with the CLAUS framework is shown. The ICL had a designed emission wavelength of 6.15 µm and utters a calculated absorption loss of 26 cm^{-1}. The absorption coefficient relates to the refractive index of the material by $\alpha = \frac{4\pi Im(n)}{\lambda}$.

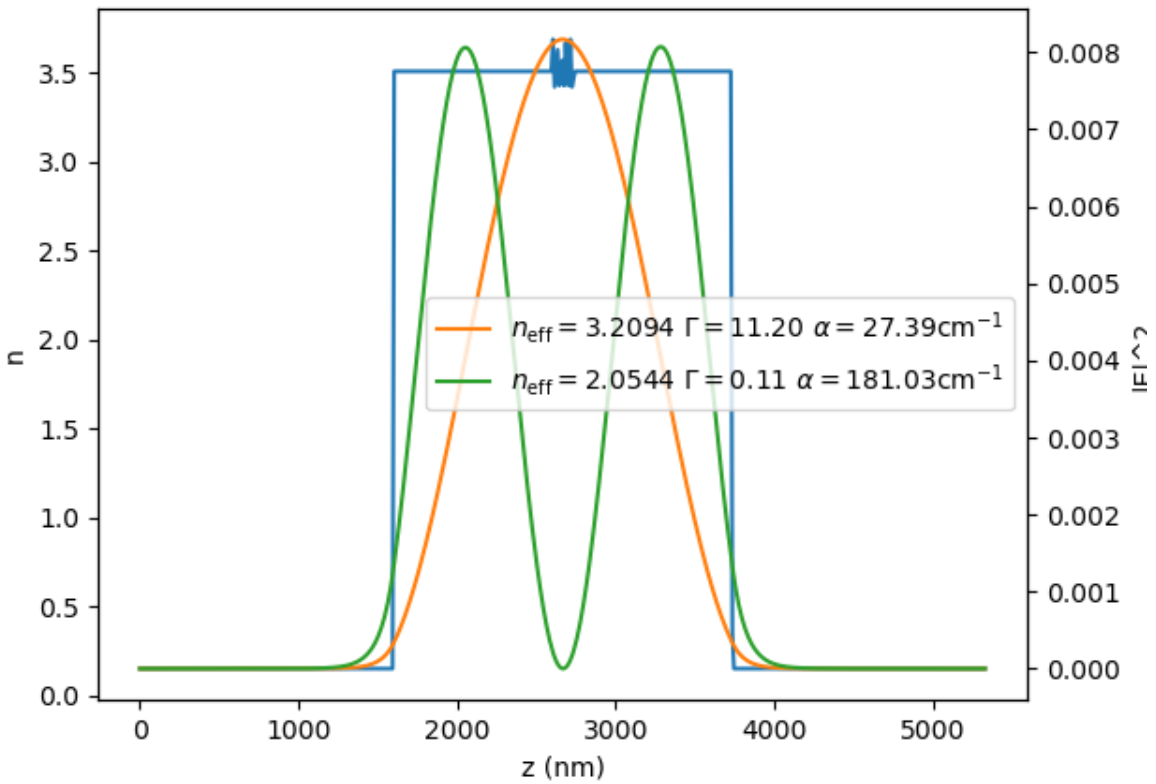

Figure 2.18: Plasmonic waveguide for an ICL structure. The InAs cladding layers are doped with $3 \times 10^{19}\mathrm{cm}^{-3}$. The waveguide loss α summarizes absorption of the designed emission wavelength of the active region of 6.15 µm. Figures produced by the author himself.

Moreover, the substrate material changes the approach. InAs-based systems showed to work with undoped InAs SCLs and a highly n-doped InAs layer as plasmon enhanced

claddings. Best performance devices used an additional cladding between the InAs layers consisting of a InAs/AlSb superlattice [86].

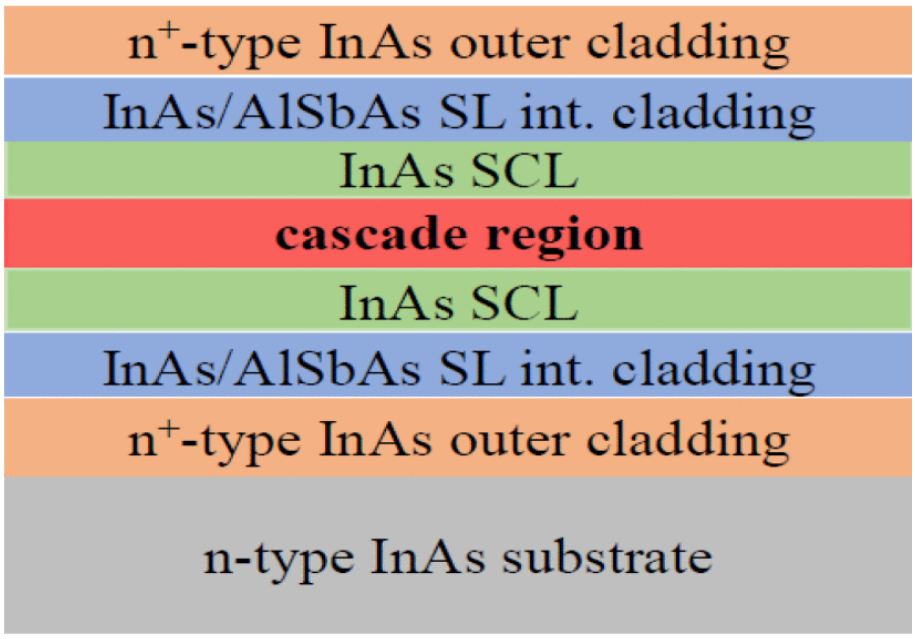

Figure 2.19: ICL structure with cladding and transition layers. The cladding superlattice is combined with the separate confinement layer (SCL). Reproduced from [18] with permission of IEEE (2019).

2.5 Frequency Combs

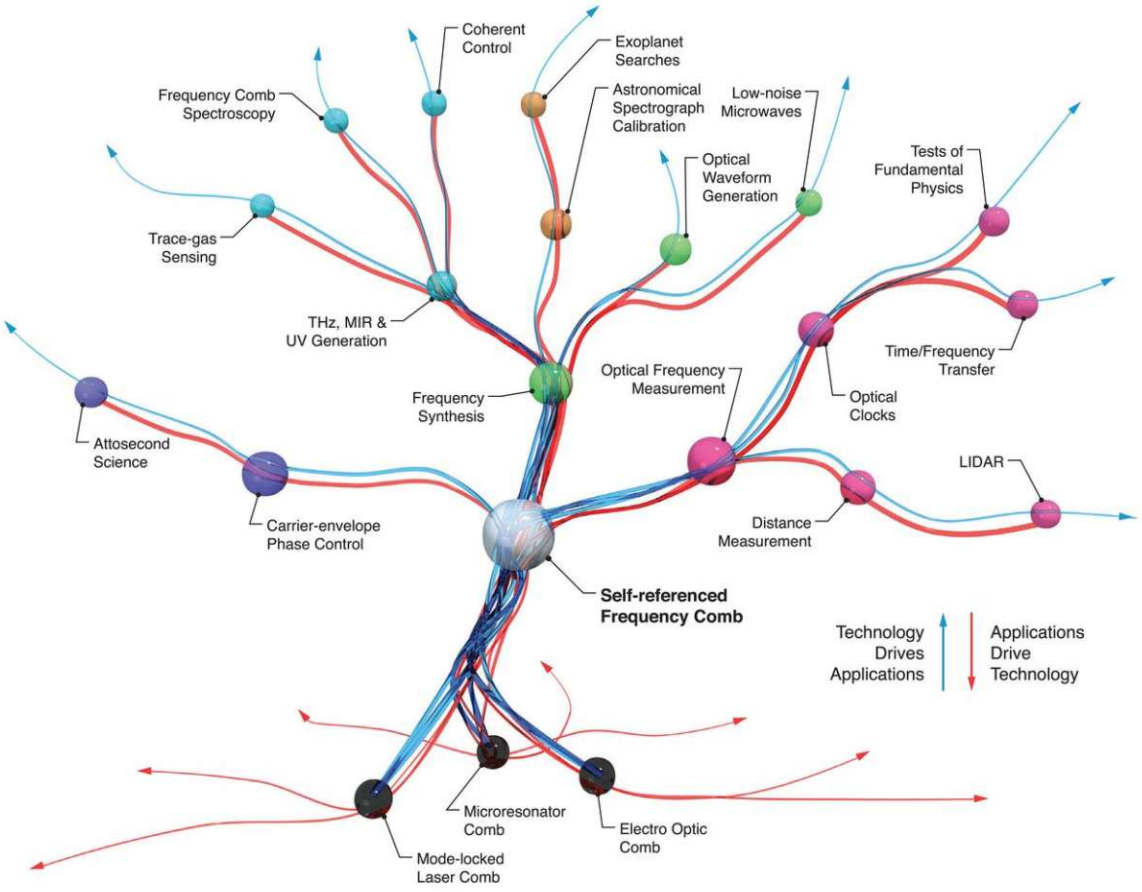

Figure 2.20: Evolutionary tree of the frequency comb technology. Centerpiece towards linking multiple comb spectroscopy techniques is a self-referenced comb. Reproduced from [87] with permission from AAAS (2020).

A frequency comb is defined as a multitude of equally spaced lines in the optical domain, alternatively called comb teeth. Frequency combs can be fully characterized by two essential parameters. Firstly the repetition frequency f_{rep} defining the spacing of the comb teeth in the optical domain and the carrier envelope offset frequency f_{CEO} giving the offset of the comb from the origin (see section 2.5.1). Frequency combs where first observed in mode-locked femtosecond lasers two decades ago and in succession facilitated high precision measurements in atom physics in previously unimaginable precision [88, 23]. Since their first demonstration, frequency combs have fundamentally impacted a vast field of different research areas, from fundamental science, e.g. by development of novel atomic clocks [22], to fascinating applied sciences like e.g. real time observation of protein foldings [26]. Figure 2.20 highlight the branching of self-referenced combs as research hub and link to a manifold of technologies. Over time, more platforms for frequency comb generation emerged including novel laser gain media and Kerr comb generators based on their inherent nonlinearities. In the following the most relevant approaches are discussed. One

approach to comb generation are ultrafast mode-locked lasers that govern a pulse that circulates in the cavity and couples out a fraction of the pulse energy at the facet with every roundtrip. Lasers with femtosecond pulsewidths can be produced using dopants like chromium or iron in II-VI laser gain materials. Astonishing short pulse widths were achieved with passive mode-locking, where a passive element absorbs pulse energy within its saturation time. A semiconductor saturable absorber mirror can be used to allow the generation of femtosecond mode-locked lasers [89]. However, beyond 3 µm light sources for mid infrared comb generation become scarce. Non-linear optical effects allow to connect the visible and the near-infrared spectral range. Difference-frequency generation (DFG) mixes the modes of a frequency comb with a CW laser. This mechanism is strongly limited by phase-matching, where the nonlinear crystals emitted radiation has to constructively interfere in the crystal [90]. Normally the efficiency in the nonlinear optical photon-conversion is low, which gets circumvented by optical parametric oscillators. A mode-locked laser pumps the signal modes of a resonator and the gain profile rises the amplification above the parametric oscillation threshold. Utilizing a special form of parametric oscillation allows the frequency comb generation within an optical microresonator. Typically a sub-milimetre diameter ring gets pumped with a cw source and triggers the third order Kerr nonlinearity of the dielectric resonator material. Kerr combs can span over a whole optical octave [91]. If the pumping wavelength is in the mid-infrared and the resonator material is infrared-enabled, mid-infrared 'super-continua' are generated. High power per modes were achieved with ultrahigh-Q finesse cavity materials like calcium and magnesium fluoride [92, 93]. The large mode-spacing of 100 GHz allows a power per mode in the milliwatt range, enabling multiple emerging applications in spectroscopy and metrology. Especially the mid-infrared spectral region is of particular interest for integrated on-chip sensing devices in science and technology, often referred to as molecular fingerprint region. A manifold of molecules own strong absorption and rovibrational lines in this domain, allowing their analysis with high precision mid-infrared spectroscopy. It composes an impressive tool to perform non-invasive diagnostics of biomarker molecules e.g. aromatics, carbon dioxide or acetates in breath-gas, potentially revolutionizing wearable health diagnostic systems. Power efficient laser devices in the mid-infrared are QCLs and ICLs. The cascading scheme allows the recycling of carriers and consequently leading to wall plug efficiencies up to 27% [94]. The first characterization of QCLs as FM combs in 2012 [95] and also the later on demonstrated active mode-locking of ICLs [28] underlines the potential of monolithic integrated frequency combs in the mid-infrared. From initial tabletop setup sizes, nowadays a frequency comb is feasible with spatial dimensions in the micrometer range. For an extensive discussion and detailled review of mid-infrared frequency combs see [29, 96].

2.5.1 Fundamentals of Frequency Combs

Optical frequency combs are named for their coherent radiation. Their spectrum consists of a set of equidistant lines, equally spaced by the repetition frequency f_{rep} [23, 29]. Initially the first demonstration of optical frequency combs was done with mode-locked femtosecond lasers. The hereby generated pulse circulates in the cavity with a roundtrip time corresponding to a radiofrequency. However, with every roundtrip a fraction of the pulse is emitted as a pulse train (Figure 2.21). The pulse train separation is the cavity roundtrip time

$$T_{rep} = \frac{2L}{v_g} \qquad v_g = \frac{\partial \omega}{\partial k}, \tag{2.50}$$

which gives the repetition frequency

$$f_{rep} = \frac{1}{T_{rep}} = \frac{v_g}{2L}. \tag{2.51}$$

In figure 2.21 the carrier envelope propagation velocity of the pulse train differs to the group velocity due to dispersion. This shifts the pulses by a phase, the carrier envelope offset phase ϕ_{CEO}.

$$E(t) = \sum_n E_n \exp(i(n\omega_{rep} + \omega_{CEO}t) + c.c. \tag{2.52}$$

The mentioned basic requirement of a frequency comb is the equidistant spacing in the frequency domain with the roundtrip frequency $\omega_{rep} = 2\pi/T_{rep}$

$$\omega_n = n \cdot \omega_{rep} + \omega_{CEO} \qquad \omega_{CEO} = \frac{\phi_{CEO}}{T_{rep}}, \qquad n \in \mathrm{N} \tag{2.53}$$

Equation 2.5.1 bears the innovative aspect of combs within, the measurement of frequency differences instead of absolute frequencies. Therefore to achieve equidistant modes, we crucially require a mode-locked laser. The equidistance of the comb teeth can be confirmed with the measurement of the intermodal beatnote, the distribution of the intermodal difference frequencies.

$$E(\omega) = \mathcal{F}(E(t)) = \sum_n A_n \exp(i\phi_n)\delta(\omega - n\omega_{rep} - \omega_{CEO}) \tag{2.54}$$

Frequency comb spectroscopy One of the earliest applications of frequency combs was the precise measurement of the 1s frequency of the hydrogen atom. Such fundamental measurements allow metrology and the realization of atomic clocks, due to the convenient link of microwaves with optical frequencies. Over the last decades direct spectroscopy with frequency combs emerged to its most widespread application. There the laser shines

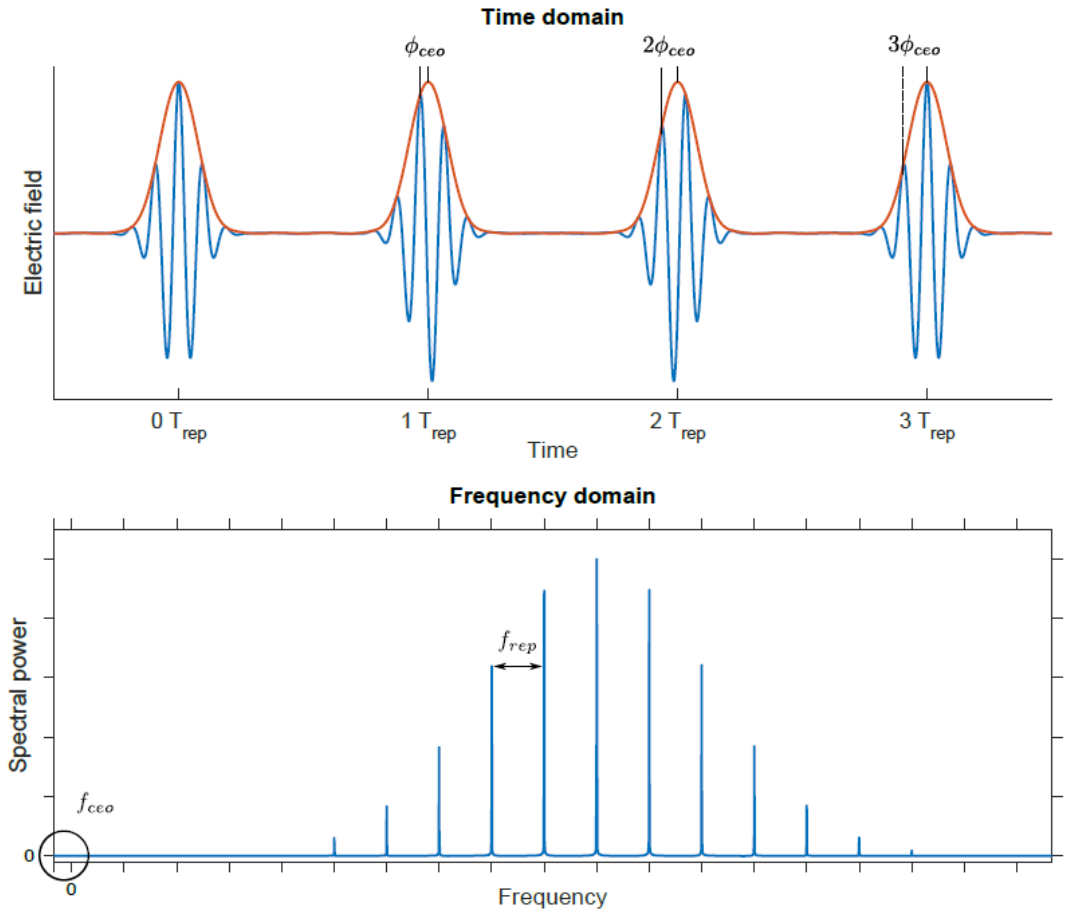

Figure 2.21: Principle of an optical frequency comb. The mode-locked laser emits a pulse train, which governs equidistant frequency teeth. Figure reproduced with permission from [97].

through a gas cell with a sample in the gas phase. In terms of integration this is not convenient and as alternative dual-comb spectroscopy emerges to a promising candidate for monolithic integrated spectrometers. Compared to the Michelson-interferometer based FTIRs, dual-comb spectroscopy is a rather novel method, where two combs with a different line spacing are passing the cell. The two frequency combs differ slightly in their repetition frequency and the comparison of the absorption spectra gives a characteristic molecular absorption profile.

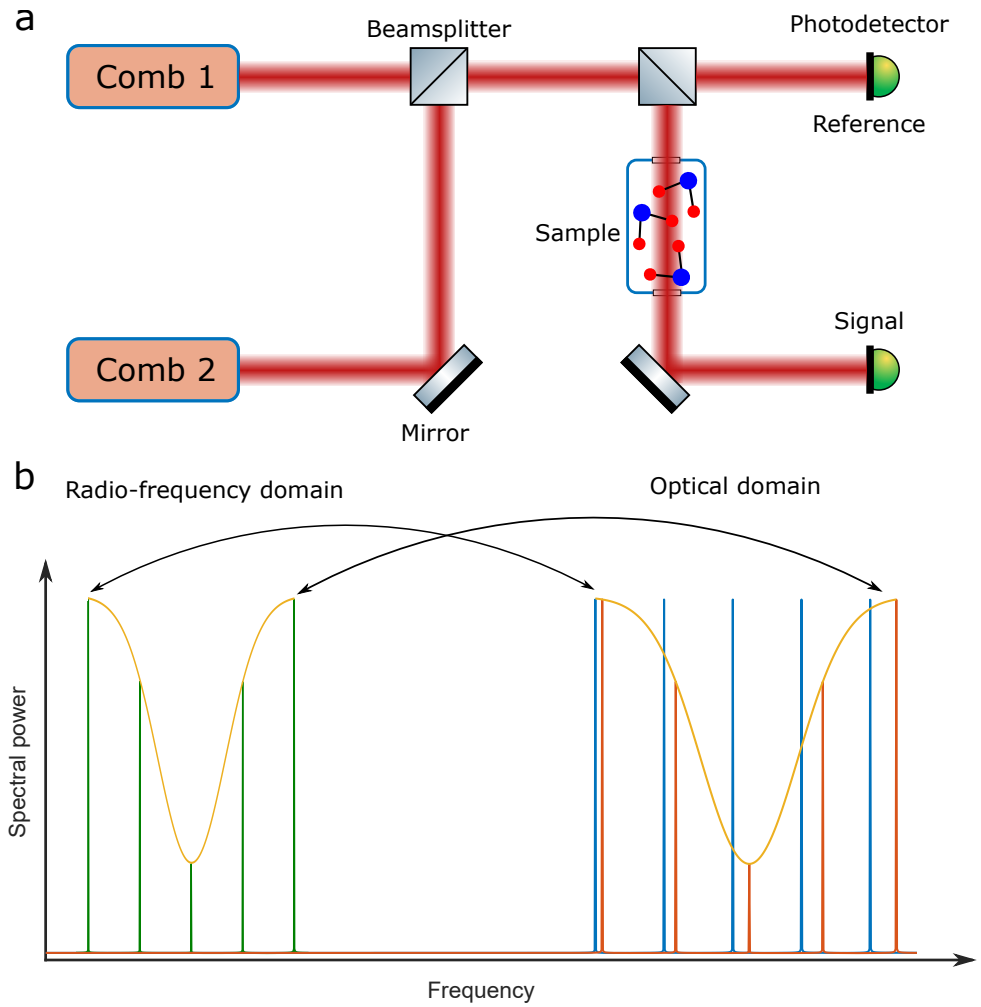

Figure 2.22: Principle method of dual-comb spectroscopy. (a) Experimental schematic of the method: A reference comb 1 shines on a photodetector and the sample comb 2 shines through the interaction region with the analyte onto the signal photodetetor. Comb 1 and comb 2 own slightly different repetition frequencies. (b) In the frequency domain a comb links optical with radio frequencies. The difference signal of the combs is characteristic for a specific molecule. Figure reproduced with permission from [97].

Semiconductor frequency combs Asides from their usability for fundamental science, their table top size is unpractical for applications. Mostly this setups are based on femtosecond mode-locked lasers operating in the near-infrared. Over the course of the last fifty years, semiconductor lasers enabled a manifold of novel applications and technologies.

Their cost efficiency and mature manufacturing technology make them excellent candidates for integrated frequency combs. QCLs and ICLs as semiconductor mid-infrared lasers are therefore promising candidates for this emerging technology. A key requirement for the operation of semiconductor lasers as frequency combs is a broad gain medium. QCLs typically own bandwidths of hundreds of inverse centimetres, which should allow pulse widths down to a couple hundred femtoseconds. QCL combs can be fabricated as Fabry-Perot cavity or ring cavity. In contrast to QCLs with an upper state lifetime of picoseconds, ICLs own an interband transition in the nanosecond range. First experiments to generate ICL combs started with a two section device for passive mode-locking. One section was bombarded with ions to induce a fast saturable absorber in the short section and the other section operated as gain section [20]. The authors published a narrow beatnote, but neither an interferometric autocorrelation nor did they employ another pulse characterization method. It has to be noted that during the time of this work an important insight was made to distinguish FM and AM combs [98, 99]. In general the emission of pulses is not a requirement for comb generation. A stronger statement is the periodicity of the waveform. Mode and phase-locked lasers can be considered as amplitude-modulated (AM) combs. In contraposition there are lasers, that emit a constant intensity profile, where the laser output frequency follows a periodic sweep of the instantaneous frequency.

2.5.2 Mode-locking

Mode-locking depicts the coupling of the phases of each lasing mode to a defined phase relation. This can be either a chirped linear, or solely constant phase relation. It is distinguished between phase and mode-locking, the latter is only verified by characterization of the laser pulses. A mathematical simple expression of mode-locking would be the following. The wave equation can be multiplied with a unitary function $e^{i\phi_\omega}$. Then the phase function has no time dependence and it can be varied in the time domain. If the function has a definite relation to the frequencies ω, then the phases lock and stay constant for every mode. This is therefore called mode-locking, because the modes have a defined phase relation over time. Semiconductor lasers can be modulated by injecting a radio frequency (RF) in the cavity and modulate the losses.

Active mode-locking

Active mode-locking works by implementing a modulator into the cavity to couple the modes and establish a phase relation. Modulators can be acousto-optic or electro-optic elements to change the cavity losses. In semiconductor lasers, the active region can be operated as modulator too, as long as the bandwidth of the modulation exceeds the cavity round trip time. The periodic change of the losses has then to open a small window of

net gain to amplify the laser modes of the pulse. The time domain picture is given in figure 2.23. The short window where the net gain exceeds the losses allows the pulse to evolve. The frequency domain shows side bands of the modulation. The side bands are generated by the frequency of the neighboring modes. These side bands establish the fixed phase relation and induces the mode-locking. Injection locking and the interaction of the modulation side bands. The pulse width of active mode-locking can be calculated

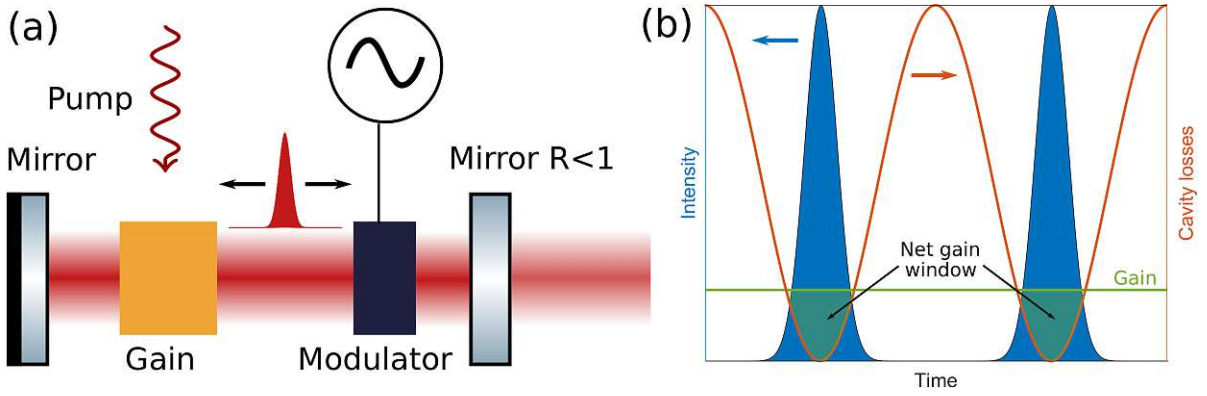

Figure 2.23: Principle of active mode-locking. The inserted modulator in the cavity injects a periodic modulation to the cavity loss. Figures produced by the author himself.

by the derivation from Kuizenga and Siegman [100]

$$T_p \propto \left(\frac{g}{\sqrt{P_{mod}}}\right)^{1/4} \frac{1}{\sqrt{\omega_{mod}\gamma_g}}, \tag{2.55}$$

with the unsaturated gain g and the modulation power P_{mod}. The gain bandwidth reads as γ_{mod} and the modulation frequency ω_{mod}. Hereby, the pulse width is inversely related to the square root of the modulation frequency and the gain bandwidth. Therefore the generation of ultrashort pulses that are gain limited is not feasible with active modulation of the cavity and rather only achievable by passive mode-locking.

Passive mode-locking

Inserting a passive non-linear element to the laser system can mode-lock the system without any additional external injection of a time-dependent signal. The passive element is a saturable absorber, that satisfies the transition lifetime condition. The dominant mechanism in nearly all-passively mode-locked (PML) lasers is pulse shortening during transmission through the absorbing element. PML is of particular interest, as picosecond pulses and femtosecond lasers outscale the limited frequency range of electronics.

$$\alpha_{abs} = \frac{\alpha_0}{1 + \frac{I}{I_{sat}}}, \tag{2.56}$$

$$T_p \propto \sqrt{\frac{g}{\kappa A_0^2}} \frac{1}{\gamma_g}. \tag{2.57}$$

Pulses that are limited by the gain bandwidth can only be generated by passive mode-locking, in the past this allowed pulse width down to femtoseconds. Depending on the lifetime condition, it is distinguished between fast and slow saturable absorbers, leading to different theoretical treatments [101]. Figure 2.24 gives a schematic of PML. The saturable absorber opens a net gain window and the modes get amplified. The saturation threshold cuts off the time-dependent amplification and the pulse is formed.

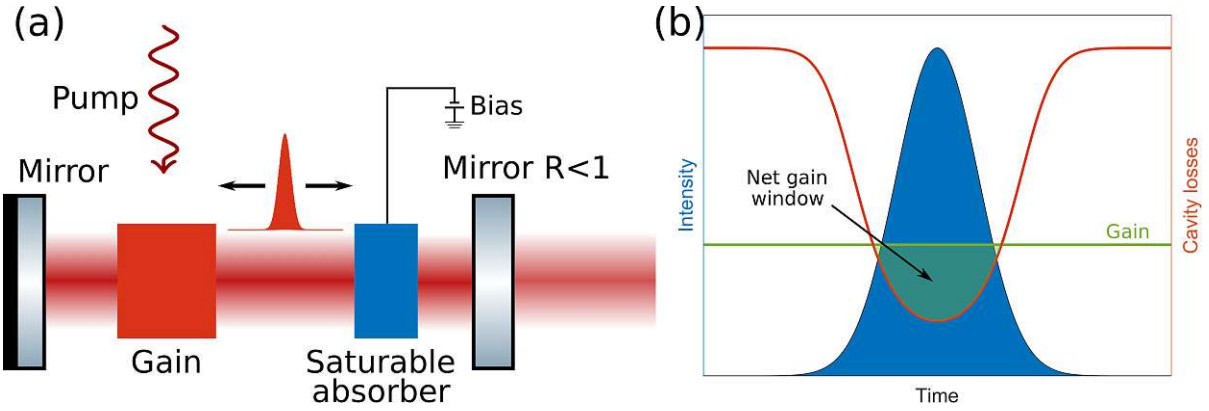

Figure 2.24: Principle of passive mode-locking. The inserted modulator in the cavity injects a periodic modulation to a laser parameter. Figures produced by the author himself.

2.5.3 Characterization of frequency combs

Optical pulses are difficult to characterize due to their short timescales. The characterization of their pulse shape, peak power, pulse width and the phase relation has lead to a lot of different measurement methods in the past. Detecting the comb properties can be done with non-linear or high-speed detectors [102], e.g. the non-linear method frequency resolved optical gating (FROG) or spectral phase interferometry for direct electric-field reconstruction (SPIDER) [103, 104]. Both concepts recombine the emitted pulse with a time delayed copy of the pulse itself. A non-linear crystal allows to recover the time information and the complex spectrum can be extracted. The non-linear effects of the crystal are power dependent, which does not give femtosecond lasers with peak powers up to megawatts any issues. Semiconductor lasers are exluded intrinsically from this methods due to their significantly lower power (Watts) and the physical difference that was discovered recently [105]. The FM comb formation of QCLs and ICLs excludes them from established pulse characterization methods. A novel method to characterize FM frequency combs is shifted wave interference Fourier transform spectroscopy (SWIFTS) introduced by Burghoff et al. in 2015 [106]. It is the method of choice for semiconductor

laser frequency combs as it allows the retrieval of the temporal waveform and the reconstruction of the phase relation. It requires a QWIP and a FTIR. The method will be explained below, with some details about the FTIR first.

Fourier Transform Infrared Spectroscopy

Fourier Transform Infrared spectrometers (FTIR) enable spectral measurements over a wide spectral range [107]. The main principle is the interference of two light beams in the interferometer (figure 2.5.3). The beam of a single frequency source pinges the beamsplitter, with one part shining on a movable mirror and the other part on the fixed mirror. If the beam path difference δ of the reflected beam of the movable mirror with

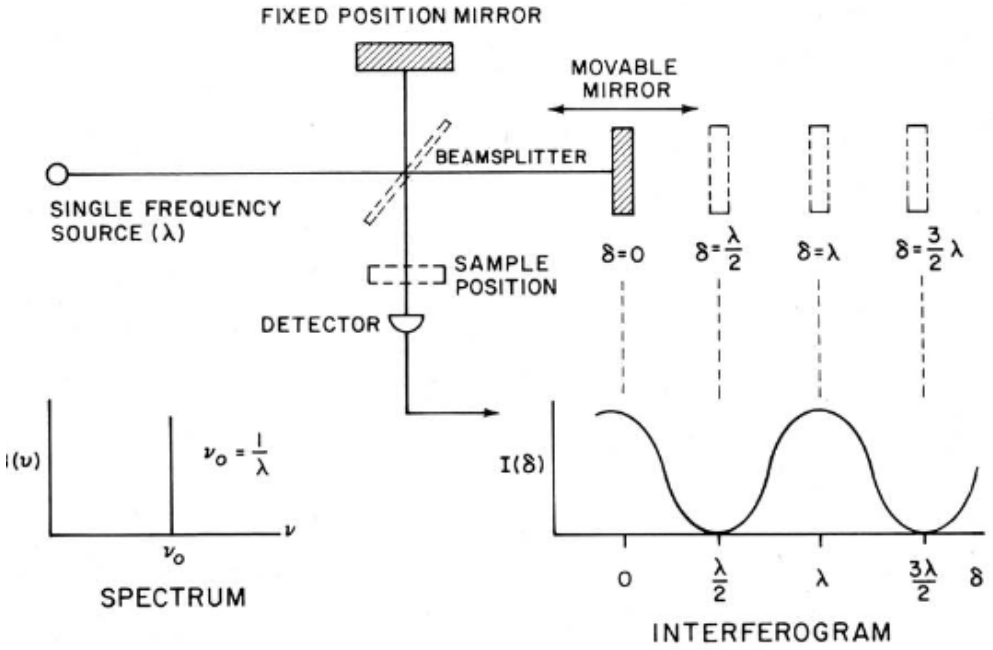

Figure 2.25: Working principle of an FTIR. The frequency source interferes with the second beam passing through the beam splitter. Figure adapted and reproduced from [108] with permission of ACS Publishing (1986).

the reflection of the fixed mirror satisfies the multiple of the wavelength λ

$$\delta = n \times \lambda \qquad n \in \mathbf{N}, \tag{2.58}$$

the beam interferes constructively. The interferogram can be written as

$$I(\delta) = B(\nu)\cos(2\pi\frac{\delta}{\lambda}) = B(\nu)\cos(2\pi\delta\nu). \tag{2.59}$$

either in terms of wavenumber of frequency with $I(\delta)$ as intensity and $B(\nu)$ as brightness of the source. The corresponding spectrum is calculated with the Fourier transform of

the intensity

$$B(\nu) = \int_{-\infty}^{\infty} I(\delta)\cos(2\pi\delta\nu)d\delta. \tag{2.60}$$

One has to consider that the assumed single source interferes only once, leading to a single line as spectrum. In reality the light source is a broadband infrared glow-bar, which allows measurements over a wide spectral range, as its emission spectrum is similar to a blackbody radiator. The interferogram then reads as

$$I(\delta) = \int_{-\infty}^{\infty} B(\nu)\cos(2\pi\delta\nu)d\nu. \tag{2.61}$$

Lock-in amplifier

The lockin amplifer can extract amplitude and phase of a noisy signal. It combines a low-pass filter with a homodyne signal detection. The noisy signal gets coupled to a reference signal and the result is low-pass filtered. The response signal V_s and the reference signal V_r are fed in the amplifier. The mixing of the signals is a multiplication

$$V_m(t) = V_s(t) \cdot V_r(t) \tag{2.62}$$

$$V_m(t) = R\cos(2\pi f_s t + \theta_s) \cdot \cos(2\pi f_r t), \tag{2.63}$$

with the mixed signal V_m, the input frequency f_s, the reference frequency f_r, the amplitude R and the phase θ. The amplitude R consists of the in-phase component X and the quadrature component Y. The quadrature signal gets calculated as the reference is phase-shifted by $\pi/2$ and multiplied with the signal V_s. The amplitude R can also be extracted with coordinate transformation

$$R = \sqrt{X^2 + Y^2} \qquad \theta = \arctan(Y, X). \tag{2.64}$$

The lock-in amplifier is a key instrument for extracting the phases of semiconductor laser frequency combs, see section 2.5.3.

Shifted wave interference Fourier transform spectroscopy (SWIFTS)

Frequency combs own a manifold of equidistant modes with a correlating amplitude and phase. In order to characterize the temporal form of the frequency comb we need a method to measure the coherence and extract information about the spectral phases. The experimental setup consists of a fast two-photon QWIP, a Lock-in amplifier and a FTIR (figure 2.26). The coherent characterization of semiconductor laser combs was already

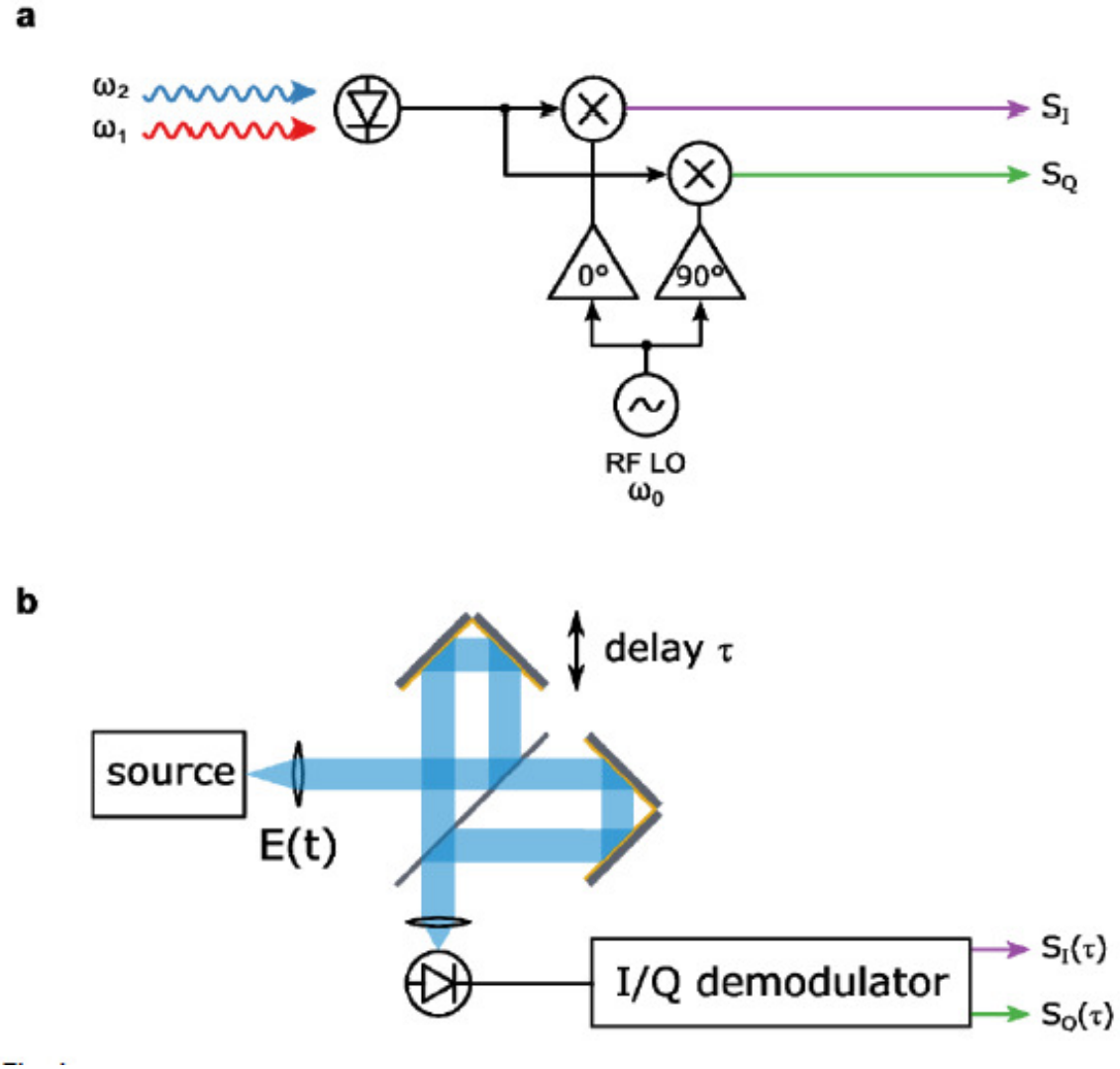

Figure 2.26: Experimental setup for SWIFTS characterization. (a) Two different frequency sources ω_1 and ω_2 shine on the fast QWIP.Demixing with the RF local oscillator gives the signals S_I and S_Q (b) The frequency comb shines on a fast two photon QWIP and the signal gets demodulated by a Lock-in amplifier. Reproduced from [106] with permission of Optica Publishing (2015).

demonstrated for mid-infrared and terahertz QCLs [109, 110, 111] and basic experiments were also carried out to show pulse formation in ICLs [28], which will discussed in more detail later on. The mathematical background of SWIFTS will be explained and derived in the following based on [97, 14]. A frequency comb emits a set of equidistant modes E_n, with an amplitude A_n and the correlating phase ϕ_n. The comb mode generates a signal at the difference frequency to the adjacent neighboring modes, a beating of E_n and E_{n+1} with $f_{rep} = f_{n+1} - f_n$. Furthermore is the phase difference of neighboring modes $\phi_{n,n+1} = \phi$. The individual beating $B_{n,n+1}$ start to influence the light intensity at their beating frequency f_{rep} and results in the laser beatnote B of the equidistant frequency comb modes

$$B = \sum_n B_{n,n+1}, \tag{2.65}$$

with the phases ϕ_n of the beating signals

$$\phi_n = \sum_{k<n} \phi_{n,n+1}. \tag{2.66}$$

The beating signals need to be measured with a frequency resolution. The fast two photon QWIP in the SWIFTS setup (figure 2.26) divides the comb beatings. The laser beam shines through the FTIR which sweeps the mirror and therefore varies the measurement time dependent. The comb beatnote before and after the FTIR gets compared and the local oscillator allows the demixing with the Lock-in amplifier. The X and Y quadrature components of the lock-in amplifier contain the information for the corresponding retrieval of the spectral phases and amplitudes. The mathematical derivation for the SWIFTS interferogram on the QWIP can be as the following [14]. The frequency comb field is given by

$$E(t) = \sum_n E_n \exp(i\omega_n t) + c.c. \tag{2.67}$$

The FTIR sweeps the mirror with one arm only and induces the time delay τ

$$E(t)E(t+\tau) = \sum_{n,m} (E_n \exp(i\omega_n t) + c.c.)(E_m \exp(i\omega_m t) + c.c.) \tag{2.68}$$

$$= \sum_{n,m} (E_n E_m \exp((i(\omega_n + \omega_m)t) \exp(i\omega_m \tau) + \tag{2.69}$$

$$+ E_n E_m^* \exp(i(\omega_n - \omega_m)t) \exp(-i\omega_m t))) + c.c.). \tag{2.70}$$

The DC signal of the QWIP is the equivalent of $m = n$, which results in the intensity interferogram. The retrieval of the intermodal phase relation is the the summation over

the neighboring beating modes with $m = n \pm 1$. Their frequency is the laser beatnote frequency of the comb and allows the summation over the lowest and highest comb mode N_{min} and N_{max}

$$E(t)E(t+\tau) = \sum_{n,m}(E_n \exp(i\omega_n t) + c.c.)(E_m \exp(i\omega_m t) + c.c.) \tag{2.71}$$

$$= \sum_{n,m}(E_n E_m \exp((i(\omega_n + \omega_m)t) \exp(i\omega_m \tau) + \tag{2.72}$$

$$+ E_n E_m^* \exp(i(\omega_n - \omega_m)t) \exp(-i\omega_m t))), \tag{2.73}$$

with the intermodal difference frequency $\delta\omega = \omega_{n+1} - \omega_n$. Regrouping the equation and adapting the summation from n+1 to n leads to

$$E(t)E(t+\tau) = 2 \sum_{n=N_{min}}^{N_{max}} |E_n^2| \cos(\omega_m \tau) + B(t,\tau) \tag{2.74}$$

with the beating between neighboring modes $B_{n-1,n} = E_n E_{n-1}^*$. the first term represents the DC signals interferogram of the intensity on the QWIP $I(\tau)$ with the interferogram as Fourier transform

$$I(\omega)\mathcal{F}(I(\tau))(\omega) = \sum_n |A_n|^2 \delta(\omega - \omega_n). \tag{2.75}$$

The two quadrature component X and Y of the Complex SWIFTS interferogram defined by

$$S(\tau) = X(\tau) + iY(\tau), \tag{2.76}$$

are given by

$$X(\tau) = \int_0^{T_{LI}} B_1(t,\tau) \cos(\omega_{rep} t) dt, \tag{2.77}$$

and

$$Y(\tau) = \int_0^{T_{LI}} B_1(t,\tau) \sin(\omega_{rep} t) dt. \tag{2.78}$$

The beatnotes interferometric signal is noted as $B(t,\tau)$. The Fourier transform gives us then the complex spectrum

$$S(\omega) = (S(\tau) = X(\tau) + iY(\tau)) = \sum_n < A_{n-1} A_n \exp(i(\phi_n - \phi_{n-1} > \delta(\omega - \omega_n). \tag{2.79}$$

The coherence characterization of the comb reads then as the intermodal beatings correspond to the SWIFTS spectral modes. If the laser is periodic, the intermodal phases are satisfying a constant relation in time and the average yields zero. Therefore the comb spacing stays constant too, which gives us the coherence of the comb. This can be written as $|B_{n-1,n}| = A_{n-1}A_n$. The key points of this analysis and finally the results of the characterizing measurements are the equidistance of the laser comb modes (the amplitudes A_nA_{n-1}) and the retrieval of their constant phase relation in time. The constant phase relation of the intermodal phase difference $\Delta\phi = \phi_n\phi_{n+1}$ gives information about the state of the mode-locking. The equidistance with the repetition frequency of the spectral mode.

CHAPTER

THREE

MOLECULAR BEAM EPITAXY OF III-V SEMICONDUCTOR HETEROSTRUCTURES

Quantum cascade devices consist of semiconductor materials with layer thicknesses down to the distance of single atomic layers. The growth of functional devices requires an extraordinary high level of precision and control over growth parameters. This can be performed with Molecular Beam Epitaxy (MBE) or Metal-Organic Chemical Vapor Deposition (MOCVD). MBE is a crystal growth technology that can produce semiconductor, metal, or oxide layers. The distinguishing feature of MBE growth to other techniques is the beam of non-interacting atoms or molecules directed onto the substrate in an ultra-high vacuum environment. This chapter gives background information about the epitaxial growth and the MBE technology. A more in depth discussion of epitaxial growth methods and related engineering can be found in [112, 113].

3.1 Thin Film Epitaxy

The term 'epitaxy' originates from the greek words 'epis' and 'taxis', meaning 'top' and 'order'. It relates to the deposition of atoms or molecular beams on top of a crystal template as continuation of the substrates crystal structure. The crystal growth technique is a phase transition from the gas or liquid phase to a solid, crystal phase, driven by deviation from the thermodynamic equilibrium. This is a requirement for the generation of atomically abrupt and sharp interfaces. It suppresses diffusion between layers, a key requirement for the design of semiconductor heterostructures like QCLs. Epitaxial growth can differ by the used materials, although the main tools are the same. It requires a substrate heater to establish the thermodynamic potential for crystal growth and a source material with a shutter to interrupt the molecular beam, in-situ tools like Reflective High Energy Electron Diffraction (RHEED) for determining the growth rate and a pyrometer for temperature measurement (see Figure 3.1). The reactor chamber employs ultrahigh

vacuum conditions and is therefore equipped with multiple pumps to maintain this state. Furthermore a cryo shroud around the chamber can be filled with liquid nitrogen (LN2) at 77 K to further lower the pressure by working as thermal insulation and as a cold trap for ions and atoms. Figure 3.2 gives an overview over the material systems grown by

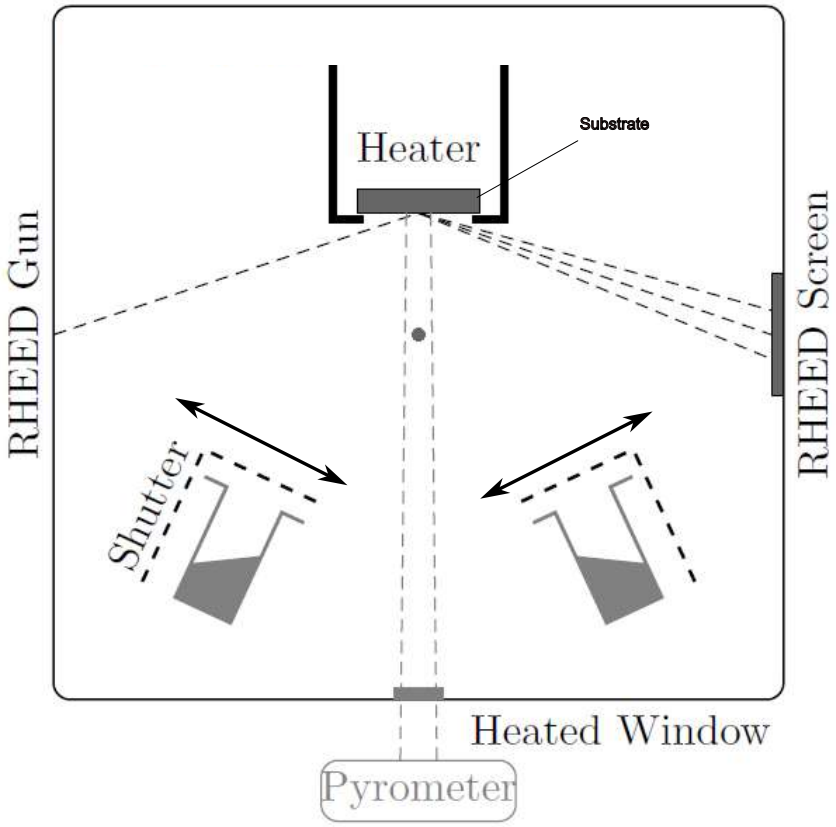

Figure 3.1: Scheme of an MBE reaction chamber. Effusion cells oppose the substrate for the crystal growth. By thermal evaporation, the target material is deposited on the substrate material. The shutters can block the molecular flux to alternate material compositions and growth of heterostructures.

MBE that were significant for this work. InSb is a low bandgap material with a much higher lattice constant than the common 6.1Å family materials, which makes it difficult to implement as substrate or layer material. A key material for ICLs is the ternary InGaSb layer, it gives the active W quantum well its band gap for the interband transition.

3.1.1 Homo- and heteroepitaxy

The lattice constant of deposited materials can differ from the substrate, which leads to stress in the films. Homoepitaxy describes the crystal growth of identical atoms to the substrate and heteroepitaxy for different deposited atoms to the substrate. The growth

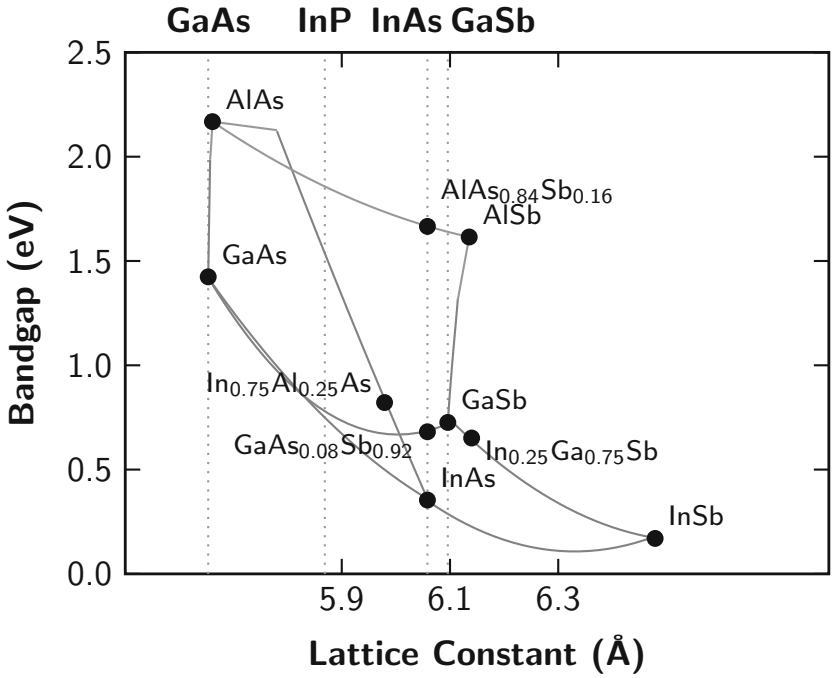

Figure 3.2: Bandgap map of III-V elements with the bandgap energy versus the lattice constant. AlAsSb can be lattice matched to InAs and GaSb, common substrates for ICL growth in the 6.1 Å family.

of the substrate material as an epilayer demands excellent control of growth parameters [114]. Especially heteroepitaxial growth can require lattice matching techniques to the substrate. If the lattice constant mismatch is too large, then epitaxial crystal growth is not feasible. If an epilayer consists of more than two components, the lattice constant can be calculated by linear interpolation of the binary constituents with fitting parameters A, B and C, using Vegards law [115]:

$$a(A_xB_{1-x}C) = xa(AC) + (1-x)a(BC) \tag{3.1}$$

The growth of heteroepitaxial layers for III-V semiconductors is a topic of extensive research since the beginning of its research [116]. Mixed group V materials are a key ingredient for ICLs (3.2). MBE growth of high-quality antimonide layers can be challenging [117, 118]. The intermixing of antimony with arsenic counteracts a controlled growth of these layers and makes their MBE growth a complex task.

3.2 Strain and relaxation

Lattice mismatch between the epilayers can lead to stress during crystal growth and to strain in the heterostructure. Strain changes the designed bandstructure and it helps MIR QCLs with the performance of the devices. Excessive strain can induce defects and deformations by exceeding the energy required to generate a dislocation. Hook's law is

given with the stress-strain relation

$$\sigma = \mathbf{E}\mathbf{e}, \tag{3.2}$$

with the stress tensor σ, the elasticity matrix $\mathbf{E}$ and the strain tensor $\mathbf{e}$ [119]. The consequent strain matrix in a cubic crystal structure is the result of the stress-strain relation

$$\begin{pmatrix} \sigma_{xx} \\ \sigma_{yy} \\ \sigma_{zz} \\ \sigma_{yz} \\ \sigma_{xz} \\ \sigma_{xy} \end{pmatrix} = \begin{pmatrix} C_{11} & C_{12} & C_{12} & - & - & - \\ C_{12} & C_{11} & C_{12} & - & - & - \\ C_{12} & C_{12} & C_{11} & - & - & - \\ - & - & - & C_{44} & - & - \\ - & - & - & - & C_{44} & - \\ - & - & - & - & - & C_{44} \end{pmatrix} \begin{pmatrix} \epsilon_{xx} \\ \epsilon_{yy} \\ \epsilon_{zz} \\ \epsilon_{yz} \\ \epsilon_{xz} \\ \epsilon_{xy} \end{pmatrix} \tag{3.3}$$

with the stress tensor components σ_{ij}. the strain tensor components ϵ_{ij} and the stiffness coefficients C_{ij}. The strain component ϵ_{ii} of the crystal direction i

$$\epsilon_{ii} = \frac{a_i^L - a_0^L}{a_0^L}, \tag{3.4}$$

with the relaxed layer lattice constant a_0^L and the strained lattice constant a_i^L in the direction i. If the in-plane biaxial stress in the growth direction and its component is zero, the layers lattice constant is given by

$$a_{x,y,z}^L = a_0^L \left[1 - 2\frac{C_{12}}{C_{11}} \left(\frac{a_0^S - a_0^L}{a_0^L} \right) \right]. \tag{3.5}$$

If the in-plane biaxial stress due to the mismatch of lattice constants is non-zero, there is tetragonal distortion of the crystal

$$a_x^L = a_y^L \neq a_z^L, \neq a_0^L. \tag{3.6}$$

The layer is then called pseudomorphic, when the film is fully strained and the relaxation through the introduction of misfit dislocations has not occurred. Figure 3.3 highlights the scheme of strained and relaxed epilayers.

3.3 Critical Thickness

An important term in MBE growth is the critical thickness h_c of a strained layer material. The critical layer thickness refers to the point at which the accumulation of strain in the material structure results in the formation of defects. Beyond this thickness, the continued growth of the layer can result in an increased density of defects, potentially

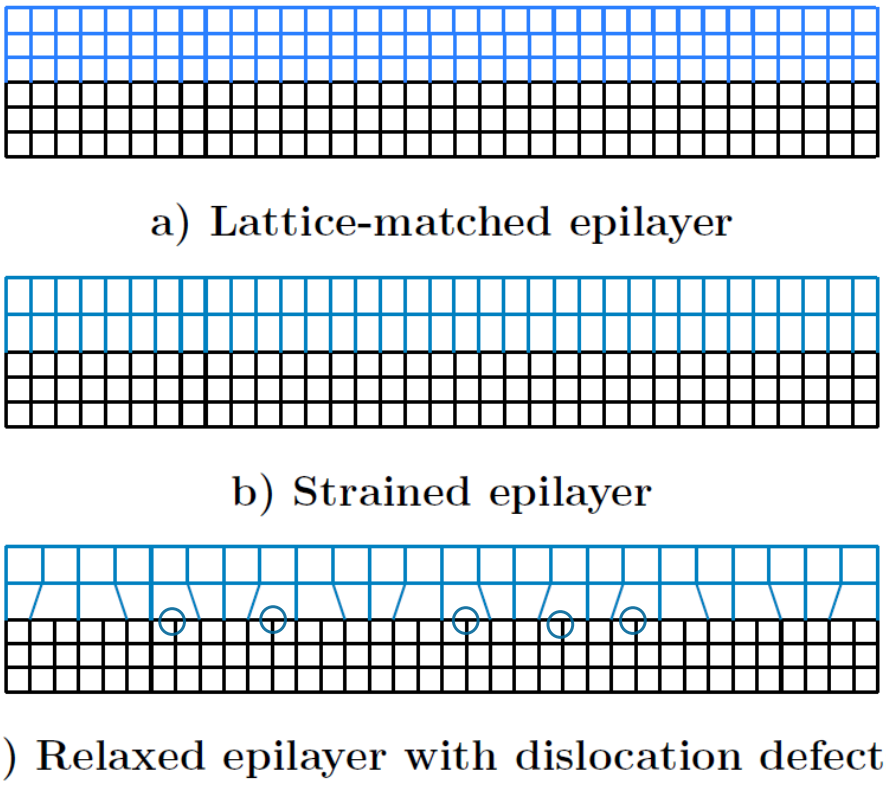

Figure 3.3: (a) Lattice-matched epilayer (b) Compressively strained epilayer (c) Relaxed epilayer with dislocation defects. Figure reproduced with permission from [43].

compromising the quality and performance of the material. The critical thickness is therefore a fundamental parameter in the growth and characterization of thin films, and an understanding of its value and dependence on various growth conditions is essential for the successful development of high-quality materials. Increasing this parameter is therefore particularly interesting. Beyond this thickness the strain energy in the mismatched layers is large enough to induce a dislocation to relieve the strain [120], as illustrated in figure 3.4. A study of Matthews and Blakeslee investigated the impact of balanced energy densities

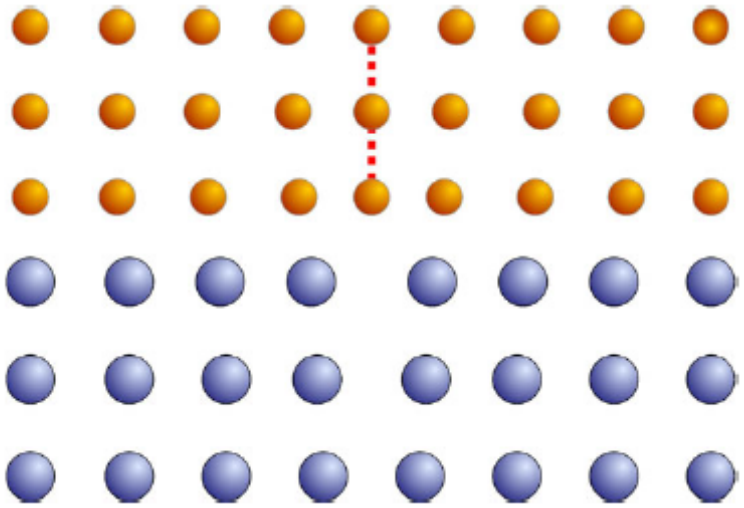

Figure 3.4: Schematic of an edge dislocation in a heterostructure. The dislocation relaxes the misfit energy and induces a defect in the lattice. Figure reproduced from [38] with permission of Springer Nature Group (2020).

by dislocations and strain [120]. Using Lamberts W-function, the criterion can be written as

$$h_c = \frac{-b}{4\pi e \sin(\theta)\cos(\lambda)} \frac{1-\nu\cos^2(\theta)}{1+\nu} W\left(\frac{-4\pi e \sin(\theta)\cos(\lambda)}{\alpha} \frac{1+\nu}{1-\nu\cos^2(\theta)}\right). \tag{3.7}$$

with the critical thicknes h_c, Burgers vector b, the angles θ and Hereby ν is given by

$$\nu = \frac{C_{12}}{C_{11}+C_{12}}, \tag{3.8}$$

with the elements C_{ij} of the stress-strain matrix and the dislocation parameter core parameter α, a fitting parameter between 1 and 4 [121]. A good estimate for the critical thickness in fcc crystals is the relation of the elastic strain with the Burgers vector $b_f = a/\sqrt{2}.$, where a is the lattice constant. It is known that this relation inclines to overestimate the actual critical thickness, but works well as a figure of merit [122]. It reads then as

$$\epsilon \approx \frac{a_f - a_s}{a_f}, \tag{3.9}$$

resulting in

$$h_c \approx \frac{b_f}{\epsilon}, \tag{3.10}$$

with the strain ϵ, the thin film thickness a_f, the substrate lattice constant a_s and the critical thickness h_c. In the context of this work, the critical thicknesses of ICL materials is important, especially the critical cumulated thickness of InGaSb, as it is given in figure 3.5.

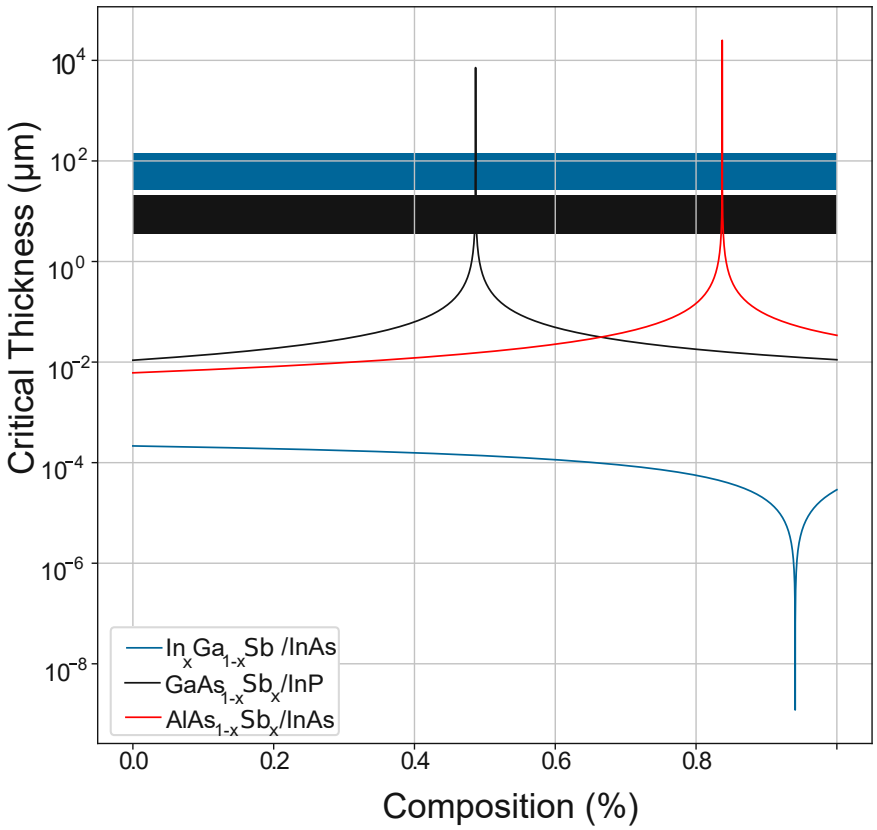

Figure 3.5: Critical thickness of different material systems vs. alloy composition. The colored rectangular areas in the background highlight the parameter space in which QCLs can be grown. InGaSb is an important material for ICL growth. Clearly, the critical thickness for growing InGaSb is very low with 12 nm.

Extending the critical thickness Dislocation free growth of heterostructures is the goal for state of the art optoelectronics. Defects and material inhomogeneities harm device performance and increase material degrading [123]. The critical thickness for layers describes the thickness beyond which misfict disloactions grow and multiply with increasing stress. Strained-superlattices can alternate the strain and can be engineered to balance down the strain by either grading of the layer composition or by adjusting layer thicknesses and

thereby lowering the defect densities. A different concept is epitaxial lateral overgrowth, a method that is usable if the growth rate parallel to the substrate surface is comparably higher than the growth rate perpendicular to the substrate. This method is selected for the growth of nitrides on mismatched substrates [124]. Aside from adjusting the growth within the layers, one can also change the approach and use extremely thin substrates that absorb the strain, which gets split up then between the epitaxial grown layer and the thin substrate. The substrate works then primarily as seeding layer for the epilayer, leading to a layer thickness limited more by the heterostructure design and reasonable growth time. Note, that this method is not often suitable, too thin substrates increase fabrication problems and make the substrate handling difficult. Flip-chip bonding or thinning the substrate after epitaxial growth are methods with a high risk of breaking the sample and are not recommended.

3.4 Crystal growth modes and kinetics

Epitaxial growth is not simply a deposition of atoms. The crystalline growth has different growth modes with different properties. The crystal growth mode is influenced by multiple parameters, e.g. the substrate temperature, surface saturation of bonding sites on the substrate, beam flux of evaporated source materials etc., which affect the whole system. In the end, this leads to different growth modes and kinetics, as explained in the following section.

Thermodynamics The MBE system can be viewed as an open thermodynamic system, which minimizes the Gibbs free energy

$$G = U + pV - TS = G^{\alpha} + G^{\beta}, \tag{3.11}$$

with the entropy S, the intrinsic energy U, the different phases α and β and the free energy of a phase $G^{\alpha,\beta}$. The thermodynamic equilibrium balances the particle number per phase. The partial derivations of the particle numbers are the chemical phase potentials μ as partial derivative of the Gibbs energy

$$(\partial_n G^{\alpha})_{T,p,n} = \mu^{\alpha} - \mu^{\beta} = 0. \tag{3.12}$$

The vapor phase of the evaporated source material and the crystallization phase on the substrate surface are governed by the the law of mass action

$$\mu_{\alpha}^{0} + N_A k_B T \ln(a_{\alpha}^{e}) = \mu_{\beta}^{0} + N_A k_B T \ln(a_{\beta}^{e}), \tag{3.13}$$

with the Avogadro constant N_A and the Boltzmann constant k_B. Figure 3.6 shows the equilibrium between two phases, the interface between the solid and the energetically less favorable phase α. It is assumed to be infinitely thin, with the surface extending over an atomic layer. The activities $a^e_{\alpha,\beta}$ are related to the difference of the chemical potentials

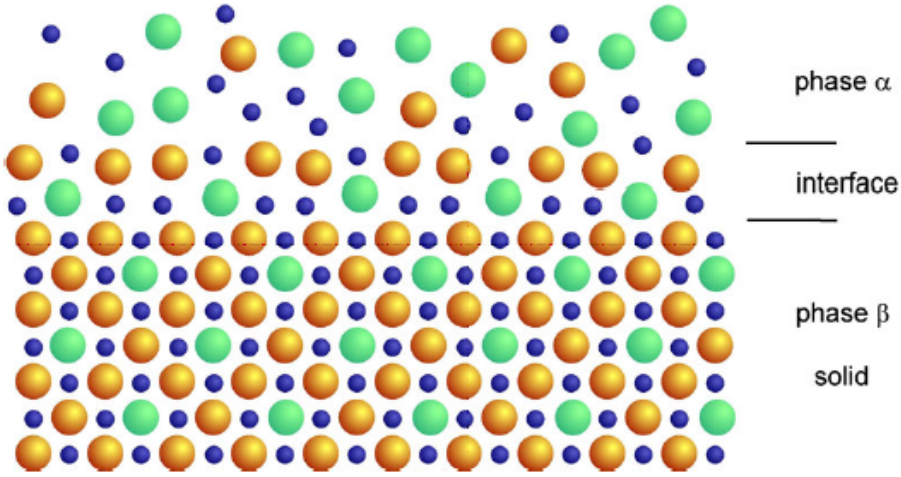

Figure 3.6: Schematic of the separation of phases α and β. The interface separates solid and vapor phase. Figure reproduced from [38] with permission of Springer Nature Group (2020).

$\mu^0_{\alpha,\beta}$, which would result in an equal distribution of particle numbers between phase α and β, if the thermodynamical system would be viewed as closed. The MBE chamber has interactions due to chamber pressure and material flux. The non-equilibrium state of the MBE growth is maintained by a saturated vapor impinging on the substrate surface, uttering as difference in chemical potential

$$\Delta\mu = k_B T \ln(\frac{p}{p_0}), \tag{3.14}$$

with the pressure p_0. Note, that this chemical potential is the driving force of crystalline growth. If we want to introduce a transition from a stable and inert phase to a target phase, we have to control pressure and temperature of the system towards a lower chemical potential in the target phase. MBE growth allows crystalline growth of phases far from the thermal equilibrium, in contrast to equilibrium techniques like for instance liquid phase epitaxy.

Growth modes The growth mode of an epitaxial growth technique is related to the surface temperature, the strain and the surface saturation. Figure 3.7 shows three key epitaxial growth modes [113]. In order to be able to grow semiconductor heterostructures, we employ the layer-by-layer Frank-van-der-Merwe growth mode. As the structure is grown layer-by-layer it leads to sharp interfaces in the heterostructure, In contrast to the mode described above, stronger attraction between the atoms of the crystal growth

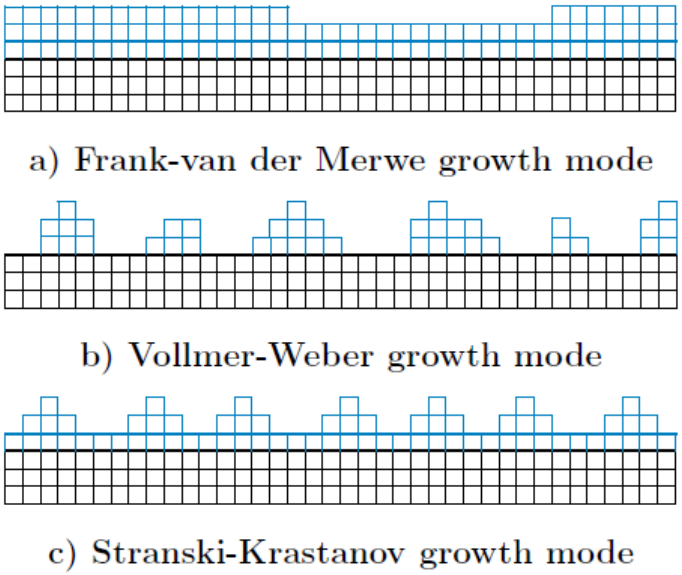

Figure 3.7: Epitaxial growth modes. (a) Layer-by-Layer growth (b) 3D Island (c) Wetting layer. Figure reproduced with permission from [43].

species and not towards the nucleation site of the substrate leads to the formation of 3D islands. This growth mode is called Vollmer-Weber growth mode. A hybrid case between the two mentioned growth regimes is the Stranksi-Krastanov growth mode. A characteristic feature is the strained wetting layer that initiates the island growth after the specific critical thickness is exceeded, continuing to grow can then lead to dislocations and defects. This growth mode can also be used as technique for quantum dot and quantum wire growth. A gallium free ICL structure is shown in figure 3.8. A compressively strained wetting layer is grown on a substrate (e.g. InSb on GaSb) until the layer relaxes and 3D islands start to from. Sufficient control of flux and temperature allows then for instance the growth of quantum dots [125]. It furthermore indicates that a rough surface can be more stable than a flat surface, a reason why specific MBE growth of optoelectronics requires substrate miscuts in order to achieve layer-by-layer growth modes. Recent efforts managed to grow QCLs on silicon substrates with a miscut of 6 degrees [126]. Fabricated devices performed on a comparable level to QCL grown on InP substrates.

Surface reactions and reconstructions An excess of molecules in relation to the available bonding sites on the substrate template is called supersaturation. The supersaturation on the crystalline surface during growth leads to different kinetics on the growth side. The molecular beam of the growth species can be adsorbed, migrate on the surface or interact otherwise with the crystal [113]. Figure 3.9 shows the principle interaction mechanisms, when atoms impinge on the surface. The possible interactions of the molecular beam on the surface are diffusion, incorporation, aggregation and desorption. A model

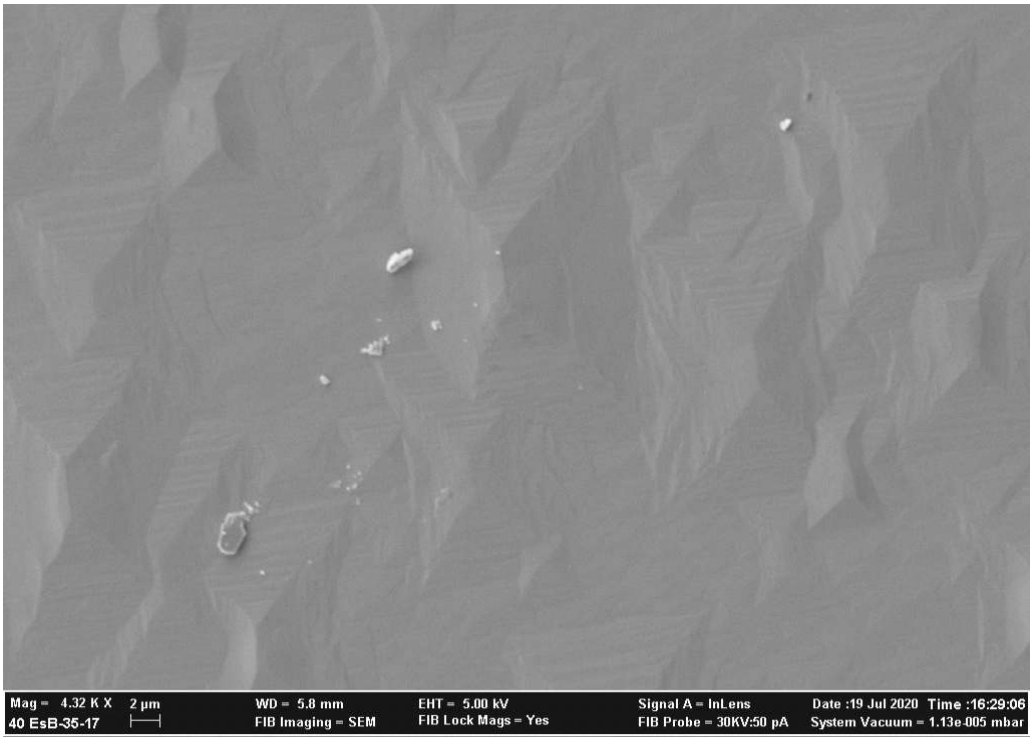

Figure 3.8: SEM micrography of an antimonide heterostructure that was grown with a Stranski-Krastanov-like growth mode. Sample C0890 was grown with an emptying gallium source cell. Mid-growth the flux dropped by 90%. The peak-valley heights of the pyramid shaped structures are roughly 700 nm. Figures produced by the author himself.

system for this is the epitaxial growth of GaAs. GaAs can be grown with either arsenic

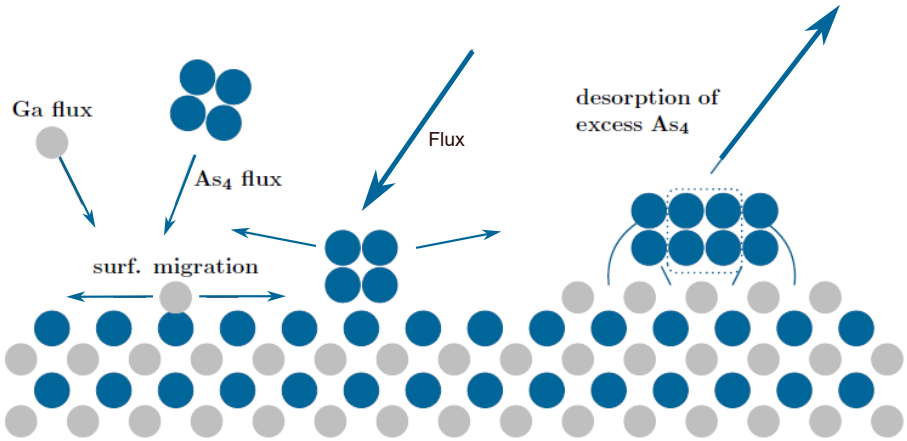

Figure 3.9: Surface Kinetics of impinging atoms on a crystalline surface. The Ga atoms can migrate on the surface, while excess tetramer arsenic gets desorbed.

as dimer or tetramer, depending on the temperature of the cracking zone

$$2As_4 + 4Ga \rightarrow 4GaAs + As_4, \tag{3.15}$$

$$As_2 + 2Ga \rightarrow 2GaAs. \tag{3.16}$$

The chemical reactions listed are particularly significant for the oxide desorption before the deposition of materials (see chapter 5) The situation is slightly different for antimony. A very important mechanism takes place for mixed group V heterostructures, where antimony and arsenic dimers are deposited [127]. The As-for-Sb exchange is favoured due to the higher binding energy of arsenic. Negative enthalpy means. that the product is energetically lower than the educt and energy is released, an exothermal reaction takes place. The reactions with the relating forming enthalpy ΔH_0 are given by:

$$As_2 + 2GaSb \rightarrow 2GaAs + Sb_2, \qquad \Delta H^0 = -47.6\,\mathrm{kJmol}^{-1} \tag{3.17}$$

$$As_2 + GaSb \rightarrow GaAs + AsSb_2, \qquad \Delta H^0 = -33.9\,\mathrm{kJmol}^{-1} \tag{3.18}$$

$$Sb_2 + 2GaAs \rightarrow 2GaSb + As_2, \qquad \Delta H^0 = 47.6\,\mathrm{kJmol}^{-1} \tag{3.19}$$

$$3Sb_2 + 2GaAs \rightarrow 2GaSb + 2AsSb_2, \qquad \Delta H^0 = 13.7\,\mathrm{kJmol}^{-1}. \tag{3.20}$$

3.5 Ultrahigh Vacuum Technology

In the following key parts of our MBE system are described and discussed. The main technological requirement for MBE is ultrahigh vacuum, which is the $1{\times}10^{-11}$ torr or lower vacuum range. One goal is to achieve the mean free path lengths required to deposit material from the source cells on the substrate, lowering background deposition and allowing precise doping of layers. The preparation of high-quality interfaces and layers strongly requires negliglible contamination with ambient pressures around $1{\times}10^{-11}$ torr. An Ultrahigh Vacuum (UHV) system typically has a stainless-steel reaction chamber as core of the machine. Additional equipment serves either analysis of the internal process or maintaining the UHV condition. The pressure range is not straightforward to reach. Multiple pump types need to be used for different purposes and pressure ranges. The aim are partial pressures below $1{\times}10^{-14}$ torr for background doping below $1{\times}10^{15}\mathrm{cm}^{-3}$.

Turbomolecular pump Commonly after a MBE maintenance event, the growth chamber gets pumped down from atmosphere with a turbomolecular pump to the $1{\times}10^{-8}$ torr regime. The high-speed rotor shuffles the gas molecules from the UHV side to the high pressure side. At the high-pressure side a membrane pump extracts them. This pumping process depends on the molecule type and impact processes between the molecule and

Pressure [Torr]	Mean Free path [m]	Monolayer deposition time
1000	3.4×10^{-9}	3 ns
1	3.4×10^{-6}	3 µs
1×10^{-3}	0.003	3 ms
$\times10^{-6}$	3360	3.1 s
1×10^{-9}	336000	$\approx$ 5 days
1×10^{-12}	$3.36\ \times10^{6}$	1 month

Table 3.1: Mean free path and deposition time. Below 1×10^{-9} torr the deposition time for a monolayer is considered low enough for MBE growth of highly doped devices.

the rotor blade. The rotation speed and the rotating part are the clear disadvantage with this class of pumps, problems with the rotating blade require a full replacement of the pump part, this is costly and results in a lack of pumping capacity to the chamber that can potentially lead to a chamber maintainance event. In addition light gases do not get pumped that easily (hydrogen). The purely mechanical pumping with no chemical reactions is an advantage. As the range from turbomolecular pumps is limited, the MBE is equipped with additional pumps too. They differ both in pumping speed and operation range. After a service event, the vented chamber needs massive and quick pumping from e.g. a conventional roughing pump to remove the air out and reach 1×10^{-5} torr. Afterwards the roughing pump gets turned off and additional pumps take over to maintain UHV conditions.

Titanium sublimation pump A trapping or absorbtion type of pump is the titanium sublimation pump (TSP). It sublimates titanium from a filament with an electric current of 30-60 A. The reactive titanium film on the surface of the cold shroud reacts with gases and traps in the growth chamber and thus lowers the chamber pressure. TSP pumps are not operated continuously, but in time intervals, due to reaction times. This has to be taken care of as this leads to spikes in the chamber pressure over time.

Ion pump Ion-getter pumps do not own any moving parts and work as standby pumps to dominantly maintain UHV conditions. Nowadays they are designed as multicell pumps, where a single pumping element produces a discharge between anode and cathode at several thousand volts. The few thousand Gauss strong magnetic field induces a helical path in the electron and increases their pathway. The formed ions are accelerated towards the Ti cathode, where they are captured.

Cryo pump A cryo pump further contributes to pumping below $1\ \times10^{-4}$ torr . A Helium cooling circuit transports heat away from a cold head. It works both as a cold trap for ions and as a pump. The cryo pumps working principle is that if a surface in vacuum gets

cooled, gas molecules condense on the surface and thereby reduce the ambient pressure. Cryo pumps cannot be used above 1×10^{-4} torr, where the cooling capacity is exceeded.

Ionization gauge A key device for measuring pressures below 1×10^{-5} Torr to the 1×10^{-11} torr range is the ionization gauge. Residual gas atoms exposed to an electron beam can be ionized. Both the rate of ionization and the induced current are directly correlated to the ambient gas pressure. An ionization gauge also needs to be calibrated against other absolute standards.

The most expensive, but also the most impactful method for lowering the chamber pressure is the liquid nitrogen (LN2) cooling shroud. Both the growth chamber walls and the TSP have LN2 cooled features. The consumption of LN2 during MBE growth time is one of the key parameters to track. A lack of LN2 requires a shut down procedure for the machine, since the chamber pressure can increase by four orders of magnitude. This might harm the machine, the effusion cells, gauges and pumps and is not a desirable state for the system. If the named pumps are used correctly, background pressures down to $\times10^{-12}$ torr can be achieved, whereas this is referred to as ultrahigh vacuum. Furthermore the background needs to allow for a background doping below $5\times10^{14}\,\mathrm{cm}^{-3}$ that is below the designed doping of THz QCLs of $0.5\text{-}8\times10^{16}\mathrm{cm}^{-3}$. Another important part of the UHV technology is the bake-out process. During MBE maintainance the reactor chamber gets exposed to air and thereby with water. The chamber is pumped down after closing the chamber, without baking the water molecules would desorb slowly, aside from the fact that water could react with the arsenic to form AsO_x. Maximum achievable pressure would be around 1×10^{-9} torr, clearly not sufficient for excellent growth. Therefore the whole equipment is wrapped in insulation material and baked up to an excess of 100 °C until the chamber pressure starts to stabilize in the low 1×10^{-8} range. Switching off the bake drops the chamber pressure then to the UHV regime in the low 1×10^{-11} torr range due to $pV = nRT$.

RIBER C21 growth chamber In this work a solid source RIBER C21 MBE was used, equipped with a cracker for antimony (VEECO) and a cracker for arsenic. The upwards facing Knudsen cells are tilted 45 ° and placed circularly below the substrate, which faces downwards below the substrate holder level. The manipulator is on top of the reaction chamber and rotates the substrate holder with the centered substrate up to 60 revolutions per minute. The arsenic cracker has a needle valve with an adjustable position from fully closed (determined by a closing torque) to open (determined by an external end position screw). The main shutter blocks all beams towards the substrate, the effusion cells get blocked with their individual tantalum shutter. The dopant sources are Si and GaTe (initially Be, source material was exchanged in 2021) for n- and p-type doping of samples. For high uniformity of the grown layers, the substrate holder rotates with typically 30

or 60 rpm. The substrate platen can either be two or three inch, depending on the substrate material and the price of the substrate (we only use three inch wafers for GaAs growth). The C21 growth chamber has substrate holders for either free standing or In bonded substrate mounting. In both cases, the substrate backside faces the heater of the manipulator. An important parameter for heating the samples is the substrate doping. Undoped or low doped substrates are more transparent to a significant ratio for the heater radiation wavelengths, in comparison to doped substrates. This results in different heater power settings required for the growth temperatures.

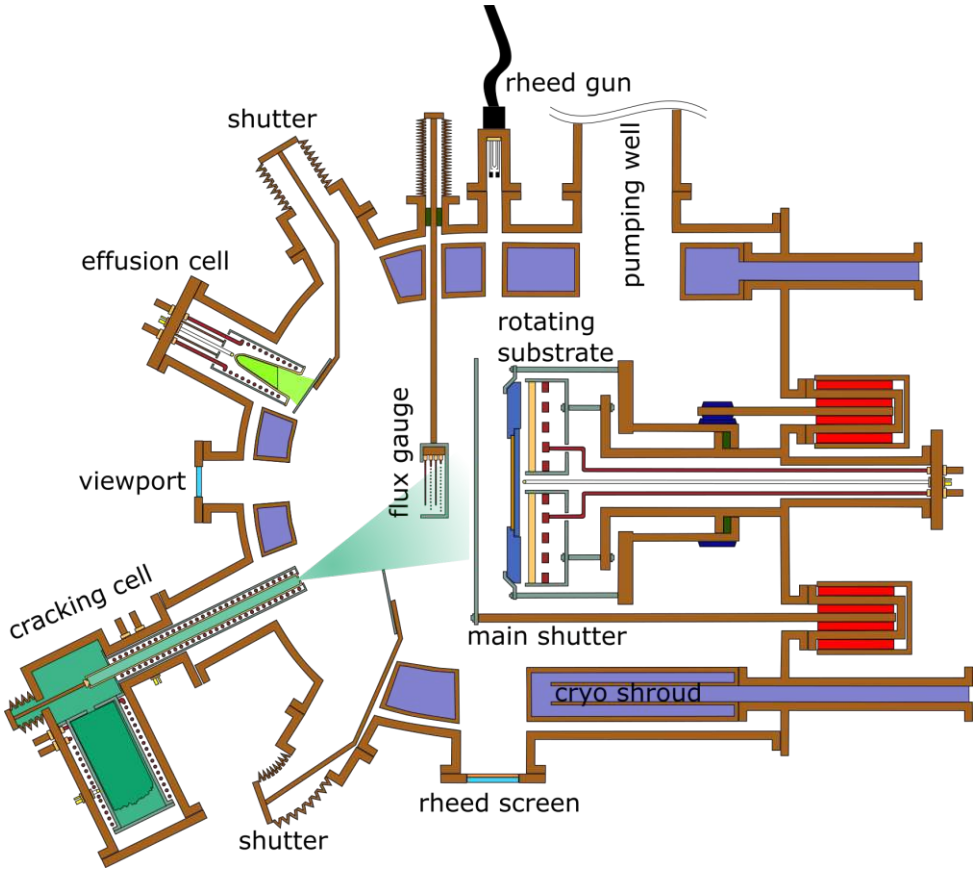

Figure 3.10: Scheme of the C21 RIBER compact MBE growth chamber. Figure reproduced with permission from [127].

3.5.1 Temperature measurement

The temperature of substrate and source material are the main adjustable parameters. In the UHV environment of the MBE, all heat is transported by radiation. Precise measurements are required to achieve the high level of control required to grow mid-infrared optoelectronics. For this, one needs to measure the temperature of the evaporating/-sublimating source materials and the substrate temperature. State-of-the-art Knudsen cells are equipped with thermocouples in sufficient distance to the bottom of the crucible, which gives a real time feedback and allows for PID loop temperature control. The

temperature measurement of the substrate depends on the substrate material, emissivity, surface roughness. The deviation for the substrate temperature should ideally be about one degree and measured without surface contact or other interference to the molecular beam. Infrared pyrometers face the sample through a heated viewport and are calibrated on a specific wavelength of the substrate. The C21 Riber is equipped with a Modline Pyrometer and a k-space Bandedge Bandit Pyrometer. Pyrometer measurements depend on multiple parameters and if not adjusted accordingly, e.g. the value can differ by 50 degrees between the Bandit and the Modline Pyrometer. The Bandit pyrometer has an InGaAs spectrometer and can therefore act as a pyrometer at any wavelength between 950–1650 nm.

3.5.2 Molecular flux sources

In the case of solid-source MBE, the source materials are evaporated from effusion cells, that contain as pure as possible elemental material. Typically we order purities of 7N (99.99999 purity). There are two dominantly used cell types for effusion of high purity materials. Knudsen cells and crackers. The group III materials are evaporated from a standard conical effusion cell that consists of a crucible made of pyrolythic bore nitride (pBN) and an outside attached heater.

Crackers In contrast to group III materials, the group V sources are not evaporated out of molten material, the arsenic and antimony sources are sublimated from bulk. The molecular beam is cracked with a high temperature zone from tetramers to dimers or even single atoms. Arsenic is supplied by a source a cracking zone that is separated from the reservoir by a needle valve. The cracking zone allows supply of either As_2 or As_4, with either 650 or 1000 °C. Regularly the bulk has an ever increasing temperature over the time of the growth of 375 to 450 °C, as the bulk material lowers in mass over time due to the evaporation. A scheme of the cracker cell design used in the Riber C21 is shown in figure 3.11. The cell design for arsenic is not sufficient for antimony due to the corrosivity of antimony. In contrast to the arsenic cracker, the antimony cell consists therefore of one big pBN crucible (figure 3.12), which is also operated with a needle valve to control the beam flux. Due to the constant flux of arsenic during the substrates oxide desorption and during the crystal growth, a typical charge size is 2.3 kg, which lasted on average for two years since we installed the MBE system in 2013. The charge can be supplied by either a single cylinder or as an ingot material. The bulk reservoir is normally operated between 500 to 550 °C and the cracking zone of the antimony cell is set to 1000 °C to supply antimony dimers.

Deposition profiles The deposition profile of the effusion cell is a central figure for homogeneous growth of heterostructures. In order to escape the equilibrium state of the

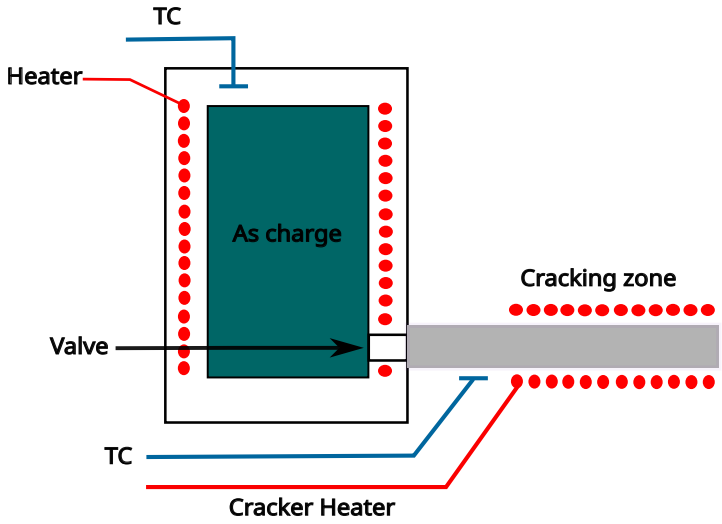

Figure 3.11: Detailled schematic of the arsenic cracker cell.The arsenic charge is heated for evaporation. The cracking zone can supply arsenic as dimer or tetramer species.

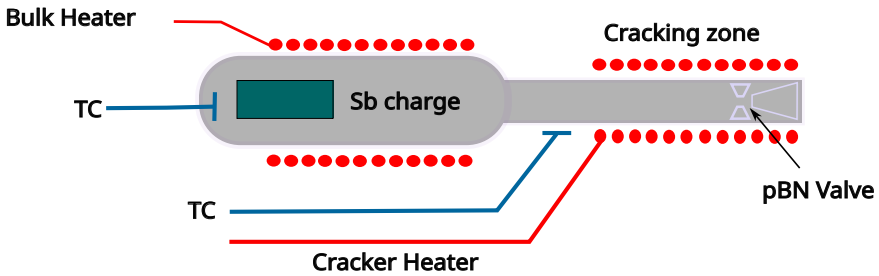

Figure 3.12: Detailled schematic of the antimony cracker cell. The pBN tube is filled with source material and gets heated for evaporation and to prevent material sticking and building droplets. The cracking zone can supply antimony as dimer or tetramer species.

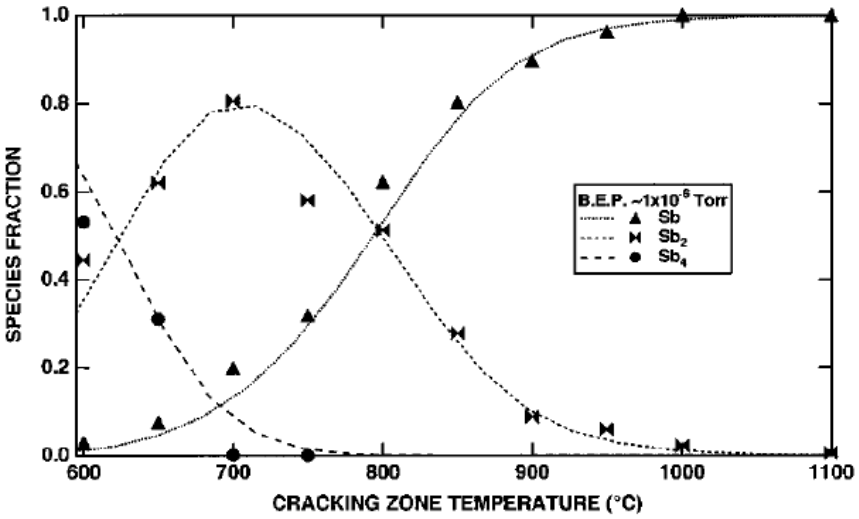

Figure 3.13: Efficiency of cracking antimony vs. temperature. The balance between the dimer and tetramer supply is temperature dependent. Our used operating temperature of 1000 °C gives antimony as a dimer. Figure reproduced from [128] with permission of Elsevier B.V. (1995).

material with the vapor phase inside the cell, we can treat it in approximation as point source. The trajectory of atoms or molecules emitted by the cell is proportional to the orifice of the cell A_e . In terms of controllable growth parameters, the flux of the cell reads as

$$d\Gamma(\theta) \approx A_e \cos(\theta) \frac{\Gamma_e}{A_e} \sin(\theta) d\theta, \tag{3.21}$$

with the unit [particles per m^2s], Γ denotes the number of molecules per unit time, A_e is the surface area of the evaporating material, θ is the tilted angle of the cell. The evaporation of source material can be characterized by the Hertz-Knudsen equation

$$\Gamma_e = \frac{dN_e}{dt} = A_e(p_{eq} - p_v)\sqrt{\frac{N_A}{2\pi M k_B T}}, \tag{3.22}$$

with the number of molecules per unit time $\frac{dN_e}{dt}$, the Avogadro constant N_A, the Boltzmann constant k_B and the vacuum pressure p_v. The equilibrium pressure of the vapor p_{eq} at the growth temperature T and the atomic mass of the material M. The flux I_A of the center axis A and the flux I_B of the off-axis point B is given by

$$I_A = \frac{\Gamma_e}{\pi r_A^2} \cos\phi, \tag{3.23}$$

$$I_B = \frac{\Gamma_e}{\pi r_B^2} \cos(\theta) \cos(\phi + \theta), \tag{3.24}$$

where Γ_e is the evaporation rate, r_A is the distance of cell and substrate and ϕ is the incidence angle of the molecular beam.

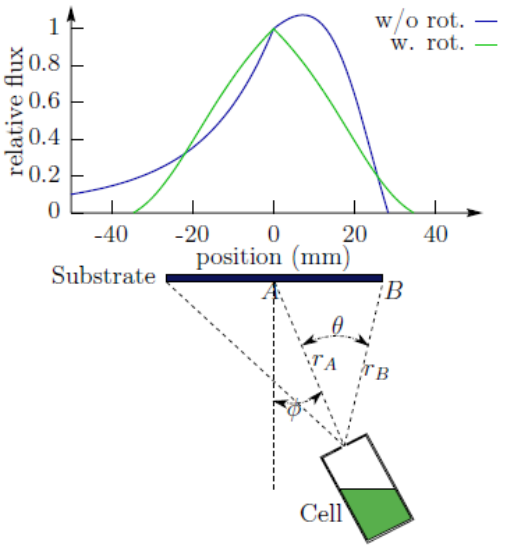

Figure 3.14: Deposition profile of a point source cell aimed at the substrate center. Figure reproduced with permission from [127].

The in-situ tool to measure the beam equivalent pressure (BEP), which is proportional to the flux, is a Bayard-Alpert ion gauge [129], which determines the current of secundary electrons between its cathode and anode. The ion collecting wire is a tungsten or iridium coated wire in the center of a spiral anode. The cathode is attached nearby. The upper limit of the measurement range for the pressure is 7×10^{-4} torr . The gauge allows to measure the flux ratios and calculate the material fractions of aluminium and gallium by the formula

$$\frac{\phi_{Al}}{\phi_{Ga}} = \frac{P_{Al}}{P_{Ga}} \times \frac{\eta_{Ga}}{\eta_{Al}} \left(\frac{T_{Al} M_{Ga}}{T_{Ga} M_{Al}} \right)^{1/2} . \tag{3.25}$$

Note, that the formula gives the relative flux of ϕ_{Al} or ϕ_{Ga}, when one flux value is known, with the BEP ratio for the correlating materials $\frac{P_{Al}}{P_{Ga}}$, the Temperatures T_{Al}, T_{Ga}, the molar mass M_{Ga}, M_{Al} and the measurement number at the flux gauge η_{Ga}, η_{Al}.

CHAPTER

FOUR

NON-DESTRUCTIVE ANALYSIS OF EPITAXIAL FILMS

The assessment of the epitaxial growth of III-V compound semiconductor devices requires the use of non-destructive techniques to analyze the samples without altering their intrinsic crystalline structures or surfaces. These techniques serve to determine the growth rates of the materials and evaluate the crystalline quality of the samples. Reflection High Energy Electron Diffraction (RHEED) is a useful in-situ method that allows for direct measurement of growth rates and observation of surface transitions and changes in growth modes. X-ray diffraction is another well-established technique that is widely used to determine layer thicknesses, compositions of mixed alloys, strain and relaxation ex-situ. Atomic Force Microscopy (AFM) provides a useful first imaging of the quality of the grown structure by yielding high-resolution micrographs at the nanometer scale. It allows to measure topology with nanometer resolution. The characterization methods described here will be explored in greater detail in the following sections. The theoretical part of X-Ray Diffraction is based on [130].

4.1 Reflection High Energy Electron Diffraction

Besides the possibility to analyze the grown structure after growth, Reflective High Energy Electron Diffraction (RHEED) provides an in-situ characterization of the MBE growth. The RHEED diffraction pattern gives important insight into the substrate surface reconstruction during growth and especially during the oxide desorption, a crucial step before the growth of heterostructures. The experimental setup for RHEED is shown in figure 4.1, it consists of a high voltage electron gun that points to the substrate, where the electron beam gets diffracted. The angle of the incoming electrons to the substrate surface is around 2 degrees. Opposite of the electron gun a phosphorus screen is mounted with an additional external window on the backside and a protecting mechanical shutter towards the growth chamber. An acceleration voltage of 10 kV is used in the currently equipped

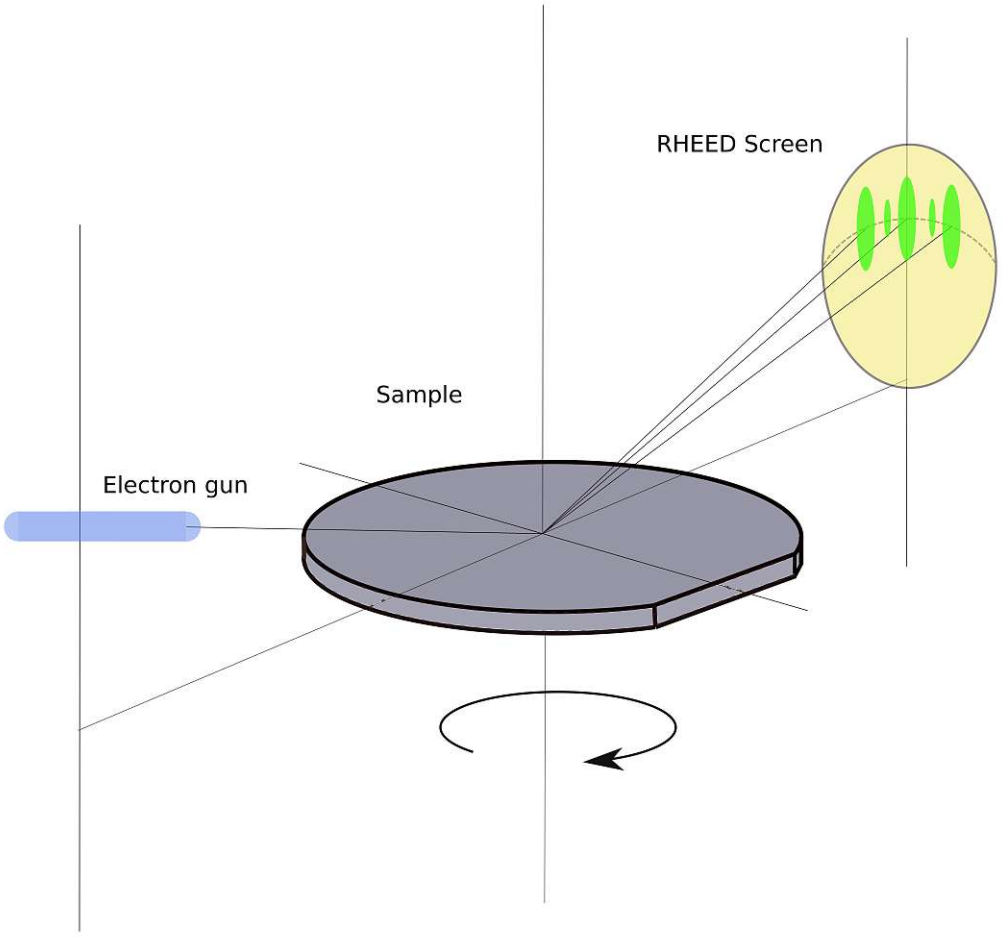

Figure 4.1: RHEED setup and its components. The electron beam gets diffracted onto the phosphorus RHEED screen. The substrate rotation allows the extraction of information depending on the crystal orientation.

RHEED gun, gives the de Broglie wavelength of the incident electrons with

$$\lambda = \sqrt{\frac{\hbar^2}{2m_0 E_{kin}}} \approx \frac{1.2286 \times 10^{-9}}{\sqrt{V}}, \tag{4.1}$$

with the electron mass m_e, Plancks constant h and the electrons kinetic energy E_{kin}. For a high voltage of 10 kV the wavelength is 1.23 nm.

4.1.1 Diffraction of reconstructed surfaces

The Ewald sphere is a geometric construct in reciprocal space used in crystallography to relate the positions of atoms in a crystal with the diffraction pattern observed in experiments. It is a sphere with a radius proportional to the wavelength of the probing radiation and centered at the position of the reciprocal lattice origin. When the Ewald sphere intersects with the diffraction spots in reciprocal space, it indicates the allowed scattering conditions that satisfy the Bragg's law, providing information on the crystal structure and crystal orientation. The Ewald sphere is illustrated in figure 4.2. The in-

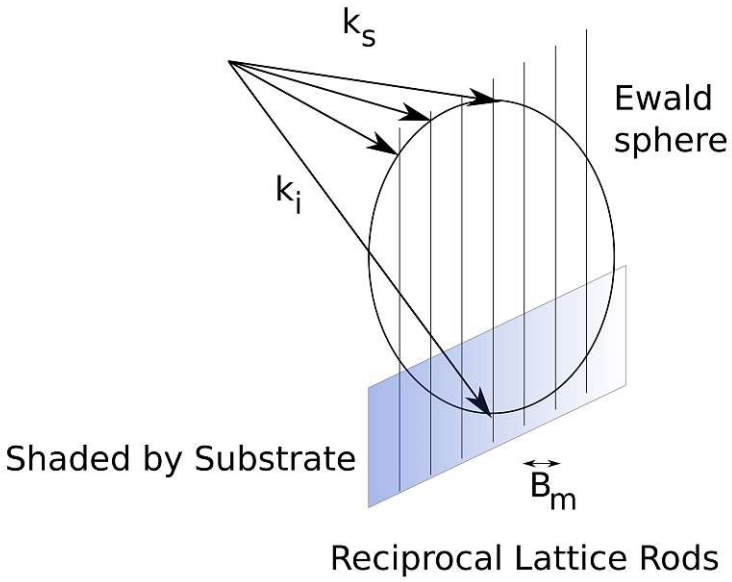

Figure 4.2: Ewald reconstruction on the RHEED screen. The lower half on the screen is shaded due to the substrates shadow. The intersection of the Ewald sphere with the rods of the reciprocal lattice show as diffraction spots on the RHEED screen. A smooth surface results in rods, a rough surface in spots.

tensity of the RHEED screen diffraction spots is also dependent of the surface roughness. The growth of a single monolayer gives a maximum intensity when the surface is fully covered, and a minimum when the surface is in an intermediate filling state. The oscillation of the intensity over time, in relation to the number of grown monolayers gives then the growthrate. Calibrating the growth rate with RHEED intensities can be used for binaries where lattice-matching is not an issue, e.g. GaAs/AlGaAs.

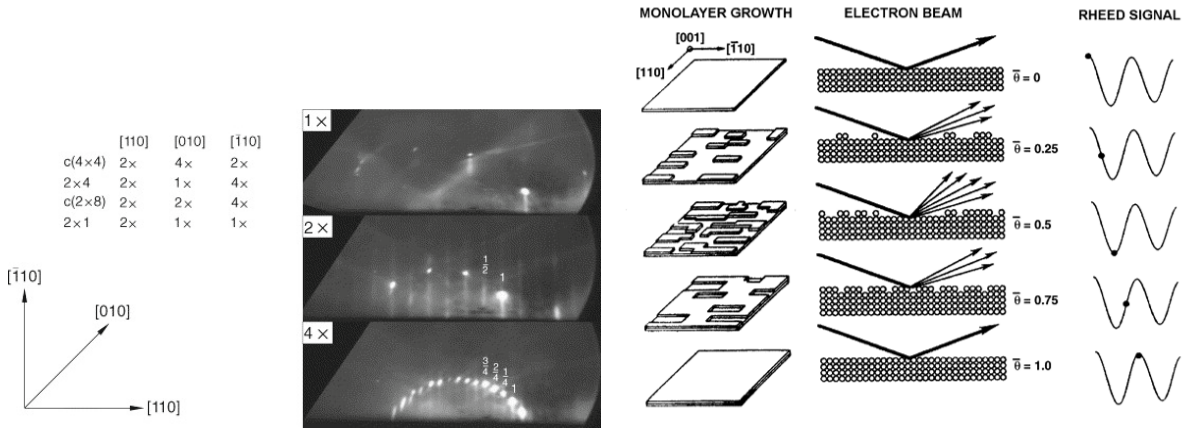

(a) (b)

Figure 4.3: (a) RHEED screen pattern of GaAs reconstructions. (b) Growth rate measurement with RHEED intensity oscillations. The RHEED intensity for measuring the growth rate oscillates due to monolayer filling. At 50 % filling the intensity is at a minimum, caused by the destructive interference. Figure reproduced from [131] with permission of Elsevier B.V. (2005).

4.2 X-Ray diffraction theory

The interaction of electromagnetic waves and periodic atomic lattices was firstly examined by von Laue in 1912. Bragg Jr. and Bragg Sr. later on stated this within Braggs law

$$2d_{hkl}\sin(\theta_B) = n\lambda, \tag{4.2}$$

where d_{hkl} represents the distance between the diffraction planes, where $\{hkl\}$ are the Miller indices of the planes, θ_B the diffraction angle and λ the constructively interfering wavelength of the impinging electromagnetic wave. For the atoms in crystals, the center sites of scattering events are periodic, therefore either constructive or destructive interference takes place. The diffraction vector $G = \mathbf{k}_f - \mathbf{k}_i$ is composed of the incident wave vector $\mathbf{k}_i$ and the diffracted wave vector $\mathbf{k}_i$. A maximum diffraction peak occurs when the scattering vector equals the reciprocal lattice vector.

4.2.1 High-resolution X-Ray diffraction

High resolution X-ray diffraction (HR-XRD) is a characterization method to determine relevant parameters e.g. the strain in a heterostructure, the periodicity of a superlattice or its composition. The HR-XRD machine uses a vacuum tube for X-ray generation, where high voltage (5-10 kV) accelerates electrons onwards a metal (copper for the XPert

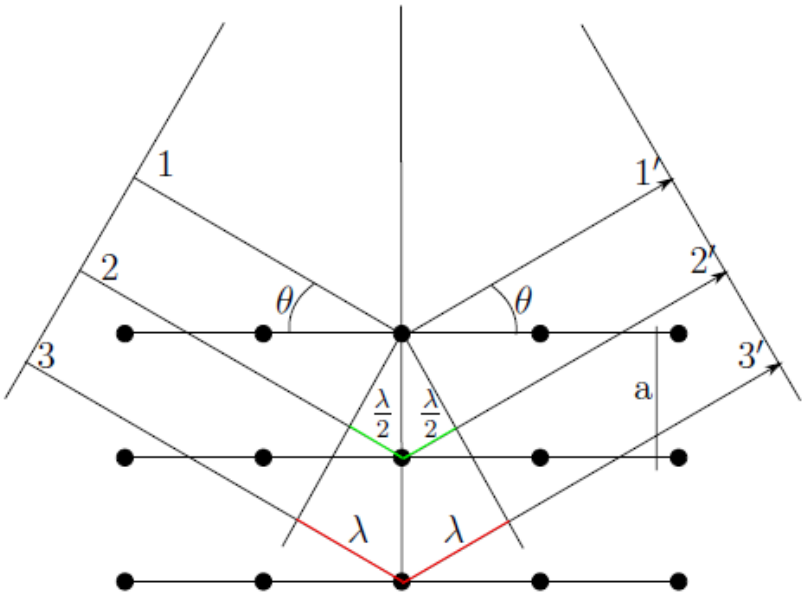

Figure 4.4: Crystal lattice scattering of an impinging X-ray beam. Figure reproduced with permission from [127].

Analytics Pro in this work). The resolution of a XRD is given by

$$\frac{\Delta d}{d} = \frac{\Delta \lambda}{\lambda} - \frac{\Delta \theta}{\tan \theta}. \tag{4.3}$$

The goal with HR-XRD is to get a narrow spectral resolution of the lines, therefore a Bartels monochromator is used to narrow the beam. It consists of two Germanium crystals, configured as shown in figure 4.5. The entering beam gets reflected four times at the (220) Germanium crystals and exits the monochromator (MC). The device is built for the specific X-ray wavelength, which can only exit the window under the proper reflection angles. The sample and the detector can be tilted to perform measurements (Figure 4.6). The most common measurement modes are double and triple axis. A double axis measurements reflects the beam first at the MC and then the sample. A triple axis measurement adds an analyzer crystal, which is placed in front of the detector, narrowing the window for passing beams even further. The angle of the incoming X-ray wave is ω and the angle of the detector position relative to the sample is 2θ. The standard procedure is a double axis $\theta - 2\theta$ measurement.

Diffraction peaks In figure 4.7 the reciprocal space of different Bragg peaks of a heterostructure is shown. Starting from the ideal case of fully lattice matched grown layers (Figure 4.7a), we distinguish relaxed (b) and strained (c,d) epilayers. Figure 4.7a presumes a lattice matched film. The reciprocal lattice points of film and substrate overlay

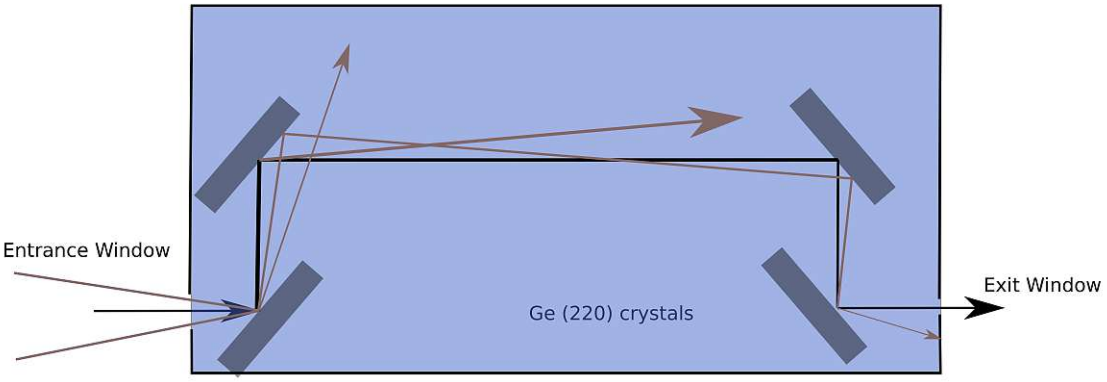

Figure 4.5: Bartels monochromator designed for a specific X-ray wavelength. The beam gets reflected at the Ge (220) crystals. Only the X-ray wavelength that is designed to pass can transmit.

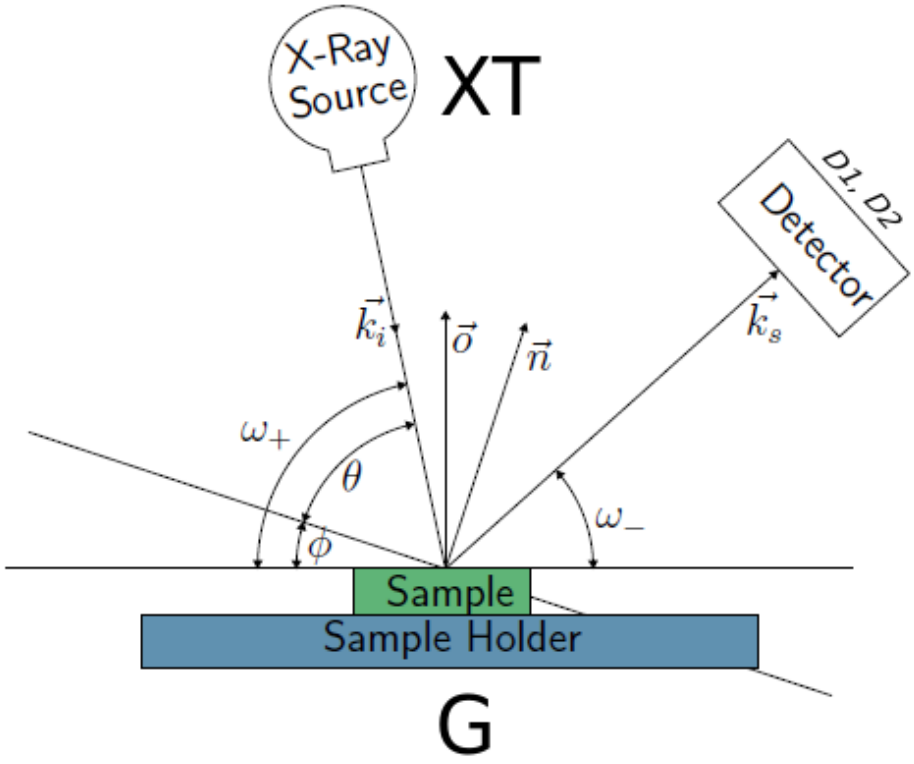

Figure 4.6: Schematic of the measurement setup for HR-XRD. XT: X-ray tube, M Bartels monochromator, G goniometer with detector D1 and detector D2.

each other in succession. Compressively and tensily strained epilayers reciprocal space are displayed in figure 4.7, where the reciprocal space points scale in relation to the difference of the lattice-constant. Relaxed layers own the unstrained, intrinsic natural lattice constant of the material. Figure 4.7b displays a shift along the trajectory of the lattice points along the reciprocal points of the substrate and the origin of the reciprocal space. A consecutive scan of ω-2θ scans allows then to correlate the diffraction peaks with the peak position relative to the substrate peak and the origin of reciprocal space. This measurement is commonly referred to as reciprocal space maps and is discussed further below.

4.2.2 Determination of layer thickness and composition

Crystalline growth with MBE allows to grow combinations or superlattices of different III-V epilayers. For heteroepitaxial growth, the lattice constants are different and can be distinguished in the XRD measurement [132]. The oscillations around the first order peak in figure 4.8 are called Pendelloesung fringes and are induced by the finite thickness of the three layers. The calculation of their separation in angle, allows the back calculation of the layer thickness.

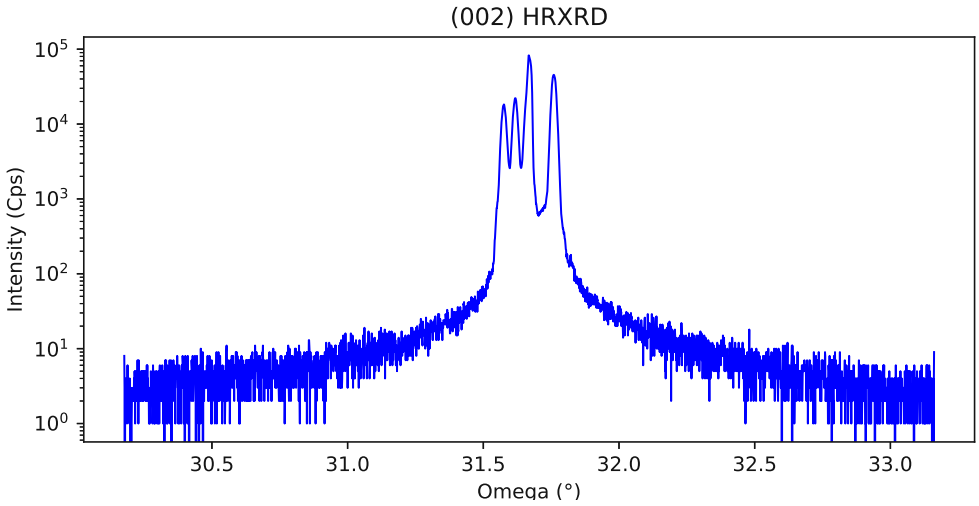

Figure 4.8: (002) $\theta - 2\theta$ diffraction peak scan of a calibration for lattice matching of InAlAs on InP.

Composition We can use a grown structure of three consecutive, different material layers with different growth temperatures to determine their layer composition. In figure 4.9 a (002) $\theta - 2\theta$ XRD-scan is displayed. The relaxation can be determined from

$$r = \frac{a_{\parallel} - a^S}{a_0^L - a^S}. \tag{4.4}$$

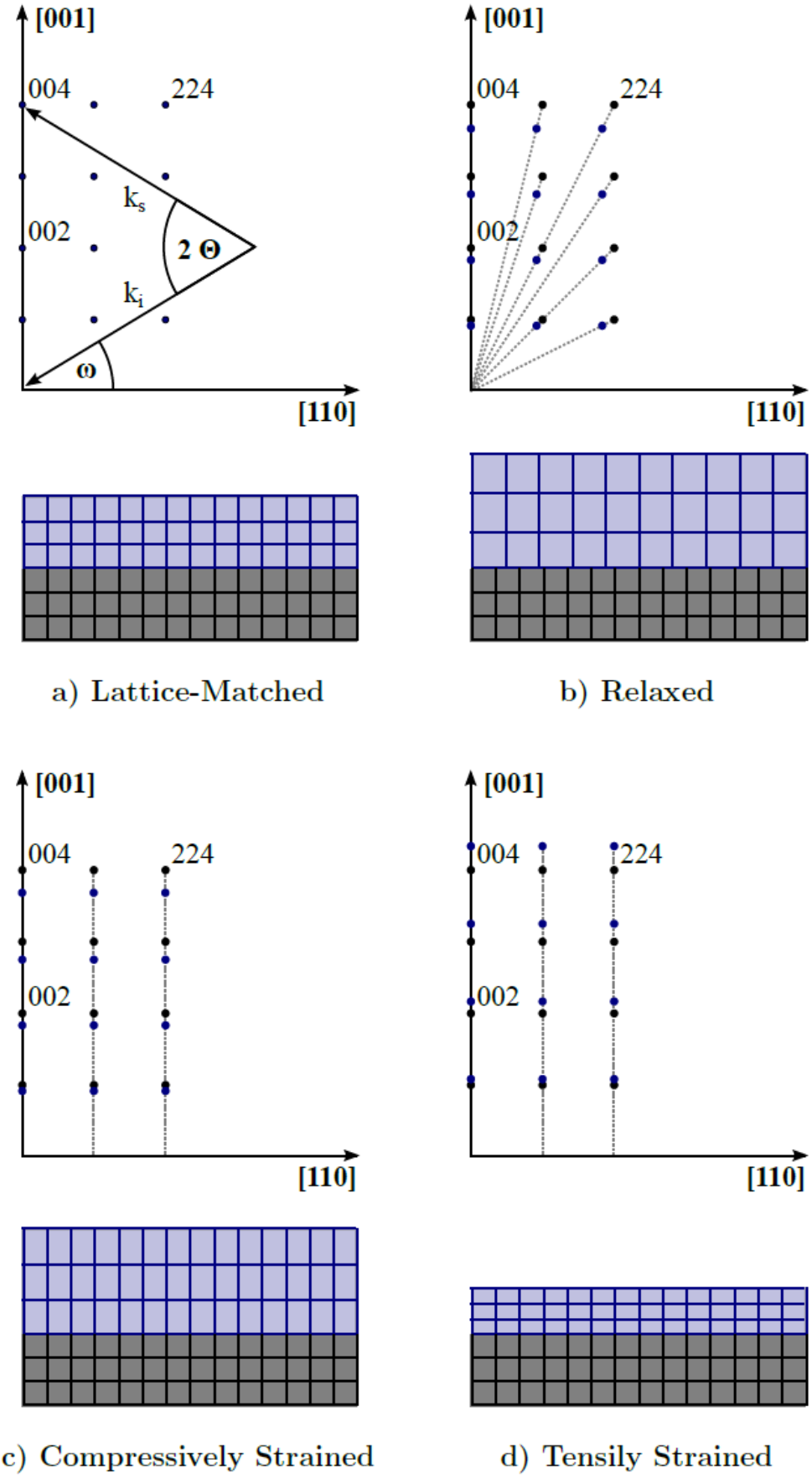

Figure 4.7: Diffraction peaks of (a) lattice-matched (b) relaxed (c) compressively strained (d) tensily strained. Figure reproduced with permission from [43].

$$a_0^L = \frac{C_{11}}{C_{11} + 2C_{12}}(a_\perp^L - a_\parallel^L) + a_\parallel^L \tag{4.5}$$

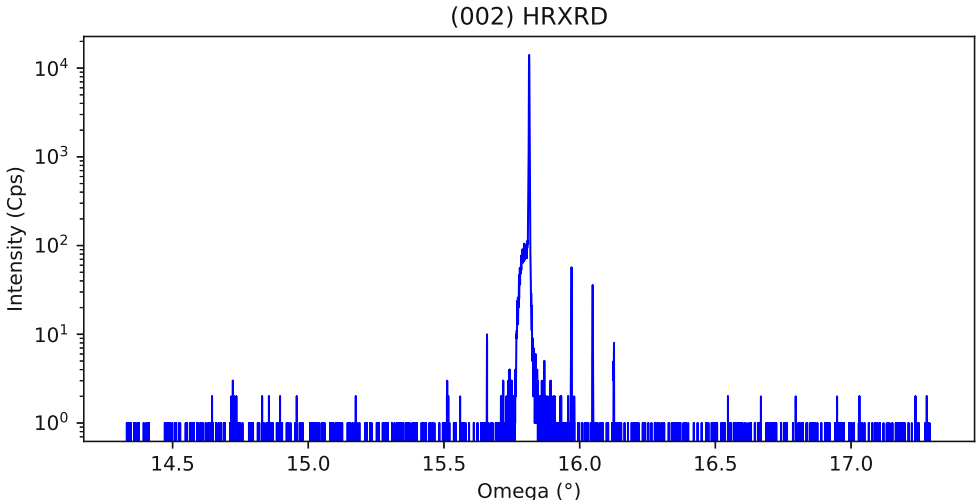

Figure 4.9: (002) $\theta - 2\theta$ diffraction peak scan of a GaAs/AlGaAs THz QCL with 15%-Al fraction in the barriers.

Superlattice period Aside from in-situ methods to characterize or measure epitaxial grown heterostructures, the measurement of the superlattice period allows the determination of growth rates with high precision in order to calibrate the effusion cells for high performance device growth. In comparison to a (004) diffraction peak, the (002) diffraction allows the more precise calculation of the SL period

$$D = \frac{(L_i - L_j)\lambda}{2(\sin(\theta_i) - \sin(\theta_j)}, \tag{4.6}$$

with $L_{i,j}$ as the order of the fringe peaks and the angular positions $\theta_{i,j}$ and the X-ray wavelength λ. Figure 4.9 shows the 002 scan of a THz QCL. The SL period was 38.7 nm (nom. 40nm). The SL period of grown THz QCL is a good hint for the functionality of the device. It showed over time that a small $\pm 2 - 3\%$ interval of the nominally designed superlattice period strongly indicates if the lasing is limited by the MBE growth. Exceeding this interval regularly lead to failing laser structures. The displayed structure contributed to a publication [133].

4.2.3 Reciprocal Space Maps

The standard ω-2θ scan can give us material compositions of superlattices, but we cannot determine precise information about the strain and relaxation in the actual internal structure. As soon as lattice matching of material compositions to the substrate comes into play, we need a characterization method to determine this. Therefore we measure a

specific diffraction to see the alignment of the diffraction peaks in the [110] plane. The reciprocal space map (RSM) is the collection of uni-dimensional ω-2θ scans, where each scan has an offset in ω towards the next consecutive scan. In the end this gives a 2D map with insight on strained and relaxed layers, as can be seen in figure 4.10 below. Besides the strain information with the (224) RSM, we can also measure the miscut of

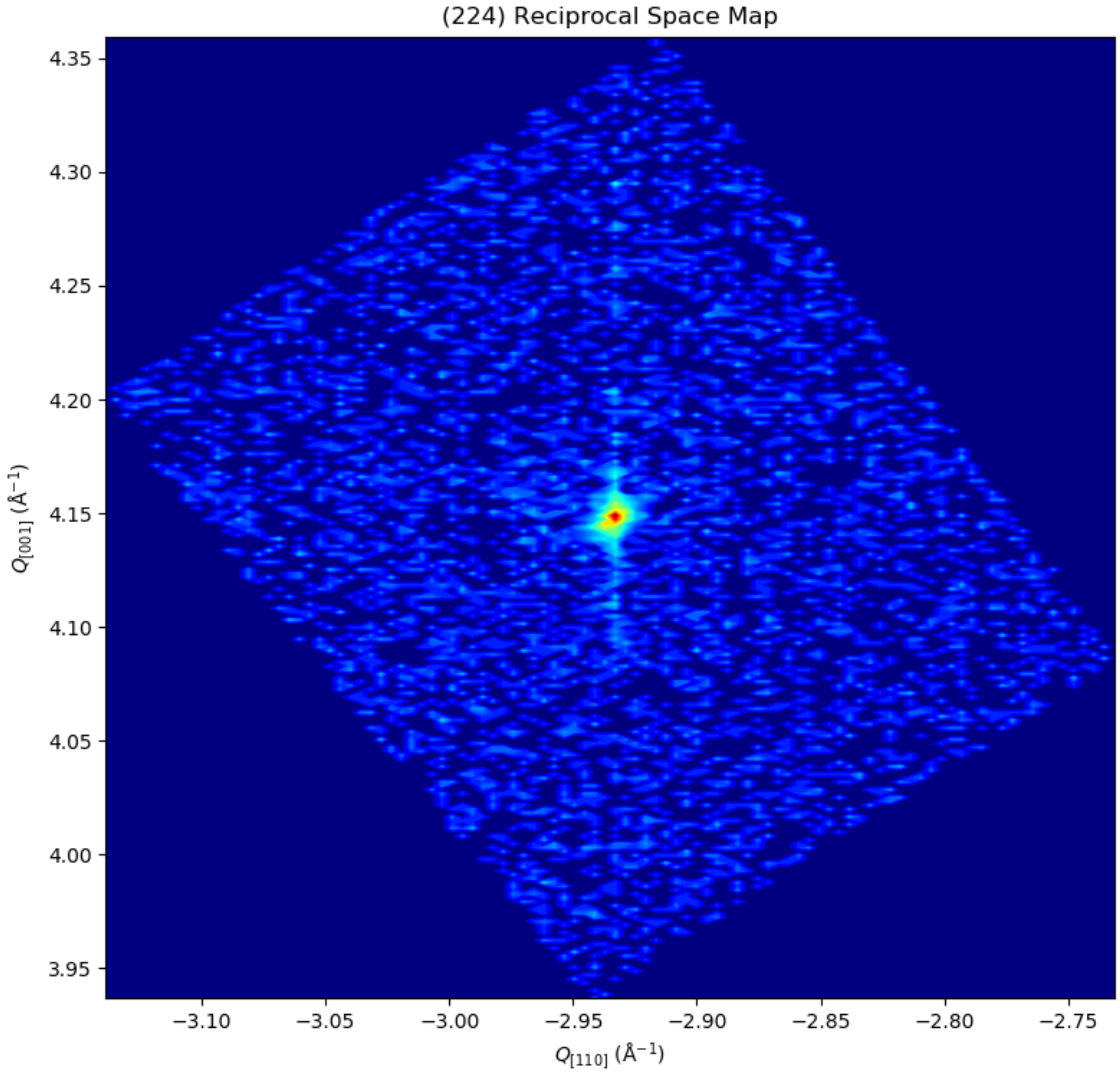

Figure 4.10: (224) RSM of an nominally strain balanced test structure for the growth of InGaSb. The superlattice peaks are lightly visible due to low cumulative thickness.

the substrate with the (004) RSM. Within a study of the temperature performance of THz QCLs on different miscut angles, the correlating RSMs were measured, as displayed in figure 4.11 below. The RSM show an increasing linear slope with the higher miscuts. The X-Pert Pro software allows then to calculate the substrate miscut angle. Beyond the 0.2 degree miscut, the MBE grown structure does not follow the angle anymore

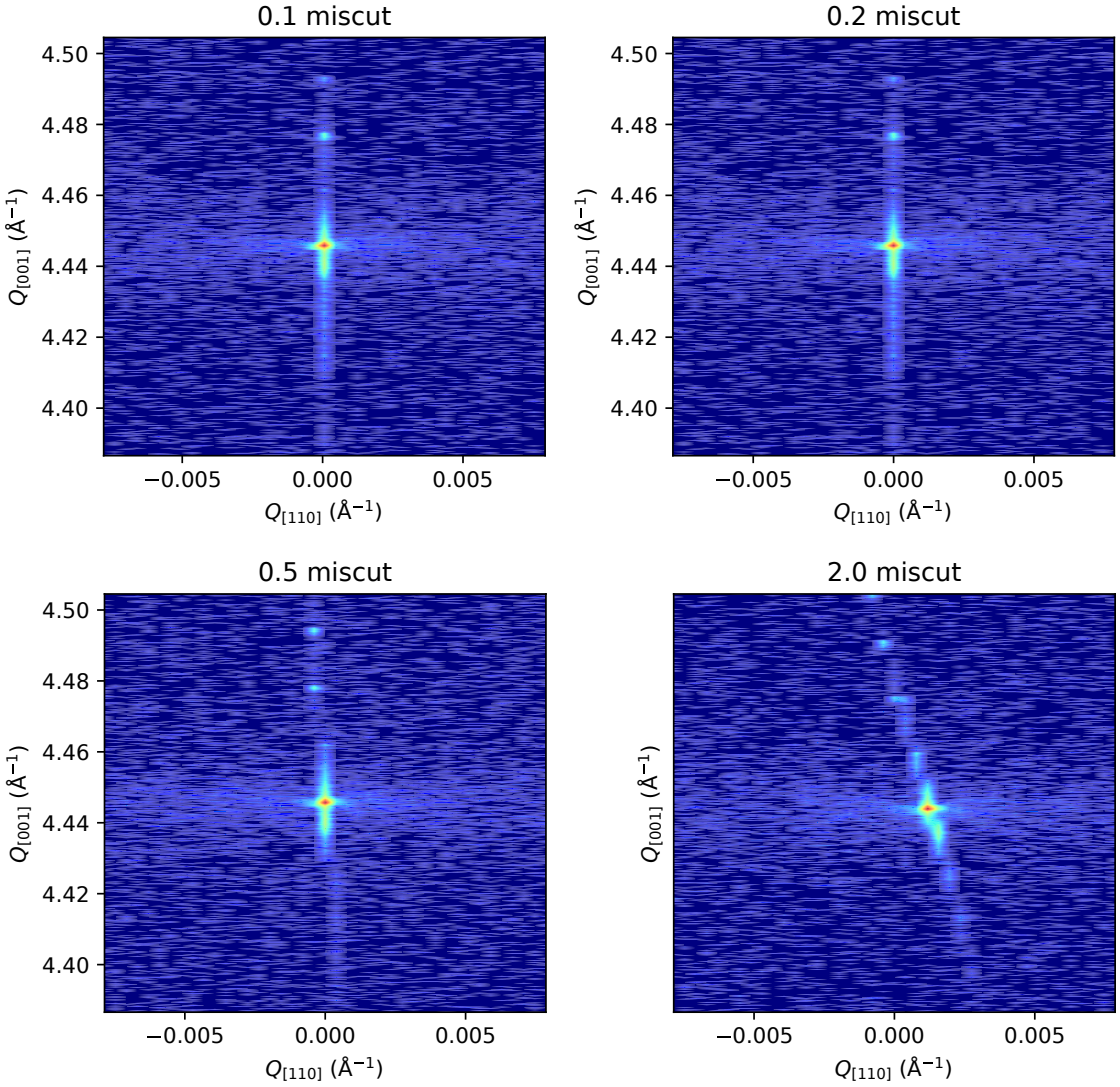

Figure 4.11: RSM of THz QCL structures grown on four different substrate miscuts from zero to two degrees. The growth does not follow the miscut beyond 0.2 degrees. The progressive tilting of the vertical line indicates the growth of a strained heterostructure.

4.3 Atomic force microscopy

Atomic force microscopy (AFM) is a measurement method to analyze the surface roughness of thin films. III-V optoelectronics requires thin layers with a few nanometres and roughness values below 0.1 nm RMS as a figure of merit. The method works by using a sharp tip on a cantilever to scan a sample's surface in a non-destructive manner. As the tip moves over the sample, it experiences interactions between the tip and the surface, which are measured by detecting the cantilever's deflection using a laser beam. These interactions can be used to generate high-resolution images of the sample's surface, as well as to measure various material properties such as surface roughness, adhesion, and stiffness. The measurement schematic is illustrated in figure 4.12. This leads to two different measurement methods with the AFM. In contact mode the tip is touching the surface of the sample and moved across the sample surface and the selected measurement area. The laser deflection of the tip on the photodetector gives the topography signal and allows control of the cantilevers height. The other method is the tapping method. The cantilevers oscillation is detuned from its resonance frequency and brought close to the sample surface and taps it. The characterization of MBE grown samples with AFM can

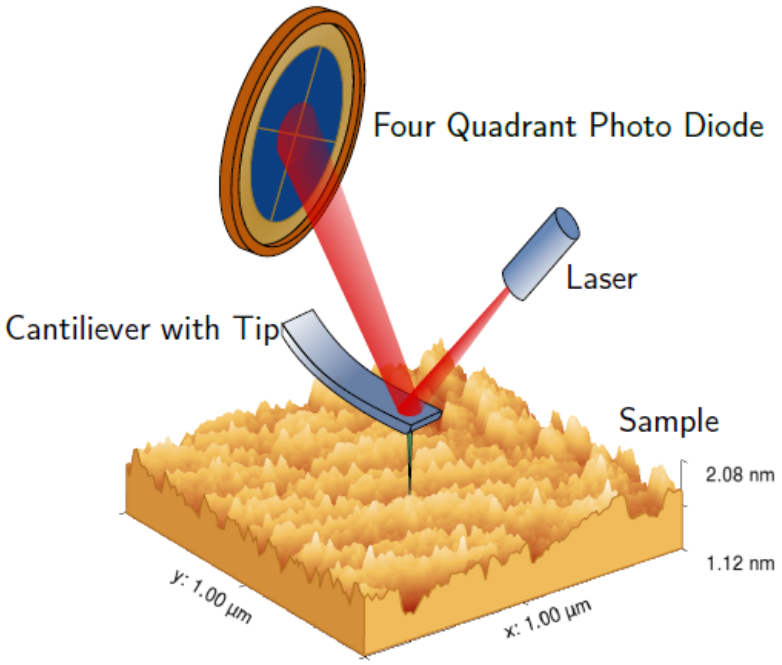

Figure 4.12: Schematic of an AFM setup. The tip is brought into contact with the sample surface and its deformation is measured with a laser. The four quadrant photo diode compares the photocurrent of each area and determines the deformation. Figure reproduced with permission from [127].

provide valuable information about growth modes or III/V ratios, substrate temperature,

etc. The surface can show relaxation of mismatched lattice constants or even 3D growth modes, which further increases the surface roughness. As an example of how surfaces can change with different MBE growths, figure 4.13 shows the AFM measurements of THz QCLs grown on substrates with different miscut angles. Miscut angles ranging from 0.1 to 2 degrees were used to study the influence of surface steps and correlating interface steps on the temperature performance, but no indication for an influence was found. Figure 4.13 still shows interesting behaviour of successive increase of surface steps with the miscut angle and a surface merge at 2 degrees.

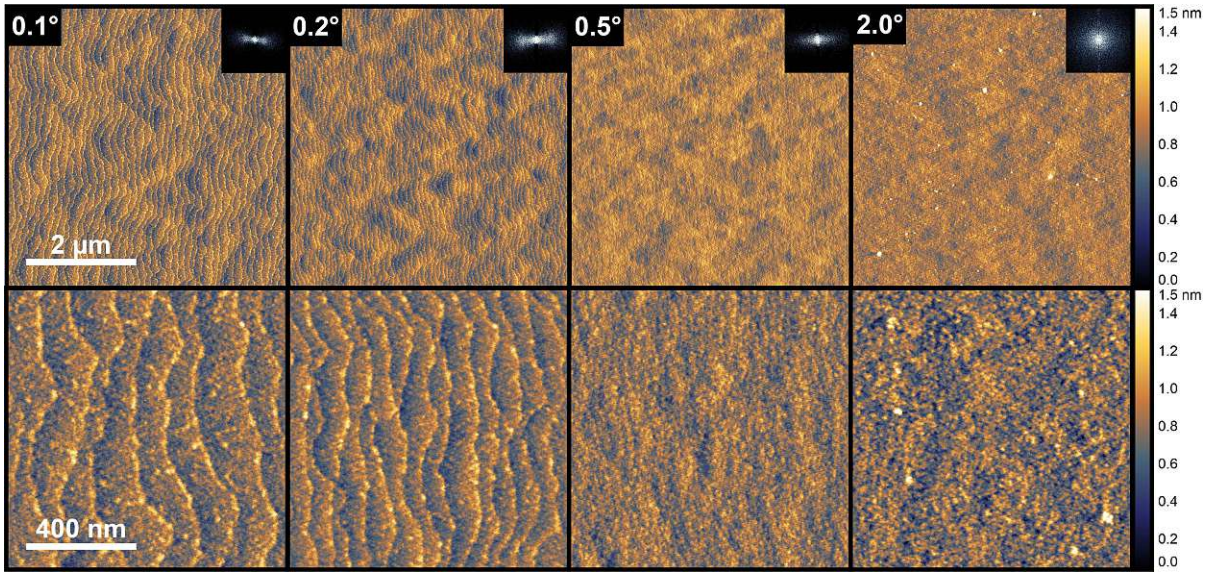

Figure 4.13: AFM study of THz QCL structures grown by MBE on four different substrates with a substrate miscut. The miscut angle increases from left to right from 0.0, 0.1, 0.5, 2.0. In the upper right the fast Fourier transform of the data is displayed. All four structures were measured after the MBE growth without further surface treatment. Note, that the number of surface steps (bright vertical lines) is clearly visible until the 0.5 degrees substrate miscut. Figure produced by the author in collaboration with Jakob Genser.

4.4 Transmission Electron Microscopy

A highly useful method to get insight into the internal structure of samples is Transmission Electron Microscopy (TEM). The machine consists of an electron gun, a high voltage electron accelerator and deflection optics with attached detectors. Transmission electron microscopy (TEM) patterns are formed when an electron beam (typically 50-200 keV) propagates through the sample and gets scattered. Astonishing resolutions can be reached, resolving bulk materials and material interfaces on a single atomic scale. The principle setup is displayed in figure 4.14. In general the sample preparation is the challenging part of the process. It has also to be noted that the sample preparation is a destructive process, as the thinning and slicing of the sample does not allow further use after the preparation procedure. Commonly a 5x5 mm or 2x2 mm sample is processed into a thin foil. The reader is given an example below of TEM micrographies of MBE grown samples (figure 4.14). The double superlattice calibrations of AlSb and InAs show abrupt and sharp interfaces with clear layer separation and a homogeneous high-quality growth.

4.5 Electron Dispersive X-ray spectroscopy

Energy dispersive X-Ray spectroscopy (EDX) is a characterization method to determine the elemental composition of a material. EDX spectroscopy measures the relative intensities of the different characteristic X-Ray lines. The energy difference between the vacancy of the emitted secondary electron and its filling of an electron from an upper shell is converted to an X-Ray photon. If an L shell electron fills a K shell vacancy, it is referred to as K_α line, a commonly used reference line. The measurement distinguishes different elements by using their characteristic X-Ray lines [134] and correlates them spatially. A focussed beam of electrons transfers their energy to electrons in inner shells, leading to emission of secondary electrons. The filling of the free electron spot can be done by any electron from any shell, although with different probabilities.

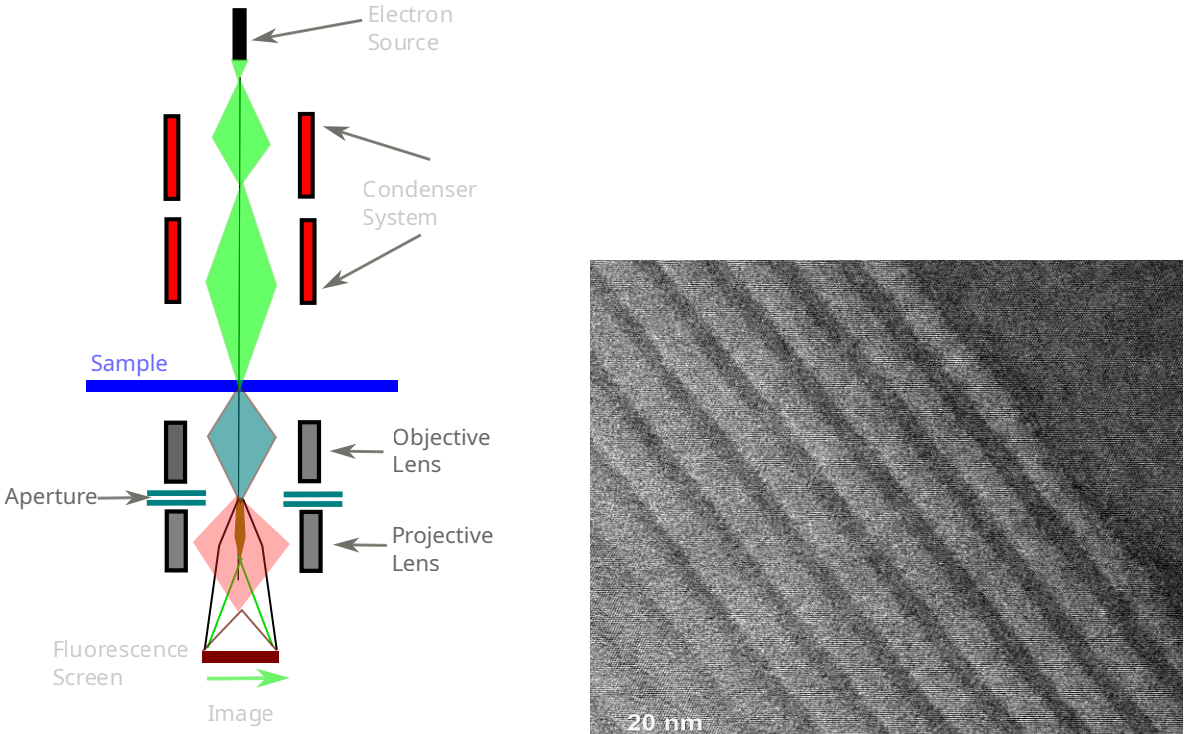

(a) (b)

Figure 4.14: (a) Schematic of a TEM setup. The electron beam passes through the sample and gets focussed by electromagnetic lenses onto a screen. The transmitted diffraction pattern allows to reconstruct information about the internal structure. (b) TEM image of sample C1072, a superlattice calibration of AlSb InAs. Dark layers are AlSb barriers, light grey layers are InAs wells. The periodicity changes after 50 periods for the InAs layer from 3.5 nm to 5.0 nm. The TEM image was done by the University Service Centre for Transmission Electron Microscopy (USTEM), TU Wien.

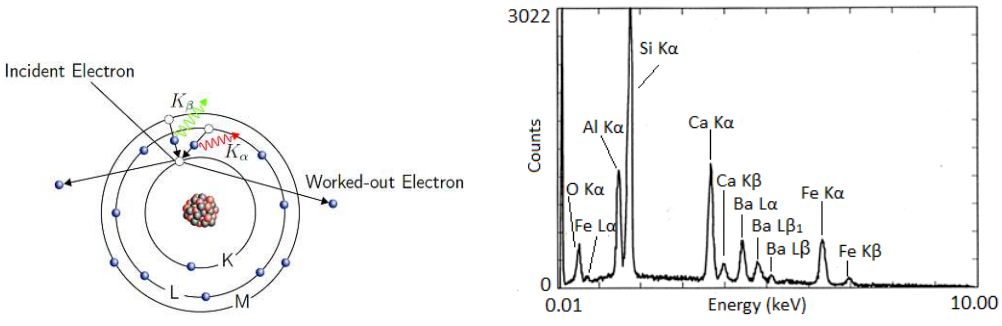

(a) (b)

Figure 4.15: (a) EDX working principle. The incident electron bumps out the worked-out electron that gives the specific transition line. Figure reproduced from [135]. (b) EDX spectrum of NIST K309 glass. Figure reproduced from [136] with permission of Springer New York (2016) and CC-BY 4.0.

CHAPTER

FIVE

RESULTS OF INAS-BASED INTERBAND HETEROSTRUCTURE GROWTH

Interband Cascade Lasers (ICLs) are ideal candidates for miniaturized spectrometers, due to their low power consumption and the possibility to monolithically integrate sensitive on-chip detectors using the same epilayer material on a single chip. In addition, ICLs can be operated as frequency combs, offering the possibility to produce monolithically integrated frequency combs and detectors on the same chip [21]. Intrinsically, the operating emission wavelength of the individual ICLs is limited, which requires different active region designs. ICLs were demonstrated to work on InAs and GaSb substrates, where InAs-based ICLs are used for long wavelength emission (beyond the 3-4 µm sweet spot), due to the lower absorption coefficients of InAs [18, 79, 137, 138]. In order to compensate for the losses of longer wavelengths, a greater number of active regions needs to be grown. A fundamental problem thereby is the cumulative strain of the W-quantum well's InGaSb layer [139]. In this chapter a novel method to compensate for strain is shown and results of MBE growth are discussed.

5.1 MBE growth

The MBE growth of InAs-based heterostructures and ICLs is challenging. The high number of interfaces (> 2000) and the combination of a set of different materials for the active regions requires a high level of precision and defined alloy compositions. Aside from that, significant interface roughness and/or defect densities will prohibit the functionality of a device and the cumulation of strain can prevent the layer-by-layer growth mode. As explained earlier in (chapter 2), ICLs require a broken bandgap for the semimetallic interface, typically used materials are GaSb and InAs. These materials are due to their lattice constants, commonly referred to as the 6.1 Å family. In table 5.1 the lattice constants of important materials in the 6.1Å family are listed.

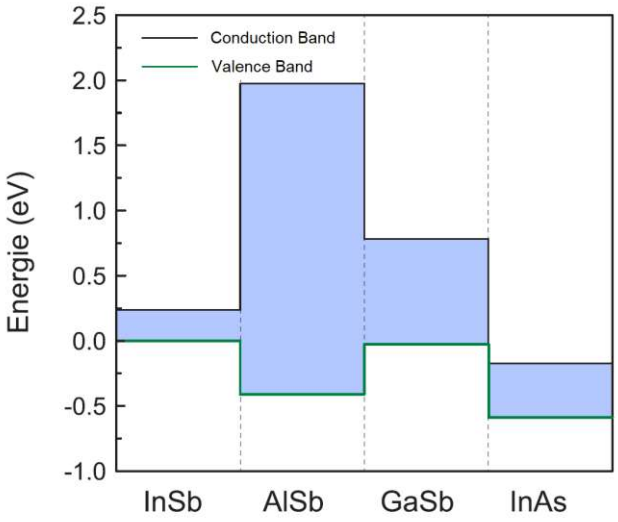

Figure 5.1: Conduction and valence band alignment of 6.1Å family based binaries at T=300 K. The valence band edge of InSb was set to 0 eV. Data used from [140].

Material	Lattice Constant at 300 K [Å]
InAs	6.058
GaSb	6.096
AlSb	6.136
InSb	6.479

Table 5.1: Lattice constants of materials in the 6.1Å family that form binaries.

Key challenges and issues In order to be able to grow ICL structures one has to overcome and solve a couple of issues. The most significant issue is cumulative strain due to the InGaSb layers. They will induce tensile strain as the lattice constant differs from the substrate. Long wavelength ICLs on InAs require more active regions to compensate the losses, as the oscillator strength of the emission wavelength decreases and the hereby higher number of active regions cumulates layer thicknesses beyond the calculated critical thickness of the material. Exceeding this value leads to defects and subsequently to low device performance. Secondly, the incorporation of arsenic into barriers and layers needs to be examined. Literature and befriended groups claim, that the AlSb barriers have AlAs interfaces on top and can be used for strain engineering. An analysis of AlSb/InAs superlattices should give insight to this. A related issue, but not so much a challenge in terms of MBE growths is defect density. The high strain in the heterostructure induces dislocations and high defect densities. A study of their origin could bring novel insights for laser design and device improvement.

5.2 Strain compensation layer

In order to grow a higher number of active regions to compensate for the lower gain at longer wavelengths, the strain needs to be compensated. Throughout the community, the dominant method is interface engineering [141, 142] of the AlSb/InAs superlattices. At the interface either InSb-like or AlAs-like bonding sites can be forced, which shifts the strain in the superlattice to either tensile for InSb or compressive for AlAs.

Interface engineering revisited The cladding superlattices and the electron injector regions consist of AlSb/InAs superlattices. Their lattice constants are smaller (InAs -0.038Å) and bigger (AlSb 0.04Å) than GaSb. Typical layer thicknesses of 2 to 3 nm are in a range where the interface impact can not be neglected anymore, especially as the binarys group V anion and also the group III cation change [143, 142, 144]. In addition the waveguide cladding layers of commonly used ICL structures contain AlSb/InAs interfaces. At the bonding site either AlAs- or InSb- like bonding sites can be favored by adjusting the growth conditions accordingly with the group V beam pressure. There are multiple techniques to enforce either InSb or AlAs like interfaces [145, 146], ranging from shutter sequences to changing group V fluxes or growth pauses and interrupts for arsenic or antimony soaking [147, 144, 148, 149]. In literature it is reported, that with InSb-like interfaces, higher material quality can be achieved [150, 151]. A key observation in the interface formation is the As-for-Sb exchange mechanism. Arsenic has a stronger bond than antimony and is therefore more likely to occupy bonding sites [135, 127].The reason for the higher material quality with InSb-like interfaces is unclear, it can be assumed, the cumulative strain is lower, leading to lower defect densities and better device performance.

If one can not avoid intermixing, a different approach would be the growth of the nominally non-mixed group V layer as intentionally mixed group V layer, e.g. growing a layer of InSb with unintentionally incorporated arsenic (closed shutter during InSb layer growth) would result in a InSb(As) layer with a non controllable arsenic ratio. Growth of a InSbAs layer with open shutter and controlled arsenic flow offers a higher level of control. In general this requires excellent control of growth parameters and is difficult to achieve with established growth methods. Aside from this, the used C21 Riber System is not equipped with a second set of group V crackers, which would allow for changed group V compositions from layer to layer. It is therefore useful if this can be avoided and a different solution is feasible, e.g. as explained in chapter 3, one can also insert a layer for strain compensation.

Strain compensation layer Strain compensation layers were not used in publications on record before. The InGaSb layer is the biggest contribution for cumulative strain as it features the biggest lattice mismatch with the substrate. Increasing the overall grown thickness with a growth method would allow for a higher number of active regions (see figure 5.2). To avoid the problems of MBE growth with no-common-atom interfaces as interface engineering, we developed a straight forward idea to compensate for the InGaSb induced strain. Revisiting the 6.1Å family highlights a couple of candidates for strain compensation materials: InAlAs, InGaAs, GaAsSb and AlAsSb. The proper candidate is InAlAs, as it not only has no mixed group V compounds, it further can serve as barrier in the electron injector and replace AlSb, lowering the cumulative tensile strain of the active region even more. Aside from InAlAs also InGaAs allows a detuning of its lattice constant away from the 6.05Å of InAs. The main difference between InAlAs and InGaAs is their different effective electron mass of 0.075 m_0 and 0.043 m_0 respectively. Furthermore the RIBER C21 was not equipped with a second gallium effusion cell, which would be a requirement to grow with different growth rates for InGaAs and GaSb. The concluding hypothesis is that an additional layer of InAlAs could serve as strain compensation layer for balancing out the InGaSb induced cumulative strain. We tested this idea with growth of specific samples.

5.2.1 Growth parameters

For the MBE growth, the group V constituents were supplied as dimers with their correlating crackers. The InAs substrates were heated with an As flux of 1.2e-5 torr for the oxide desorption at 515 ° C . The temperature measurement to the ox-off temperature was done with the Bandit pyrometer. After a 10 minute time window, where the oxide desorption was observed with RHEED, the substrate heater was ramped down to the growth temperature, which was between 415 and 450 ° C initially. Calibration growths

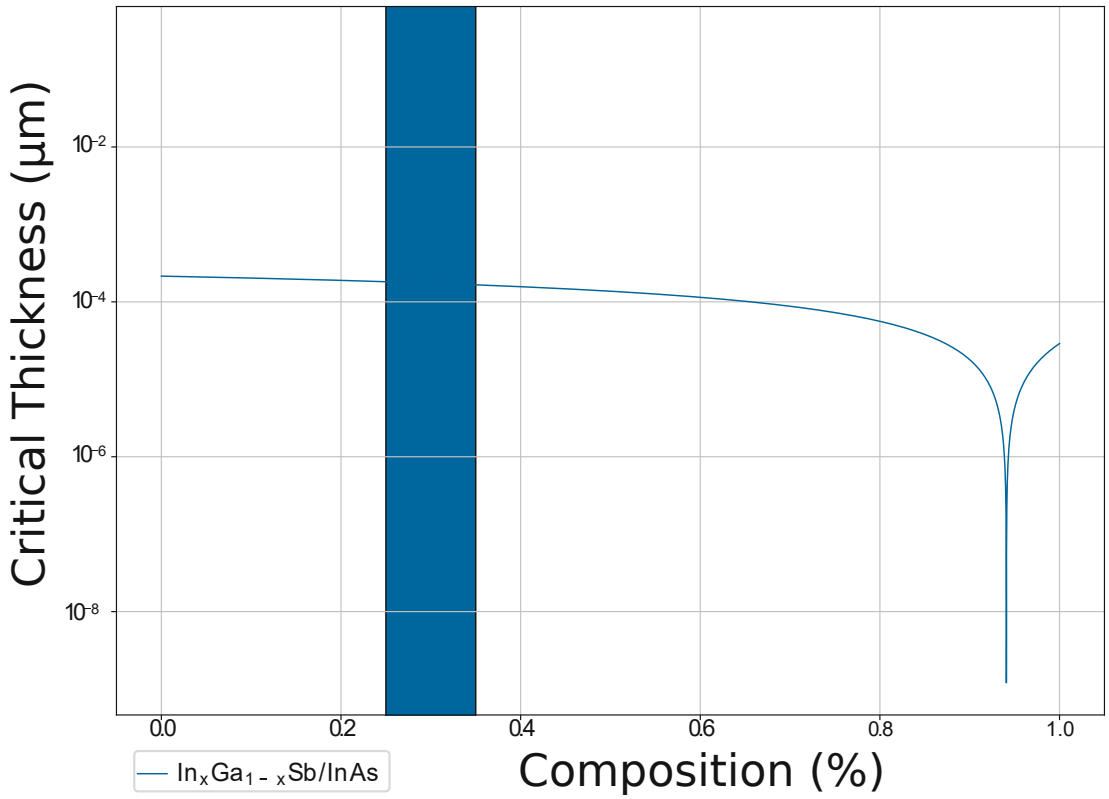

Figure 5.2: Critical thickness of InGaSb vs. In content. The grey shaded area highlights the typical parameter space, where InGaSb layers for long wavelength InAs-based ICLs are grown. The critical thickness of InGaSb on a InAs substrate is around 20 nm.

Parameter	Value
As_2 flux	1.2e-6 torr BEP
Substrate temperature at ox-off	515 °C (Bandit pyro)
Sb_2 flux	2.7e-6 torr BEP
InAs GR	0.72 µm/h
AlSb GR	0.55 µm/h
InSb GR	0.84 µm/h

Table 5.2: Growth parameters for InAs based heterostructures.

for sample quality of InAs and AlSb barriers showed an optimum at 435 ° C, which was kept for the growth afterwards. The cool down procedure was performed with open As shutter and a substrate rotation of 30 rpm. Table 5.2 gives an overview for the most important parameters.

5.3 Experimental verification with prototype structures

We intended to verify our novel idea with the growth of a nominally strain balanced heterostructure. The structure design and strain calculation for this was done with the simulation framework CLAUS, developed by our group. The heterostructure design includes the barrier material AlSb and the central hole quantum well material InGaSb. The substrate and the well material is InAs and does not contribute to the cumulative strain.

Proof of principle test structure C0886 For a W-quantum well the strain inducing layers in an InAs ICLs are InGaSb and AlSb. The structure was solely intended for a growth study. The Al content was set to 25%, which yields in a 2% maximum lattice constant mismatch, the limit for layer-by-layer growth. The sample growth was done accordingly with values of table 5.2. The (004) XRD scan (Fig. 5.4) reveals excellent layer quality, as the superlattice overall thickness is only 60 nm, which utters in a low number of counts per seconds (cps), and the scan still shows good periodicity and narrow diffraction peaks. As discussed in chapter 4, a RSM can give important insight into the heterostructure strain. We measured the (224) RSM with a two-axis scan. In general it is difficult to measure and resolve the pattern for such small thicknesses. As shown in figure 5.5, we were able to do this though. To give a figure of merit for the strain in the structure, we performed a two axis reciprocal space map scan (fig. 5.5) of the (224) diffraction peak. The small signal intensity of the peaks still align in the vertical direction and show the RSM pattern of a strain balanced heterostructure with little or no relaxation. The AFM micrography (figure 5.6 shows a surface roughness of 0.3 nm and displays the initial stages of cross-hatching [122]. This mechanism takes place if a lattice disposition or lattice shift exceeds the energy to induce a defect. The surface topography measured

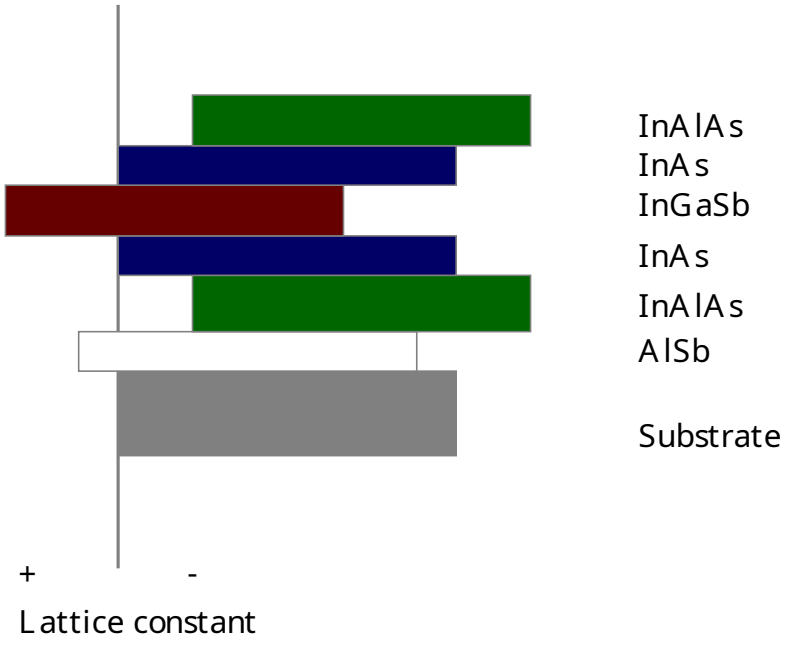

Figure 5.3: Schematic of the strain balanced heterostructure. The additional InAlAs layer compensates the AlSb and InGaSb layers. The overall cumulative strain of the structure is neglectible (Calculated with CLAUS to less than 1E-13). The growth sheet of C0886 is in Appendix A.

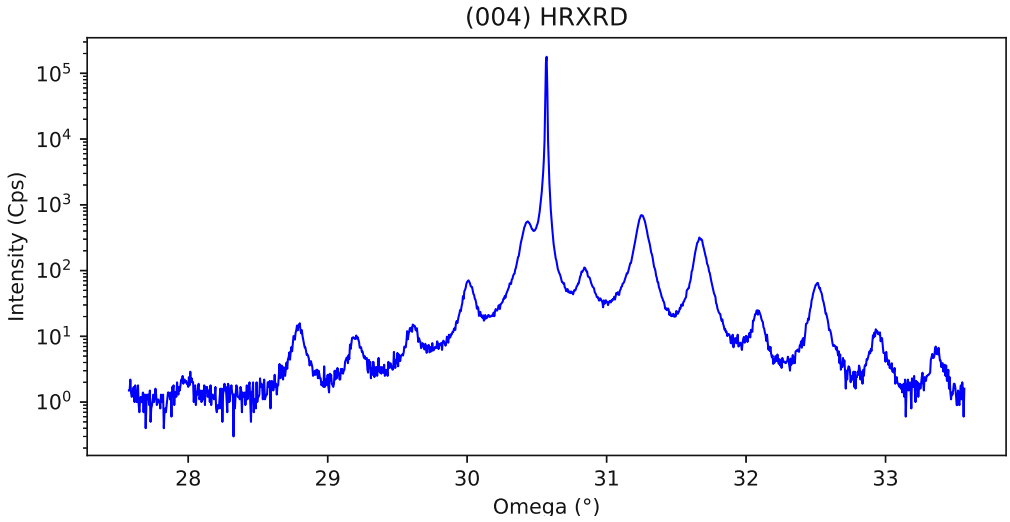

Figure 5.4: (004) XRD scan of test sample C0886. The heterostructure period was 5.7 nm in relation to 6 nm nominally.

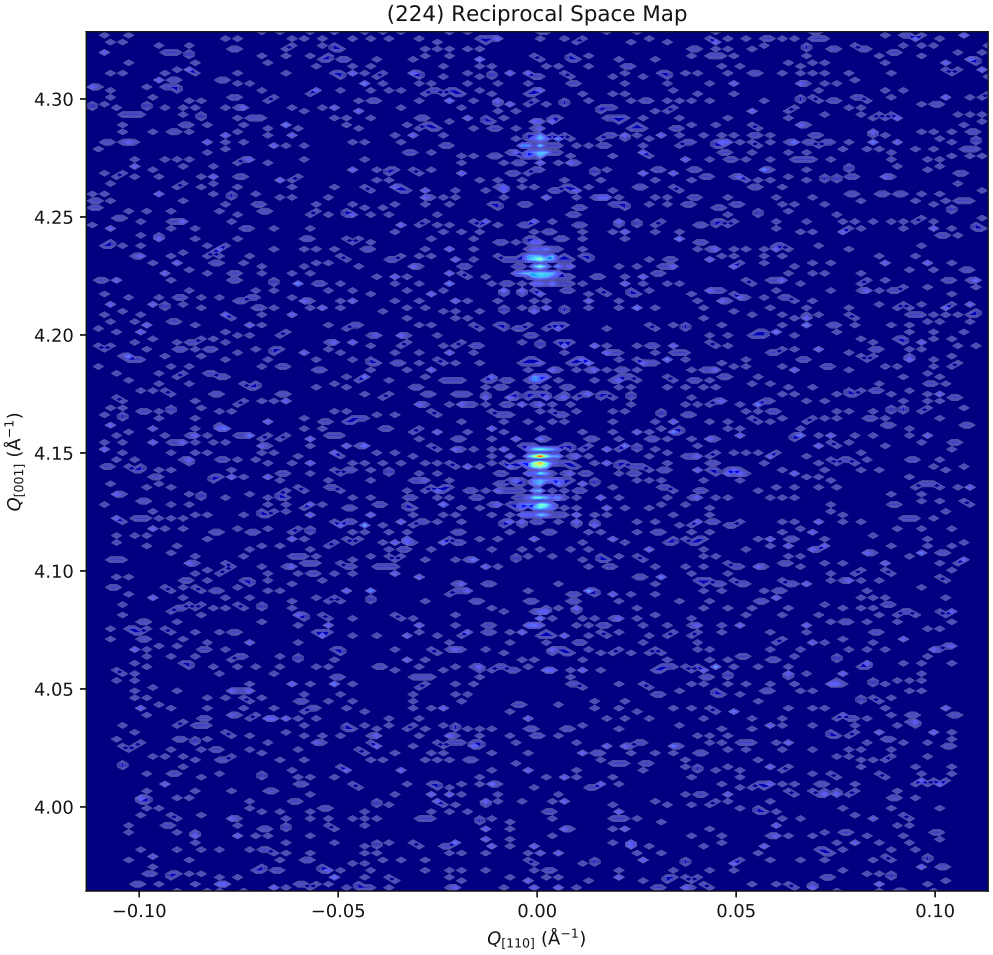

Figure 5.5: HR-XRD (224) reciprocal space map of sample C0886. Despite low cumulative layer thickness the RSM is visible. The RSM shows a strained heterostructure as expected from the design of the grown sample. Although the overall thickness is 100 nm, the superlattice pattern is visible, underlining the high quality MBE growth.

with AFM shows a 0.3 nm RMS. The observed surface pattern is the early stage of what is commonly referred to as cross-hatching, which happens when the lattice mismatch leads to relaxing of the crystal [122]. The idea to use InAlAs as strain compensation

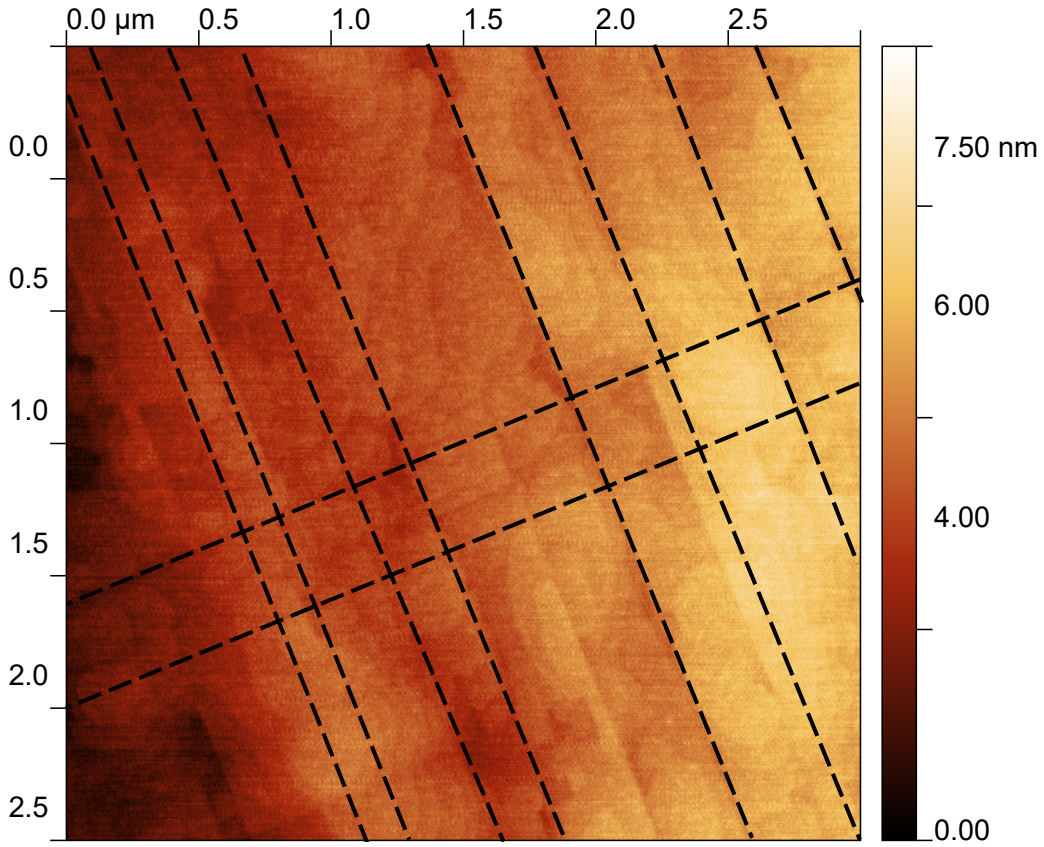

Figure 5.6: AFM micrography of a 3x3 µm area of the surface of sample C0886. The subtle cross-hatch pattern indicates the early onset of strain relaxation. Cross-hatching names the surface lines with 90 degrees.

buffer layer allows the growth of strained heterostructures with crosshatched surfaces. The cross-hatching indicates, that our designed structure was not as close to the grown sample as we anticipated. The materials composition demands further investigation.

Closing the Arsenic needle valve Aside from the successful demonstration of the InAlAs strain balancing scheme, high quality growth of the ternary InGaSb layer is a requirement for further investigations. AlSb and InAs layers were both grown previously in the growth of short wavelength QCDs [152], therefore we had previous knowledge and experience about this material systems. The InGaSb layer strongly determines device performance and is a crucial layer for both the active lasing transition and the hole injector. On the one hand, the group III composition has to be precise, and the group V intermixing has to be controlled. Although some arsenic incorporation in AlSb, GaSb and InGaSb cannot be prevented, it has to be kept at a minimum to grow type-II quantum

wells and achieve sufficient bandgap separation. If the arsenic content exceeds 10 percent, the band structure design is not in accordance with the growth. Initial experiments to grow high quality InGaSb layers started with a fixed ratio of group III components and started with InGaSb/InAs superlattices. We assumed that the main problem was the group V composition. To solve this, we came up with the idea to not only interrupt the arsenic beam flux with the shutter, but furthermore to interrupt the flux more drastically with the needle valve of the cracker cell.

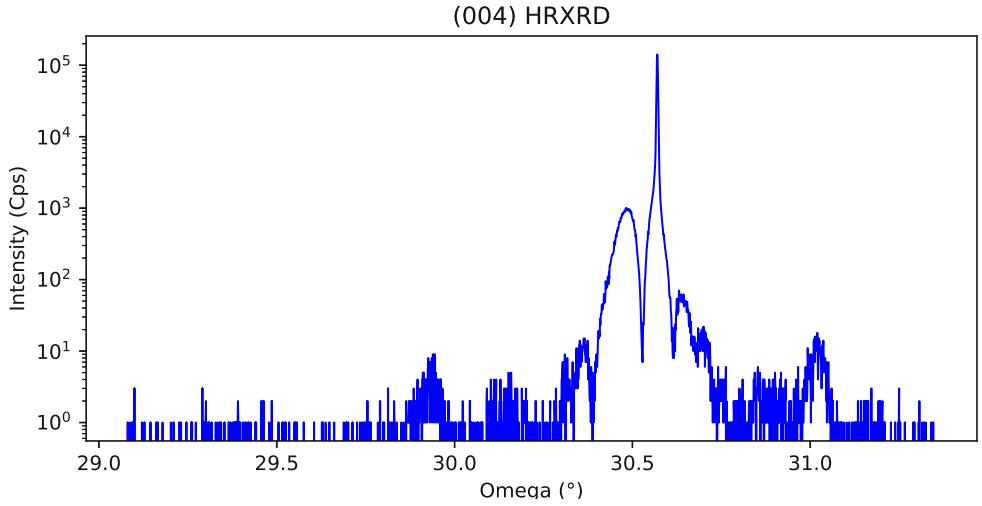

Figure 5.7: HR-XRD (004) rocking curve of C1052 sample growth WITHOUT closing the As needle valve. The As content is 27 %. The three center peaks are close to merging with each other and show non-optimal layer quality. Growth parameters were kept the same for both samples (see table 5.2). Growth sheet is in Appendix A.

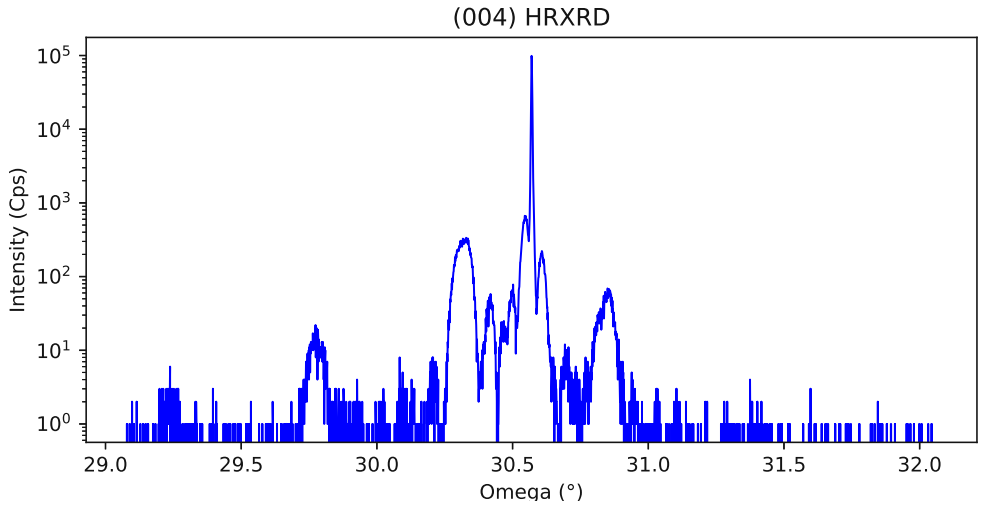

Figure 5.8: HR-XRD (004) rocking curve of the C1053 sample growth WITH closing the needle valve. The As content is lowered to 7 %. The three dominant center peaks are clearly separated from the InAs substrate peak at 30.6 degrees. Growth parameters were kept the same for both samples (see table 5.2). Growth sheet is in Appendix A.

The resulting XRD analysis in figure 5.7 and 5.8 obviously reveals the advantage of closing the arsenic needle valve. The composition of the InGaSb layer with initially 27% arsenic was lowered to 7%, a parameter value where we can grow working devices. We further investigated the samples C1052 and C1053 with TEM and EDX (for growth sheets see the appendix A). The TEM in figure 5.9 shows the consecutive growth of quantum wells. The EDX measurement verifies the alternating layer composition. The nominal layer composition measured with EDX differs from the nominal designed heterostructure and based on the contrast of the TEM micrography, the intermixing can not be neglected. This can be rooted in a surplus of arsenic in the chamber, although the needle valve gets closed. It can be assumed further that an antimony cracker with a rapidly closing needle valve between layers is preferable. The excess antimony supply smears out the antimonide to arsenide interface, which is not a desired effect. The TEM picture shows good contrast

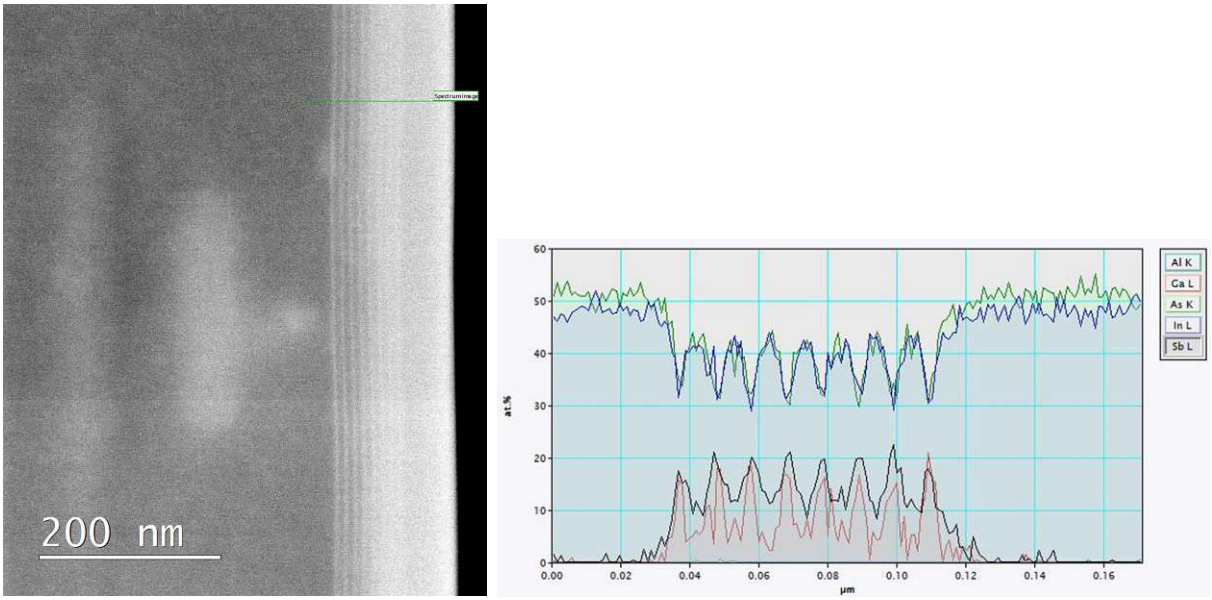

(a) (b)

Figure 5.9: (a) TEM image of sample C1053, a InGaSb/InAs 2.5/7.0 nm superlattice (b) EDX characterization of sample C1053. The spectrum reveals a InGaSb(As) layer composition of 35 %In and 15 % As. The TEM measurement was performed by the University Service Centre for Transmission Electron Microscopy (USTEM), TU Wien.

of the grown heterostructure to the substrate. The EDX spectrum shows a periodic and sharp superlattice of InGaSb(As) with an arsenic incorporation of 15%. The dissent between XRD and TEM can originate from multiple effects, the major reason is the point selective measurement characteristic of TEM in contraposition to the averaging of the XRD measurement. Furthermore, the XRD X'Pert Pro software can shift the fitted curve by an offset, when there are too many free parameters. Although the interface abruptness is acceptable in the TEM and XRD characterizations, the group V intermixing is difficult to characterize. The low layer thickness results in low diffration peak intensities and in

conclusion it is difficult to analyze.

5.4 Characterization of AlSb / InAs superlattices

As we want to grow the designed laser structures, we need a model system to study the arsenic incorporation and ideally grow a part of the material of the ICL laser. The arsenic incorporation into the AlSb barriers needs to be examined in a reasonable framework. During growth we did not intentionally employ growth interrupts, our initial experiments revealed a decline in device performance in comparison to the non-paused growths, a behaviour that also other groups and companies confirmed. Multiple reports and studies of AlSb/InAs superlattices with strain engineering of the interfaces and TEM measurements of the interface exist in literature. Mostly all these studies used growth interrupts or sophisticated shutter sequences and shutter timings. We do no share this point of view. Our goal is to grow active regions without growth interrupts for high quality crystal growth. For further examination we used a standard calibration sample structure for InAs and AlSb growth rates. We use a double superlattice calibration with a different InAs thickness in one of the superlattice parts to determine the growth rates for InAs THz QCLs and InAs QCDs. Our theory is that the commonly claimed fact, that arsenic builds an AlAs-like interface monolayer is not the case. We think that As gets incorporated into the whole layer, leading to AlSb(As) barriers. This mechanism is induced by the well known As-for-Sb exchange and as we are talking about barriers for the W quantum well and the injectors, our focus is to get insight about the composition and material quality. The precise composition can be included in the strain compensation calculation and the band structure design. We grew sample C1072 for the examination with 50 periods of 4.4 nm AlSb and 3.5 nm InAs and 50 periods of 4.4 nm AlSb and 5.0 nm InAs. The HR-XRD (002) scan in figure 5.10 reveals narrow and sharp peaks with high intensity. The

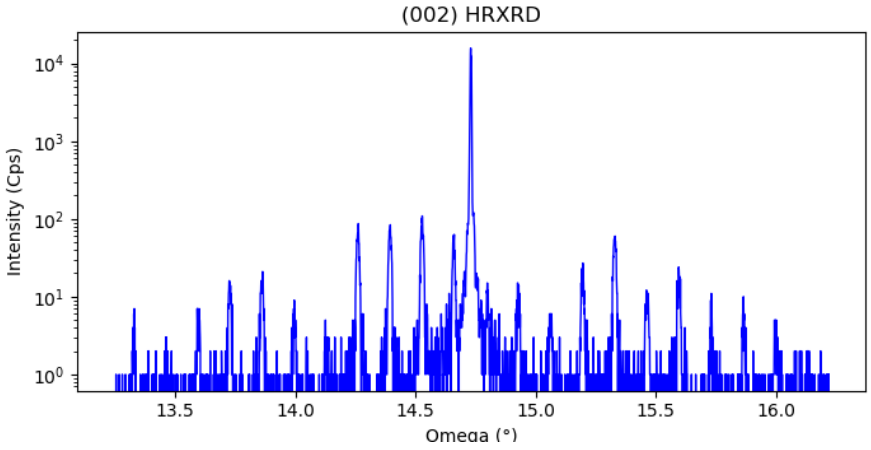

Figure 5.10: HR-XRD (002) scan of sample C1072.

interface analysis was performed in collaboration with the USTEM institute of TU Wien.

The STEM micrographies show sharp and abrupt interfaces. We discussed the impact of

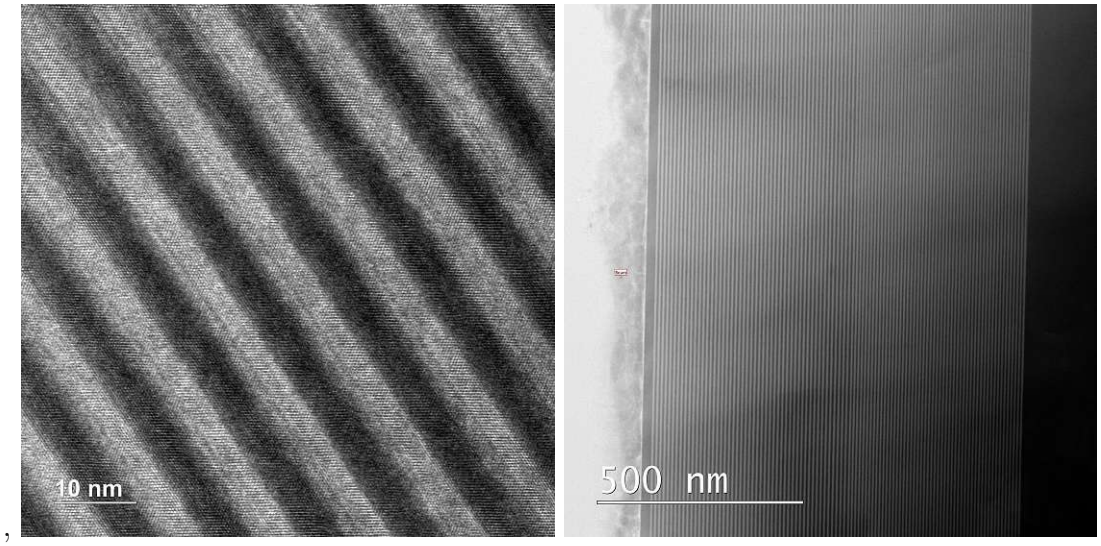

(a) (b)

Figure 5.11: STEM micrography of sample C1072, an AlSb/InAs double superlattice. Bright colour indicates an InAs layer and dark colour an AlSb layer. (a) is a magnification of (b). The TEM measurement was performed by the University Service Centre for Transmission Electron Microscopy (USTEM), TU Wien.

AlAs-like and InSb-like bonding sites for the strain engineering already. The TEM analysis allows for the backcalculation of the material strain. The resulting strain map is shown in figure 5.12. The strain map shows no striking peaks for the strain perpendicular to

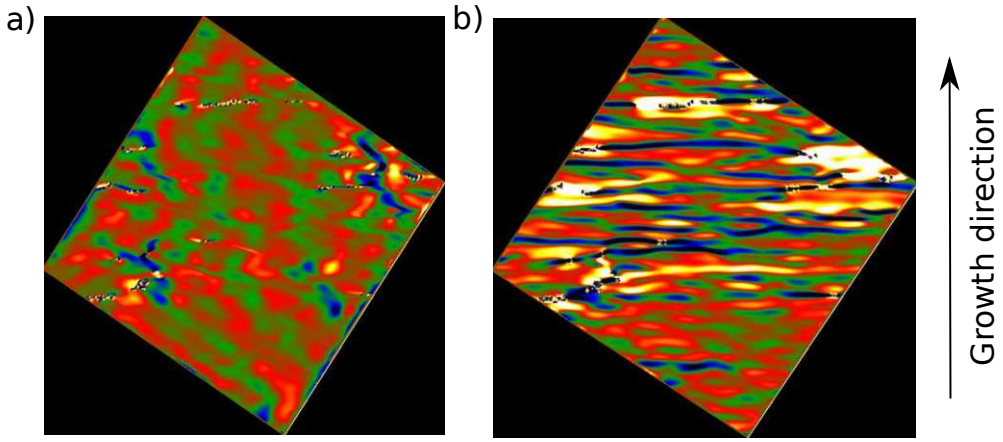

Figure 5.12: Strain map of sample C1072. (a) Strain perpendicular to the growth direction. (b) Strain in growth direction. The TEM strain map measurement was performed by the University Service Centre for Transmission Electron Microscopy (USTEM), TU Wien.

the growth direction. This can be considered as uniform and homogeneous layer-by-layer growth. In contrast to this, the strain map in growth direction shows a couple spikes. The bright colored islands in the figure indicate regions, where massive strain is accumulated.

Although the strained regions did not propagate through the heterostructure, the regions in the lower left and upper right correlates to the region in figure 5.11a where a small strain spike is visible. A consecutive study is planned to relate the bright islands with high strain with the EDX spectrum. A correlation would allow the linking of the material composition with strain and allow to use it as knob for strain balancing.

5.5 C1074 - ICLBK1

A dominant problem with the development of InAs-based heterostructures was the limited Sb growth time available. As we learned within the last campaign, over time the Sb cracker developed a leaky needle valve due to the aging of its spring-loaded valve driving mechanism. This leads to significant time issues with growth as the structures can not be processed and tested in time to establish a feedback loop of growth and design. Nevertheless, after solving the growth related structural issues, we skipped a step and designed a first laser structure that could be used for related projects with a designed emission wavelength of 6.25 µm. The design adaption was the replacement of the the GaSb hole injector layer with InGaSb and an InAlAs barrier before the lasing transitions W quantum well. The structure served a double function aside from the laser design. A successful and ideal growth would give us a laser device. If the device is not functional, we still would have a thick nominally strain compensated structure with a cumulative thickness of 72 nm InGaSb. The previous published thickness we considered a "record" were 62 nm by Jiang et al. [153]. Aside from the active region design, the designed waveguide cladding were highly doped InAs layers, this worked as plasmonic waveguides (see Appendix D).

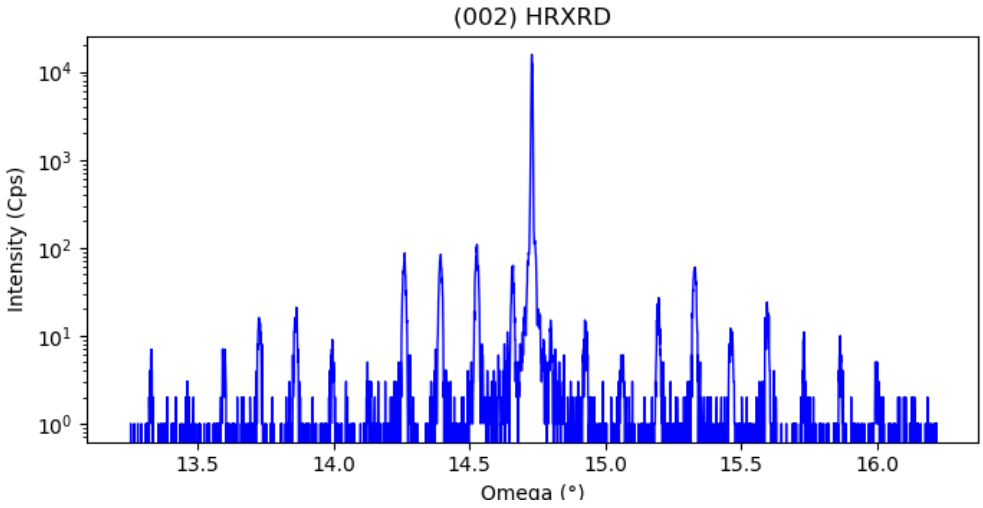

Figure 5.13: (002) HR-XRD characterization of sample C1074, the laser structure ICLBK1. The XRD scan of the sample shows sharp and defined peaks, indicating high quality MBE growth.

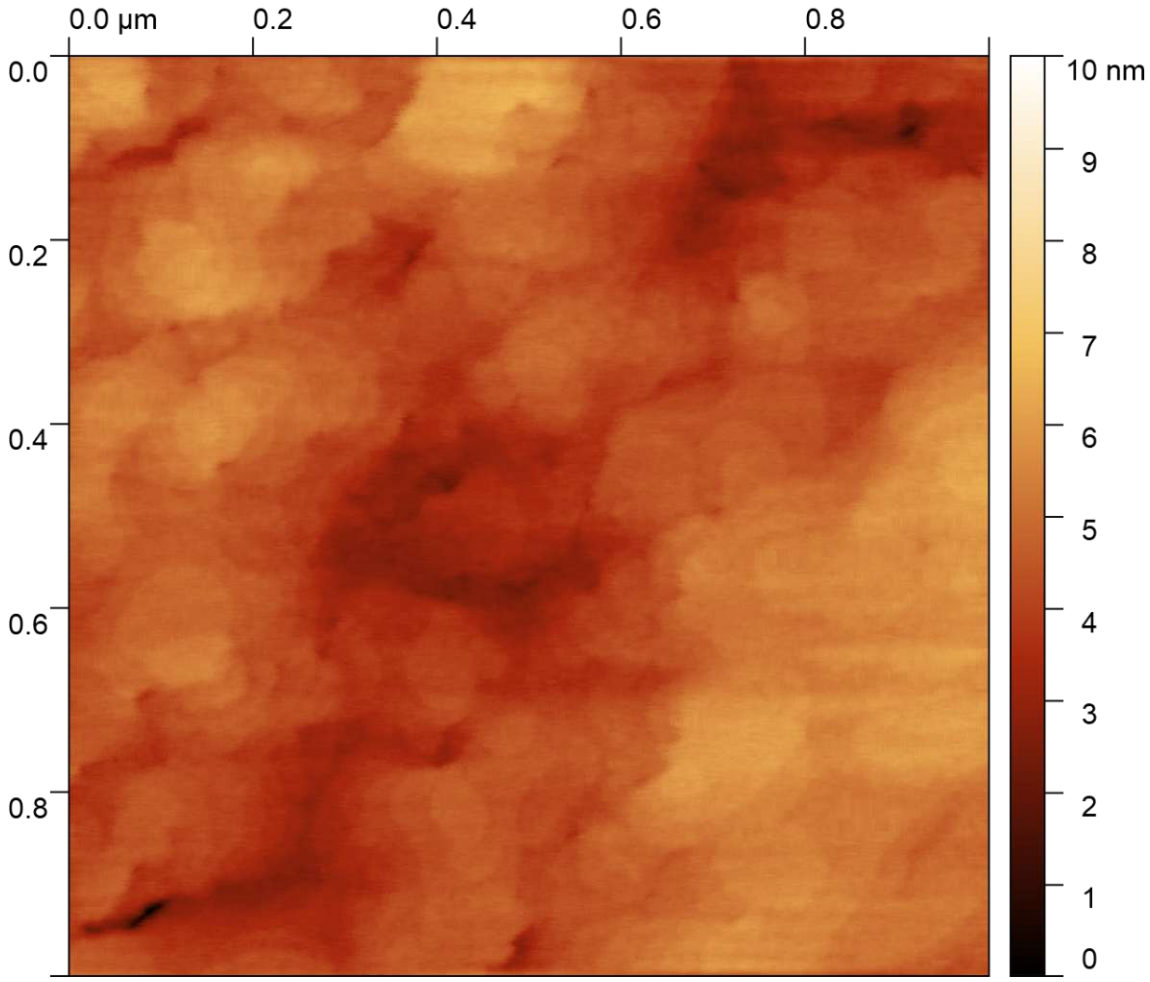

Figure 5.14: AFM micrography of sample ICLBK1. The RMS of the surface is 0.2 nm. A possible reason for the surface pattern is spiral growth along threading dislocations.

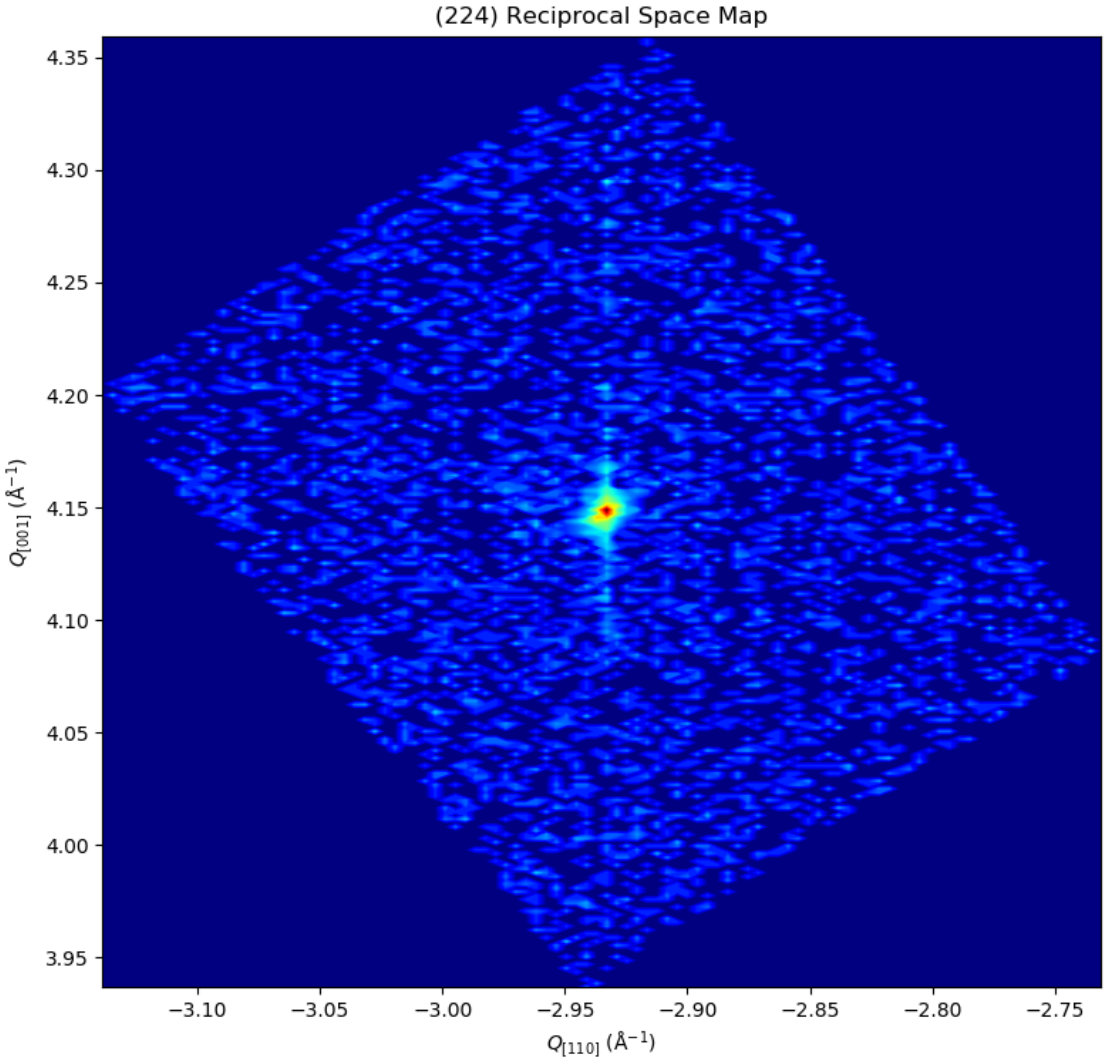

Figure 5.15: RSM map of sample ICLBK1. The RSM pattern is linear, as the nominally strain balanced heterostructure was intended to. The poor signal-to-noise ratio originates in less than ideal interface quality and a probably too high arsenic incorporation in the mixed group V interfaces.

Although the growth analysis looks promising, the fabricated laser ridge samples did not show lasing or a laser-like LIV. The reasons can be manifold, probably the biggest contribution is the connection of a design tool as CLAUS with the real grown structure is a time intense and difficult task. Putting the growth in context we achieved a cumulative thickness of 84 nm of InGaSb. In theory this would allow for 20-25 active InGaSb quantum wells, depending on the design. The thickest published structure by Jiang et al. featured 20 periods with a cumulative thickness of 62 nm. Therefore the growth aspect of effective strain compensation can be considered a success.

5.6 Discussion

The proof-of-principle was successful and highlights the exciting possibilities of the strain compensation method for long wavelength InAs-based ICLs. The intermixing of AlSb and InAs was investigated in a model sample and showed high quality MBE growth. An early laser structure was grown with an accumulated InGaSb thickness of 72 nm, which would allow the growth of up to 23 active W quantum wells. The laser did not show light emission. In addition to the characterization with AFM, TEM and HR-XRD, we intended to characterize the samples with a photoluminescence measurement (PL). For the measurement of the spectrum we used a sample with a set of five stacked W quantum wells and designed the transition wavelength to 6.15 µm. In order to further use the samples for electric characterizations, we added a highly doped InAs top layer. As we learned later on this killed the extraction of a PL spectrum, as the high doping is absorbing the excitation, therefore the PL data is missing. For future work it will be a crucial step towards laser operation to characterize the PL spectrum. An additional reason could be poor interface quality. Typically with low measurement temperatures this effect can be counteracted to not interfere too much. Our friends at nanoplus GmbH did this, but were not able to extract PL data at 77 K too. The TEM analysis does not show at poor interface quality. It shows clear and abrupt change of materials within the superlattice. The EDX analysis showed group V intermixing that exceeds the HR-XRD determination. If this effect is too strong, the arsenic incorporation in the background level can shift the band structure design to a region, where no band alignment occurs. It is still possible to grow the structure within the strain window and the thickness tolerance of one percent, but the energy levels are not aligned and light emission is not possible. Based on the TEM data and the HR-XRD, the offset in arsenic content is an explanation to this. Aside from the successful growth of a high cumulative InGaSb thickness, the ICLBK1 structure did not show any lasing. This is a typical MBE growth vs. heterostructure design problem. Aligning a numerical model to the grown structure requires a lot of effort. Future growth studies will have to be done to align CLAUS with the epitaxy. The ongoing research and work on the CLAUS simulation framework will allow this for sure for subsequent work. As in

every high risk topic, it is always a trade off between too many steps at once or not getting anywhere. The proof-of-principle demonstration of the strain compensation method will be highly useful, if future work heads for more active regions. The fundamental studies with InAs/AlSb superlattices and InGaSb growth will be building blocks for future TU Wien inhouse grown ICLs and antimonide based interband devices.

CHAPTER

SIX

FABRICATION OF HIGH-PERFORMANCE QCLS AND ENGINEERING OF HIGH BANDWIDTH FREQUENCY COMBS

This chapter intends to summarize the efforts and research regarding the technological aspect of fabricating high-performance QCLs and their characterization as frequency combs. Dedicated efforts to fabricate outstanding devices with excellent performance led to multiple publications in peer-reviewed journals [28, 21, 154, 155, 156]. Multiple breakthroughs were enabled by high resolution lithography of functionality defining features. The width of the crucial slit feature [156] did span 0.8 µm and got successfully transfered by lithography onto the sample. Aside from the fabrication a further examination of high bandwidth frequency combs was done. A numerical study showed how to engineer QCL frequency combs in order to obtain broad-bandwidth frequency combs that contain a large number of modes and was published as 'Engineering the spectral bandwidth of quantum cascade laser frequency combs', Optics Letters 46 (14), 3416 (2021). In good scientific manner, the correlation of theory and experiment was demonstrated with the growth of an ultra broad terahertz QCL, spanning an emission window over a full optical octave. Such a broad spectrum could pave the way towards closing the THz gap in the future. The mentioned study comprised results that are current subject of the publication in ACS Photonics as "Ultra-Broadband Heterogeneous THz Quantum Cascade Laser". In the following a review of fabrication will be given, followed by a in depth discussion of the publications regarding the engineering of high bandwidth frequency combs.

6.1 Fabrication of high-performance QCLs

Reliable high-performance devices are a prerequisite in order to investigate semiconductor lasers working principle and dynamics. In this context high-performance means a stable

high power output and RF injection capabilities. A key requirement is the clean and rigorous fabrication of ridge lasers optimized for frequency comb operation. The fabrication procedure starts with a MBE grown sample, from either collaboration partners or the TU Wien MBE lab.

Fabrication flow scheme State of the art devices require a high level of parameter control during the fabrication work flow. The fabrication for frequency laser comb devices differs from the standard ridge process (figure 6.1). The work flow is listed below and the typical process parameters are specified in appendix A.

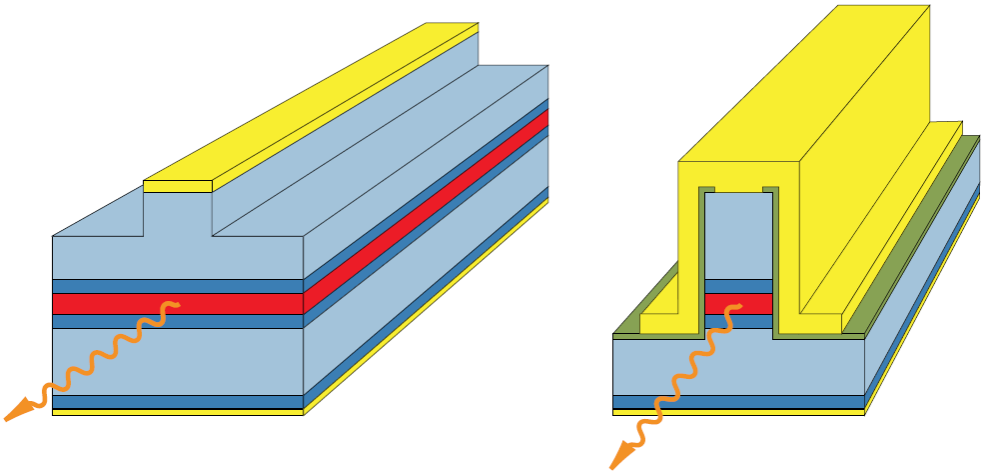

Figure 6.1: (a) Broad ridge geometry for device testing purposes. Note, that solely the top surface is metalized. Typical ridge widths for broad devices are 10-50 µm with a varying cavity length between 1-4 mm. (b) Narrow ridge geometry, e.g. as used for high-performance frequency combs owns a ridge width slightly above the wavelength. A 8 µm QCL typically has a 10 µm wide ridge. The encapsulating metalization increases the heat dissipation and device performance. Figure reproduced with permission from [58].

- Deposition of the hard mask material
- Transfer the geometry with lithography on the hard mask
- Dry etching of the hard mask and of the waveguide afterwards
- Removal of the hard mask
- Deposition of the passivation layer (silicon nitride or silicon dioxide)
- Dry etching of the passivation layer opening
- Metalization of the top contacts with titanium and gold
- Substrate thinning to 150-200 µm

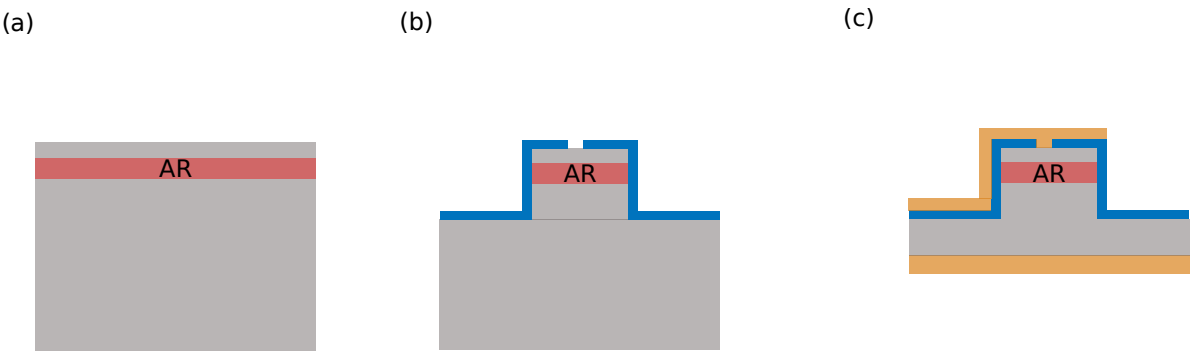

Figure 6.2: Fabrication flow for a high-performance laser ridge. (a) Epimaterial with the active region (AR in red) (b) Dry etching of the waveguide with deposition and opening of the passivation layer (blue). (c) Metalization (yellow) and substrate thinning.

- Metalization of the bottom contact with titanium and gold

Fabrication starts to become difficult with connecting high-performance and frequency combs. High-performance requires narrow laser ridges (4.5-5.5 µm width) and a sidewall roughness that minimizes losses. The efficient RF injection that locks the frequency comb beatnote requires a two step passivation layer deposition. The first step deposits and defines the modulator section passivation with 1.2 µm of silicon nitride. In order to increase the efficiency of the RF injection a part of the laser ridge is electrically separated - labelled as the modulator section area (figure 6.3). The passivation layer of the gain section has a thickness of 250 nm and critical need for an opening window with a width of 2-4 µm that needs to be straight over a distance of 4 to 8 mm. The opening of the passivation layer is a crucial step for successful laser operation. If the window shifts too much, the dry etching could overetch at the waveguide borders and short the electrical circuit, thereby preventing a working device. A SEM micrography of a finished RF injection pad is displayed in figure 6.3. The success that has to be highlighted to achieve the lower limit of the feasible resolution of the current cleanroom equipment was the lithography for the defect/ring comb. The defect in the ring cavity is supposed to be small enough to not work as facet, but be big enough to push the comb in a noisy regime. The slit width (see figure 6.4) was below 1 µm. The final result is shown below in figure 6.4 and 6.5.

Focussed Ion Beam milling Separating features on a micrometer scale is a challenging task to do with lithography. A different approach is Focussed Ion Beam milling (FIB). A beam of gallium ions in the Zeiss SEM is directed on the sample and the physical abrasive interaction works similar to a scalpel. Problematic with this technology is the implantation of gallium ions on the surface of the heterostructure, e.g. if the cutting or milling area exceeds certain areas and depth limits. Figures 6.6 and 6.7 highlight two exemplary projects with FIB cut features. In the very beginning of ICL fabrication the electrical separation of modulation and gain section was done with a FIB cut. The close distance of

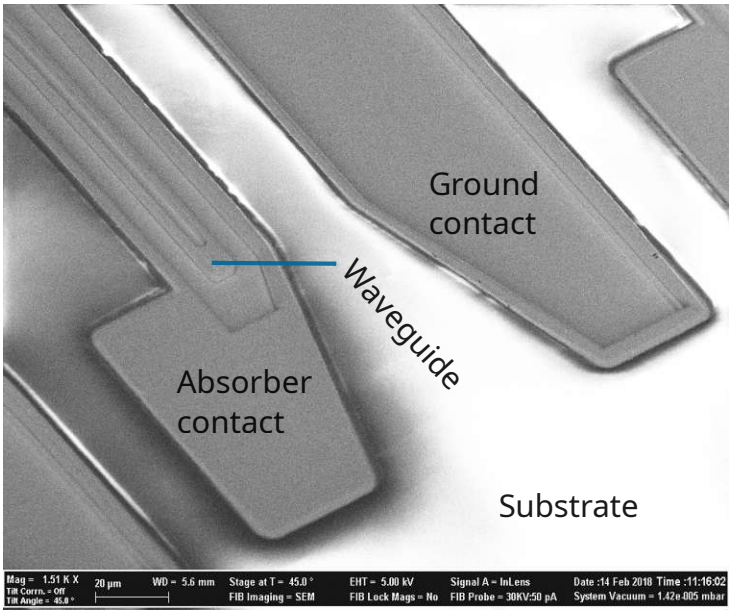

Figure 6.3: SEM micrography of the shorter and separately biases section fabricated with lithography. The processed devices were used for the measurement of picosecond pulses in interband cascade laser frequency combs [28].

the contact pads lead to multiple shorts before. The second figure shows a novel approach to self-reference frequency combs with a ring coupler. Two parallel straight ridge lasers get coupled with a ring waveguide. The key problem with the coupling is the waveguide separation and the correlating power transfer. One possibility is again the separation with a FIB cut as displayed in figure 6.7. The waveguide geometry was conserved successfully and the FIB cut was penetrating the full depth of the laser waveguide with 4 µm.

Electrochemical plating process An important step to further optimize the laser performance is the electrochemical deposition of gold. The regular titanium gold deposition with a sputterer is not sufficient as depositions above ca. 300 nm lead to removal problems in the liftoff step. The long deposition time and missing heat dissipation lead to a quasi softbake of the resist, which is hardly removable afterwards without destroying the TiAu gold layer or the waveguide of the device. Obviously it is of high interest to deposit a thick metalization layer without destroying the sample. A convenient method to circumvent this problems is electroplating. After the sputtering deposition of a seeding TiAu layer with 50 to 100 nm, the areas where no gold should be deposited are covered with resist. Neither thickness nor positive or negative resist properties matter, it only needs to cover the area sufficiently. Within this work AZ5214 was used in combination with an additional lithography mask field to cover the final fabricated laser structures.

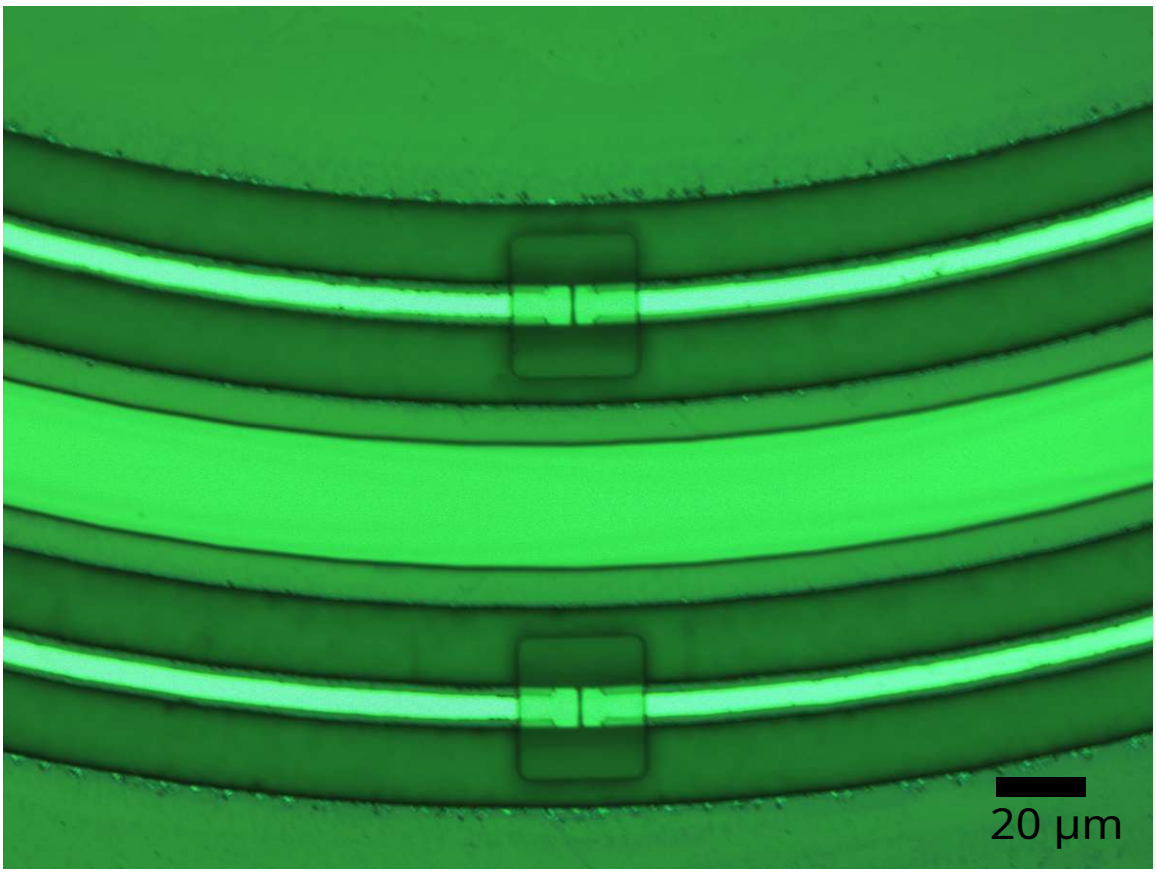

Figure 6.4: Micrography of the slits fabricated with lithography. The processed devices were used for the measurement of phase-noise induced frequency combs [156]. The slit is covered by the nLof lift-off resist mask before the metalization step.

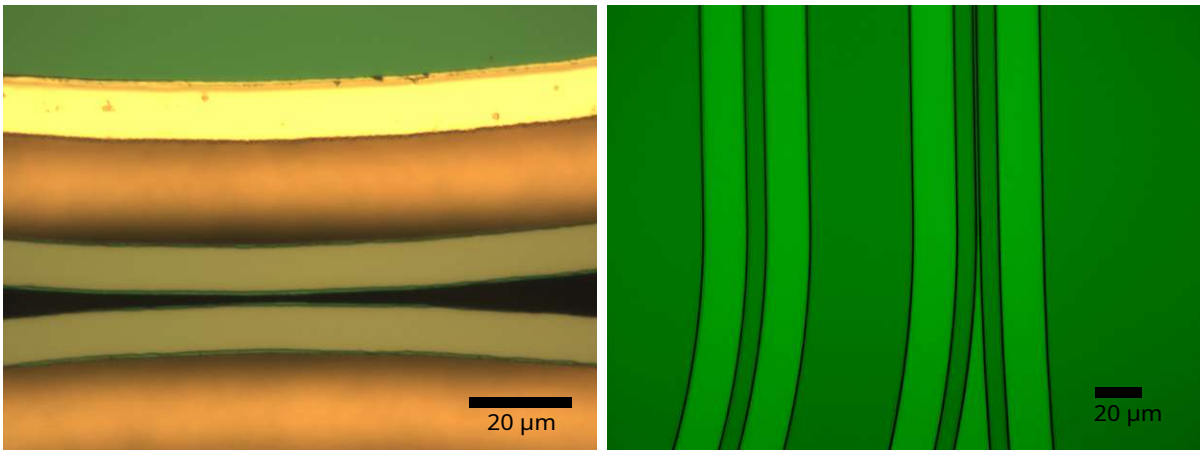

(a) (b)

Figure 6.5: (a) Micrography of the waveguide coupling lithography. Note, the extraordinarily narrow resolved slit width below one micrometer. The light grey areas are the top surface of the laser waveguide. (b) Micrography of the waveguide coupling lithography. The picture was taken after the silicon nitride hard mask removal. The bright green areas are trenches of the waveguide structure.

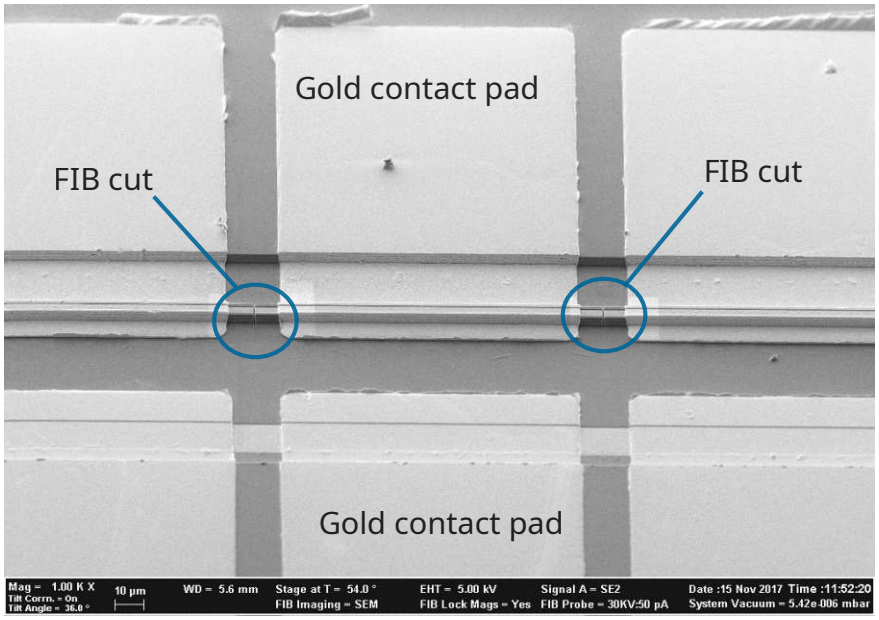

Figure 6.6: SEM micrography of the separation of gain and absorber section with a FIB cut. The laser active region was seperated in a first attempt to allow different bias values for the gold contact pads. The FIB cut is highlighted with the blue circles.

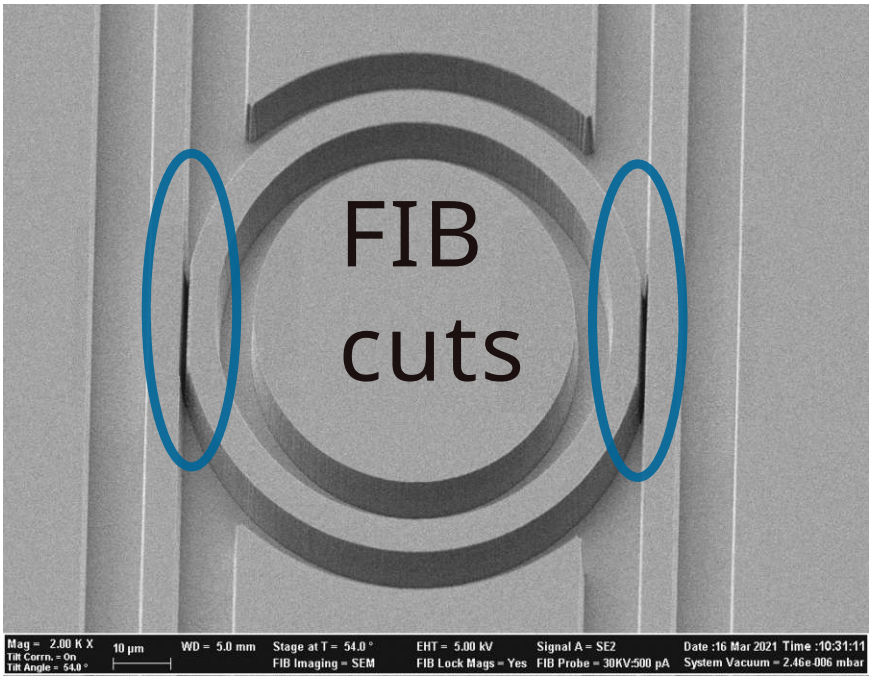

Figure 6.7: SEM micrography of the separation of coupling ring and gain section (straight ridge) with a FIB cut. The FIB cut width between the ring and the laser is 1.1 µm wide. The FIB cuts in the blue ellipses were done after the silicon nitride hard mask removal. The visible material is solely the QCL material.

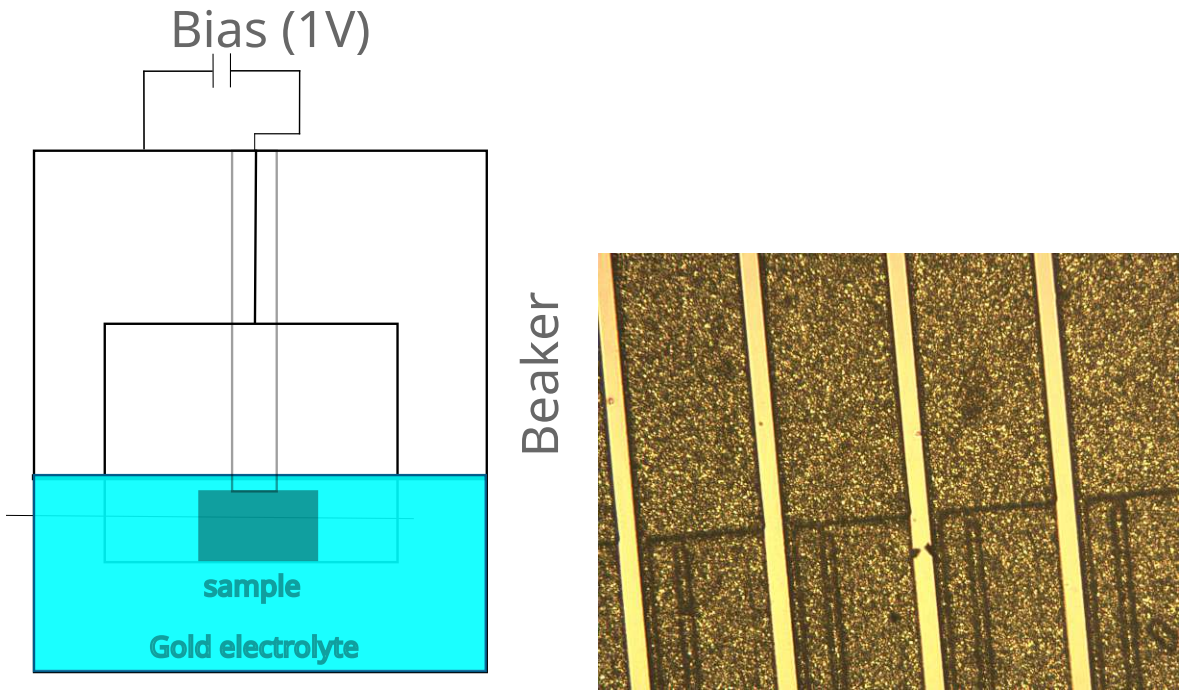

(a) (b)

Figure 6.8: (a) Scheme of the plating process. The deposition occurs with 1mA current and 1V bias. The placement of the contact needle on the chip is a fragile and crucial step. (b) Nomarksy micrography after deposition. The bright surface origins from the sputtered part. Typical deposition rates are 6 µm/h.

6.2 Engineering the spectral bandwidth of QCL frequency combs

This section is based on the publication 'Engineering the spectral bandwidth of QCL frequency combs', published in Optics Letters and rewarded with an Editors Pick [157]. Mid-infrared dual-comb spectroscopy using QCLs has the potential to revolutionize high-precision spectroscopy due to their on-chip integration. This technique has been demonstrated [33] and its viability for real-time monitoring of chemical reactions has been proven [158, 159]. Injection of a microwave signal at the cavity roundtrip frequency allows locking of the repetition rate of a QCL [160], providing coherent control of the FM comb states using conventional RF electronics [161]. The FM comb states have also been demonstrated in other laser types such as interband cascade lasers [21], quantum dot lasers [98], and laser diodes [162]. However, the key missing element for the widespread use of QCLs in broadband high-precision spectroscopy is reliable control and enhancement of the FM comb states' optical bandwidth [99, 105].

The dispersion properties of quantum cascade laser (QCL) waveguides have been recognized as a crucial factor in the formation of frequency-comb (FM-comb) structures. One established technique for tuning the group velocity dispersion (GVD) involves the

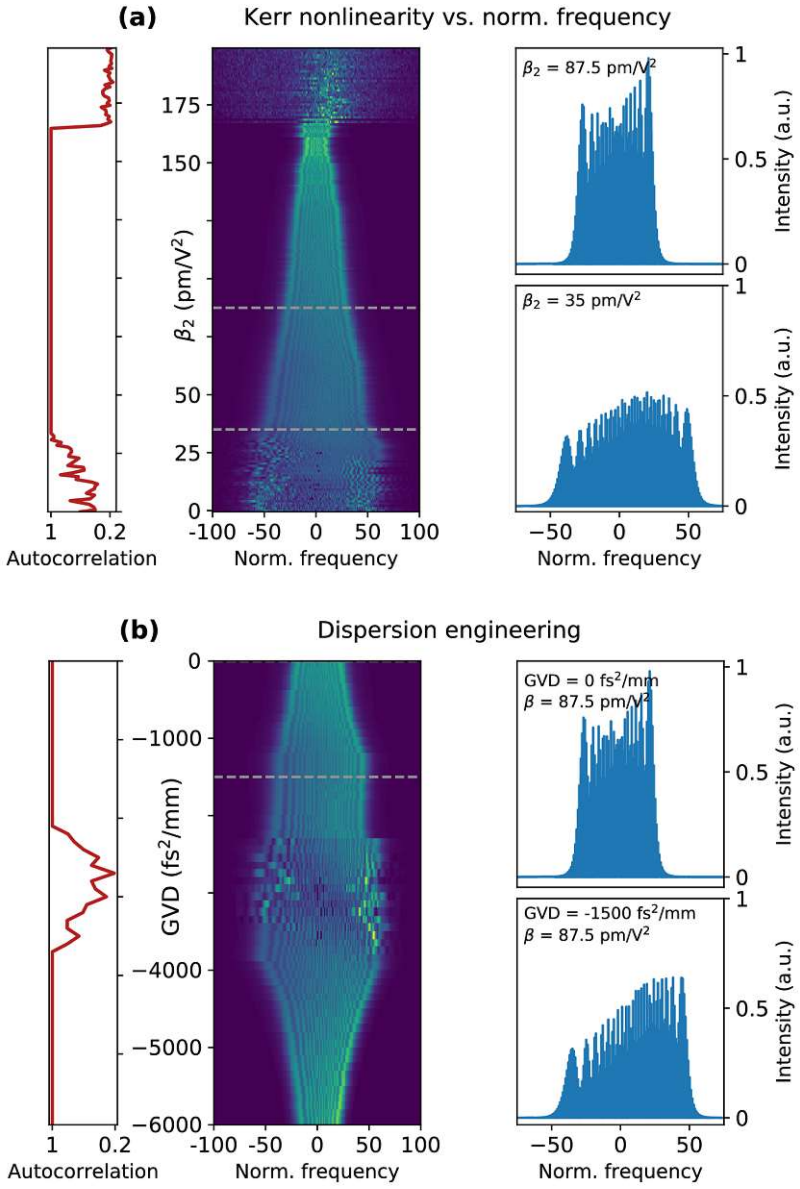

Figure 6.9: (a) Evolution of the intensity spectrum with the increase of the resonant Kerr nonlinearity β for a dispersion compensated cavity (GVD = 0). Small β leads to unlocked states, indicated by the autocorrelation value smaller than unity. FM comb formation appears between β =35 and 165 pm/V^2 with the autocorrelation equal to unity. Increase of the Kerr nonlinearity narrows the spectrum. Unlocked states are obtained above β =165 pm/V^2. Two insets on the right depict spectra taken at β =35 pm/V^2, with maximum spectral width and at 87.5 pm/V^2, with smaller number of comb modes. (b) Evolution of the spectrum for β =87.5 pm/V^2 as the GVD is tuned. The maximum optical bandwidth is recovered for GVD of -1500 fs^2/mm or -4000 fs^2/mm.. Figure reproduced from [157] with permission of Optica Publishing (2021).

utilization of a Gires-Tournouis etalon, where a planar mirror is positioned behind the laser facet to induce a group delay that varies with wavelength [163, 164]. An alternative method involves the coupling of the dielectric waveguide to a plasmonic resonance, with the aim of decreasing the waveguide dispersion [165]. Experimental studies of FM combs in QCLs have predominantly been conducted in lasers with relatively low GVD, leading to the widely accepted conclusion within the scientific community that full dispersion compensation is a necessary condition [166, 164]. However, recent theoretical research has highlighted the crucial interplay of multiple factors in the formation of frequency combs, including the group velocity dispersion (GVD), the Kerr nonlinearity, the intracavity light intensity profile, and other effects, as discussed in [99, 167]. It has been demonstrated that full compensation of dispersion does not necessarily result in broad comb spectra spanning the entire available gain bandwidth or in comb operation. The presented study numerically examines the roles of the GVD and resonant Kerr nonlinearity and investigates the impact of cavity facet reflectivities. The maximum spectral width achievable through optimization of the parameters is determined by the gainwidth of the laser's active medium and is independent of the specific set of optimal parameters utilized. All sets of optimal parameters lead to the same maximum spectral width, which is predefined by the gainwidth of the laser active medium. A theoretical analysis of the maximum bandwidth of quantum cascade laser (QCL) frequency combs can be found in [168]. In addition, numerical and experimental evidence is presented, demonstrating that the maximum spectral width can be achieved through the use of RF modulation of the injected current. This provides a desirable alternative to spectral width optimization, as it does not necessitate any modifications or adaptations to the laser. In cavities with compensated group velocity dispersion (GVD), the laser modes are evenly spaced, which might appear to facilitate mode-locking and frequency comb formation. However, this is not the case for FM comb operation, where the linear frequency chirp results from the complex synchronization of neighboring comb modes, similar to anti-phase synchronization among coupled clocks [98]. The rapid gain recovery time of quantum cascade lasers (QCLs) causes a spectral gain asymmetry due to Bloch gain, leading to a significant Kerr nonlinearity [99, 169]. This resonant nonlinearity affects the optimal conditions for comb formation, explaining why FM combs are often observed in GVD compensated cavities [165]. The impact of the Kerr nonlinearity on the intensity spectrum of a dispersion-compensated quantum cascade laser (QCL) with uniform, uncoated facets is depicted in Figure 6.9. The simulation, based on a master equation approach derived from the Maxwell-Bloch equations, takes into account spatial hole burning, dispersion, and the Kerr nonlinearity [99]. The laser was modeled to operate above the threshold with an injection current 1.5 times greater than the threshold value. The complete simulation parameters can be found in the supplementary material. The autocorrelation between two temporally-separated roundtrips of the laser intensity was calculated to determine the periodic comb state of the laser. The result of unity indi-

cates a perfectly periodic comb state while smaller values suggest an unlocked state. The impact of the Kerr nonlinearity on the intensity spectrum was investigated using a simulation based on a master equation formalism derived from the Maxwell-Bloch equations. This simulation considered the spatial hole burning, dispersion, and the Kerr nonlinearity. The laser was modeled to operate above the threshold, with the injection current set at 1.5 times the threshold value. Based on the results, three regimes were identified based on the value of the Kerr nonlinearity. At zero nonlinearity, the laser is unlocked and produces a broad spectrum. Above a minimum threshold value of nonlinearity (around β=35 pm/V^2), FM comb operation is observed. It was observed that further increases in the Kerr nonlinearity lead to a narrowing of the spectrum, although the laser remains locked up to β=165 pm/V^2. The detailed simulation parameters can be found in the supplementary document. In the optimal regime, where the Kerr nonlinearity is equal to 35 pm/V^2, the broadest spectral width is observed. However, in a non-optimal scenario with a Kerr nonlinearity value of 87.5 pm/V^2, the laser emits a narrower spectrum. The value of the Kerr nonlinearity depends on the band structure design, and thus optimizing it would necessitate a comprehensive redesign of the active region to reach the maximum spectral width. In this study, we discuss three methods to broaden the spectral width from a non-optimal active region with a Kerr nonlinearity of 87.5 pm/V^2. The utilization of dispersion engineering can be utilized to optimize the FM operation of a laser for varying values of nonlinearity. Figure 6.9b presents the simulation results for a nonlinearity of β=87.5 pm/V^2 and a range of GVD values from -6000 fs^2/mm to zero. By adjusting the GVD from zero to -1500 fs^2/mm, the maximum spectral span can be achieved, similarly to the case of β=35 pm/V^2. The interplay between non-zero GVD and Kerr nonlinearity has a significant impact on the FM comb spectrum. However, further increases in the GVD value lead to an unlocked state and then a locked state with a shrinking spectral span.

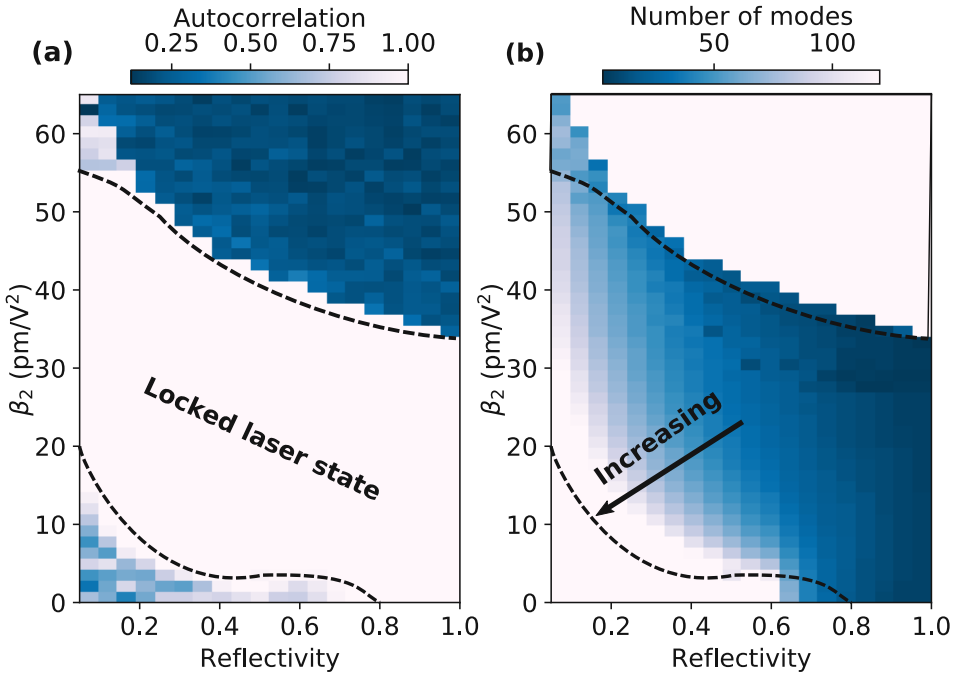

Figure 6.10: The autocorrelation for tuning (a) the Kerr nonlinearity and the reflectivity of one facet with the other facet fixed to one. (b) Sweeping the same parameter set for the spectral width. The arrow indicates the increasing number of modes. Figure reprinted with permission from [157].

As a third alternative, we propose a method that does not require precise cavity adjustment for a specific active region, namely, the injection of an RF signal near the cavity's roundtrip frequency. To evaluate the impact of modulation on the FM comb spectrum, we employ the coherent master equation, which is in line with recent studies [170]. The laser under consideration has a non-optimal Kerr nonlinearity of 87.5 pm/V^2 and a zero group velocity dispersion (GVD). The current modulation is applied to a 10% portion of the laser cavity. In Figures 6.11a and b, we present the results of our investigation on the impact of current modulation on the FM comb spectrum. In the absence of modulation, the comb spectrum is composed of 74 modes with linearly arranged intermodal phase differences. However, when a strong current modulation (10%) is applied, the number of modes in the comb spectrum expands from 74 to 134, and the slope of the intermodal phase differences reduces, indicating the establishment of a locked and coherent FM comb state. In order to validate the predicted behavior, we conducted an experimental evaluation using a high-performance mid-infrared quantum cascade laser (QCL) frequency comb emitting at 8 µm. The cavity of the QCL was split into two parts - a 3.15 mm long gain section and a 350 µm modulation section that was optimized for efficient RF signal injection. The active material's band structure was designed as a single-stack bifunctional active region, which allowed for more efficient modulation with larger modulation depths. The modulation section was operated at a DC bias of 2.8 V to maximize modulation efficiency, and the modulation power was increased up to 35 dBm using a Mini-Circuits

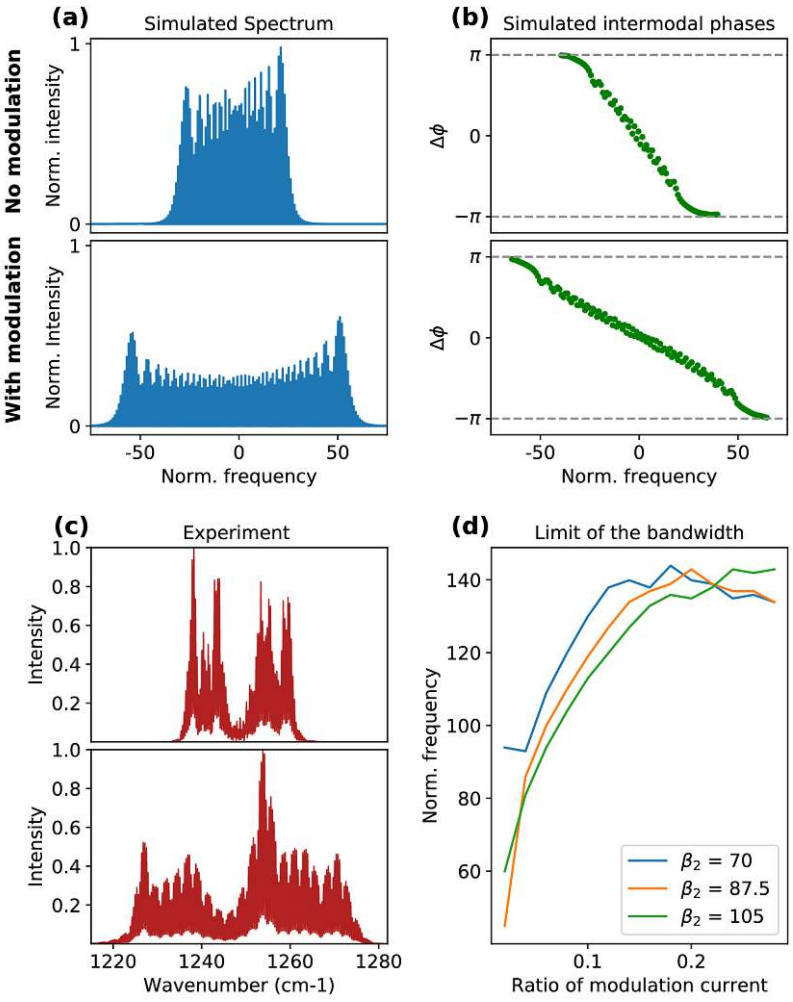

Figure 6.11: Simulated (a) intensity spectrum and (b) intermodal phase differences with (bottom) and without (top) the modulation of the injection current. (c) Experimental intensity spectrum with (bottom) and without (top) the modulation of the injection current. (d) Simulated spectral width depending on the modulation depth. Figure reproduced from [157] with permission of Optica Publishing (2021).

ZVE-3W-183+ power amplifier. The experimental testing of the predicted behavior was conducted using a high-performance mid-infrared quantum cascade laser (QCL) frequency comb emitting at 8 µm. The QCL cavity was divided into a 3.15 mm-long gain section and a 350 µm-long modulation section optimized for efficient RF injection. The active material's band structure was designed as a single-stack bifunctional active region to allow for more efficient modulation with larger modulation depths. The modulation section was operated at a 2.8 V DC bias to maximize modulation efficiency and the modulation power was increased up to 35 dBm using a Mini-Circuits ZVE-3W-183+ power amplifier. A portion of the 35 dBm (15 dB) was lost due to parasitic capacitance in the QCL. Further information on modulation capabilities and an effective modulation depth estimate can be found in the supplementary material of the published paper. The results of the experiment are shown in Figure 6.2, where it can be seen that the QCL operates with a 30 cm^{-1} optical bandwidth without modulation, but the spectrum broadens to 50 cm^{-1} when RF power is injected at the roundtrip frequency of the laser. This experiment demonstrates that RF injection not only stabilizes the FM comb [161], but also optimizes its state and recovers its maximum spectral width, which is determined by the laser gainwidth. To investigate the potential of RF modulation in optimizing the FM comb, we conducted a comprehensive simulation study. The simulation was performed to assess the spectral broadening effect of RF modulation at different modulation depths ($I_{RF}/I_{DC} = 0 - 0.3$), while keeping the values of the Kerr non-linearity constant (70, 87.5, and 105 pm/V^2) and the injection frequency 10 MHz below the cold cavity roundtrip frequency. The results, as illustrated in Figure 6.11, show a consistent pattern across different non-linearity values. As the modulation depth increases to 0.15, the spectral width expands significantly, reaching a stable width of 140 modes. The results demonstrate the potential of RF modulation in optimizing the FM comb and expanding its spectral width. The maximum optical bandwidth achievable through RF modulation is approximately equal to the width of the unlocked state. This conclusion supports previous findings that the spectral width of the FM comb does not surpass that of the unlocked laser [170, 168]. The modulation section is injected above the 3 dB cutoff frequency with an injection frequency of 12 GHz and a loss of 25 dB, as demonstrated in Figure 6.13. In this study, we provided guidelines for the engineering of FM combs for broadband spectroscopic applications. We examined the impact of various cavity parameters on FM combs through numerical models and a proof-of-concept experiment. Our findings indicate that reducing and compensating for GVD alone is not sufficient to attain an optimal frequency comb regime, contrary to prior beliefs. Instead, controlling the intracavity light intensity profile through tuning the laser facet reflectivities is crucial in FM comb formation and can broaden the comb spectra. Additionally, high mirror losses were found to be beneficial. By using a master equation approach, we simulated the response of the FM comb to a strong current modulation around the cavity round trip frequency. The results of our experiment with an

injection-locked, high-performance bifunctional QCL frequency comb demonstrated excellent agreement with the modeled behavior. RF injection was found to be an effective technique for broadening the spectrum of the FM comb, as it enables circumvention of restrictions imposed by laser design. The use of RF modulation for FM comb broadening will further advance the applications of QCLs in dual-comb spectroscopy.

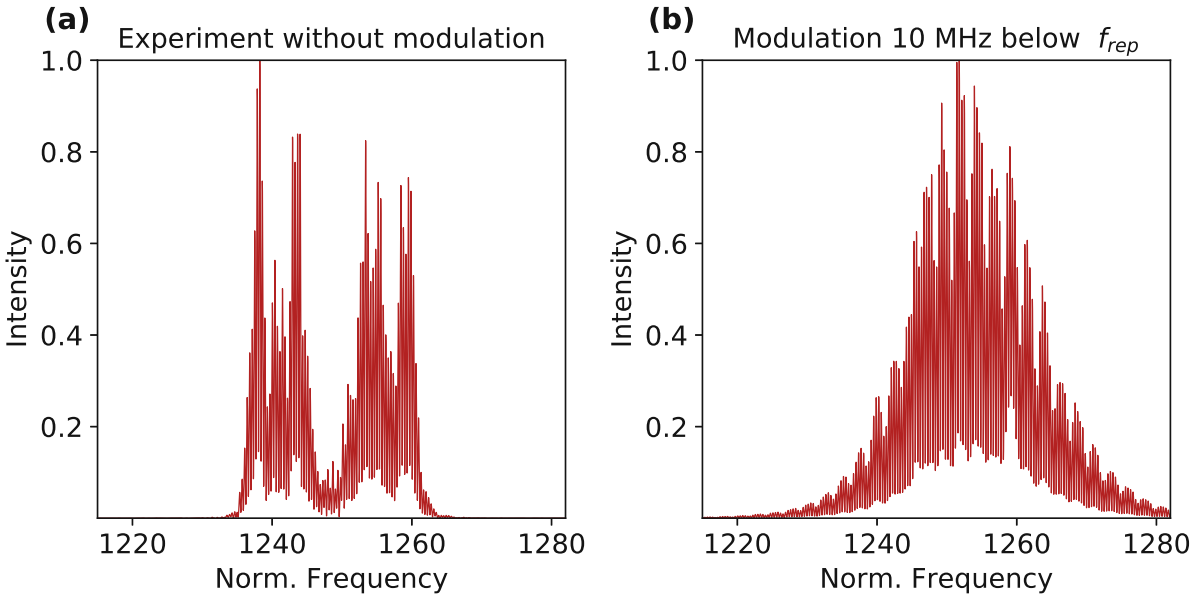

Figure 6.12: Optical spectrum of the FM comb (a) without modulation and (b) Modulation 10 MHz below the repetition frequency. Injection below the roundtrip frequency gave the broadest spectrum. Figure reproduced from [157] with permission of Optica Publishing (2021).

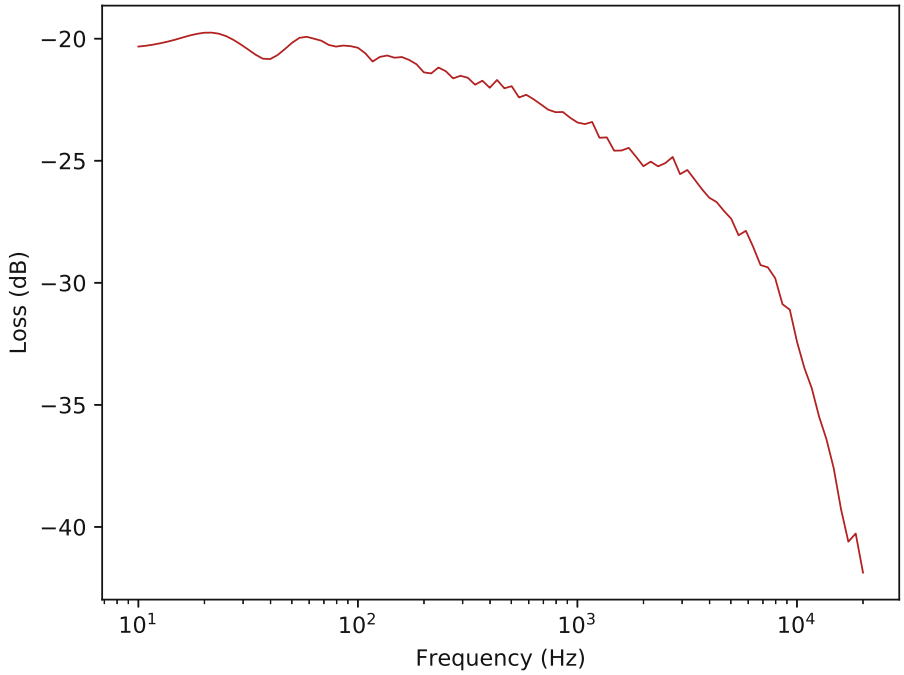

Figure 6.13: Frequency response of the modulation section. The injection frequency of 12 GHz yields a loss of 25 dB. Figure reproduced from [157] with permission of Optica Publishing (2021).

6.3 Growth of high bandwidth terahertz quantum cascade lasers

This section is based on the publication 'Ultra broadband heterogeneous THz Quantum Cascade Laser' [171]. The Terahertz region is a particular interesting spectral region for spectroscopy. THz quantum cascade lasers progressed to become a reliable source as they offer high output powers up to the Watt range [172]. Its non-ionizing nature offers exciting possibilities in medical applications and also security implementations e.g. as body-scanner at airports. An on-going challenge and current object of interest in many research groups is the THz gap between 0.3 and 3 THz. As mentioned QCLs, allow the tailoring of their bandstructure to specific requirements, by adjusting the thickness of wells and barriers. A limit for the operation of compact spectroscopic devices is the width of the emission window. One approach to circumvent this, is the design of multiple stacked units for a specific emission wavelength to get a broadband THz QCL emission spectrum [173], [174], [175]. This specific stack owns a defined emission profile. Heterogeneous QCLs consist of different unit cell designs on top of each other, the sub-stacks. Engineering such heterogeneous QCLs can be challenging. The current propagating through the device has to match the lasing threshold of every sub stack it passes. From an engineering perspective

the knobs for adjustment are doping and well thickness. A common method is to adjust the injector regions accordingly to align the energy levels and tune the doping of the wells to align the lasing thresholds. Our work lead to an ultra-broadband QCL, covering a full octaves and therefore ranging over basically the full emission range of current THz QCls is discussed. Originated from mid-infrared QCLs [176], the initial concept span over 1.1 to 5 THz. An ultrabroadband THz QCL could enable applications for spectroscopy or microelectronics as amplifier.

Active region design The introduced THz QCL active region consists of a stacked 3-well LO-phonon depopulation design utilizing a GaAs substrate. The laser design is based on a temperature-optimized THz QCL structure [65], with intersubband transitions at 3.3 and 3.8 THz. The designed laser was optimized for high-temperature operation up to 196 K [70] with a dynamic range of 72%. The stack of 5 different THz QCL designs on top of each other could be harmed by electrical instabilities. In order to lower this behaviour to a non-significant magnitude, we aligned the injector energy levels with the extractor energy levels. The optical transitions of every stack from level 3 to level 2 depopulate by LO-phonon emission to level 1. The electrons get then injected to the next levels. However, the lasers design constitues five substacks with different emission wavelengths for every substack. The substacks were stapled in a ABCDE combination, where the wavelength decreases from figure 6.14 shows a scetch of the ABDCE stack and a contacted laser ridge device.

MBE Growth For this project, GaAs was chosen as the material system because of its maturity and well-understood properties. Over time, GaAs-based THz QCLs have achieved numerous milestones, including rising maximum operation temperatures, color switching, and studies of barrier heights. These advancements led to the demonstration of thermoelectric cooled THz QCLs [70, 177]. To maintain the high quality of the crystal structures, triple-axis high-resolution X-ray diffraction (HRXRD) was performed and the result is shown in figure 6.15.

Region	Periods	Emission frequency
A	52	4.4 to 3.9 THz
B	56	4.2 to 3.8 THz
C	58	3.8 to 3.3 THz
D	62	3.4 to 2.7 THz
E	66	3.3 to 2.4 THz

Table 6.1: Number of periods of the five different sub-stacks and their correlating, centered emission frequencies. The number of periods results from the measurements of the single-stack testing active regions and the adjustment to normalize the gain.

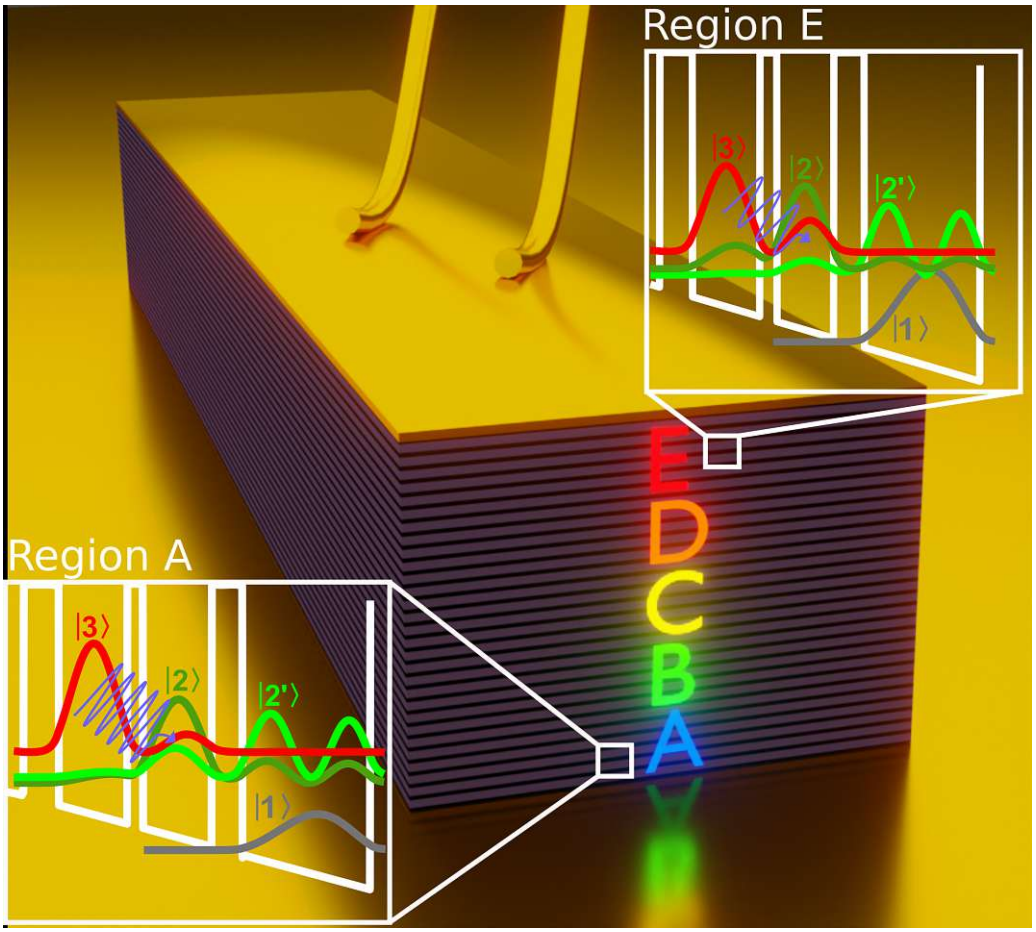

Figure 6.14: Schematic double-metal waveguide ridge device. The insets highlight the optical transitions from the upper lasing level 3 to the lower lasing level 2. Level 1 is the injector state for the next period. Figure reproduced from [171] with permission of ACS (2022), Copyright CC BY-ND 4.0.

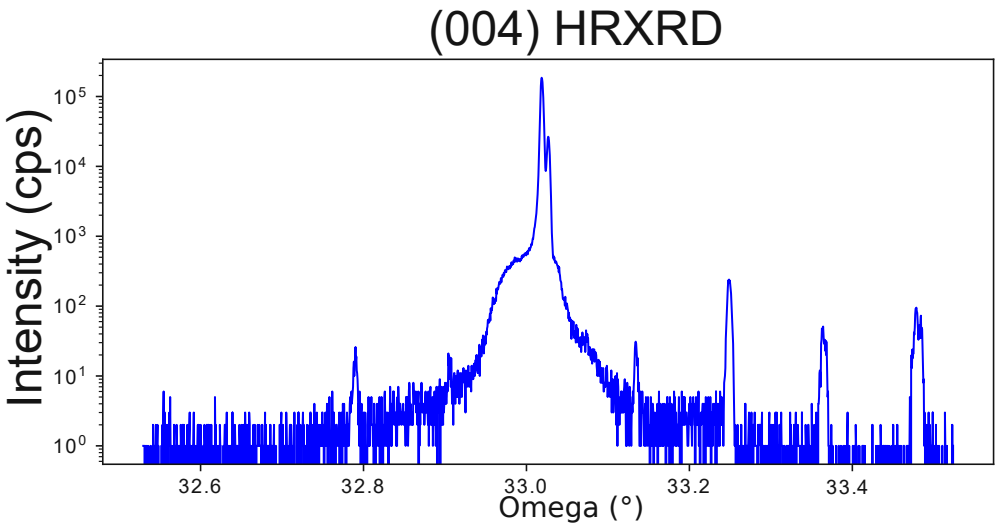

Figure 6.15: (004) XRD scan of the fully stacked active region.

The growth of the THz QCL was accomplished using the Riber Compact 21 molecular beam epitaxy (MBE) system on n+ GaAs (100) substrates to ensure high crystal quality. The quality of the crystal was confirmed by Triple-axis high-resolution X-ray diffraction (HRXRD) measurements. The design process entailed multiple iterations due to deviations in the initial light-current-voltage (LIV) curve. The lasing threshold was altered by each stacked active region, necessitating adjustments to prevent absorption. Separate single-stack active regions (A, C, and E) were grown to obtain information regarding the current densities at the maximum signal and emission wavelengths. Based on the LIV measurements of the single-stacks, the design and doping of each sub-stack were altered to achieve the desired wavelengths at equivalent current densities. The doping of sub-stacks B and D was also modified to match current densities at maximum signal. Subsequently, the final ABCDE structure (C1107) was grown after further iteration with minor adjustments to sub-stacks B and D to optimize the emission wavelength. The number of periods per sub-stack was adjusted to normalize gain for all five designs based on the output power from single-stack measurements. The thickness of the final active region was 13 µm.

Performance The fabrication process of the THz QCL involved the formation of double-Metal waveguides for enhanced optical confinement and minimal loss. The grown structure was flip-chip bonded onto a n+ GaAs substrate through Au-Au thermo-compression bonding, followed by substrate removal via polishing and wet etching (HCl). The ridge geometry was defined through optical lithography and dry etching, and the final chip was metallized with TiAu metal layers of thicknesses 100 nm and 200 nm for top and bottom contacts, respectively. The sample was then electrically connected through indium soldering and attached to the coldfinger of a He flow cryostat.
The laser was driven either by a voltage pulse generator (AVTECH AVR-3HF-B) or a DC source-measurement-unit (Keithley 2602A). The emitted light was focused into a FTIR spectrometer (Bruker Vertex 80) with a resolution of 2.25 GHz, and spectra were recorded using an internal DGTS detector. The thermal output power was measured using a thermopile detector (Dexter 6M) integrated into the cryostat housing. The results of the optical and electrical characterization are presented in Figure 6.16.

The maximum operating temperatures of the laser devices in this project were determined to be 143 K in pulsed operation and 58.5 K in continuous wave (CW) mode. All laser devices used in this study operated in CW mode. The characteristic kinks observed in the light-current-voltage (LIV) curve, shown in Figure 6.16, are a result of the onset of photon-assisted transport, induced by the staggered start of emission from the sub-stack active regions. The sub-stack active regions were designed to match the current densities at the maximum output power, resulting in varying dynamic ranges and kinks in the LIV. The key outcome of the project is presented in Figure 6.17, which shows the broad emission spectra spanning from 1.9 to 4.5 THz, covering an optical octave. The overlapping of

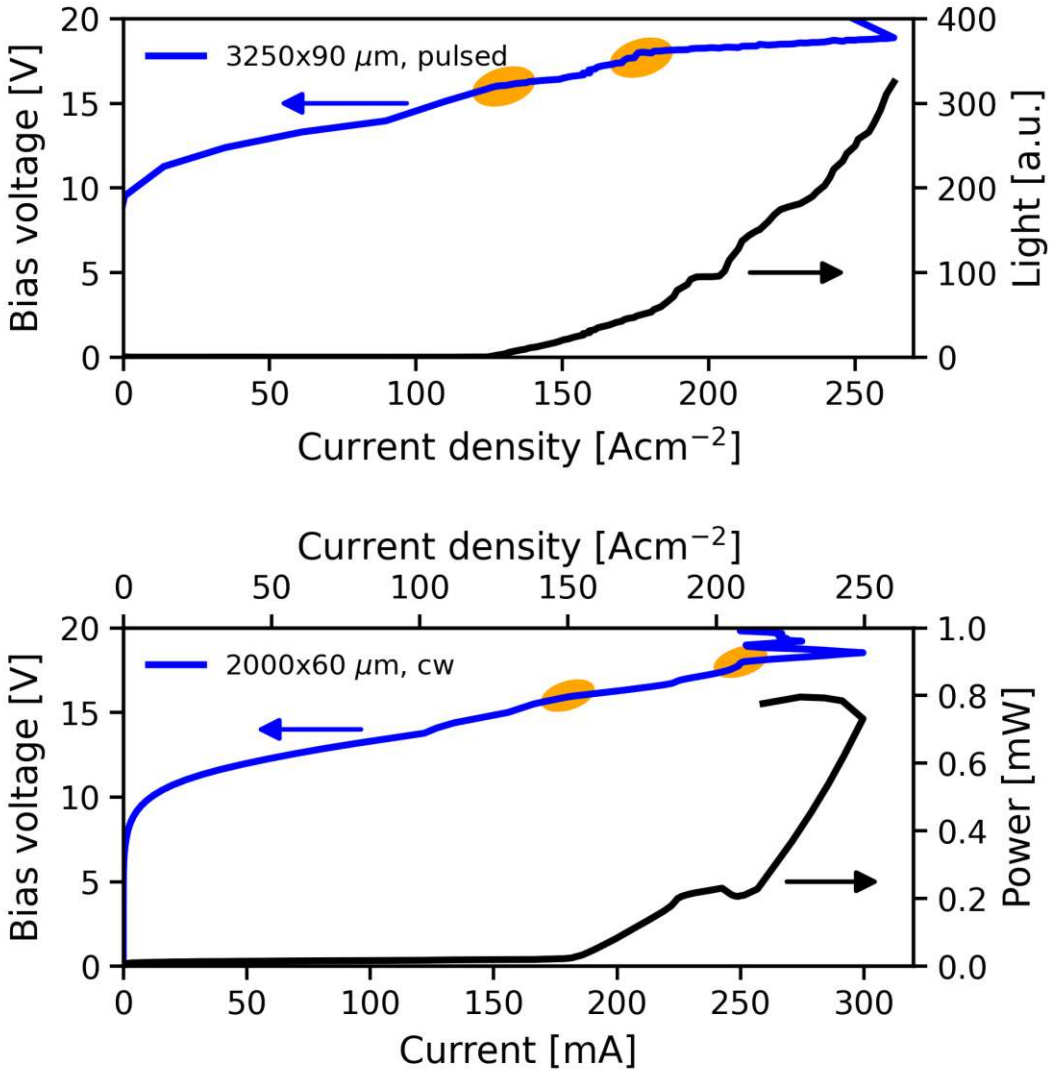

Figure 6.16: Light-current-voltage (LIV) curves of two devices in (top) pulsed and (bottom) CW operation. The heat sink temperature for both measurements was 5 K. The highlighted ares underline the kinks due to photon driven transport. Figure reproduced from [171] with permission of ACS (2022), Copyright CC-BY.

the gain spectra of the sub-stacks results in the stimulation of active regions with lower gain, leading to the ultra-broad emission window.

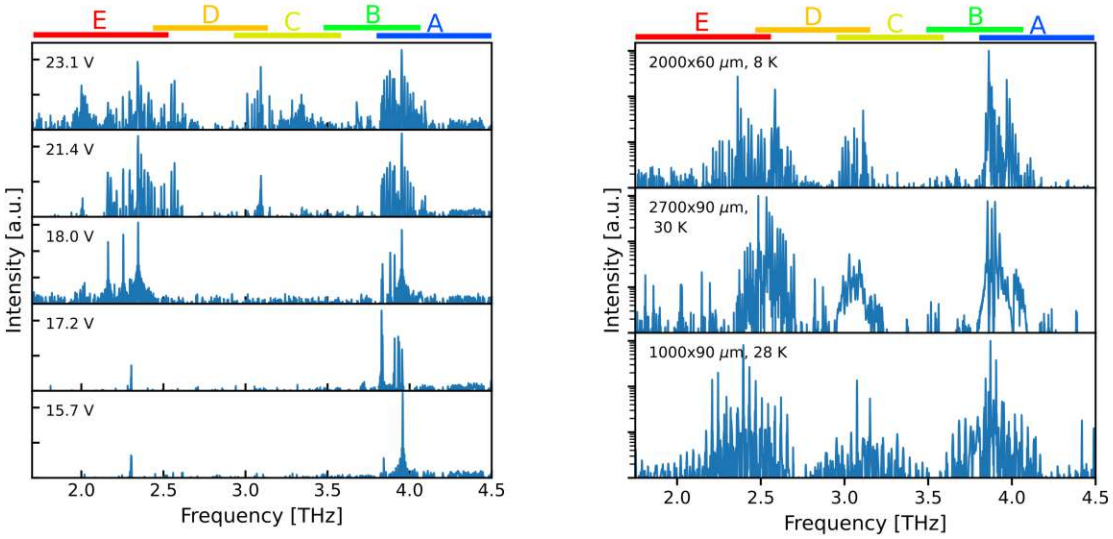

(a) (b)

Figure 6.17: (a) The mode evolution in pulsed operation was studied for a 2 mm long and 60 µm wide ridge device at a heat sink temperature of 5 K. Results showed that as the bias voltage or current increased above the threshold, the modes at the edges of the gain region began to lase. The spectrum broadened as the bias was further raised, resulting in emission that covered the entire gain region between 1.9 and 4.5 THz. (b) The broadband spectra of three differently sized devices in continuous wave (CW) operation were also analyzed. The results showed that the devices exhibited emission over the entire gain region in CW operation. The spectra of the ridge devices with dimensions of 2000x60 µm, 2700x90 µm, and 1000x90 µm were measured at heat sink temperatures of 28 K, 30 K, and 8 K, respectively. The colored bars on top indicate the frequency range of each sub-stack, respectively. The y-axis is shown in log-scale. Figure reproduced from [171] with permission of ACS (2022), Copyright CC-BY.

Outlook In conclusion, the heterogeneous THz quantum cascade laser (QCL) developed in this project features a unique five-active-region design based on a three-well LO-phonon depopulation scheme. The device showcases broad emission across a frequency range of 2.6 THz, spanning from 1.9 to 4.5 THz, in both pulsed and continuous wave operation. The maximum output power measured in CW mode was 800 mW and the maximum operating temperature was 58.5 K in CW and 143 K in pulsed operation, which are record-high values for heterogeneous THz QCLs. This design presents a combination of the high-temperature operation characteristics of the three-well design and the ultra-broadband emission capabilities.

6.4 Ring combs

As alternative to ridge-type waveguides, ring resonators can be used as cavity for quantum cascade lasers. A ring resonator is symmetric and ideally bares outcoupling points. Therefore either a standing-wave pattern is formed in the cavity or - if present - cavity defects allow for light emission (outcoupling). The standing wave pattern of the first lasing mode induces a spatially different gainshape, which is referred to as spatial hole burning (SHB). In Fabry-Perot semiconductor lasers, specific side modes own a abetter spatial overlap with the SHB pattern and exceed the lasing threshold. The ring cavity owns uniddirectional operation, so clockwise or counterclockwise modes can lase. The unidirectionality of the lasing does not give the SHB pattern and the laser should operate in theory in single-mode. Experiments showed surprising results in mid-IR QCLs [178], where multimode operation was observed, soon afterwards also in THz ring QCLs the same behaviour was reported [133, 179]. This instability mechanism was explained brilliantly within the framework of the complex Ginzburg-Landau formalism [180] The exciting result is the connection of semiconductor laser physics with a potential soliton generation on a compact, electrically-pumped frequency comb platform. Our work was published as 'Frequency combs induced by phase turbulence' [156], and the same devices were used for 'Defect-engineered ring laser harmonic frequency combs' [155]. A more in depth and detailled examination of the research results is given there as well. It should act here as examples of the work performed in this thesis. In the paragraph below two specific research highlights are presented based on high-performance fabrication of mid-IR QCL frequency combs, asides from my contribution as a grower to related projects in THz QCLs [133, 179]. The main challenge was to achieve a high resolution of the defect feature with the lithography equipment in the CMNS cleanroom. The resolution of the mask aligner and the mask were beyond challenging. It required a step by step iteration to get to the right parameter space, where the resist stayed on the material sample, and the resist could be developed deep enough without harming the ring geometry. Frequently the resist got overdeveloped and stripped the whole resist layer, or did not develop the feature in a sufficient resolution. The solution was an exposure break before the last third of the development time.

6.4.1 Defect engineered ring lasers

A particular exciting result of high-performance frequency comb fabrication was the defect engineered comb operation of ring QCLs. The initial proposal and project goal was the measurement of harmonic comb states in ring QCLs. As outcoupling mechanism we intended to use a defect in the ring cavity. Over multiple iterations the resulting device displayed not only the comb state, it also showed phase turbulence combs in ideal rings without any defect or slit. The underlying physical principle is governed by the complex

Ginzburg-Landau equation. The resulting measurements by Piccardo et al. [156] allowed the connection of semiconductor lasers with microresonator frequency combs, an impactful insight in the scientific community. Early on the fabrication appeared to be the bottle neck before measurements could even take place. As mentioned above, the main issue was the slit width aside from multiple struggles with non functioning sputtering machines, crystallized flakes in the resist that required the and tested before usage, pin holes and poor quality of the silicon nitride passivation layers or simply a lithography glass mask, that had scratches or poor development of the laser writer. During the project time the CMNS cleanroom facilities were move from the old location in the Floragasse to the newly built Gusshaus, obviously inducing time delays and a restart of processing. Nevertheless does successful engineering base on relentless moving forwards and obviously all fabrication problems could be solved. The QCL ring laser was fabricated by standard photo lithography and waveguide definition with dry etching. A 250 nm silicon nitride passivation layer was deposited with PECVD. The metalization consisted of a sputtered 10 nm titanium and 300 nm gold layer on top of the silicon nitride passivation layer. After the metalization step the substrate was thinned to 140 µm for optimal heat dissipation and conductivity. The back contact was a 10 nm titanium, 80 nm gold layer.
It required around 30 iterations to figure out the optimal parameter space for the defect features in the first lithography. It can be stated that the first lithography for the ridge definition is the crucial one. The main problem to solve was the resolution of the slit width with a standard lithography mask and its feature size of below 1 µm over the waveguide depth of 11 µm (Figure 6.18).

The devices of [156] were used for consecutive work in [155]. The devices did fulfil the initial goal to measure harmonic frequency comb states. The initially mentioned connection of solitons with microresonator combs lead to multiple connected research projects. One project aimed to inject Kerr solitons into a QCL racetrack resonator (Figure 6.19). Another publication based on this work is currently pending [181]. Several projects were ignited after this successful demonstration of ring combs.

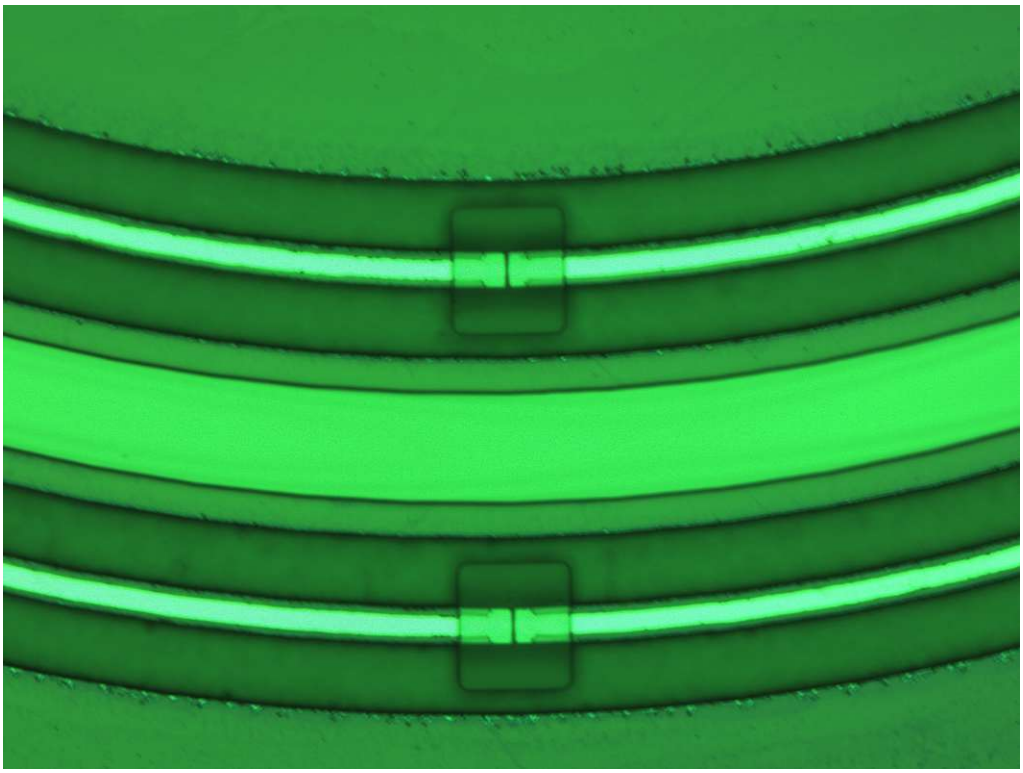

Figure 6.18: Nomarsky microscope picture of the ring laser with the slit feature region. The slit width between the ring laser ends is 1.2 µm.

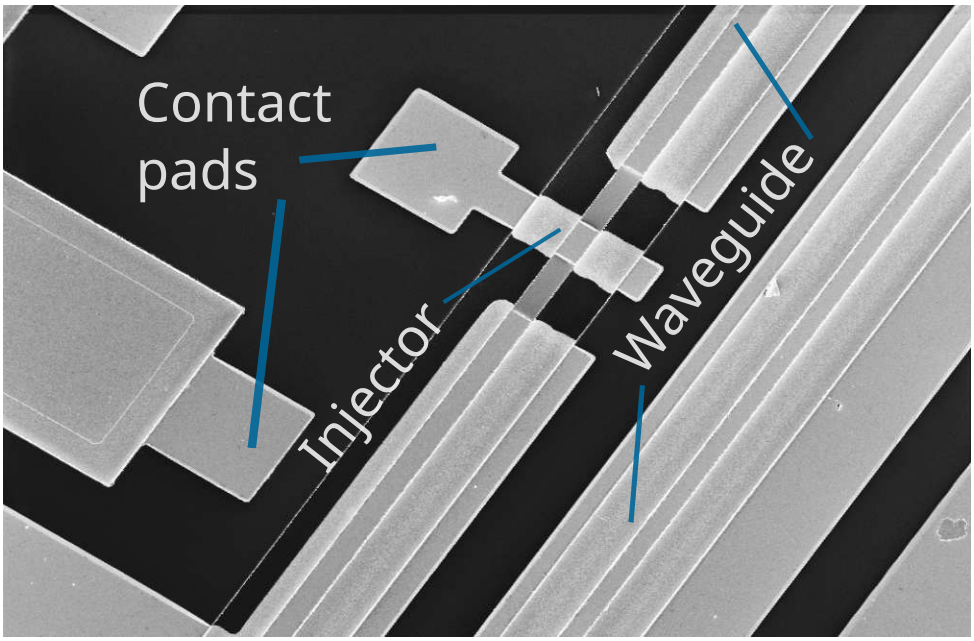

Figure 6.19: SEM micrography of the coupling region for soliton injection. The fabricated devices were used in [181]. The micrography shows the modulator of the racetrack resonator.

CHAPTER

SEVEN

HIGH PERFORMANCE ICL FREQUENCY COMBS

7.1 Interband Cascade Laser frequency combs

Monolithically integrated laser systems operating in the mid-infrared range are a key step towards handheld mobile spectroscopy. The generation of frequency combs with short pulse widths (and therefore wide spectral coverage) will allow the integration of monolithic integration of entire dual-comb spectrometers including frequency comb generators and fast photodetectors on a single chip and overcome the initial limitation to tabletop sized experiments [182]. ICLs are especially favorable for this, the gain profile, i.e. the gain shape, does not necessarily lead to low threshold current. It's rather the large amplitude of the gain, which itself is a consequence of the ns long lifetime of the laser transition and the interband transitions lifetime around one nanosecond leads to lower threshold current densities compared to QCLs. Furthermore, the minimal pulse widths achieved in QCLs are limited due to the upper state lifetime in the picosecond range. In contrast ICLs are excellent candidates for integrated on-chip sensing devices. The lower threshold current densities are a decisive advantage for battery-driven devices. To enable on-chip integration of dual-comb spectroscopy, the frequency comb generation of ICLs needs to be demonstrated and well understood. [53]. Although an experiment with a type-I quantum well cascade diode laser showed emission of 10 ps pulses with a 180 kHz intermodal beatnote and the second-order autocorrelation [183, 184], no experimental proof with a second-order autocorrelation ratio of 8:1 was demonstrated yet. The following chapter summarizes the work regarding ICLs as a potential monolithic platform in the future to enable integrated dual-comb spectroscopy, starting from the first conclusive proof of their operation as frequency comb and the emission of picosecond pulses.

7.2 Monolithic frequency comb platform based on interband cascade lasers and detectors

This section is based on the publication "Monolithic frequency comb platform based on interband cascade lasers and detectors" [21]. The authors contribution was the fabrication and assistance with the measurements.

Dual-comb spectroscopy is a promising approach for mid-infrared spectroscopy because it allows for the direct link between the optical spectrum and the RF domain, enabling high resolution and sensitivity in a compact, integrated format. Unlike Fourier transform infrared (FTIR) spectrometers, dual-comb spectrometers do not require movable parts and can achieve high resolution without sacrificing accuracy. These advantages make dual-comb spectroscopy a valuable tool for a variety of applications in the mid-infrared region, where many molecular fingerprints can be found.

Small systems were developed through the use of difference-frequency generation or passive microresonators that harness the Kerr nonlinearity. ICLs are a more energy-efficient alternative that operate at up to 6 µm. The power consumption of ICLs is one to two orders of magnitude lower than that of QCLs, but their output power and efficiency are approaching the level of QCLs. ICLs offer a monolithic platform for a low-power, highly tunable lasing system that can be designed for specific wavelengths and has potential for dual-comb spectroscopy. The presented research showcases a monolithic frequency comb and an ultra-fast photodetector that is made from the same material.

Frequency-modulated combs using ICLs To study the FM comb states in ICLs, a device was fabricated with a two-part design, consisting of a short modulation section and a long gain section. The short section was optimized to minimize parasitic capacitance and efficiently inject radio-frequency signals. The DC bias applied to the modulation section can be used to precisely adjust group velocity dispersion (GVD). A narrow beat note is a strong indication of frequency comb operation, resulting from the beating of neighboring cavity modes. The intermodal spacing is equidistant and each pair beats at their difference frequency. The beat note can be measured optically with a fast photodetector or indirectly as a periodic modulation of the laser driving current, as shown in Figure 7.1b. SWIFTS was used to verify comb operation by measuring the coherence and phase between each pair of comb lines. The phase pattern provides valuable information, with the intermodal phases displaying a chirped pattern over a range of $2\,\pi$, similar to QCLs. The time domain signals in Figure 7.1e and f show both frequency combs have linearly chirped instantaneous frequencies with suppressed amplitude modulations, indicating four-wave mixing as the governing mechanism [95, 169]. A small amplitude modulation maximizes the round-trip gain in fast-gain media, whereas passive mode-locking in slow gain media requires a slow recovery time and fast saturable absorber. The ICL absorber section is too slow to react

to intermodal beatings. An RF injection technique can be used to stabilize the mode spacing, as shown in Figure 7.2a-c. The beat note is controlled by the RF oscillator in the locking range, which depends on the injected power.

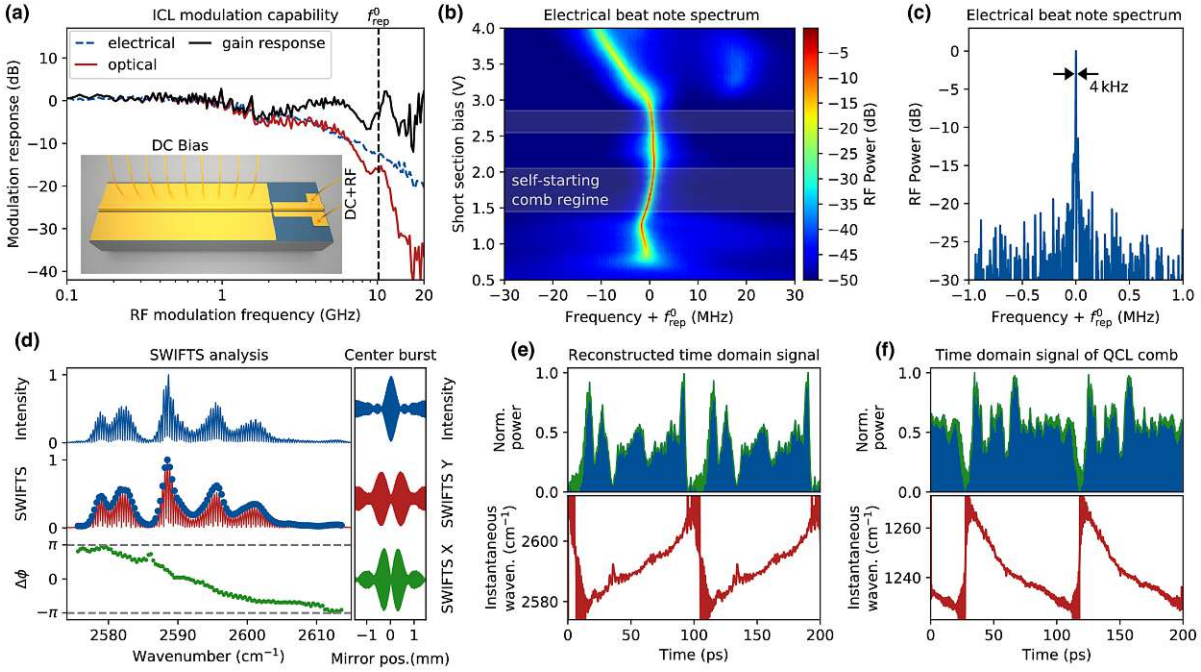

Figure 7.1: ICL frequency comb. (a) FM modulation capabilities of the device with a fast QWIP (b) The modes of the frequency comb spectrum beat with each other resulting in a modulation of the intensity at the cavity roundtrip frequency. This modulation is translated into a modulation of the driving current by the gain medium, which can be measured as electrical beatnote at the short modulation section. (c) Optical beat note with a linewidth of 4 kHz measured on the ICD (d,e) SWIFTS analysis and time domain signal. (f) QCL frequency comb time domain signal, which shows a similar linear chirp as the ICL frequency comb. Figure published in [21] (2019).

Monolithic ultra-fast detectors using ICLs From an engineering point of view, integrating a complete dual-comb spectrometer onto a chip requires both the ability to operate the laser as a comb and to perform heterodyne detection. A more advanced approach is to combine these properties in the same material system as a bi-functional system, resulting in a monolithic lab-on-a-chip. Interband cascade lasers (ICLs) have a step-like density of states, making them well-suited for bi-functional operation as both a laser and detector, without requiring additional design. Figure 7.2d shows the responsivity of an ICL-based detector (ICD) made from the same material. It achieved a broadband responsivity of over 100 mA/W and a noise-equivalent-power (NEP) of 2.5 pW/$\sqrt{Hz}$ at room temperature, which outperforms other bi-functional quantum cascade material. To further demonstrate its capabilities, the ICD was measured optically with the ICL (figure 7.2f), showing a detection bandwidth that enables beat note characterization of the ICL comb with a signal-to-noise ratio of 22 dB at room temperature and a high-frequency

cutoff of around 5 GHz.

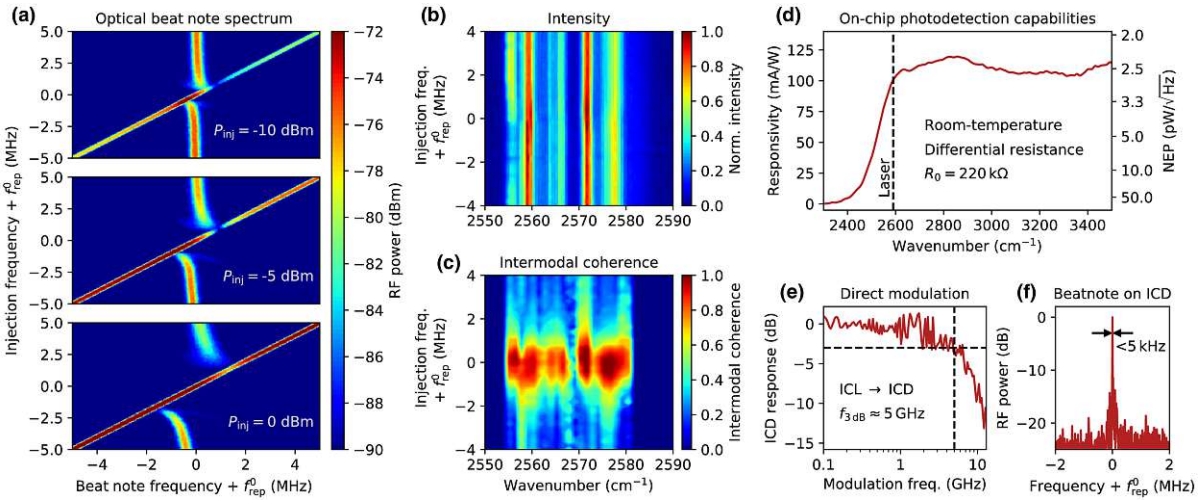

Figure 7.2: Coherent injection-locking and on-chip detection capabilities (a) Optical beat note spectrum for three different injection powers, while the frequency of the injected signal (diagonal line) is swept across the ICL beatnote frequency. (b,c) Intensity and SWIFTS spectral maps at 5 dBm injected power (d) Responsivity and noise-equivalent power of the on-chip interband cascade detector (ICD) (e) Modulation response of the ICL measured with the ICD (f) Narrow beat note measured using the ICD, which was fabricated from the same material as the ICL frequency comb. f_{rep}=10.17 GHz. Figure published in [21] (2019)

Device fabrication and measurement setup The ICLs were fabricated from material grown at the University of Würzburg and nanoplus GmbH. The laser ridges (6 µm wide, 4 mm long) were processed at TU Wien and the Center of Micro- and Nanostructures using photolithography and reactive ion etching. A 350 nm silicon nitride passivation layer and a TiAu metalization layer were deposited. The devices were mounted epi-side-up on a copper block with indium bonding and had a thinned down 160 µm substrate with a TiAu metalization layer on the backside. The mounted samples were stabilized at 15 °C to ensure the stability of the comb, which depends on laser driver noise and temperature stability. The laser was driven by a Keithley source-meter in voltage mode with a first-order low-pass filter (3 dB cut-off frequency around 30 Hz) to smooth the output voltage ripple. Further details can be found in reference [21].

Discussion In conclusion it was demonstrated that ICLs have all the preconditions for mid-infrared integrated on chip sensing solutions. Employing the dual-comb technique would further reduce electrical crosstalk. ICL combs provide all the requirements to enable ultra-compact and battery-driven sensors. The monolithic ICL platform reduces power consumption below 1 W and provides sensitive and high-speed photodetection capabilities. The low power consumption allows future battery-driven sensors with exceptionally sensitive detection capabilities.

7.3 Picosecond pulses from an mid-infrared ICL

This section is based on the publication "Picosecond pulses from a mid-infrared interband cascade laser," Optica 6, 1334-1337 (2019)" [28]. The authors contribution was the fabrication and assistance with the measurements.

In summary, the authors demonstrated a two-section ICL that was capable of generating picosecond pulses with a 6 µm wide and 4 mm long waveguide. The Fabry-Perot cavity was separated into a gain section (3520 µm long) and a modulation section (480 µm long), with the latter designed to lower parasitic capacitances for RF injection. The ICL active region was made up of 6 stages, resulting in a thickness of 350 nm and emitting 4.2 mW at a wavelength of 3.85 µm in continuous wave operation. The laser output power decreased as the modulation section bias was increased. The laser was coated with silicon nitride and titanium and topped with gold. The stability of the comb was dependending on laser driver noise and temperature stability.

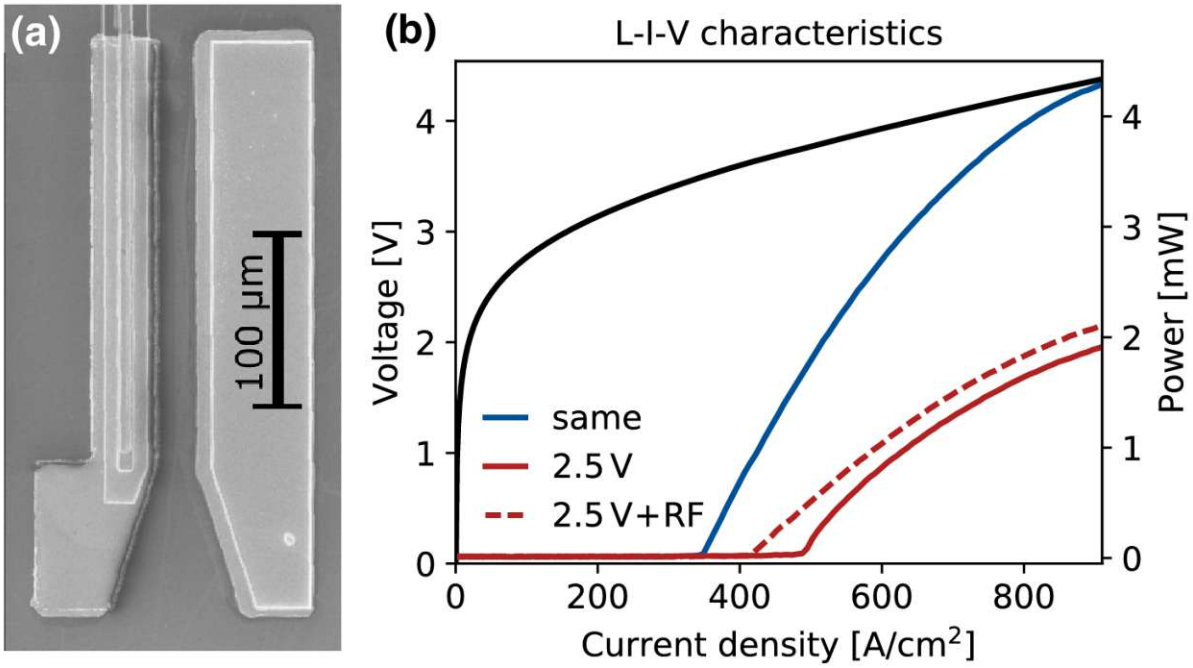

Figure 7.3: (a) SEM micrography of the modulation section optimized for RF injection (b) Light-current-voltage(LIV) curve of the ICL at 15 °C. A modulation section bias of 2.5 V increases the losses. The losses are further decreased by the RF injection at the roundtrip frequency. Figure reproduced from [28] with permission from Optica Publishing (2019).

For characterization of the temporal output intensity and to extract the laser phase relation we employed SWIFTS, a measurement technique explained in more detail in section 2.5.3. To operate the ICL as a frequency comb we modulate the cavity losses by injecting a RF with increasing power in the modulation section (figure 7.4).

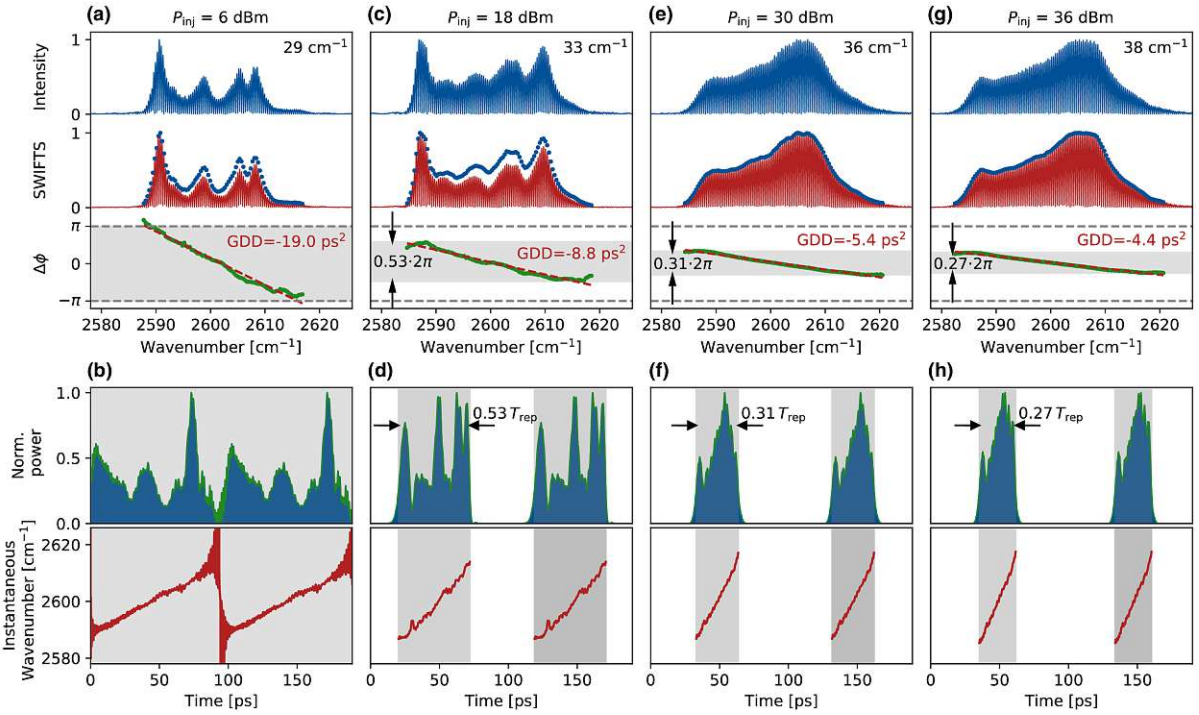

Figure 7.4: SWIFTS characterization of the ICL comb for increasing RF injection power from (a) 6 dBm to (g) 36 dBm. with the correlating GDD below. The intermodal difference phases increase the chirp with the increasing injection power (b) to (h). The normalized power output narrows down to 0.27 times the roundtrip time. The modulation section was biased with 2.5 V , the gain section was pumped with 800 A/cm^2. Figure reproduced from [28] with permission of Optica Publishing (2019).

The laser is operated in cw mode and the injected modulation frequency is slightly detuned from the repetition frequency. With 6 dBm injection power the lasers intermodal difference phases $\Delta\phi$ splay over 2π and the output spectrum consists of multiple lobes of different peak intensities. The reconstructed temporal intensity shows no pulses. Increasing the injection power to 18 dBm narrows the range of $\delta\phi$ down to $\approx \pi$. Doubling the injection power from 18 to 36 dBm leads to a further decrease of the pulse width of an initial multilobe spectrum to a broad single lobe spectrum. The phases approach a nearly constant line at 0, ranging $0.27 \cdot \pi$ and confining the temporal output to $0.27 \cdot T_{rep}$, which correspond to 27 ps pulse width. The final step to minimize the pulse width and maximize the duty-cycle is the detuning of the injection frequency. Sufficient optimization of the parameters lead to the resulting 3.2 ps pulse width (figure 7.5).

The modulation frequency gets detuned by 15 MHz off the free-running laser repetition frequency and injected with 32 dBm. The formerly right leaning spectrum shifts to the right and spreads cohererently over 45 cm^{-1}. The intermodal difference phases are not chirped anymore, the phase range can be considered as small with $0.13 \cdot 2\pi$. The time signal shows a FWHM of 3.16 ps with a peak power of 114 mW. This is by 40 times higher than the average power output of 2.7 mW. Further optimizations of the ICL material and the laser waveguide dispersion will probably even allow the pulse widths below ps.

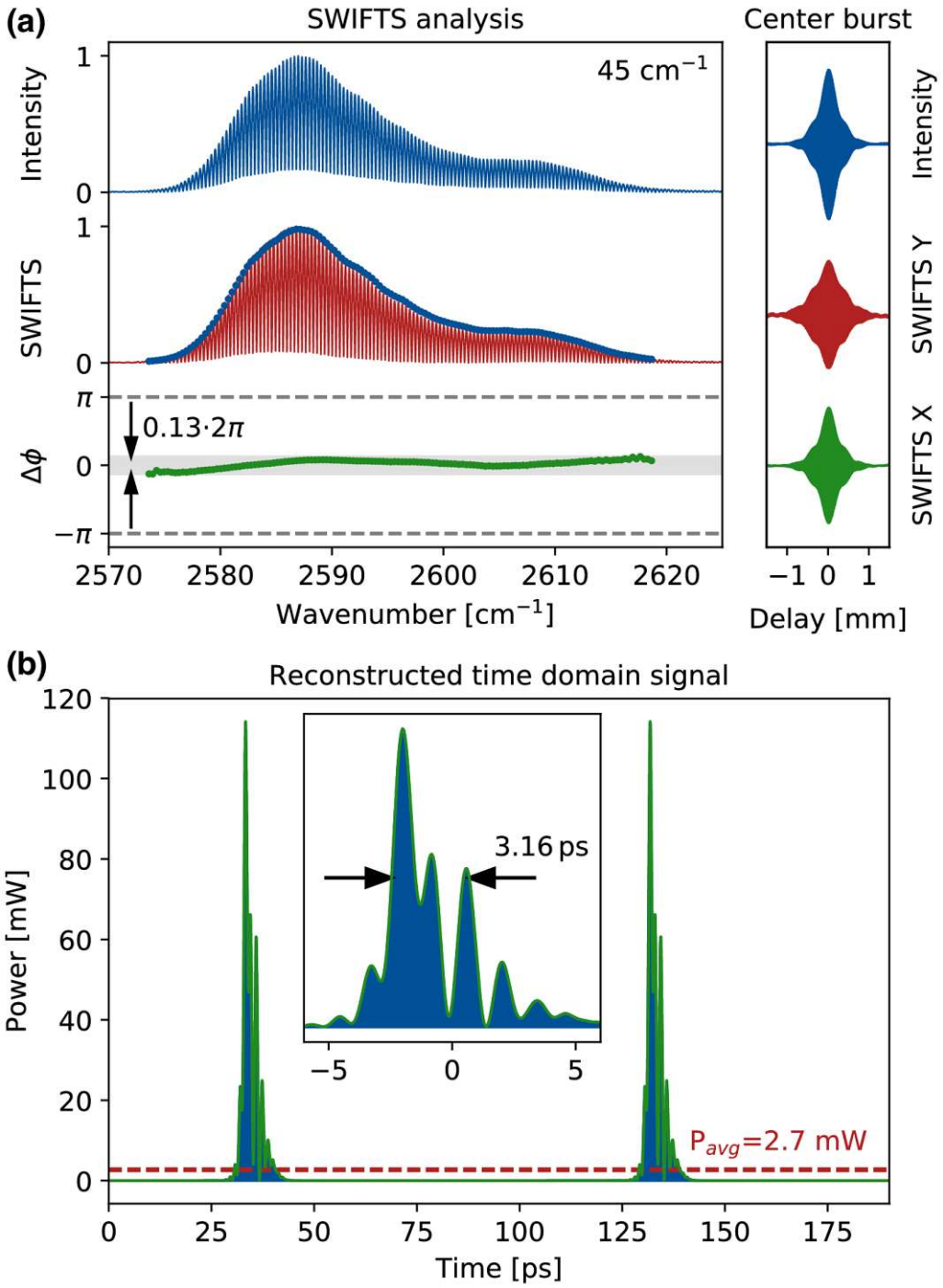

Figure 7.5: (a) SWIFTS characterization for picosecond pulse emission. (b) The reconstructed time domain signal shows the FWHM pulse width of 3.16 ps. Figure reproduced from [28] with permission of Optica Publishing (2019).

CHAPTER

EIGHT

CONCLUSION

Long wavelength ICLs and highly integrated dual-comb spectroscopy systems will pave the way towards on-chip sensing solutions. This work ranged far from numerical studies to fundamental MBE growth how to redesign and engineer ICLs. Over the last couple years, the potential of ICLs as promising monolithic platform was demonstrated, showing their capabilities as sources for frequency combs and high speed detectors [21, 154, 28]. The development and proof-of-principle work about InAs-based heterostructures showed, that ICLs can still be optimized towards a higher degree of freedom to design laser structures. Lowering the cumulative strain opens the window for more active regions at longer emission wavelengths.

The editors pick of the publication "Engineering the spectral bandwidth of quantum cascade laser frequency combs" in Optics Letters showed both the high scientific quality of the published paper and the impact in the community. The provided guideline how to change the bandwidth using straight forward and easy to implement engineering knobs underlines the high usability of RF injection as method of choice. Furthermore it shows the surprising result that the go-to method used for years in the QCL community to change the reflectivity of the facets bears its base, contradicting the consent. Rigorous numeric simulations showed that the small regime where locked laser states appear, consists of a high number of modes. An exciting and outstanding result of this works is the successful realization of an ultrabroadband THz laser. The stacking of 5 different active regions with different emission wavelengths and the rigorous adjustment of every active regions doping lead to this breakthrough. Over the span of 1.37 optical octaves (1.9 to 4.5 THz) the laser emits a high number of optical modes. A scientific highlight is the connection of high performance QCL fabrication with deep theoretical insight about frequency combs, which allowed the combination of both state-of-the-art comb research and chaos theory in close collaboration with our friends in overseas [156, 155].

Outlook I want to conclude this thesis with a short outlook, where this work could lead to and be used as base for further research. The demonstrated novel method to compensate for the cumulative strain in ICLs, should allow the conclusive redesign of the hole injector and replacing the GaSb wells that were used since the beginning with InGaSb layers and aligning the hole energy levels. Furthermore I want to point out that the simulation framework CLAUS is still in a developing phase. It is one of the biggest challenges of III-V optoelectronics to tune sophisticated modelling to be in accordance with the MBE grown material. In the following years it will surely be possible to grow antimonide structures to characterize material properties and optimize the growth parameters with the RIBER C21 MBE. The mounting of a new state-of-the-art antimony cracker will allow to grow layers with a close valve inbetween. Such a technique can enable the next step towards new developments in ICL growth. For El Monstro, possible next steps for further development are the gradual chirped emission of the multistacks active region emission wavelengths and adjusting the doping of the injector levels to the subsequent active region. Further research is encouraged to improve the heterogeneous THz QCL. By increasing the number of active regions and gaining a deeper understanding of the relationship between their respective threshold current densities, it is possible to broaden the emission even further. Furthermore, it would be worthwhile to evaluate the performance of the device using material grown later in the molecular beam epitaxy (MBE) process, as the source material tends to be cleaner towards the end of the campaign. The findings from this project build upon recent breakthroughs from the MIT group [185], and it would be exciting to explore the potential of incorporating the 3-well design into a multi-stack configuration to enhance both operating temperature and broad emission. Potential applications of ultra broadband THz QCLs could be free-space communication, THz imaging and next generation devices for sensing and imaging. In summary the research in the field of integrated frequency combs and photonics is growing in both knowledge and invested capital and can lead to applications for users in our increasingly digitalized world.

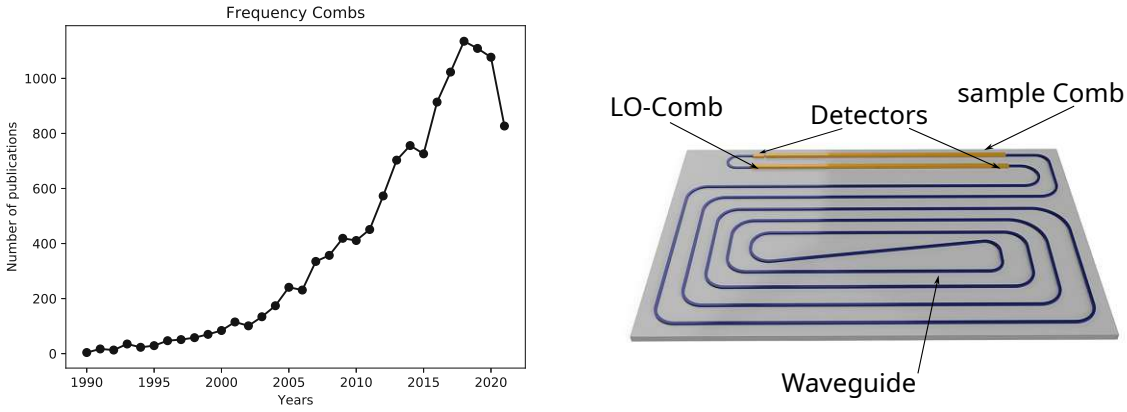

(a) (b)

Figure 8.1: (a) Frequency comb research over the last decades. Data taken from [186]. (b) Exemplary rendered picture of a possible chip geometry with integrated dual-comb spectroscopy and waveguiding all based on the same ICL material.

APPENDIX

ONE

GROWTH SHEETS

This section of the appendix gives an overview over the layer order of the MBE grown samples for the InAs based heterostructure strain compensation, a first ICL structure and the growth of the THZ multistack QCL called "El Monstro".

A.1 C0886 - strain balancing proof-of-concept

7 periods superlattice				
Material	**Thickness (nm)**	**x(%)**	**Doping (cm^{-3})**	**Description**
AlSb	2.0	-	-	-
$In_xAl_{1-x}As$	3.0	70	-	-
InAs	2.0	-	-	-
$In_xGa_{1-x}Sb$	4.6	25	-	-
InAs	2.0	-	-	-
In_xAl_1-xAs	3.5	70	-	-

Table A.1: Growth sheet overview for C0886 strain compensation calibration. The additional InAlAs layer compensates for the AlSb and InGaSb strain.

A.2 C1052 - InGaSb InAs superlattice

8 periods superlattice				
Material	**Thickness (nm)**	**x(%)**	**Doping (cm^{-3})**	**Description**
$In_xGa_{1-x}Sb$	2.5	25	-	-
InAs	7.0	-	-	-

Table A.2: Growth sheet overview for C1052. The needle valve was not closed between layers.

A.3 C1053 - InGaSb InAs superlattice

8 periods superlattice				
Material	**Thickness (nm)**	**x(%)**	**Doping (cm^{-3})**	**Description**
$In_xGa_{1-x}Sb$	2.5	25	-	-
InAs	7.0	25	-	-

Table A.3: Growth sheet overview for C1053. The needle valve was closed between layers.

A.4 C1072 - AlSb InAs double superlattice

50 periods superlattice				
Material	**Thickness (nm)**	**x(%)**	**Doping (cm^{-3})**	**Description**
AlSb	4.4	-	-	-
InAs	3.5	-	-	-
50 periods superlattice				
AlSb	4.4	-	-	-
InAs	5.0	-	-	-

Table A.4: Growth sheet overview for C1072 strain compensation calibration.

A.5 C1074 - ICLBK1

9 periods active region				
Material	**Thickness (nm)**	**x(%)**	**Doping (cm^{-3})**	**Description**
$In_xGa_{1-x}Sb$	2.9	25	-	-
AlSb	1.0	-	-	-
$In_xGa_{1-x}Sb$	2.6	25	-	-
AlSb	1.0	-	-	-
InAs	3.5	25	-	-
$In_xGa_{1-x}Sb$	3.5	25	-	-
InAs	2.9	25	-	-
AlSb	2.5	-	-	-
Si:InAs	2.6	25	2E18	-
AlInAs	3.3	70	-	-
Si:InAs	2.3	25	2E18	-
AlInAs	3.3	25	-	-
Si:InAs	4.9	25	2E18	-
AlSb	2.5	-	-	-

Table A.5: Growth sheet overview for C1074 ICLBK1.

A.6 C1107 - El Monstro, 3 Well, LO-phonon depopulation design, stacked active region

Material	Thickness (nm)	x(%)	Doping (cm^{-3})	Description
SI:GaAs	-	650 ± 20 μm	-	Substrate
GaAs	300	-	-	-
$Al_xGa_{1-x}As$	300	55	-	Etch stop layer
Si:GaAs	70		-	5E18
52 periods active region A				
$Al_xGa_{1-x}As$	4.6	24	-	-
GaAs	8.95	-	-	-
$Al_xGa_{1-x}As$	2.03	24	-	-
GaAs	9.0	-	-	-
$Al_xGa_{1-x}As$	4.0	24	-	-
GaAs	4.0	-	-	-
Si:GaAs	4.12	-	3E16	-
GaAs	8.58	-	-	-
End Loop				
56 periods active region B				
$Al_xGa_{1-x}As$	4.6	24	-	-
GaAs	9.02	-	-	-
$Al_xGa_{1-x}As$	2.07	24	-	-
GaAs	8.84	-	-	-
$Al_xGa_{1-x}As$	4.02	24	-	-
GaAs	4.0	-	-	-
Si:GaAs	4.11	-	3E16	-
GaAs	8.55	-	-	-
End Loop				
58 periods active region C				
$Al_xGa_{1-x}As$	4.6	24	-	-
GaAs	9.2	-	-	-
$Al_xGa_{1-x}As$	2.25	24	-	-
GaAs	8.5	-	-	-
$Al_xGa_{1-x}As$	4.12	24	-	-
GaAs	4.0	-	-	-
Si:GaAs	4.02	-	3E16	-
GaAs	8.48	-	-	-
End Loop				

Table A.6: C01107 - El Monstro, 3 Well, LO-phonon depopulation design, stacked active region

Material	Thickness (nm)	x(%)	Doping (cm^{-3})	Description
62 periods active region D				
$Al_xGa_{1-x}As$	4.6	24	-	-
GaAs	9.38	-	-	-
$Al_xGa_{1-x}As$	2.36	24	-	-
GaAs	8.21	-	-	-
$Al_xGa_{1-x}As$	4.22	24	-	-
GaAs	4.0	-	-	-
Si:GaAs	3.44	-	3E16	-
GaAs	8.95	-	-	-
End Loop				
66 periods active region E				
$Al_xGa_{1-x}As$	4.6	24	-	-
GaAs	9.5	-	-	-
$Al_xGa_{1-x}As$	2.4	24	-	-
GaAs	8.0	-	-	-
$Al_xGa_{1-x}As$	4.28	24	-	-
GaAs	4.0	-	-	-
Si:GaAs	2.86	-	3E16	-
GaAs	9.43	-	-	-
End Loop				

Table A.7: C01107 - El Monstro, 3 Well, LO-phonon depopulation design, stacked active region

APPENDIX

TWO

DEVICE FABRICATION

This chapter of the appendix displays important processing values and data used throughout the fabrication of the devices in this work.

B.1 Fundamental processing steps

B.1.1 Sample Cleaning

The provided samples from the MBE lab are normally cleaved to 10x10 mm. On the sample surface can be dust or small particles which we have to get rid of.

- acetone in ultrasonic bath: 1-2 min with step 1
- rinsing in isopropanol, drying with N_2 gun at the fumehood

B.1.2 Photoresist removal

After dry etching the photoresist needs to be removed.

- acetone in ultrasonic bath: 1-2 min with step 1
- rinsing in isopropanol, drying with N_2 gun at the fumehood

B.1.3 Removal of residual photoresist

Mostly, the photoresist can be removed with acetone. However, in some cases (e.g. after dry etching) parts of the resist harden and will not be removed with simple acetone cleaning. In this case, the residual resist can be burned with an oxygen plasma followed by acetone cleaning. In some cases additional ultrasonic cleaning can help, e.g. for lift-off processes. Some resists, e.g. nLof2070, do not dissolve well in acetone when they are

hardened. Alternative solvents can be used in this case. It has to be noted, that alternative solvents are often much more toxic, e.g. NEP or NMP.

Hardend photoresist removal

- PLOX (oxygen plasma): 5–15 min @ 300 W
- acetone or other solvent (maybe in ultrasonic bath with 60 s @ 10%)
- rinsing in isopropanol, drying with N_2

B.1.4 Deposition of silicon nitride

Silicon nitride can serve as hard mask material or passivation layer for electrical insulation. The etching process for the waveguide definition of the laser would etch the photoresist away before the waveguide depth is reached. Therefore a hardmask of silicon nitride is used. Furthermore we employed a two step deposition process for the passivation layer with layer thicknesses of 250-300 nm and the thick insulation layer of 1200 nm for the modulator section within the laser frequency comb fabrication. The deposition takes place with plasma enhanced chemical vapour deposition (PECVD). Precursor gases are ignited to form a plasma that reacts on the surface to form a layer.

$$3SiH_4 + 4NH_3 \rightarrow Si_3N_4 + 12H_2 \tag{B.1}$$

The deposition thickness is determined with the Filmetrix. The table temperature can be lowered to 275 for InP based materials, in the past this showed to suppress pin hole formation in the SiN layer. **Recipe:**

Oxford Plasmalab 80 plus
$p_{work} = 1.33$ mbar,
$p_{base} = 0.08$ mbar,
gas flow 700 sccm SiH_4N_2 (2%), 18 sccm NH_3,
10 W RF power, $T = 275/300$ °C,
typical deposition rate 9.12 nm/min

B.1.5 Dry etching with reactive ion etching (RIE)

Etching of lithography patterns into the semiconductor material can be done with either wet or dry etching. In this work mostly dry etching with RIE was used. A The SiN layer was etched with a CHF process. The SiN layer removal was done with a SF6 process. The QCL material was etched with the InGaAs/InAlAs recipe. The ICL material was etched with the Cl_2/Ar recipe.

B.1.6 Metalization layer deposition

The electrical contacting of lasers necessitates a metalization layer, which was deposited on the sample using a vonArdenne magnetron sputtering system. The underlying principle of sputtering is the physical ejection of target particles by a plasma. For all samples, the metalization layer consisted of a thin layer of titanium (10-20 nm) and 250-300 nm of gold. An important step is the removal of oxide on the titanium target, and the number and duration of gold deposition steps can affect the soft baking of the lift-off resist, potentially leading to failed fabrication runs. To address this, the duration was reduced from 40 s to 15 s for high-performance devices during this study. The sputtering recipe varies for top and back contacts, with back contacts not requiring any lithography, thereby allowing deposition without consideration of heating after substrate thinning, resulting in longer deposition steps than for top contacts.

Sputter recipe for Ti/Au top contacts: pbase=2×10^{-5} mbar pwork=8×10^{-3} mbar

- Ti oxide removal 60s @ 100 W RF
- Ti 4x30s @ 25 W RF ($\sim$ 5 nm/min)
- Au 35x15s @ 25 W RF ($\sim$ 30 nm/min)

Sputter recipe for Ti/Au back contacts:
pbase=2×10^{-5} mbar pwork=8×10^{-3} mbar

- Ti oxide removal 2x60 s @ 100 W RF
- Ti 2x60s @ 25 W RF ($\sim$ 5 nm/min)
- Au 8x60s @ 25 W RF ($\sim$ 30 nm/min)

B.1.7 Electrochemical plating on the metalization layer

In order to fabricate high performance laser frequency combs we also examined the electrochemical plating of gold on the sample. Sputtering layer thicknesses beyond 500 nm is not desirable as it demands high machine times and wastes a lot of target material. A convenient method to deposit thick layers of gold is electroplating. The metalization lithography intends to protect the already processed and metalized laser waveguide structures. A small area close to the sample edge gets clamped onto the plating mount and then put into the electrolyte solution.

B.1.8 Lithography

Lithography is employed to transfer the mask pattern onto the sample, and high-quality lithographies are characterized by cleanliness and the use of clear solvents. This work was hampered by the lack of either of these factors in multiple fabrication runs. It is advisable

to verify the expiration dates of developers and solvents before using them, and glassware should be oven-baked and replaced after one year. Resists should be refrigerated if not in use, and individuals performing the lithography should shave before processing and avoid bending over the sample. Standard recipes for the resists utilized in this study are provided, with exposure times specified for the SÜSS MicroTec MJB-4 mask aligner. The hardmask definition was accomplished with the AZ5214 resist, the maP1275 resist was employed as a thick resist for passivation layer etching, and the nLof2070 was utilized for the lift-off lithography of the metalization.

Resist AZ5214

- sample cleaning
- short evaporation bake on the hot plate, 1min at 100C
- spin coating: photoresist AZ5214 (QCL group, AZ5214 program) (1:0), 35 s @ 8000 rpm
- soft bake: 1 min @ 100 °C
- edge remove: 50s
- developing: 726MIF (1:0), 30 s and rinsing in water
- drying with N_2-gun
- structure exposure: 5.5 s
- developing: 726 MIF (1:0),16-21 s, rinsing in water
- drying with N_2-gun

Resist maP1275

- sample cleaning
- spin coating: photoresist maP1275 (1:0), 35 s @ 8000 rpm
- baking: 5 min @ 100 °C
- exposure: removing of the edges, 50 s
- developing: maD331 (1:0), 100 s, rinsing in water, drying with N_2
- exposure: particular structure, 10s
- developing: maD331 (1:0), 40–60 s, rinsing in water
- drying with N_2-gun

Resist nlof2070

- sample cleaning
- spin coating: photoresist nLof2070 (1:0), 35 s @ 8000 rpm, spinner program 'HMDS'
- baking: 5 min @ 100 °C
- exposure: particular structure, 7 s
- baking: 56s @ 110 °C, very important to hit the target time
- developing: AZ726MIF, 80s
- drying with N_2-gun

B.2 Device recipes

B.2.1 Ring QCLs

- initial sample cleaning
- trenches/ridge waveguide:
  1.2–1.5 µm SiN hardmask deposition
  AZ5214 standard lithography
  SiN hardmask dry etching with CHF_3
  photoresist removal
  InAlAs/InGaAs/InP dry etching with SiCl4
  SiN hardmask removal with SF_6
- electric insulation:
  400 nm SiN depostition
  maP 1275 standard lithography
  SiN dry etching with SF_6
  photoresist removal
- top contact:
  oxide removal
  maP1275 standard lithography (neg. mask)
  Ti/Au (10 nm/300 nm) sputter deposition
  lift-off
- sample cleaving (typically 2-4 mm long)
- mounting on copper plates with InP
- wire bonding

B.3 High performance ICLs frequency combs

- initial sample cleaning
- trenches/ridge waveguide:
  1.2–1.5 µm SiN hardmask deposition
  AZ5214 standard lithography
  SiN hardmask dry etching with CHF_3
  photoresist removal
  InAlAs/InGaAs/InP dry etching with SiCl4
  SiN hardmask removal with SF_6
- electric insulation:
  400 nm SiN depostition
  maP 1275 standard lithography
  SiN dry etching with SF_6
  photoresist removal
- top contact:
  oxide removal
  maP1275 standard lithography (neg. mask)
  Ti/Au (10 nm/300 nm) sputter deposition
  lift-off
- sample cleaving (typically 2-4 mm long)
- mounting on copper plates with InP
- wire bonding

B.4 Fast Interband Cascade Detectors

- initial sample cleaning
- trenches/ridge waveguide:
  1.2–1.5 µm SiN hardmask deposition
  AZ5214 standard lithography
  SiN hardmask dry etching with CHF_3
  photoresist removal
  InAlAs/InGaAs/InP dry etching with SiCl4
  SiN hardmask removal with SF_6

- electric insulation:
  400 nm SiN deposition
  maP 1275 standard lithography
  SiN dry etching with SF_6
  photoresist removal

- top contact:
  oxide removal
  maP1275 standard lithography (neg. mask)
  Ti/Au (10 nm/300 nm) sputter deposition
  lift-off

- sample cleaving (typically 2-4 mm long)

- mounting on copper plates with InP

- wire bonding

B.4.1 Lift-off process

The lift-off process is a frequently employed technique for depositing thin structured layers, which involves using a photoresist layer as a sacrificial layer patterned with an inverted structure. A target material layer, such as a metal contact, is deposited onto the patterned sacrificial layer. The remaining sacrificial layer is then removed, resulting in the partial lifting off of the target material, leaving it only in regions where it has direct contact with the sample surface. A major challenge of this process is the deposition of target material on the sidewalls, which can hinder the lift-off process or cause the formation of residual edges. To address this issue, negative or dual resist recipes are commonly employed for thicker layers, which enable an undercut to prevent sidewall deposition during sputter processes.

BIBLIOGRAPHY

[1] L. S. Rothman, I. E. Gordon, Y. Babikov, A. Barbe, D. C. Benner, P. F. Bernath, M. Birk, L. Bizzocchi, V. Boudon, L. R. Brown, A. Campargue, K. Chance, E. A. Cohen, L. H. Coudert, V. M. Devi, B. J. Drouin, A. Fayt, J.-M. Flaud, R. R. Gamache, J. J. Harrison, J.-M. Hartmann, C. Hill, J. T. Hodges, D. Jacquemart, A. Jolly, J. Lamouroux, R. J. LeRoy, G. Li, D. A. Long, O. Lyulin, C. Mackie, S. T. Massie, S. Mikhailenko, H. S. M"uller, O. Naumenko, A. Nikitin, J. Orphal, V. I. Perevalov, A. Perrin, E. R. Polovtseva, C. Richard, M. A. H. Smith, E. Starikova, K. Sung, S. Tashkun, J. Tennyson, G. C. Toon, Vl. G. Tyuterev, and G. Wagner. The hitran 2012 molecular spectroscopic database. *Journal of Quantitative Spectroscopy and Radiative Transfer*, 130:4–50, 2013. – cited on page 2.

[2] K. Wörle, F. Seichter, A. Wilk, C. Armacost, T. Day, M. Godejohann, U. Wachter, J. Vogt, P. Radermacher, and B. Mizaikoff. Breath analysis with broadly tunable quantum cascade lasers. *American Chemical Society (ACS)*, 85(5):2697–2702, February 2013. – cited on page 3.

[3] J. Faist, C. Gmachl, F. Capasso, C. Sirtori, D. L. Sivco, J. N. Baillargeon, and A. Y. Cho. Distributed feedback quantum cascade lasers. *Applied Physics Letters*, 70(20):2670–2672, May 1997. – cited on pages 3 and 4.

[4] C. R. Webster, P. R. Mahaffy, S. K. Atreya, G.J. Flesch, M. A. Mischna, P. Meslin, K. A. Farley, P. G. Conrad, L. E. Christensen, A. A. Pavlov, J. Martín-Torres, M. Zorzano, T. H. McConnochie, T. Owen, J. L. Eigenbrode, D. P. Glavin, A. Steele, C. A. Malespin, P. D. Archer, B. Sutter, P. Coll, C. Freissinet, C. P. McKay, J. E. Moores, S. P. Schwenzer, J. C. Bridges, R. Navarro-Gonzalez, R. Gellert, and M. T. Lemmon. Mars methane detection and variability at gale crater. *Science*, 347(6220):415–417, January 2015. – cited on pages 3 and 5.

[5] T. H. Maiman. Stimulated optical radiation in ruby. *Nature*, 187(4736):493–494, August 1960. – cited on page 3.

[6] A.Y. Cho and J.R. Arthur. Molecular beam epitaxy. *Progress in Solid State Chemistry*, 10:157–191, 1975. – cited on page 4.

[7] C. Gerl, S. Schmult, H.-P. Tranitz, C. Mitzkus, and W. Wegscheider. Carbon-doped symmetric GaAs/AlGaAs quantum wells with hole mobilities beyond 106cm^2/Vs. *Applied Physics Letters*, 86(25):252105, June 2005. – cited on page 4.

[8] R. F. Kazarinov and R. A. Suris. Possibility of the amplification of electromagnetic waves in a semiconductor with a superlattice. *Fiz. Tech. Poluprovodn.*, 5(4):707, 1971. – cited on pages 4 and 27.

[9] F. Capasso. Avalanche photodiodes with enhanced ionization rates ratio: Towards a solid state photomultiplier. *IEEE Transactions on Nuclear Science*, 30(1):424–428, 1983. – cited on pages 4 and 27.

[10] F. Capasso, K. Mohammed, and A. Y. Cho. Sequential resonant tunneling through a multiquantum well superlattice. *Applied Physics Letters*, 48(7):478–480, February 1986. – cited on pages 4 and 27.

[11] J. Faist, F. Capasso, D. L. Sivco, C. Sirtori, A. L. Hutchinson, and A. Y. Cho. Quantum Cascade Laser. *Science*, 264(5158):553–556, 1994. – cited on pages 4 and 27.

[12] C. Gmachl, F. Capasso, D. L. Sivco, and A. Y Cho. Recent progress in quantum cascade lasers and applications. *Reports on Progress in Physics*, 64(11):1533–1601, oct 2001. – cited on pages 4 and 27.

[13] R. Q. Yang. Infrared laser based on intersubband transitions in quantum wells. *Superlattices and Microstructures*, 17(1):77–83, 1995. – cited on pages 4, 5, and 31.

[14] Opačak N. *Theory and modelling of FM semiconductor laser frequency combs*. TU Wien, 2022. – cited on pages 4 and 52.

[15] C. Pflugl. High-power continuous-wave quantum-cascade lasers at room temperature. *SPIE Newsroom*, 2008. – cited on page 5.

[16] C. H. Lin, R. Q. Yang, D. Zhang, S. J. Murry, S. S. Pei, A. A. Allerman, and S. R. Kurtz. Type II interband quantum cascade laser at 3.8 µm. *Electronics Letters*, 33(7):598–599, Mar 1997. – cited on page 5.

[17] I. Vurgaftman, R. Weih, M. Kamp, J. R. Meyer, C. L. Canedy, C. S. Kim, M. Kim, W. W. Bewley, C. D. Merritt, J. Abell, and S. Höfling. Interband cascade lasers. *Journal of Physics D: Applied Physics*, 48(12):123001, 2015. – cited on pages 5, 23, and 32.

[18] R. Q. Yang, L. Li, W. Huang, S. M. Shazzad Rassel, J. A. Gupta, A. Bezinger, X. Wu, S. G. Razavipour, and G. C. Aers. InAs-based interband cascade lasers.

IEEE Journal of Selected Topics in Quantum Electronics, 25(6):1–8, November 2019. – cited on pages 5, 32, 34, 39, 40, and 91.

[19] Y. Li, Z. Song, Z. Li, G. Sun, C. Seng Tan, W. Fan, and Q. Jie Wang. Theoretical design of mid-infrared interband cascade lasers in SiGeSn system. *New Journal of Physics*, 22(8):083061, aug 2020. – cited on pages 5 and 34.

[20] M. Bagheri, Clifford Frez, Lukasz A. Sterczewski, Ivan Gruidin, Mathieu Fradet, Igor Vurgaftman, Chadwick L. Canedy, W. W. Bewley, C. D. Merritt, Chul Soo Kim, Mijin Kim, and Jerry R. Meyer. Passively mode-locked interband cascade optical frequency combs. *Scientific Reports*, 8(1), February 2018. – cited on pages 6 and 46.

[21] B. Schwarz, J. Hillbrand, M. Beiser, A. M. Andrews, G. Strasser, H. Detz, A. Schade, R. Weih, and S. Höfling. Monolithic frequency comb platform based on interband cascade lasers and detectors. *Optica*, 6(7):890, July 2019. – cited on pages 6, 34, 91, 109, 115, 134, 135, 136, and 141.

[22] T. Udem, S. A. Diddams, K. R. Vogel, C. W. Oates, E. A. Curtis, W. D. Lee, W. M. Itano, R. E. Drullinger, J. C. Bergquist, and L. Hollberg. Absolute frequency measurements of the Hg and Ca optical clock transitions with a femtosecond laser. *Physical Review Letters*, 86(22):4996–4999, May 2001. – cited on pages 6 and 41.

[23] T. Hänsch. Nobel lecture: Passion for precision. *American Physical Society (APS)*, 78(4):1297–1309, November 2006. – cited on pages 6, 41, and 43.

[24] T. Udem, R. Holzwarth, and T. W. Haensch. Optical frequency metrology. *Nature*, 416(6877):233–237, March 2002. – cited on page 6.

[25] A. Hugi, G. Villares ans S. Blaser, H.C. Liu, and J. Faist. Mid-infrared frequency comb based on a quantum cascade laser. *Nature*, 492:229–233, Dez 2012. – cited on page 6.

[26] J. L. Klocke, M. Mangold, P. Allmendinger, A. Hugi, M. Geiser, P. Jouy, J. Faist, and Tilman Kottke. Single-shot sub-microsecond mid-infrared spectroscopy on protein reactions with quantum cascade laser frequency combs. *Analytical Chemistry*, 90(17):10494–10500, August 2018. – cited on pages 6 and 41.

[27] M.-G. Suh, X. Yi, Y.-H.Lai, S. Leifer, I. S. Grudinin, G. Vasisht, E. C. M., M. P. Fitzgerald, G. Doppmann, J. Wang, D. Mawet, Sc. B. Papp, S.A. Diddams, C. Beichman, and K. Vahala. Searching for exoplanets using a microresonator astrocomb. *Nature Photonics*, 13(1):25–30, December 2018. – cited on page 6.

[28] J. Hillbrand, M. Beiser, A. M. Andrews, H. Detz, R. Weih, A. Schade, S. Höfling, G. Strasser, and B. Schwarz. Picosecond pulses from a mid-infrared interband cascade laser. *Optica*, 6(10):1334–1337, Oct 2019. – cited on pages 6, 22, 42, 52, 109, 112, 137, 138, 139, and 141.

[29] N. Picqué and T. W. Hänsch. Frequency comb spectroscopy. *Nature Photonics*, 13(3):146–157, February 2019. – cited on pages 7, 42, and 43.

[30] G. Villares, A. Hugi, S. Blaser, and J. Faist. Dual-comb spectroscopy based on quantum-cascade-laser frequency combs. *Nature Communications*, 5(1), oct 2014. – cited on page 6.

[31] L. Consolino, M. Nafa, M. De Regis, F. Cappelli, K. Garrasi, F. P. Mezzapesa, L. Li, A. Giles Davies, E. H. Linfield, M. S. Vitiello, S. Bartalini, and P. De Natale. Quantum cascade laser based hybrid dual comb spectrometer. *Communications Physics*, 3(1), April 2020. – cited on page 6.

[32] P. Jouy, J. M. Wolf, Y. Bidaux, P. Allmendinger, M. Mangold, M. Beck, and J. Faist. Dual comb operation of a 8.2 µm quantum cascade laser frequency comb with 1 W optical power. *Applied Physics Letters*, 111(14):141102, October 2017. – cited on page 6.

[33] G. Villares, A. Hugi, S. Blaser, and J. Faist. Dual-comb spectroscopy based on quantum-cascade-laser frequency combs. *Nature Communications*, 5:5192, Oct. 2014. – cited on pages 7 and 115.

[34] A. Bravais. Les systemes formes par des pointes distribues regulierement sur un plan ou dans l'espace. *J.Ecole.Polytech.*, XIX:1–128, 1850. – cited on page 9.

[35] N. W. Ashcroft and N. D. Mermin. *Solid State Physics*. Saunders College Publishing, Philadelphia, 1976. – cited on page 11.

[36] C. Kittel. *Introduction to Solid State physics*. J. Wiley and sons, Inc., New York, 2005. – cited on pages 11 and 15.

[37] M. L. Frankenheim. Ueber die Verbindung verschiedenartiger Krystalle. *Annalen der Physik und Chemie*, 113(3):516–522, 1836. – cited on page 11.

[38] U. Pohl. *Epitaxy of semiconductors : physics and fabrication of heterostructures*. Springer, Cham, 2020. – cited on pages 13, 21, 39, 60, and 63.

[39] B. Schwarz. *Monolithic integration of mid-infrared photonics*. PhD thesis, TU Wien, 2015. – cited on page 15.

[40] G. Bastard. Superlattice band structure in the envelope-function approximation. *Physical Review B*, 24:5693–5697, Nov 1981. – cited on page 15.

[41] G. Bastard. *Wave mechanics applied to semiconductor heterostructures*. Monographies de physique. Les Éditions de Physique, 1988. – cited on page 15.

[42] G. Bastard. Superlattice band structure in the envelope-function approximation. *Physical Review B*, 24(10):5693–5697, November 1981. – cited on page 15.

[43] Detz H. *Epitaxy of InGaAs GaAsSb Heterostructures for Intersubband Optoelectronics*. TU Wien, 2011. – cited on pages 17, 59, 64, and 82.

[44] Evan O. Kane. Band structure of indium antimonide. *Journal of Physics and Chemistry of Solids*, 1(4):249–261, January 1957. – cited on page 16.

[45] J. Faist. *Quantum cascade lasers*. Oxford University Press, 2013. – cited on pages 16, 20, and 27.

[46] Schwarz B. *Monolithic integration of mid-infrared photonics*. TU Wien, 2015. – cited on pages 19 and 25.

[47] Kroemer H. *Quantum mechanics, for engineering, Materials Science and Applied Physics*. Prentice Hall Series in Solid State Physical Electronics, 1994. – cited on page 20.

[48] E. Fermi. *Nuclear physics*. University of Chicago Press, 1950. – cited on page 20.

[49] R. J. Malik. Doping limits of c, be, and si in GaAs grown by solid source molecular-beam epitaxy with a thermally cracked as2 source. *Journal of Vacuum Science & Technology B: Microelectronics and Nanometer Structures*, 10(2):850, March 1992. – cited on page 21.

[50] N. Opacak S. Hoefling J. Koeth R. Weih H. Knoetig, J. Nauschuetz and B. Schwarz. Mitigating valence intersubband absorption in interband cascade lasers. *Laser Photonics Review*, 16(2200156), 2022. – cited on pages 22 and 37.

[51] C. Jirauschek and T. Kubis. Modeling techniques for quantum cascade lasers. *Applied Physics Reviews*, 1(1):011307, 2014. – cited on page 22.

[52] J. Faist. *Quantum Cascade Laser*. Oxford University Press, 2002. – cited on pages 22 and 27.

[53] M. Bagheri, C. Frez, L. A. Sterczewski, I. Gruidin, M. Fradet, I. Vurgaftman, C. L. Canedy, W. W. Bewley, C. D. Merritt, C. S. Kim, M. Kim, and J. R. Meyer. Passively mode-locked interband cascade optical frequency combs. *Scientific Reports*, 8(1), February 2018. – cited on pages 22 and 133.

[54] Per Hyldgaard and John W. Wilkins. Electron-electron scattering in far-infrared quantum cascade lasers. *Physical Review B*, 53(11):6889–6892, March 1996. – cited on page 23.

[55] C. Deutsch, H. Detz, T. Zederbauer, M. Krall, M. Brandstetter, A. M. Andrews, P. Klang, W. Schrenk, G. Strasser, and K.l Unterrainer. InGaAs/GaAsSb/InP terahertz quantum cascade lasers. *Journal of Infrared, Millimeter, and Terahertz Waves*, 34(5):374–385, 2013. – cited on page 23.

[56] W. Shockley and W. T. Read. Statistics of the recombinations of holes and electrons. *Physical Review*, 87(5):835–842, September 1952. – cited on page 24.

[57] J. Faist, A. Tredicucci, F. Capasso, C. Sirtori, D. L. Sivco, J. N. Baillargeon, A. L. Hutchinson, and A. Y. Cho. High-power continuous-wave quantum cascade lasers. *IEEE Journal of Quantum Electronics*, 34(2):336–343, 1998. – cited on page 25.

[58] Weih R. *Interbandkaskadenlaser für die Gassensorik im Spektralbereich des mittleren Infrarot*. University of Wuerzburg, 2017. – cited on pages 28, 36, and 110.

[59] C. Sirtori, J. Faist, F. Capasso, D. L. Sivco, A. L. Hutchinson, S. N. G. Chu, and A. Y. Cho. Continuous wave operation of midinfrared (7.4-8.6 µm) quantum cascade lasers up to 110 K temperature. *Applied Physics Letters*, 68(13):1745–1747, March 1996. – cited on page 27.

[60] M. Beck, D. Hofstetter, T. Aellen, J. Faist, U. Oesterle, M. Ilegems, E. Gini, and H. Melchior. Continuous wave operation of a mid-infrared semiconductor laser at room temperature. *Science*, 295(5553):301–305, January 2002. – cited on page 27.

[61] R. Köhler, A. Tredicucci, F. Beltram, H. E. Beere, E. H. Linfield, A. G. Davies, D. A. Ritchie, R. C. Iotti, and F. Rossi. Terahertz semiconductor-heterostructure laser. *Nature*, 417(6885):156–159, May 2002. – cited on page 27.

[62] R. Colombelli, F. Capasso, C. Gmachl, A. L. Hutchinson, D. L. Sivco, A. Tredicucci, M. C. Wanke, A. M. Sergent, and A. Y. Cho. Far-infrared surface-plasmon quantum-cascade lasers at 21.5 µm and 24 µm wavelengths. *Applied Physics Letters*, 78(18):2620–2622, April 2001. – cited on page 27.

[63] J. Devenson, O. Cathabard, R. Teissier, and A. N. Baranov. InAsAlSb quantum cascade lasers emitting at 2.75-2.97µm. *Applied Physics Letters*, 91(25):251102, December 2007. – cited on page 27.

[64] M. S. Vitiello, G. Scalari, B. W.s, and P. De Natale. Quantum cascade lasers: 20 years of challenges. *Opt. Express*, 23(4):5167–5182, Feb 2015. – cited on page 27.

[65] M. A. Kainz, S. Schönhuber, A. M. Andrews, H. Detz, B. Limbacher, G. Strasser, and K. Unterrainer. Barrier height tuning of terahertz quantum cascade lasers for high-temperature operation. *ACS Photonics*, 5(11):4687–4693, October 2018. – cited on pages 29 and 124.

[66] J. Faist, F. Capasso, Deborah L. Sivco, C. Sirtori, Albert L. Hutchinson, and Alfred Y. Cho. Quantum cascade laser. *Science*, 264(5158):553–556, April 1994. – cited on page 29.

[67] C. Deutsch, H. Detz, T. Zederbauer, Michael Krall, M. Brandstetter, A. M. Andrews, Pavel Klang, Werner Schrenk, G. Strasser, and Karl Unterrainer. InGaAs/-GaAsSb/InP terahertz quantum cascade lasers. *Journal of Infrared, Millimeter, and Terahertz Waves*, 34(5-6):374–385, June 2013. – cited on page 29.

[68] A.M. Andrews, M. Nobile, H. Detz, P. Klang, E. Mujagić, W. Schrenk, and G. Strasser. A new aluminum-free material system for intersubband emitters and detectors. *Journal of Physics: Conference Series*, 193(1):012065, 2009. – cited on page 29.

[69] M. Brandstetter, M. A. Kainz, T. Zederbauer, M. Krall, S. Schönhuber, H. Detz, W. Schrenk, A. M. Andrews, G. Strasser, and K. Unterrainer. InAs based terahertz quantum cascade lasers. *Applied Physics Letters*, 108(1):011109, January 2016. – cited on page 29.

[70] M. A. Kainz, M. P. Semtsiv, G. Tsianos, S. Kurlov, W. T. Masselink, S. Schönhuber, H. Detz, W. Schrenk, K. Unterrainer, G. Strasser, and A. M. Andrews. Thermoelectric-cooled terahertz quantum cascade lasers. *Optics Express*, 27(15):20688, July 2019. – cited on pages 30 and 124.

[71] Boyu Wen and Dayan Ban. High-temperature terahertz quantum cascade lasers. *Progress in Quantum Electronics*, 80:100363, November 2021. – cited on page 30.

[72] R. Q. Yang, J. L. Bradshaw, J. D. Bruno, J. T. Pham, D. E. Wortman, and R. L. Tober. Room temperature type-II interband cascade laser. *Applied Physics Letters*, 81(3):397–399, July 2002. – cited on page 31.

[73] M. Kim, C. L. Canedy, W. W. Bewley, C. S. Kim, J. R. Lindle, J. Abell, I. Vurgaftman, and J. R. Meyer. Interband cascade laser emitting at 3.75 µm in continuous wave above room temperature. *Applied Physics Letters*, 92(19):191110, May 2008. – cited on pages 31 and 38.

[74] R. Q. Yang, C. J. Hill, and B. H. Yang. High-temperature and low-threshold mid-infrared interband cascade lasers. *Applied Physics Letters*, 87(15):151109, October 2005. – cited on page 31.

[75] C. L. Felix, W.W. Bewley, I. Vurgaftman, J.R. Meyer, D. Zhang, C.-H. Lin, R.Q. Yang, and S.S. Pei. Interband cascade laser emitting 1 photon per injected electron. *IEEE Photonics Technology Letters*, 9(11):1433–1435, November 1997. – cited on page 31.

[76] J. Meyer, W. Bewley, C. Canedy, C. Kim, M. Kim, C. Merritt, and I. Vurgaftman. The interband cascade laser. *Photonics*, 7(3):75, September 2020. – cited on pages 31, 33, 34, and 37.

[77] W. W. Bewley, C. L. Canedy, C.S. Kim, M. Kim, C. D. Merritt, J. Abell, I. Vurgaftman, and J. R. Meyer. Continuous-wave interband cascade lasers operating above room temperature at $\lambda = 4.7$ - 5.6 µm. *Optics Express*, 20(3):3235–3240, Jan. 2012. – cited on page 32.

[78] M. von Edlinger, J. Scheuermann, R. Weih, C. Zimmermann, L. Nahle, M. Fischer, J. Koeth, S. Hofling, and M. Kamp. Monomode interband cascade lasers at 5.2 µm for nitric oxide sensing. *IEEE Photonics Technology Letters*, 26(5):480–482, March 2014. – cited on page 32.

[79] L. Li, H. Ye, Y. Jiang, R. Q. Yang, J. C. Keay, T. D. Mishima, M. B. Santos, and M. B. J.son. Mbe-grown long-wavelength interband cascade lasers on inas substrates. *Journal of Crystal Growth*, 425:369–372, 2015. The 18th International Conference on Molecular Beam Epitaxy (MBE 2014). – cited on pages 34 and 91.

[80] J. A. Massengale, Y. Shen, R. Q. Yang, S. D. Hawkins, and J. F. Klem. Long wavelength interband cascade lasers. *Applied Physics Letters*, 120(9):091105, February 2022. – cited on page 34.

[81] A. Spott, E. J. Stanton, A. Torres, M. L. Davenport, C. L. Canedy, I. Vurgaftman, M. Kim, C. S. Kim, C. D. Merritt, W. W. Bewley, J. R. Meyer, and J. E. Bowers. Interband cascade laser on silicon. *Optica*, 5(8):996–1005, Aug 2018. – cited on page 34.

[82] F. Wang, S. Slivken, D. H. Wu, and M. Razeghi. Room temperature quantum cascade lasers with 22% wall plug efficiency in continuous-wave operation. *Optics Express*, 28(12):17532, May 2020. – cited on page 34.

[83] I. Vurgaftman, W. W. Bewley, C. L. Canedy, C. S. Kim, M. Kim, J. R. Lindle, C. D. Merritt, J. Abell, and J. R. Meyer. Mid-IR type-II interband cascade lasers. *IEEE Journal of Selected Topics in Quantum Electronics*, 17(5):1435–1444, September 2011. – cited on page 37.

[84] I. Vurgaftman, R. Weih, M. Kamp, J. R. Meyer, C. L. Canedy, C. S. Kim, M. Kim, W. W. Bewley, C. D. Merritt, J. Abell, and S. Höfling. Interband cascade lasers. *Journal of Physics D: Applied Physics*, 48(12):123001, mar 2015. – cited on page 37.

[85] R. Weih, A. Bauer, M. Kamp, and S. Höfling. Interband cascade lasers with algaassb bulk cladding layers. *Opt. Mater. Express*, 3(10):1624–1631, Oct 2013. – cited on page 38.

[86] L. Li, Y. Jiang, H. Ye, R. Q. Yang, T. D. Mishima, M. B. Santos, and M. B. J.son. Low-threshold InAs-based interband cascade lasers operating at high temperatures. *Applied Physics Letters*, 106(25):251102, June 2015. – cited on page 40.

[87] S. A. Diddams, K. Vahala, and T. Udem. Optical frequency combs: Coherently uniting the electromagnetic spectrum. *Science*, 369(6501), July 2020. – cited on page 41.

[88] D. J. Jones, S. A. Diddams, J. K. Ranka, A. Stentz, R. S. Windeler, J. L. Hall, and S. T. Cundiff. Carrier-envelope phase control of femtosecond mode-locked lasers and direct optical frequency synthesis. *Science*, 288(5466):635–639, April 2000. – cited on page 41.

[89] U. Keller, K.J. Weingarten, F.X. Kartner, D. Kopf, B. Braun, I.D. Jung, R. Fluck, C. Honninger, N. Matuschek, and J. Aus der Au. Semiconductor saturable absorber mirrors (SESAM's) for femtosecond to nanosecond pulse generation in solid-state lasers. *IEEE Journal of Selected Topics in Quantum Electronics*, 2(3):435–453, 1996. – cited on page 42.

[90] M. Zhang, C. Wang, R. Cheng, A. Shams-Ansari, and M. Lončar. Monolithic ultra-high-Q lithium niobate microring resonator. *Optica*, 4(12):1536–1537, Dec 2017. – cited on page 42.

[91] M. H. P. Pfeiffer, C. Herkommer, J. Liu, H. Guo, M. Karpov, E. Lucas, M. Zervas, and T. J. Kippenberg. Octave-spanning dissipative kerr soliton frequency combs in silicon nitride microresonators. *Optica*, 4(7):684, June 2017. – cited on page 42.

[92] G. S. Qin, X. Yan, M. Liao, A. Mori, T. Suzuki, and Y. Ohishi. Wideband supercontinuum generation in tapered tellurite microstructured fibers. *Laser Physics*, 21(6):1115–1121, May 2011. – cited on page 42.

[93] B. Kuyken, X. Liu, R. M. Osgood, R. Baets, G. Roelkens, and W. M. J. Green. Mid-infrared to telecom-band supercontinuum generation in highly nonlinear silicon-on-insulator wire waveguides. *Opt. Express*, 19(21):20172–20181, Oct 2011. – cited on page 42.

[94] Y. Bai, N. Bandyopadhyay, S. Tsao, S. Slivken, and M. Razeghi. Room temperature quantum cascade lasers with 27% wall plug efficiency. *Applied Physics Letters*, 98(18):181102, May 2011. – cited on page 42.

[95] A. Hugi, G. Villares, S. Blaser, H. C. Liu, and J. Faist. Mid-infrared frequency comb based on a quantum cascade laser. *Nature*, 492(7428):229–233, dec 2012. – cited on pages 42 and 134.

[96] A. Schliesser, Nathalie Picqué, and Theodor W. Hänsch. Mid-infrared frequency combs. *Nature Photonics*, 6(7):440–449, June 2012. – cited on page 42.

[97] Hillbrand J. *Microwave photonics using semiconductor laser frequency combs*. TU Wien, 2020. – cited on pages 44, 45, and 52.

[98] J. Hillbrand, D. Auth, M. Piccardo, N. Opačak, E. Gornik, G. Strasser, F. Capasso, S. Breuer, and B. Schwarz. In-phase and anti-phase synchronization in a laser frequency comb. *Phys. Rev. Lett.*, 124:023901, Jan 2020. – cited on pages 46, 115, and 117.

[99] N. Opačak and B. Schwarz. Theory of frequency-modulated combs in lasers with spatial hole burning, dispersion, and kerr nonlinearity. *Phys. Rev. Lett.*, 123:243902, Dec 2019. – cited on pages 46, 115, and 117.

[100] D. Kuizenga and A. Siegman. FM and AM mode locking of the homogeneous laser - part i: Theory. *IEEE Journal of Quantum Electronics*, 6(11):694–708, November 1970. – cited on page 47.

[101] H. Haus. A theory of forced mode locking. *IEEE Journal of Quantum Electronics*, 11(7):323–330, July 1975. – cited on page 48.

[102] M. Piccardo, N. A. Rubin, L. Meadowcroft, P. Chevalier, H. Yuan, J. Kimchi, and F. Capasso. Mid-infrared two-photon absorption in an extended-wavelength InGaAs photodetector. *Applied Physics Letters*, 112(4):041106, January 2018. – cited on page 48.

[103] D. J. Kane and R. Trebino. Characterization of arbitrary femtosecond pulses using frequency-resolved optical gating. *IEEE Journal of Quantum Electronics*, 29(2):571–579, 1993. – cited on page 48.

[104] C. Iaconis and I. A. Walmsley. Spectral phase interferometry for direct electric-field reconstruction of ultrashort optical pulses. *Optics Letters*, 23(10):792, May 1998. – cited on page 48.

[105] J. Hillbrand, A. M. Andrews, H. Detz, G. Strasser, and B. Schwarz. Coherent injection locking of quantum cascade laser frequency combs. *Nature Photonics*, 13(2):101–104, December 2018. – cited on pages 48 and 115.

[106] D. Burghoff, Y. Yang, D. J. Hayton, J.-R. Gao, J. L. Reno, and Q. Hu. Evaluating the coherence and time-domain profile of quantum cascade laser frequency combs. *Opt. Express*, 23(2):1190, 2015. – cited on pages 48 and 51.

[107] P. R. Griffiths and J. A. de Haseth. *Fourier Transform Infrared Spectrometry*. J. Wiley & Sons, Inc., April 2007. – cited on page 49.

[108] W. D. Perkins. Fourier transform-infrared spectroscopy: Part l. instrumentation. *Journal of Chemical Education*, 63(1):A5, January 1986. – cited on page 49.

[109] M. Singleton, P. Jouy, M. Beck, and J. Faist. Evidence of linear chirp in mid-infrared quantum cascade lasers. *Optica*, 5(8):948, August 2018. – cited on page 52.

[110] D. Burghoff, T.-Y. Kao, N. Han, C. W. I. Chan, X. Cai, Y. Yang, D. J. Hayton, J.-R. Gao, J. L. Reno, and Q. Hu. Terahertz laser frequency combs. *Nature Photonics*, 8(6):462–467, May 2014. – cited on page 52.

[111] J. Hillbrand, N. Opačak, M. Piccardo, Harald Schneider, G. Strasser, F. Capasso, and B. Schwarz. Mode-locked short pulses from an 8 µm wavelength semiconductor laser. *Nature Communications*, 11(1), November 2020. – cited on page 52.

[112] Materials Fundamentals of Molecular Beam Epitaxy. *Scanning Electron Microscopy and X-ray Microanalysis: Third Edition*. Academic Press Inc., 1994. – cited on page 55.

[113] M. A. Herman and A. Sittner. *Molecular Beam Epitaxy*. Springer Series in Materials Science. Springer Verlag, 1988. – cited on pages 55, 63, and 64.

[114] H. Ye, L. Li, R. T. Hinkey, R. Q. Yang, T. D. Mishima, J. C. Keay, Michael B. Santos, and M. B. J. Son. MBE growth optimization of InAs (001) homoepitaxy. *Journal of Vacuum Science &amp Technology B, Nanotechnology and Microelectronics: Materials, Processing, Measurement, and Phenomena*, 31(3):03C135, May 2013. – cited on page 57.

[115] A. R. Denton and N. W. Ashcroft. Vegard's law. *Phys. Rev. A*, 43:3161–3164, Mar 1991. – cited on page 57.

[116] H. Kroemer. (invited) Heterostructures for everything: Device Principle of the 1980's. *Japanese Journal of Applied Physics*, 20(S1):9, January 1981. – cited on page 57.

[117] P. D. Brewer. Atomic antimony for molecular beam epitaxy of high quality III–v semiconductor alloys. *Journal of Vacuum Science &amp Technology B: Microelectronics and Nanometer Structures*, 14(3):2335, May 1996. – cited on page 57.

[118] W.W. Bewley, C.L. Canedy, C.S. Kim, I. Vurgaftman, M. Kim, and J.R. Meyer. Antimonide type-II "w" lasers: growth studies and guided-mode leakage into substrate. *Physica E: Low-dimensional Systems and Nanostructures*, 20(3-4):466–470, January 2004. – cited on page 57.

[119] R Hooke. De potentia restitutiva, edited by martyn j. *Royal Society, London*, 1678(3):171–172. – cited on page 58.

[120] J. W. Matthews and A.E. Blakeslee. Defects in epitaxial multilayers. *Journal of Crystal Growth*, 29(3):273–280, July 1975. – cited on page 60.

[121] A. Braun, K.M. Briggs, and P. Böni. Analytical solution to matthews' and blakeslee's critical dislocation formation thickness of epitaxially grown thin films. *Journal of Crystal Growth*, 241(1):231–234, 2002. – cited on page 60.

[122] A. M. Andrews, R. LeSar, M. A. Kerner, J. S. Speck, A. E. Romanov, A. L. Kolesnikova, M. Bobeth, and W. Pompe. Modeling crosshatch surface morphology in growing mismatched layers. part II: Periodic boundary conditions and dislocation groups. *Journal of Applied Physics*, 95(11):6032–6047, June 2004. – cited on pages 60, 96, and 99.

[123] C. A. Wang, B. Schwarz, D. F. Siriani, L. J. Missaggia, M. K. Connors, T. S. Mansuripur, D. R. Calawa, D. McNulty, M. Nickerson, J. P. Donnelly, K. Creedon, and F.Capasso. MOVPE growth of LWIR AlInAs/GaInAs/InP quantum cascade lasers: Impact of growth and material quality on laser performance. *IEEE Journal of Selected Topics in Quantum Electronics*, 23(6):1–13, November 2017. – cited on page 61.

[124] P. Gibart. Metal organic vapour phase epitaxy of gan and lateral overgrowth. *Reports on Progress in Physics*, 67(5):667–715, apr 2004. – cited on page 62.

[125] V. M. Ustinov, E. R. Weber, S. Ruvimov, Z. Liliental-Weber, A. E. Zhukov, A. Yu. Egorov, A. R. Kovsh, A. F. Tsatsul'nikov, and P. S. Kop'ev. Effect of matrix on InAs self-organized quantum dots on InP substrate. *Applied Physics Letters*, 72(3):362–364, January 1998. – cited on page 64.

[126] H. Nguyen-Van, A. N. Baranov, Z. Loghmari, L. Cerutti, J. Rodriguez, J. Tournet, G. Narcy, G. Boissier, G. Patriarche, M. Bahriz, E. Tournié, and R. Teissier. Quantum cascade lasers grown on silicon. *Scientific Reports*, 8(1), May 2018. – cited on page 64.

[127] Zederbauer T. *Mixed group V compound semiconductors for intersubband devices*. TU Wien, 2017. – cited on pages 66, 69, 73, 79, 86, and 93.

[128] Y. Rouillard, B. Lambert, Y. Toudic, M. Baudet, and M. Gauneau. On the use of dimeric antimony in molecular beam epitaxy. *Journal of Crystal Growth*, 156(1-2):30–38, November 1995. – cited on page 72.

[129] C. E. C. Wood, D. Desimone, K. Singer, and G. W. Wicks. Magnesium- and calcium-doping behavior in molecular-beam epitaxial III-V compounds. *Journal of Applied Physics*, 53(6):4230–4235, 1982. – cited on page 73.

[130] H. Sitter M. Herman. *Molecular Beam Epitaxy: Fundamentals and Current Status*. Springer Series in Materials Science, 1996. – cited on page 75.

[131] V. P. LaBella, M. R. Krausem, Z. Dingm, and P. M. Thibado. Arsenic-rich gaas surface structure. *Surface Science Reports*, 60(1-4):1–53, December 2005. – cited on page 78.

[132] G. Bauer A. Krost and J. Woitok. *Optical Characterization of Epitaxial Semiconductor Layers*. Springer, 1996. – cited on page 81.

[133] M. Jaidl, N. Opačak, M. A. Kainz, S. Schönhuber, D. Theiner, B. Limbacher, M. Beiser, M. Giparakis, A. M. Andrews, G. Strasser, B. Schwarz, J. Darmo, and K. Unterrainer. Comb operation in terahertz quantum cascade ring lasers. *Optica*, 8(6):780–787, Jun 2021. – cited on pages 83 and 129.

[134] J. A. Bearden. X-ray wavelengths. *Reviews of Modern Physics*, 39(1):78–124, January 1967. – cited on page 88.

[135] T. Zederbauer. *Mixed Group V Compound Semiconductors for Intersubband Devices*. PhD thesis, TU-Wien, 2017. – cited on pages 89 and 93.

[136] D. Joy C. Lyman P. Echlin E. Lifshin L. Sawyer J. Goldstein, D. Newbury and J. Michael. Scanning electron microscopy and X-Ray microanalysis. *Microscopy and Microanalysis*, 9(5):484–484, September 2003. – cited on page 89.

[137] Marcin Motyka, Grzegorz Sek, Krzysztof Ryczko, Mateusz Dyksik, R. Weih, Gilles Patriarche, Jan Misiewicz, M. Kamp, and Sven Höfling. Interface intermixing in type II InAs/GaInAsSb quantum wells designed for active regions of mid-infrared-emitting interband cascade lasers. *Nanoscale Research Letters*, 10(1), December 2015. – cited on page 91.

[138] Z. Tian, L. Li, H. Ye, R. Q. Yang, T.D. Mishima, M.B. Santos, and M.B. Jason. InAs-based interband cascade lasers with emission wavelength at 10.4 µm. *Electronics Letters*, 48(2):113, 2012. – cited on page 91.

[139] T.A. Nilsen, M. Breivik, E. Selvig, and B.O. Fimland. Critical thickness of MBE-grown ga1-xInxSb (x&lt0.2) on GaSb. *Journal of Crystal Growth*, 311(7):1688–1691, March 2009. – cited on page 91.

[140] I. Vurgaftman, J. R. Meyer, and L. R. Ram-Mohan. Band parameters for III–v compound semiconductors and their alloys. *Journal of Applied Physics*, 89(11):5815–5875, June 2001. – cited on page 92.

[141] J. Nicolai, Ch. Gatel, B. Warot-Fonrose, R. Teissier, A. N. Baranov, C. Magen, and A. Ponchet. Elastic strains at interfaces in InAs/AlSb multilayer structures for quantum cascade lasers. *Applied Physics Letters*, 104(3):031907, January 2014. – cited on page 93.

[142] B. R. Bennett, B. V. Shanabrook, and E. R. Glaser. Interface control in InAs/AlSb superlattices. *Applied Physics Letters*, 65(5):598–600, August 1994. – cited on page 93.

[143] J. Spitzer, H. D. Fuchs, P. Etchegoin, M. Ilg, M. Cardona, B. Brar, and H. Kroemer. Quality of AlAs-like and InSb-like interfaces in InAs/AlSb superlattices: An optical study. *Applied Physics Letters*, 62(18):2274–2276, May 1993. – cited on page 93.

[144] M. Losurdo, P. Capezzuto, G.i Bruno, A. S. Brown, T. Brown, and G. May. Fundamental reactions controlling anion exchange during mixed anion heterojunction formation: Chemistry of As-for-Sb and Sb-for-As exchange reactions. *Journal of Applied Physics*, 100(1):013531, July 2006. – cited on page 93.

[145] M. Vallet, Y. Claveau, B. Warot-Fonrose, C. Gatel, J. Nicolai, N. Combe, C. Magen, R. Teissier, A. N. Baranov, and A. Ponchet. Highly strained AlAs-type interfaces in InAs/AlSb heterostructures. *Applied Physics Letters*, 108(21):211908, 2016. – cited on page 93.

[146] B. Jenichen, S. A. Stepanov, B. Brar, and H. Kroemer. Interface roughness of InAs/AlSb superlattices investigated by x-ray scattering. *Journal of Applied Physics*, 79(1):120–124, January 1996. – cited on page 93.

[147] Q. Xie, J. E. Van Nostrand, J. L. Brown, and C. E. Stutz. Arsenic for antimony exchange on GaSb, its impacts on surface morphology, and interface structure. *Journal of Applied Physics*, 86(1):329–337, July 1999. – cited on page 93.

[148] L. He, L. E. Clinger, and C. J. K. Richardson. Stability of arsenide and antimonide surfaces during molecular beam epitaxy growth. *Journal of Vacuum Science &amp Technology B, Nanotechnology and Microelectronics: Materials, Processing, Measurement, and Phenomena*, 31(6):061204, November 2013. – cited on page 93.

[149] J. Wagner, J. Schmitz, D. Behr, J. D. Ralston, and P. Koidl. Interface formation in InAs/AlSb and InAs/AlAs/AlSb quantum wells grown by molecular-beam epitaxy. *Applied Physics Letters*, 65(10):1293–1295, September 1994. – cited on page 93.

[150] B. R. Bennett, B. V. Shanabrook, and E. R. Glaser. Interface control in InAs/AlSb superlattices. *Applied Physics Letters*, 65(5):598–600, August 1994. – cited on page 93.

[151] B. Jenichen, S. A. Stepanov, B. Brar, and H. Kroemer. Interface roughness of InAs/AlSb superlattices investigated by x-ray scattering. *Journal of Applied Physics*, 79(1):120–124, January 1996. – cited on page 93.

[152] M. Giparakis, H. Knötig, H. Detz, M. Beiser, W. Schrenk, B. Schwarz, G. Strasser, and A. M. Andrews. 2.7 µm quantum cascade detector: Above band gap energy intersubband detection. *Applied Physics Letters*, 120(7):071104, February 2022. – cited on page 99.

[153] Z.H. Jiang, S. Yun, F. Toor, D. H. Werner, and T. S. Mayer. Conformal dual-band near-perfectly absorbing mid-infrared metamaterial coating. *ACS Nano*, 5(6):4641–4647, 2011. PMID: 21456579. – cited on page 104.

[154] L. M. Kruger, J. Hillbrand, J. Heidrich, M. Beiser, R. Weih, J. Koeth, C. R. Phillips, B. Schwarz, G. Strasser, and U. Keller. High-speed interband cascade infrared photodetectors: photo-response saturation by a femtosecond oscillator. *Opt. Express*, 29(9):14087–14100, Apr 2021. – cited on pages 109 and 141.

[155] D. Kazakov, N. Opačak, M. Beiser, Alexey Belyanin, B. Schwarz, M. Piccardo, and F. Capasso. Defect-engineered ring laser harmonic frequency combs. *Optica*, 8(10):1277–1280, Oct 2021. – cited on pages 109, 129, 130, and 141.

[156] M. Piccardo, B. Schwarz, D. Kazakov, M. Beiser, N. Opačak, Y. Wang, S. Jha, J. Hillbrand, M. Tamagnone, W. T. Chen, A. Y. Zhu, L. Columbo, A. Belyanin, and F. Capasso. Frequency combs induced by phase turbulence. *Nature*, 582(7812):360–364, June 2020. – cited on pages 109, 113, 129, 130, and 141.

[157] M. Beiser, N. Opačak, and G. Strasser J. Hillbrand, and B. Schwarz. Engineering the spectral bandwidth of quantum cascade laser frequency combs. *Opt. Lett.*, 46(14):3416–3419, Jul 2021. – cited on pages 115, 116, 119, 120, 122, and 123.

[158] J. L. Klocke and T. Kottke. A quantum cascade laser setup for studying irreversible photoreactions in H2O with nanosecond resolution and microlitre consumption. *Physical Chemistry Chemical Physics*, 22(45):26459–26467, 2020. – cited on page 115.

[159] N. H. Pinkowski, Y. Ding, C. L Strand, R. K. Hanson, R. Horvath, and M. Geiser. Dual-comb spectroscopy for high-temperature reaction kinetics. *Measurement Science and Technology*, 31(5):055501, mar 2020. – cited on page 115.

[160] M. R. St-Jean, M. I. Amanti, A. Bernard, A. Calvar, A. Bismuto, E. Gini, M. Beck, J. Faist, H. C. Liu, and C. Sirtori. Injection locking of mid-infrared quantum cascade laser at 14 GHz, by direct microwave modulation. *Laser & Photonics Reviews*, 8(3):443–449, March 2014. – cited on page 115.

[161] J. Hillbrand, A. M. Andrews, H. Detz, G. Strasser, and B. Schwarz. Coherent injection locking of quantum cascade laser frequency combs. *Nature Photonics*, 13(2):101–104, December 2018. – cited on pages 115 and 121.

[162] L. A. Sterczewski, C. Frez, S. Forouhar, D. Burghoff, and M. Bagheri. Frequency-modulated diode laser frequency combs at 2 µm wavelength. *APL Photonics*, 5(7):076111, July 2020. – cited on page 115.

[163] J. Hillbrand, P. Jouy, M. Beck, and J. Faist. Tunable dispersion compensation of quantum cascade laser frequency combs. *Opt. Lett.*, 43(8):1746–1749, Apr 2018. – cited on page 117.

[164] G. Villares, S. Riedi, J. Wolf, D. Kazakov, M. J. Süess, P. Jouy, M. Beck, and J. Faist. Dispersion engineering of quantum cascade laser frequency combs. *Optica*, 3(3):252, March 2016. – cited on page 117.

[165] Y. Bidaux, I. Sergachev, W. Wuester, R. Maulini, T. Gresch, A. Bismuto, S. Blaser, A. Muller, and J. Faist. Plasmon-enhanced waveguide for dispersion compensation in mid-infrared quantum cascade laser frequency combs. *Opt. Lett.*, 42(8):1604–1607, Apr 2017. – cited on page 117.

[166] D. Bachmann, M. Rösch, G. Scalari, M. Beck, J. Faist, K. Unterrainer, and J. Darmo. Dispersion in a broadband terahertz quantum cascade laser. *Applied Physics Letters*, 109(22):221107, 2016. – cited on page 117.

[167] D. Burghoff. Unraveling the origin of frequency modulated combs using active cavity mean-field theory. *Optica*, 7(12):1781–1787, Dec 2020. – cited on page 117.

[168] J. B. Khurgin. Analytical expression for the width of quantum cascade laser frequency comb. *Applied Physics Letters*, 117(16):161104, October 2020. – cited on pages 117 and 121.

[169] Nikola Opačak, Sandro Dal Cin, Johannes Hillbrand, and Benedikt Schwarz. Frequency comb generation by bloch gain induced giant kerr nonlinearity. *Phys. Rev. Lett.*, 127:093902, Aug 2021. – cited on pages 117 and 134.

[170] F. Kapsalidis, B. Schneider, M. Singleton, M. Bertrand, E. Gini, M. Beck, and J. Faist. Mid-infrared quantum cascade laser frequency combs with a microstrip-like line waveguide geometry. *Applied Physics Letters*, 118(7):071101, February 2021. – cited on pages 119 and 121.

[171] M. Jaidl, M. Beiser, M. Giparakis, M .A. Kainz, D. Theiner, B. Limbacher, M. C. Ertl, A. M. Andrews, G. Strasser, J. Darmo, and Karl K. Unterrainer. Ultrabroadband heterogeneous thz quantum cascade laser. *ACS Photonics*, 10(1):111–115, 2023. – cited on pages 123, 125, 127, and 128.

[172] M. Brandstetter, C. Deutsch, M. Krall, H. Detz, D. MacFarland, Zederbauer, A. M. Andrews, W. Schrenk, G. Strasser, and K. Unterrainer. High power terahertz quantum cascade lasers with symmetric wafer bonded active regions. *Applied Physics Letters*, 103(17):171113, October 2013. – cited on page 123.

[173] D. Bachmann, N. Leder, M. Rösch, G. Scalari, M. Beck, H. Arthaber, J. Faist, K. Unterrainer, and J. Darmo. Broadband terahertz amplification in a heterogeneous quantum cascade laser. *Optics Express*, 23(3):3117–3125, February 2015. – cited on page 123.

[174] M. Rösch, G. Scalari, M. Beck, and J. Faist. Octave-spanning semiconductor laser. *Nature Photonics*, 9(1):42–47, January 2015. – cited on page 123.

[175] L. H. Li, K. Garrasi, I. Kundu, Y. J. Han, M. Salih, M. S. Vitiello, A. G. Davies, and E. H. Linfield. Broadband heterogeneous terahertz frequency quantum cascade laser. *Electronics Letters*, 54(21):1229–1231, 2018. – cited on page 123.

[176] C. Gmachl, Deborah L. Sivco, Raffaele Colombelli, F. Capasso, and Alfred Y. Cho. Ultra-broadband semiconductor laser. *Nature*, 415(6874):883–887, February 2002. – cited on page 124.

[177] M. A. Kainz, S. Schönhuber, B. Limbacher, A. M. Andrews, H. Detz, G. Strasser, G. Bastard, and K. Unterrainer. Color switching of a terahertz quantum cascade laser. *Applied Physics Letters*, 114(19):191104, May 2019. – cited on page 124.

[178] B. Meng, M. Singleton, M. Shahmohammadi, F. Kapsalidis, R. Wang, M. Beck, and J. Faist. Mid-infrared frequency comb from a ring quantum cascade laser. *Optica*, 7(2):162, February 2020. – cited on page 129.

[179] M. Jaidl, N. Opačak, M. A. Kainz, D. Theiner, B. Limbacher, M. Beiser, M. Giparakis, A. M. Andrews, G. Strasser, B. Schwarz, J. Darmo, and K. Unterrainer. Silicon integrated terahertz quantum cascade ring laser frequency comb. *Applied Physics Letters*, 120(9):091106, February 2022. – cited on page 129.

[180] I. S. Aranson and L. Kramer. The world of the complex Ginzburg-Landau equation. *Reviews of Modern Physics*, 74(1):99–143, February 2002. – cited on page 129.

[181] D. Kazakov, T. Letsou, M. Beiser, Y. Zhi, N. Opacak, M. Piccardo, B. Schwarz, and F. Capasso. Semiconductor ring laser frequency combs with active directional couplers, 2022. – cited on pages 130 and 131.

[182] G. Andriukaitis, T. Balčiūnas, S. Ališauskas, A. Pugžlys, A. Baltuška, T. Popmintchev, M. Chen, M. Murnane M, and H. C. Kapteyn. 90 GW peak power few-cycle mid-infrared pulses from an optical parametric amplifier. *Opt. Lett.*, 36(15):2755–2757, Aug 2011. – cited on page 133.

[183] T. Feng, L. Shterengas, T. Hosoda, A. Belyanin, and G. Kipshidze. Passive mode-locking of 3.25 µm GaSb-based cascade diode lasers. *ACS Photonics*, 5(12):4978–4985, November 2018. – cited on page 133.

[184] L. A. Sterczewski, M. Bagheri, C. Frez, C. L Canedy, I. Vurgaftman, and C. S. Kim M. Kim, C. D Merritt, W. W Bewley, and Jerry R Meyer. Interband cascade laser frequency combs. *Journal of Physics: Photonics*, 3(4):042003, oct 2021. – cited on page 133.

[185] A. Khalatpour, A. K. Paulsen, C. Deimert, Z.R. Wasilewski, and Q. Hu. High-power portable terahertz laser systems. *Nature Photonics*, 15(1):16–20, November 2020. – cited on page 142.

[186] Web of science database. Accessed on March 2, 2023. – cited on page 143.

ABBREVIATIONS

AlGaAs Aluminum Gallium Arsenide
AlGaAsSb Aluminium Gallium Arsenide Antimonide
AFM atomic force microscopy
AR anti-reflection
AZ active zone
CBO conduction band offset
CMOS complementary metal oxide semiconductor
CVD chemical vapor deposition
CW continuous wave
DFB distributed feedback
FBZ first Brillouin zone
FFT fast Fourier transformation
FP Fabry-Pérot
FWHM full width at half maximum
FTIR Fourier transformation infrared spectrometer
GaAs Gallium Arsenide
GaSb Gallium Antimonide
Ge/Au/Ni/Au Germanium/Gold/Nickel/Gold
HCl Hydrochloric acid
IB interband
ICL interband cascade laser
ICP inductively coupled plasma
ISB intersubband
IR infrared
LED light emitting diode
LWIR long-wave infrared
MBE molecular beam epitaxy
MCT mercury cadmium telluride
MIR mid-infrared

MOCVD metal-organic chemical vapor deposition
NEP noise equivalent power
NETD noise equivalent temperature difference
NIR near-infrared
PCB printed circuit board
PECVD plasma enhanced vapor deposition
PLOX plasma oxidizer
QC quantum cascade
QCD quantum cascade detector
QCL quantum cascade laser
QCLD quantum cascade laser detector
QW quantum well
QWIP quantum well infrared photodetector
RIE reactive ion etching
RTA rapid thermal annealing
SEM scanning electron microscope
SL superlattice
SNR signal to noise ratio
TE transverse-electric
TEC thermoelectric cooler
TM transverse-magnetic
UHV ultra high vacuum

List of publications

Journal publications

J1 M. Beiser*, N. Opacak*, J. Hillbrand, G. Strasser, and B. Schwarz "Engineering the spectral bandwidth of quantum cascade laser frequency combs"; *Optics Letters* (2021)

J2 M.Jaidl*, M. Beiser*, M.A.Kainz, D. Theiner, B. Limbacher, M. Giparakis, A.M.Andrews, J. Darmo and K. Unterrainer "Ultra-Broadband Heterogeneous THz Quantum Cascade Laser"; *ACS Photonics* (2022),

Journal Publications as co-author

J1 B. Schwarz, J. Hillbrand, M. Beiser, A. Schade, G. Strasser, S. Höfling, "Monolithic frequency comb platform based on interband cascade lasers and detectors"; *Optica* (2019)

J2 J. Hillbrand, M. Beiser, A.M. Andrews, H. Detz, R. Weih, A. Schade, S. Höfling, G. Strasser, B. Schwarz, "Picosecond mid-infrared pulses from an interband cascade laser"; *Optica* (2019)

J3 M. Piccardo, B. Schwarz, M. Beiser, D. Kazakov, Y. Wang, A. Belyanin, and F. Capasso, "Frequency combs induced by phase turbulence"; *Nature* (2020),

J4 M. Piccardo, N. Opacak, M. Beiser, A. Belyanin, B. Schwarz, Marco Piccardo and F. Capasso, "Defect-engineered harmonic frequency comb"; *Optica*, submitted (2020),

J5 M. Jaidl, N. Opacak, M. A. Kainz, S. Schönhuber, D. Theiner, B. Limbacher, M. Beiser, M. Giparakis, A. M. Andrews, G. Strasser, B. Schwarz, J. Darmo, and K. Unterrainer "Comb Operation in Terahertz Quantum Cascade Ring Lasers"; *Optica* (2021),

J6 L.M. Krüger, J. Hillbrand, J. Heidrich, M. Beiser, R. Weih, J. Köth, C.R.Phillips, B. Schwarz, G. Strasser and U. Keller "High-Speed mid-infrared Interband Cascade Detectors: Photo-Response Saturation by a Femtosecond Oscillator"; *Optics Express* (2021),

J7 D. Kazakov, N. Opacak, M. Beiser,A. Belyanin, B. Schwarz, M. Piccardo and F. Capasso "Defect-engineered harmonic frequency combs in ring quantum cascade lasers"; *Optica* (2021),

J8 L. Mennel, A.J.Molina-Mendoza, M. Paur, D. K. Polyushkin, D. Kwak, M. Giparakis, M. Beiser, A.M. Andrews, and T. Mueller "A photosensor employing data-driven binning for ultrafast image recognition"; *Nature Photonics* (2021),

J9 M.Jaidl,N. Opacak, M.A.Kainz, D. Theiner, B. Limbacher, M. Beiser, M. Giparakis, A.M.Andrews, J. Darmo and K. Unterrainer "Silicon Integrated Terahertz Quantum Cascade Ring Laser Frequency Comb"; *Applied Physics Letters* (2021),

J10 M. Giparakis, H. Knötig, H. Detz, M. Beiser, W. Schrenk, B. Schwarz, G. Strasser, and A. M. Andrews "2.7 µm Quantum Cascade Detector: Above Band Gap Energy Intersubband Detection"; *Applied Physics Letters* (2021),

J11 E. Bakali, W. Artner, M. Beiser, J. Bernardi, H. Detz, G. Eguchi, A. Foelske, M. Giparakis, C. Herzig, A. Limbeck , H. Nguyen, L. Prochaska, A. Prokofiev, M. Sauer, S. Schwarz, W. Schrenk, G. Strasser, R. Svagera, M. Taupin, A.S. Thirsfeld, M. Waas, X. Yan, D.A. Zocco ,A.M. Andrews and S. Paschem "A Knudsen cell approach for the molecular beam epitaxy of the heavy fermion compound $YbRh_2Si_2$"; *Journal of Crystal Growth* (2022),

J12 M. Giparakis, M. A. Kainz, M. C. Ertl, and A. M. Andrews "Anomalous temperature effect in weakly-coupled superlattices: Carrier transport in a THz quantum cascade laser"; *Physical Review Letters, submitted* (2023),

J13 D. Kazakov, T. Letsou, M. Beiser, Y. Zhi, N. Opacak, M. Piccardo, B. Schwarz, F. Capasso "Active mid-infrared ring resonators"; *Nature Communications, submitted* (2023),

J14 N. Opacak, D. Kazakov, L. Colombo, M. Beiser, T. Letsou, F. Pilat, M. Brambilla, F. Prati, M. Piccardo, F. Capasso and B. Schwarz "Nozaki-Bekki optical solitons"; *arxive, submitted* (2023),

Thesis

M. Beiser, *Monolithic frequency combs in the mid-infrared using interband cascade lasers, Technische Universität Wien, June 2018*

Poster Presentations

P1 M. Beiser, J.Hillbrand, A.M. Andrews, R. Weih, S. Höfling, G. Strasser and B. Schwarz "Picosecond Pulses in Interband Cascade Lasers"; *IQCLSW*, Teleconference, Switzerland (2020)

P2 J. Hillbrand, S. Dal Cin, B. Schwarz, M. Beiser, A.M. Andrews, G. Strasser, "RF QWIPs for Characterization of mid-IR Frequency Combs", 20th Int. Winterschool on New Developments in Solid State Physics, Mauterndorf, Austria, Feb 25 – Mar 2, 2018 M. Beiser, J. Hillbrand, S. Dal Cin, H. Detz, A.M. Andrews, G. Strasser, B. Schwarz, "QWIPs and QCDs for Mid-Infrared Frequency Combs", IQCLSW 2018, Cassis, France, Sep 2 – 7, 2018

P3 M. Beiser, B. Schwarz, A. Harrer, M. Holzbauer, H. Detz, A.M. Andrews and G. Strasser: "Bifunctional Quantum cascade laser detectors"; *MBE Workshop*, Vienna, Austria (2017)

P4 M. Beiser, J.Hillbrand, B. Schwarz, S. dal Cin, H. Detz, A.M. Andrews and G. Strasser: "Radiofrequency QWIPs and QCDs"; *IQCLSW*, Cassis, France (2018)

P5 S. Isceri, M. Giparakis, M. Beiser, H. Detz, W. Schrenk, S. Bühler-Paschen, G. Strasser, A.M. Andrews, "Epitaxy of YbRh2Si2 on Ge(001)", German MBE Workshop 2021, Göttingen, Germany, Oct 14 - 15, 2021

Oral Presentation

P1 M. Beiser J. Hillbrand, A. Schade, H. Detz, M. Andrews, G. Strasser, S. Höfling, and B. Schwarz "Mode-locked Interband Cascade Lasers", 68th Annual Meeting of the Austrian Physical Society, Graz, AUT, Sept 12 – 14, 2018

P2 M. Beiser, H. Knötig, B. Hinkov, N. Opacak, M. Holzbauer, R. Szedlak, H. Detz, R. Weih, S. Höfling, W. Schrenk, J. Koeth, and G. Strasser, "Surface emitting ring interband cascade lasers", 68th Annual Meeting of the Austrian Physical Society, Graz, AUT, Aug 19 – 23, 2018

P3 M. Beiser, M. Giparakis, H. Knötig, H. Detz, M. Giparakis, B. Schwarz, A.M. Andrews, G. Strasser, "Strain Balancing for InAs Based ICL growth", MBE XXI, Mexico, ONLINE, Sep 6 – 9, 2021

P4 M. Beiser, J. Hillbrand, A.M. Andrews, R. Weih, S. Höfling, G. Strasser, B. Schwarz, "Monolithic Frequency Comb Generation and High-speed Detection based on Interband Cascade Structures", DEMBE 2019, Würzburg, Germany, Oct 7 – 8, 2019

Oral presentation without conference proceeding as co-author

P1 B. Schwarz, F. Pilat, N. Opacak, S. Dal Cin, J. Hillbrand, M. Beiser, G. Strasser, R.

Weih, S. Hofling, M. Piccardo, F. Capasso, "Integrated mid-infrared semiconductor laser frequency combs", Nano and Photonics, Mauterndorf, Austria, Mar 15 – 17, 2023

P2 N. Opacak, D. Kazakov, L.L. Columbo, M. Beiser, F. Pilat, G. Strasser, M. Brambilla, F. Prati, M. Piccardo, B. Schwarz, "Parametric processes and nonlinear dynamics of self-starting frequency combs", Photonics West, San Francisco, USA, Jan 28 – Feb 2, 2023

P3 M. Jaidl, N. Opacak, D. Theiner, M. Ertl, B. Limbacher, M. Beiser, M. Giparakis, A.M. Andrews, G. Strasser, B.Schwarz, K. Unterrainer, "Terahertz quantum cascade ring lasers: comb operation and integration on Si-substrates", Photonics West, San Francisco, USA, Jan 28 – Feb 2, 2023

P4 M. Giparakis, H. Knoetig, S. Isceri, M. Beiser, H. Detz, W. Schrenk, B. Schwarz, G. Strasser, A.M. Andrews, "MBE Growth and Characterization of an InAs/$AlAs_{0.16}Sb_{0.88}$ quantum cascade detector at 2.7 µm", NAMBE, Reheboth Beach, USA, Sep 18 – 22, 2022

P5 M. Giparakis, H. Knoetig, M. Beiser, H. Detz, B. Schwarz, W. Schrenk, G. Strasser, A.M. Andrews, "Short-Wavelength InAs-based Quantum Cascade Detector Operating at 2.7 µm", IEEE Rapid, Miramar Beach, USA, Sep 12 – 14, 2022

P6 M. Jaidl, N. Opacak, M.A. Kainz, D. Theiner, B. Limbacher, M. Beiser, M. Giparakis, A.M. Andrews, G. Strasser, B. Schwarz, J. Darmo, K. Unterrainer, "Silicon Integrated Terahertz Quantum Cascade Ring Laser Frequency Comb", IQCLSW2022, Zürich Monte Verita, Switzerland, Aug 23 -28, 2022

P7 B. Schwarz, F. Pilat, N. Opacak, S. Dal Cin, J. Hillbrand, M. Beiser, G. Strasser, R. Weih, S. Hofling, M. Piccardo, F. Capasso, "Integrated mid-infrared semiconductor laser frequency combs", mir5ens, Wroclaw, Poland, Jul 4 – 6, 2022

P8 M. Ertl, M. Jaidl, B. Limbacher, D. Theiner, M. Kainz, M. Giparakis, M. Beiser, A.M. Andrews, G. Strasser, J. Darmo, K. Unterrainer, "Epi-down Bonded Quantum Cascade Patch Antenna Array Laser", 9th International Conference on Optical Terahertz Science and Technology (OTST 2022), Budapest, Hungary. Jun 19 - 24 2022

P9 M. Giparakis, H. Knoetig, H. Detz, M. Beiser, W. Schrenk, B. Schwarz, G. Strasser, A.M. Andrews, "Top-Side Illuminated InAS/AlAsSb Quantum Cascade Detector at 2.7µm", CLEO, San Jose, USA, May 15 – 20, 2022

P10 S. Isceri, M. Giparakis, E. Bakali, M. Beiser, H. Detz, W. Schrenk, G. Strasser, M. Waas, R. Svagera, S. Bühler-Paschen, "Single crystal growth of YbRh2Si2", DGKK/DEMBE 2022, Bremen, Germany. May 16 - 18, 2022

P11 M. Jaidl, D. Theiner, B. Limbacher, M. Beiser, A.M. Andrews, G. Strasser, J. Darmo, K. Unterrainer, "QCL and fibre laser-driven frequency combs", SPIE Photonics Europe, Strasbourg, France, Apr 3 –7, 2022

P12 B. Schwarz, N. opacak, F. Pilat, D. Kazakov, S. Dal Cin, N. Beiser, L. Columbo, J. Hillbrand, M. Piccardo, F. Capasso, "Frequency comb operation induced by a giant Kerr nonlinearity in quantum cascade lasers", SPIE Photonics Europe, Strasbourg, France, Apr 3 –7, 2022

P13 B. Schwarz, M. Beiser, F. Pilat, S. Dal Cin, J. Hillbrand, R. Weih, J. Koeth, S. Höfling, "Interband cascade laser frequency combs", SPIE Photonics Europe, Strasbourg, France, Apr 3 –7, 2022

P14 F. Pilat, N. Opacak, H. Knötig, M. Beiser, S. Dal Cin, J. Hillbrand, R. Weih, B. Schwarz, "Mid-infrared semiconductor frequency combs", Optica High-Brightness Sources and Light-Driven Interactions Congress 2022, Budapest, Hungary, Mar 23 - 25 2022

P15 A.M. Andrews, M. Giparakis, H. Knötig, S. Isceri, M. Beiser, W. Schrenk, B. Schwarz, G. Strasser, "Above band gap energy InAs/AlAsSb quantum cascade detector", Workshop on Compound Semiconductor Materials and Devices (WOCSEMMAD) 2022, Destin Beach, FL, USA, Feb 20 - 22, 2022

P16 B. Schwarz, M. Beiser, S. Dal Cin, J. Hillbrand, N. Opacak, G. Strasser, H. Schneider, M. Piccardi, F. Capasso, R. Weih, "Mid-infrared frequency combs based on semiconductor lasers", Photonics West, ONLINE, Mar 6 – 11, 2021

P17 M. Giparakis, H. Knötig, H. Detz, M. Beiser, B. Schwarz, W. Schrenk, G. Strasser, A.M. Andrews, "Growth, Design, and Characterisation of an InAs/AlAsSb-based QCD at 2.7 m", German MBE Workshop, Garching, Deutschland, Oct 13 - 14, 2022

P18 M. Piccardo et al., "Ring Laser Frequency Combs Enabled by Phase Turbulence and Their Connection to Kerr Combs," 2020 Conference on Lasers and Electro-Optics (CLEO), San Jose, CA, USA, 2020, pp. 1-2

P19 D. Kazakov, M. Piccardo, M. Beiser, N. Opacak, Y. Wang, A. Belyanin, B. Schwarz, and F. Capasso, "Shaping harmonic frequency combs in ring injection lasers by defect engineering," in Conference on Lasers and Electro-Optics, OSA Technical Digest (Optical Society of America, 2020), paper STh3E.8

P20 M. Piccardo et al., "Ring Laser Frequency Combs Enabled by Phase Turbulence and Their Connection to Kerr Combs," 2020 Conference on Lasers and Electro-Optics (CLEO), San Jose, CA, USA, 2020, pp. 1-2

P21 A.M. Andrews, M.A. Kainz, H. Detz, M. Beiser, M. Giparakis, W. Schrenk, S. Schönhuber, K. Unterrainer, and G. Strasser, "Barrier Height selection for high temperature THz quantum cascade lasers", Euro MBE Workshop, Lenggries, Germany, Feb 18, 2019

P22 B. Schwarz, N Opacak, J. Hillbrand, M. Beiser, G. Strasser, R. Weih, A. Schade, S. Höfling, D. Auth, S. Breuer, M. Piccardo, F. Capasso, "Frequency modulated combs in semiconductor lasers", IEEE IPS 2019, San Antonio, USA, Sep 29 – Oct 3, 2019

P23 B. Schwarz, J. Hillbrand, M. Beiser, N. Opacak, A.M. Andrews, H. Detz, G. Strasser, A. Schade, R. Weih, S. Höfling, "Towards monolithic and battery driven mid-infrared dual-comb spectrometers", ITQW 2019, Ojai, USA, Sep 15 – 20, 2019

P24 A.M. Andrews, M Kainz, S. Schönhuber, B. Limbacher, H. Detz, M. Beiser, M. Giparakis, W. Schrenk, G. Strasser, G. Bastard, K. Unterrainer, "Laser Level Selection in Terahertz Quantum Cascade Lasers", IEEE RAPID, Miramar Beach, USA, Aug 19 – 21, 2019

P25 M. Giparakis, M.A. Kainz, S. Schönhuber, B. Limbacher, H. Detz, M. Beiser, W. Schrenk, A.M. Andrews, G. Strasser, G. Bastard, K. Unterrainer, "Selective Emission of a THz QCL using a Magnetic Field", DEMBE 2019, Würzburg, Germany, Oct 7 – 8, 2019

P26 B. Schwarz, J. Hillbrand, M. Beiser, A.M. Andrews, G. Strasser, H. Detz, A. Schade, R. Weih, S. Höfling, "Interband Cascade Lasers for Monolithic and Battery Driven Dual-Comb Spectrometers", CLEO/Europe-EQEC 2019, Munich, Germany, Jun 23 – 27, 2019

P27 B. Schwarz, J. Hillbrand, M. Beiser, A.M. Andrews, G. Strasser, H. Detz, A. Schade, R. Weih, S. Höfling, "Interband cascade laser frequency combs for monolithic and battery driven spectrometers", CLEO 2019, San Jose, USA, May 5 - 10, 2019

P28 N. Opacak, M. Beiser, N. Opacak, S. dal Cin, H. Detz, A.M. Andrews, G. Strasser and B. Schwarz, "QWIPs and QCDs for RF", 68th Annual Meeting of the Austrian Physical Society, Graz, AUT, Aug 19 – 23, 2018

P29 B. Schwarz, J. Hillbrand, M. Beiser, M. Piccardo, P. Chevalier, A. Schade, H. Detz, M. Andrews, G. Strasser, F. Capasso, S. Höfling, "QCL and ICL frequency combs

for miniaturized sensors", SPIE Optics + Photonics, San Diego, USA, Aug 19 – 23, 2018

P30 J. Hillbrand, M. Beiser, A. Schade, H. Detz, A.M. Andrews, G. Strasser, S. Höfling, B. Schwarz, "Mid-Infrared Frequency Comb based on Actively Modelocked Interband Cascade Laser", 34th ICPS, Montpellier, France, Jul 29 – Aug 3, 2018

P31 B. Schwarz,J. Hillbrand, M. Beiser, A. Schade, G. Strasser, S. Höfling, "Actively Modelocked Interband Cascade Lasers", 8th IQCLSW, Cassis, France, Sept 2 – Sept 7, 2018

Maximilian Ludwig Beiser

max@beiser.at
in maximilian-beiser-024794170

Education

2019–2022 **PhD**, *TU Wien*, Institute of Festkörperelektronik

title *Engineering of high bandwidth frequency combs*

supervisors em. Univ.-Prof.Dr. Gottfried Strasser, Ass.-Prof. Dr. Benedikt Schwarz, Ass.-Prof. Dr. A. M. Andrews

description Molecular Beam Epitaxy of novel quantum materials for mid-infrared quantum cascade laser frequency comb, Engineering of high bandwidth quantum cascade laser frequency combs.

2016–2018 **MSc (Physics)**, *University of Innsbruck*, Institute for Experimental Physics
Thesis: Monolithic Frequency Combs using Interband Cascade Lasers

supervisors Univ.-Prof. Dr. Gregor Weihs, Dr. Robert Keil

2012–2016 **BSc (Physics)**, *Universität Innsbruck*
Thesis: Quantum Information with Photons - Multiphotoninterference

supervisors Univ.-Prof. Dr. Gregor Weihs, Dr. Robert Keil

2007–2012 **Matura (equiv. A-level) with distinction**, *Secondary Technical College of Mechanical Engineering and Automation*, Bregenz, Austria

thesis *Construction of compact Abrasive Flow Machining for high pressure tools.*

Awards and Scholarships

2017 **FWF Research Scholarship for diploma students**, M. Beiser " Mid-Infrared Frequency Combs"

Professional Experience

January 2019-March 2022 **Project assistant**, *Institute of Solid State Electronics and CMNS, TU Wien*

July-December 2018 **Technician**, *Institute of Solid State Electronics and CMNS, TU Wien*
Support for cleanroom work and assistance for moving the cleanroom equipment to the new institute building in CH

2017-2022 **Research assistant**, *Institute of Solid State Electronics and CMNS, TU Wien*, Wien
Topic: Mid-Infrared Frequency Combs

Achievements

- Growth of an octave spanning Terahertz Quantum Cascade Laser
- Demonstration of strain compensated growth of Interband Cascade Lasers
- Editors pick for "Engineering the spectral bandwidth of quantum cascade laser frequency combs", Optics Letters, 2021 (14)
- Co-Author on "Phase Noise induced Frequency Combs" Nature. 2020; 582 (7812)
- 14 peer-reviewed journal publications, of which 2 as the first author.
- h-index of 7 and 291 citations (Google Scholar, June 2022)

Languages

German	mother tongue
English	business fluent

Other Skills

Programming	Python		
Technical tools	Matlab, Origin, AutoCad, SolidWorks, Inventor, COMSOL	Productivity suites	Open/Libre Office, Microsoft Office, Latex
Operating License	Car and Fork lift driver certificate		

Competences

Languages

- German (mother tongue)
- English (business fluent)

Other skills

Programming & scripting	Python	Operating systems	Linux, Mac OS X, Windows
Technical tools	Matlab, Origin, AutoCad, SolidWorks, Inventor, COMSOL	Productivity suites	Open/Libre Office, Microsoft Office, Latex
Experimental Skills	Manufacturing and processing in clean room, optical and electrical characterization, laser optics, optics		

References

University

- Univ.-Prof. Gottfried Strasser(TUW)
- Prof. A.M.Andrews (TUW)
- Prof. Benedikt Schwarz (TUW)
- Dr. Hermann Detz

Industry

- Dr. Johannes Hillbrand, Fa. Sensirion (CH)
- Dr. Hedwig Knötig, Fa. Sensirion (CH)
- Dr. Robert Weih, Fa. nanoplus, (D)
- Markus Waibel, Fa. Beiser Galvanik

List of publications

Journal publications

J1 M. Beiser*, N. Opacak*, J. Hillbrand, G. Strasser, and B. Schwarz "Engineering the spectral bandwidth of quantum cascade laser frequency combs"; *Optics Letters* (2021)

J2 M.Jaidl*, M. Beiser*, M.A.Kainz, D. Theiner, B. Limbacher, M. Giparakis, A.M.Andrews, J. Darmo and K. Unterrainer "Ultra-Broadband Heterogeneous THz Quantum Cascade Laser"; *ACS Photonics* (2022),

Journal Publications as co-author

J1 B. Schwarz, J. Hillbrand, M. Beiser, A. Schade, G. Strasser, S. Höfling, "Monolithic frequency comb platform based on interband cascade lasers and detectors"; *Optica* (2019)

J2 J. Hillbrand, M. Beiser, A.M. Andrews, H. Detz, R. Weih, A. Schade, S. Höfling, G. Strasser, B. Schwarz, "Picosecond mid-infrared pulses from an interband cascade laser"; *Optica* (2019)

J3 M. Piccardo, B. Schwarz, M. Beiser, D. Kazakov, Y. Wang, A. Belyanin, and F. Capasso, "Frequency combs induced by phase turbulence"; *Nature* (2020),

J4 M. Piccardo, N. Opacak, M. Beiser, A. Belyanin, B. Schwarz, Marco Piccardo and F. Capasso, "Defect-engineered harmonic frequency comb"; *Optica*, submitted (2020),

J5 M. Jaidl, N. Opacak, M. A. Kainz, S. Schönhuber, D. Theiner, B. Limbacher, M. Beiser, M. Giparakis, A. M. Andrews, G. Strasser, B. Schwarz, J. Darmo, and K. Unterrainer "Comb Operation in Terahertz Quantum Cascade Ring Lasers"; *Optica* (2021),

J6 L.M. Krüger, J. Hillbrand, J. Heidrich, M. Beiser, R. Weih, J. Köth, C.R.Phillips, B. Schwarz, G. Strasser and U. Keller "High-Speed mid-infrared Interband Cascade Detectors: Photo-Response Saturation by a Femtosecond Oscillator"; *Optics Express* (2021),

J7 D. Kazakov, N. Opacak, M. Beiser,A. Belyanin, B. Schwarz, M. Piccardo and F. Capasso "Defect-engineered harmonic frequency combs in ring quantum cascade lasers"; *Optica* (2021),

J8 L. Mennel, A.J.Molina-Mendoza, M. Paur, D. K. Polyushkin, D. Kwak, M. Giparakis, M. Beiser, A.M. Andrews, and T. Mueller "A photosensor employing data-driven binning for ultrafast image recognition"; *Nature Photonics* (2021),

J9 M.Jaidl,N. Opacak, M.A.Kainz, D. Theiner, B. Limbacher, M. Beiser, M. Giparakis, A.M.Andrews, J. Darmo and K. Unterrainer "Silicon Integrated Terahertz Quantum Cascade Ring Laser Frequency Comb"; *Applied Physics Letters* (2021),

J10 M. Giparakis, H. Knötig, H. Detz, M. Beiser, W. Schrenk, B. Schwarz, G. Strasser, and A. M. Andrews "2.7 µm Quantum Cascade Detector: Above Band Gap Energy Intersubband Detection"; *Applied Physics Letters* (2021),

J11 E. Bakali, W. Artner, M. Beiser, J. Bernardi, H. Detz, G. Eguchi, A. Foelske, M. Giparakis, C. Herzig, A. Limbeck , H. Nguyen, L. Prochaska, A. Prokofiev, M. Sauer, S. Schwarz, W. Schrenk, G. Strasser, R. Svagera, M. Taupin, A.S. Thirsfeld, M. Waas, X. Yan, D.A. Zocco ,A.M. Andrews and S. Paschem "A Knudsen cell approach for the molecular beam epitaxy of the heavy fermion compound $YbRh_2Si_2$"; *Journal of Crystal Growth* (2022),

J12 M. Giparakis, M. A. Kainz, M. C. Ertl, and A. M. Andrews "Anomalous temperature effect in weakly-coupled superlattices: Carrier transport in a THz quantum cascade laser"; *Physical Review Letters, submitted* (2023),

J13 D. Kazakov, T. Letsou, M. Beiser, Y. Zhi, N. Opacak, M. Piccardo, B. Schwarz, F. Capasso "Active mid-infrared ring resonators"; *Nature Communications, submitted* (2023),

J14 N. Opacak, D. Kazakov, L. Colombo, M. Beiser, T. Letsou, F. Pilat, M. Brambilla, F. Prati, M. Piccardo, F. Capasso and B. Schwarz "Nozaki-Bekki optical solitons"; *Nature, submitted* (2023),

Thesis

M. Beiser, *Monolithic frequency combs in the mid-infrared using interband cascade lasers, Technische Universität Wien, June 2018*

Poster Presentations

P1 M. Beiser, J.Hillbrand, A.M. Andrews, R. Weih, S. Höfling, G. Strasser and B. Schwarz "Picosecond Pulses in Interband Cascade Lasers"; *IQCLSW*, Teleconference, Switzerland (2020)

P2 J. Hillbrand, S. Dal Cin, B. Schwarz, M. Beiser, A.M. Andrews, G. Strasser, "RF QWIPs for Characterization of mid-IR Frequency Combs", 20th Int. Winterschool on New Developments in Solid State Physics, Mauterndorf, Austria, Feb 25 – Mar 2, 2018 M. Beiser, J. Hillbrand, S. Dal Cin, H. Detz, A.M. Andrews, G. Strasser, B. Schwarz, "QWIPs and QCDs for Mid-Infrared Frequency Combs", IQCLSW 2018, Cassis, France, Sep 2 – 7, 2018

P3 M. Beiser, B. Schwarz, A. Harrer, M. Holzbauer, H. Detz, A.M. Andrews and G. Strasser: "Bifunctional Quantum cascade laser detectors"; *MBE Workshop*, Vienna, Austria (2017)

P4 M. Beiser, J.Hillbrand, B. Schwarz, S. dal Cin, H. Detz, A.M. Andrews and G. Strasser: "Radiofrequency QWIPs and QCDs"; *IQCLSW*, Cassis, France (2018)

P5 S. Isceri, M. Giparakis, M. Beiser, H. Detz, W. Schrenk, S. Bühler-Paschen, G. Strasser, A.M. Andrews, "Epitaxy of YbRh2Si2 on Ge(001)", German MBE Workshop 2021, Göttingen, Germany, Oct 14 - 15, 2021

Oral Presentation

P1 M. Beiser J. Hillbrand, A. Schade, H. Detz, M. Andrews, G. Strasser, S. Höfling, and B. Schwarz "Mode-locked Interband Cascade Lasers", 68th Annual Meeting of the Austrian Physical Society, Graz, AUT, Sept 12 – 14, 2018

P2 M. Beiser, H. Knötig, B. Hinkov, N. Opacak, M. Holzbauer, R. Szedlak, H. Detz, R. Weih, S. Höfling, W. Schrenk, J. Koeth, and G. Strasser, "Surface emitting ring interband cascade lasers", 68th Annual Meeting of the Austrian Physical Society, Graz, AUT, Aug 19 – 23, 2018

P3 M. Beiser, M. Giparakis, H. Knötig, H. Detz, M. Giparakis, B. Schwarz, A.M. Andrews, G. Strasser, "Strain Balancing for InAs Based ICL growth", MBE XXI, Mexico, ONLINE, Sep 6 – 9, 2021

P4 M. Beiser, J. Hillbrand, A.M. Andrews, R. Weih, S. Höfling, G. Strasser, B. Schwarz, "Monolithic Frequency Comb Generation and High-speed Detection based on Interband Cascade Structures", DEMBE 2019, Würzburg, Germany, Oct 7 – 8, 2019

Oral presentation without conference proceeding as co-author

P1 B. Schwarz, F. Pilat, N. Opacak, S. Dal Cin, J. Hillbrand, M. Beiser, G. Strasser, R. Weih, S. Hofling, M. Piccardo, F. Capasso, "Integrated mid-infrared semiconductor laser frequency combs", Nano and Photonics, Mauterndorf, Austria, Mar 15 – 17, 2023

P2 N. Opacak, D. Kazakov, L.L. Columbo, M. Beiser, F. Pilat, G. Strasser, M. Brambilla, F. Prati, M. Piccardo, B. Schwarz, "Parametric processes and nonlinear dynamics of self-starting frequency combs", Photonics West, San Francisco, USA, Jan 28 – Feb 2, 2023

P3 M. Jaidl, N. Opacak, D. Theiner, M. Ertl, B. Limbacher, M. Beiser, M. Giparakis, A.M. Andrews, G. Strasser, B.Schwarz, K. Unterrainer, "Terahertz quantum cascade ring lasers: comb operation and integration on Si-substrates", Photonics West, San Francisco, USA, Jan 28 – Feb 2, 2023

P4 M. Giparakis, H. Knoetig, S. Isceri, M. Beiser, H. Detz, W. Schrenk, B. Schwarz, G. Strasser, A.M. Andrews, "MBE Growth and Characterization of an InAs/$AlAs_{0.16}Sb_{0.88}$ quantum cascade detector at 2.7 µm", NAMBE, Reheboth Beach, USA, Sep 18 – 22, 2022

P5 M. Giparakis, H. Knoetig, M. Beiser, H. Detz, B. Schwarz, W. Schrenk, G. Strasser, A.M. Andrews, "Short-Wavelength InAs-based Quantum Cascade Detector Operating at 2.7 µm", IEEE Rapid, Miramar Beach, USA, Sep 12 – 14, 2022

P6 M. Jaidl, N. Opacak, M.A. Kainz, D. Theiner, B. Limbacher, M. Beiser, M. Giparakis, A.M. Andrews, G. Strasser, B. Schwarz, J. Darmo, K. Unterrainer, "Silicon Integrated Terahertz Quantum Cascade Ring Laser Frequency Comb", IQCLSW2022, Zürich Monte Verita, Switzerland, Aug 23 -28, 2022

P7 B. Schwarz, F. Pilat, N. Opacak, S. Dal Cin, J. Hillbrand, M. Beiser, G. Strasser, R. Weih, S. Hofling, M. Piccardo, F. Capasso, "Integrated mid-infrared semiconductor laser frequency combs", mir5ens, Wroclaw, Poland, Jul 4 – 6, 2022

P8 M. Ertl, M. Jaidl, B. Limbacher, D. Theiner, M. Kainz, M. Giparakis, M. Beiser, A.M. Andrews, G. Strasser, J. Darmo, K. Unterrainer, "Epi-down Bonded Quantum Cascade Patch Antenna Array Laser", 9th International Conference on Optical Terahertz Science and Technology (OTST 2022), Budapest, Hungary. Jun 19 - 24 2022

P9 M. Giparakis, H. Knoetig, H. Detz, M. Beiser, W. Schrenk, B. Schwarz, G. Strasser, A.M. Andrews, "Top-Side Illuminated InAS/AlAsSb Quantum Cascade Detector at 2.7µm", CLEO, San Jose, USA, May 15 – 20, 2022

P10 S. Isceri, M. Giparakis, E. Bakali, M. Beiser, H. Detz, W. Schrenk, G. Strasser, M. Waas, R. Svagera, S. Bühler-Paschen, "Single crystal growth of YbRh2Si2", DGKK/DEMBE 2022, Bremen, Germany. May 16 - 18, 2022

P11 M. Jaidl, D. Theiner, B. Limbacher, M. Beiser, A.M. Andrews, G. Strasser, J. Darmo, K. Unterrainer, "QCL and fibre laser-driven frequency combs", SPIE Photonics Europe, Strasbourg, France, Apr 3 –7, 2022

P12 B. Schwarz, N. opacak, F. Pilat, D. Kazakov, S. Dal Cin, N. Beiser, L. Columbo, J. Hillbrand, M. Piccardo, F. Capasso, "Frequency comb operation induced by a giant Kerr nonlinearity in quantum cascade lasers", SPIE Photonics Europe, Strasbourg, France, Apr 3 –7, 2022

P13 B. Schwarz, M. Beiser, F. Pilat, S. Dal Cin, J. Hillbrand, R. Weih, J. Koeth, S. Höfling, "Interband cascade laser frequency combs", SPIE Photonics Europe, Strasbourg, France, Apr 3 –7, 2022

P14 F. Pilat, N. Opacak, H. Knötig, M. Beiser, S. Dal Cin, J. Hillbrand, R. Weih, B. Schwarz, "Mid-infrared semiconductor frequency combs", Optica High-Brightness Sources and Light-Driven Interactions Congress 2022, Budapest, Hungary, Mar 23 - 25 2022

P15 A.M. Andrews, M. Giparakis, H. Knötig, S. Isceri, M. Beiser, W. Schrenk, B. Schwarz, G. Strasser, "Above band gap energy InAs/AlAsSb quantum cascade detector", Workshop on Compound

Semiconductor Materials and Devices (WOCSEMMAD) 2022, Destin Beach, FL, USA, Feb 20 - 22, 2022

P16 B. Schwarz, M. Beiser, S. Dal Cin, J. Hillbrand, N. Opacak, G. Strasser, H. Schneider, M. Piccardi, F. Capasso, R. Weih, "Mid-infrared frequency combs based on semiconductor lasers", Photonics West, ONLINE, Mar 6 – 11, 2021

P17 M. Giparakis, H. Knötig, H. Detz, M. Beiser, B. Schwarz, W. Schrenk, G. Strasser, A.M. Andrews, "Growth, Design, and Characterisation of an InAs/AlAsSb-based QCD at 2.7 m", German MBE Workshop, Garching, Deutschland, Oct 13 - 14, 2022

P18 M. Piccardo et al., "Ring Laser Frequency Combs Enabled by Phase Turbulence and Their Connection to Kerr Combs," 2020 Conference on Lasers and Electro-Optics (CLEO), San Jose, CA, USA, 2020, pp. 1-2

P19 D. Kazakov, M. Piccardo, M. Beiser, N. Opacak, Y. Wang, A. Belyanin, B. Schwarz, and F. Capasso, "Shaping harmonic frequency combs in ring injection lasers by defect engineering," in Conference on Lasers and Electro-Optics, OSA Technical Digest (Optical Society of America, 2020), paper STh3E.8

P20 M. Piccardo et al., "Ring Laser Frequency Combs Enabled by Phase Turbulence and Their Connection to Kerr Combs," 2020 Conference on Lasers and Electro-Optics (CLEO), San Jose, CA, USA, 2020, pp. 1-2

P21 A.M. Andrews, M.A. Kainz, H. Detz, M. Beiser, M. Giparakis, W. Schrenk, S. Schönhuber, K. Unterrainer, and G. Strasser, "Barrier Height selection for high temperature THz quantum cascade lasers", Euro MBE Workshop, Lenggries, Germany, Feb 18, 2019

P22 B. Schwarz, N Opacak, J. Hillbrand, M. Beiser, G. Strasser, R. Weih, A. Schade, S. Höfling, D. Auth, S. Breuer, M. Piccardo, F. Capasso, "Frequency modulated combs in semiconductor lasers", IEEE IPS 2019, San Antonio, USA, Sep 29 – Oct 3, 2019

P23 B. Schwarz, J. Hillbrand, M. Beiser, N. Opacak, A.M. Andrews, H. Detz, G. Strasser, A. Schade, R. Weih, S. Höfling, "Towards monolithic and battery driven mid-infrared dual-comb spectrometers", ITQW 2019, Ojai, USA, Sep 15 – 20, 2019

P24 A.M. Andrews, M Kainz, S. Schönhuber, B. Limbacher, H. Detz, M. Beiser, M. Giparakis, W. Schrenk, G. Strasser, G. Bastard, K. Unterrainer, "Laser Level Selection in Terahertz Quantum Cascade Lasers", IEEE RAPID, Miramar Beach, USA, Aug 19 – 21, 2019

P25 M. Giparakis, M.A. Kainz, S. Schönhuber, B. Limbacher, H. Detz, M. Beiser, W. Schrenk, A.M. Andrews, G. Strasser, G. Bastard, K. Unterrainer, "Selective Emission of a THz QCL using a Magnetic Field", DEMBE 2019, Würzburg, Germany, Oct 7 – 8, 2019

P26 B. Schwarz, J. Hillbrand, M. Beiser, A.M. Andrews, G. Strasser, H. Detz, A. Schade, R. Weih, S. Höfling, "Interband Cascade Lasers for Monolithic and Battery Driven Dual-Comb Spectrometers", CLEO/Europe-EQEC 2019, Munich, Germany, Jun 23 – 27, 2019

P27 B. Schwarz, J. Hillbrand, M. Beiser, A.M. Andrews, G. Strasser, H. Detz, A. Schade, R. Weih, S. Höfling, "Interband cascade laser frequency combs for monolithic and battery driven spectrometers", CLEO 2019, San Jose, USA, May 5 - 10, 2019

P28 N. Opacak, M. Beiser, N. Opacak, S. dal Cin, H. Detz, A.M. Andrews, G. Strasser and B. Schwarz, "QWIPs and QCDs for RF", 68th Annual Meeting of the Austrian Physical Society, Graz, AUT, Aug 19 – 23, 2018

P29 B. Schwarz, J. Hillbrand, M. Beiser, M. Piccardo, P. Chevalier, A. Schade, H. Detz, M. Andrews, G. Strasser, F. Capasso, S. Höfling, "QCL and ICL frequency combs for miniaturized sensors", SPIE Optics + Photonics, San Diego, USA, Aug 19 – 23, 2018

P30 J. Hillbrand, M. Beiser, A. Schade, H. Detz, A.M. Andrews, G. Strasser, S. Höfling, B. Schwarz,

"Mid-Infrared Frequency Comb based on Actively Modelocked Interband Cascade Laser", 34th ICPS, Montpellier, France, Jul 29 – Aug 3, 2018

P31 B. Schwarz,J. Hillbrand, M. Beiser, A. Schade, G. Strasser, S. Höfling, "Actively Modelocked Interband Cascade Lasers", 8th IQCLSW, Cassis, France, Sept 2 – Sept 7, 2018

Acknowledgements

This thesis is the summary of years of multiple events and tremendous support of many people in my life to allow me to pursue higher education and a quantum of technology. My PhD had not the typical start and not the typical end, but it was the most valuable education I ever got.

My deepest gratitude goes to Em. Univ.-Prof. Dr. Gottfried Strasser. His easy and hands-on approach to deal with physical and political problems was a master class for my career. Many times he gave thoughtful advice, I could not imagine a better fit for a doctoral father. I will be forever inspired by the quantum innovator. On a side note, my PhD journey started two weeks after I joined the group for my master thesis, when he suggested I should stay for a PhD. I hope I honored this trust, the MBE was a sensei par excellence and truely catalyzed my personal development.

Associate Prof. Dr. Benedikt Schwarz took me under his wings during his post doc and continuously motivated me to aim for high impact research and not be afraid of riskful enterprises. His deep understanding of semiconductor physics and quantum cascade lasers were truly inspiring to investigate and step up my scientific writing.

Associate Prof. Dr. Aaron Maxwell Andrews was an incredible supportive and instructive teacher in all things related to epitaxy. He allowed me to learn MBE growth in depth from scratch to cross-hatch. I never knew I could be so fascinated by technology until we disassembled the MBE in the old cleanroom for the first time. In addition I only can appreciate his rigor with presentations and tables after my time at the institute.

Dr. Hermann Detz shared my passion for coffee and exotic research topics. Many discussions started with daily life or business issues and ended up in programming problems or novel research ideas. I always appreciated his positive approach for difficult problems.

Em. Univ.-Prof. Dr. Erich Gornik is a living FKE legend and a role model for embracing the scientist way of living. I am truly inspired by his unbroken passion and drive for physics and academia.

Dr. Werner Schrenk is the godfather of the MBE lab and all fabrication related questions. Many times his simple and deep questions schooled me over and over. He is the one dotting the i,s and crossing the t,s in the cleanroom and it does not matter if brown out, black out or time out. I hope for the CMNS and future students that he stays healthy and does not play excessive football with the photonic guys, he can not be replaced.

Dr. Johannes Hillbrand was the very reason I ended up in the institute after a typical Vorarlbergian "I know somebody there" situation. His motivational skills and creative thinking allowed multiple breakthroughs and pushed me many times to not give up. His infectious enthusiasm helped me through many MBE related valley. I am excited to see what he pulls of at Sensirion.

Dr. Nikola Opacak was a great example of rigorousity and professional work attitude on

a daily base. I am very proud that our collaboration was awarded with an Editors pick. The esteemed gentleman still owes me one million dollars.
Grandmaster Sandro Dal Cin is a benchmark for sophisticated and smart engineering solutions. Aside from securing monkeyheads during climbing, he intuitively and annoyingly finds all flaws in my brain farty engineering projects. Hopefully he gets the job at Vance Refrigeration.
Dr. Hedwig Knötig shared many ups and downs during my time at the Institute and relentlessly socialized us with outstanding cooking during the pandemic. She listened to problems ranging from gallium growth rates to torn muscles or forgotten speed tickets and always lightened up my spirits.
Dr. Michael Jaidl and Dr. Martin Alexander Kainz were highly appraised photonists and under the thoughtful guidance of Univ.-Prof. Dr. Karl Unterrainer I was allowed to collaborate with them on one of the most significant technological milestones in my career. The undisputed Monster of growth sheets showed what a hands-on approach to problem solving and a short, straight forward communication can achieve. I got no clue, if we saved the world with ElMonstro, but for sure we could win a wrestling competition.
In addition I want to thank the whole FKE group Florian Pilat, Rolf Szedlak, Mikolaj Piotrowski, Miriam Giparakis, Stefania Isceri, Lucas Prohaska, Masiah Sistani, Raphael Behrle, Elena Arigliani, Borislav Hinkov, Georg Marschick, Jakob Genser, Max Bartmann and the best office plant Don MacFarland. All of you contributed to my PhD experience by socializing, practical jokes or lunch breaks.
I want to thank Johanna, Markus and Marlene for your loving support, listening to my complaints, spending time on and off the track or in nature and being such tremendous human beings over all these years. I have to stay in shape to keep up with all of your kids.
I want to thank my siblings Konstantin and Theresia Viktoria for having my back, kicking my ass when required and telling inconvenient truths. I am a rich man to have you two so close in my life.
Thank you for your love and support during the pandemic, V. You truly taught me how to let go.
I want to thank my dad for his never ending, always encouraging pragmatism in life. My inherited technical common sense apparently brought me places and I still got the way to engineering.
I dedicate this thesis in loving memory to my mom. You taught me how to fight for myself and stand up with my shoulders straight. I still aim for the stars and shoot for the moon. I know you would be proud.
Pura Vida, MB